m 60

J. Timothy Londergan John P. Carini
David P. Murdock

Binding and Scattering in Two-Dimensional Systems

Applications to Quantum Wires, Waveguides and Photonic Crystals

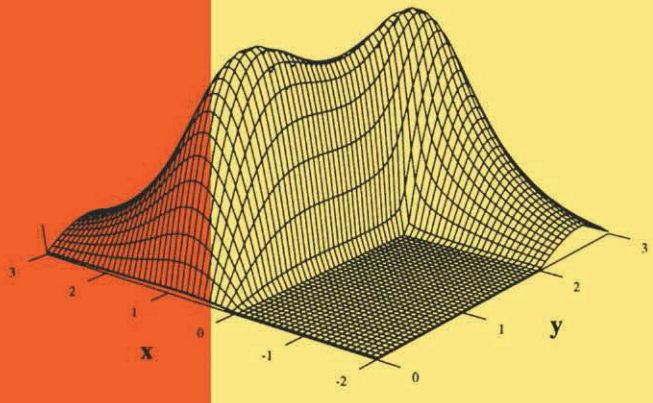

Springer

Lecture Notes in Physics

Monographs

Editorial Board

R. Beig, Vienna, Austria
J. Ehlers, Potsdam, Germany
U. Frisch, Nice, France
K. Hepp, Zürich, Switzerland
R. L. Jaffe, Cambridge, MA, USA
R. Kippenhahn, Göttingen, Germany
I. Ojima, Kyoto, Japan
H. A. Weidenmüller, Heidelberg, Germany
J. Wess, München, Germany
J. Zittartz, Köln, Germany

Managing Editor

W. Beiglböck
c/o Springer-Verlag, Physics Editorial Department II
Tiergartenstrasse 17, D-69121 Heidelberg, Germany

Springer
Berlin
Heidelberg
New York
Barcelona
Hong Kong
London
Milan
Paris
Singapore
Tokyo

The Editorial Policy for Monographs

The series Lecture Notes in Physics reports new developments in physical research and teaching - quickly, informally, and at a high level. The type of material considered for publication in the monograph Series includes monographs presenting original research or new angles in a classical field. The timeliness of a manuscript is more important than its form, which may be preliminary or tentative. Manuscripts should be reasonably self-contained. They will often present not only results of the author(s) but also related work by other people and will provide sufficient motivation, examples, and applications.
The manuscripts or a detailed description thereof should be submitted either to one of the series editors or to the managing editor. The proposal is then carefully refereed. A final decision concerning publication can often only be made on the basis of the complete manuscript, but otherwise the editors will try to make a preliminary decision as definite as they can on the basis of the available information.
Manuscripts should be no less than 100 and preferably no more than 400 pages in length. Final manuscripts should be in English. They should include a table of contents and an informative introduction accessible also to readers not particularly familiar with the topic treated. Authors are free to use the material in other publications. However, if extensive use is made elsewhere, the publisher should be informed. Authors receive jointly 30 complimentary copies of their book. They are entitled to purchase further copies of their book at a reduced rate. No reprints of individual contributions can be supplied. No royalty is paid on Lecture Notes in Physics volumes. Commitment to publish is made by letter of interest rather than by signing a formal contract. Springer-Verlag secures the copyright for each volume.

The Production Process

The books are hardbound, and quality paper appropriate to the needs of the author(s) is used. Publication time is about ten weeks. More than twenty years of experience guarantee authors the best possible service. To reach the goal of rapid publication at a low price the technique of photographic reproduction from a camera-ready manuscript was chosen. This process shifts the main responsibility for the technical quality considerably from the publisher to the author. We therefore urge all authors to observe very carefully our guidelines for the preparation of camera-ready manuscripts, which we will supply on request. This applies especially to the quality of figures and halftones submitted for publication. Figures should be submitted as originals or glossy prints, as very often Xerox copies are not suitable for reproduction. For the same reason, any writing within figures should not be smaller than 2.5 mm. It might be useful to look at some of the volumes already published or, especially if some atypical text is planned, to write to the Physics Editorial Department of Springer-Verlag direct. This avoids mistakes and time-consuming correspondence during the production period.
As a special service, we offer free of charge LaTeX and TeX macro packages to format the text according to Springer-Verlag's quality requirements. We strongly recommend authors to make use of this offer, as the result will be a book of considerably improved technical quality.
Manuscripts not meeting the technical standard of the series will have to be returned for improvement.
For further information please contact Springer-Verlag, Physics Editorial Department II, Tiergartenstrasse 17, D-69121 Heidelberg, Germany.

J. Timothy Londergan John P. Carini
David P. Murdock

Binding and Scattering in Two-Dimensional Systems

Applications to Quantum Wires, Waveguides and Photonic Crystals

Springer

Author

J. Timothy Londergan
John P. Carini
David P. Murdock
Nuclear Theory Center
Indiana University
Swain Hall West 306
Bloomington, IN 47405, USA

Library of Congress Cataloging-in-Publication Data.

Die Deutsche Bibliothek - CIP-Einheitsaufnahme

Londergan, J. Timothy:
Binding and scattering in two-dimensional systems : applications to quantum wires, waveguides and photonic crystals / J. Timothy Londergan ; John P. Carini ; David P. Murdock. - Berlin ; Heidelberg ; New York ; Barcelona ; Hong Kong ; London ; Milan ; Paris ; Singapore ; Tokyo : Springer, 1999
(Lecture notes in physics : N.s. M, Monographs ; 60)
ISBN 3-540-66684-2

ISSN 0940-7677 (Lecture Notes in Physics. Monographs)
ISBN 3-540-66684-2 Springer-Verlag Berlin Heidelberg New York

This work is subject to copyright. All rights are reserved, whether the whole or part of the material is concerned, specifically the rights of translation, reprinting, reuse of illustrations, recitation, broadcasting, reproduction on microfilm or in any other way, and storage in data banks. Duplication of this publication or parts thereof is permitted only under the provisions of the German Copyright Law of September 9, 1965, in its current version, and permission for use must always be obtained from Springer-Verlag. Violations are liable for prosecution under the German Copyright Law.

© Springer-Verlag Berlin Heidelberg 1999
Printed in Germany

The use of general descriptive names, registered names, trademarks, etc. in this publication does not imply, even in the absence of a specific statement, that such names are exempt from the relevant protective laws and regulations and therefore free for general use.

Typesetting: Camera-ready by the authors
Cover design: *design & production*, Heidelberg

Printed on acid-free paper
SPIN: 10644474 55/3144/du - 5 4 3 2 1 0

Preface

The last few years have seen revolutionary advances in our understanding of the electronic properties of quantum heterostructures. An enormous amount of research has been undertaken on both the experimental and the theoretical aspects of electronic transport in nanostructures. The field now covers a vast spectrum of topics, and an extensive number of books, review articles, papers and conference proceedings continue to be published in this area. Complete coverage of this exciting and evolving field is beyond the scope of this book. We refer the interested reader to some of the excellent and comprehensive books and conference proceedings on this subject.

Much progress has been made in our understanding of quantum confined systems. As is well known, it is possible to construct quantum heterostructures which are well approximated as quasi-two-dimensional, one-dimensional or zero-dimensional systems. Our interest here is in the properties of particles and fields in quasi two-dimensional (2-D) systems. We provide a brief introduction to the physics of 2-D systems, in particular to motion in 2-D systems confined within a finite area. For simplicity, we will generally assume that the system boundary is defined by an infinite hard wall potential. Such a confined 2-D system will be referred to as a *tube*, or interchangably as a *wire*. We will investigate the behavior of particles moving in a tube with perfect hard-wall boundary conditions, with emphasis on the qualitative effects which govern binding and transmission of particles in confined 2-D systems.

Our goal is to convince the reader that rather simple models of binding and scattering in 2-D systems can be remarkably successful in describing even rather complicated phenomena. We will first review the general conditions which produce bound states for particles in confined tubes. Some powerful theorems guarantee the existence of bound states under rather simple and general physical conditions. Next we discuss the properties of transmission and reflection, conductance and quantum probability flow in 2-D systems. Physical situations are analyzed using a transfer-matrix approach. Although this is neither the most efficient nor the most elegant method for calculating transport in 2-D systems, it is shown that transfer matrix techniques have a very straightforward physical interpretation and that they provide considerable understanding of the physics which governs particle transport. We

emphasize that much insight can be obtained from an analysis of quantum probability flow in 2-D systems.

This book is written to be accessible to anyone with an undergraduate background in quantum mechanics and electromagnetism, plus some elementary condensed matter physics. It emphasizes basic concepts throughout and describes simple models through which complex scattering phenomena can be observed and understood in these systems. For examples of these transport phenomena, we frequently refer to results involving electrons in mesoscopic systems. However, we show that analogous behavior can also be observed for electromagnetic fields in conventional waveguides. We emphasize the connections (and contrasts) between electron motion in quantum structures and electromagnetic states in waveguides. A third field, the study of optical states in photonic crystals, is much more recent and highly promising. Again, we show that the simple models employed in this book are capable of understanding the mechanisms for producing localized modes in photonic crystals, and we discuss similarities and differences between optical states in photonic crystals, electronic states in quantum heterostructures and electromagnetic fields in waveguides.

Acknowledgments

We have benefited greatly from the assistance provided by several colleagues and friends. We acknowledge especially comments and suggestions from Donald Sprung, Bob Jaffe and Pavel Exner, who carefully read all or part of this manuscript. We also thank K.-F. Berggren, Dan Goldbaum, Lee Harle, J.D. Joannopoulos, Kieran Mullen, W. Renger, Brian Serot, Dallas Trinkle, Hua Wu and Chris Yung for their contributions. The successes of this work are due largely to the assistance we have received from friends and colleagues; we take personal responsibility for any mistakes which remain.

We also wish to acknowledge several groups and institutes who have provided hospitality or support. David Murdock wishes to thank the Indiana University Nuclear Theory Center and Cyclotron Facility for their support for several visits. J.T. Londergan thanks the Special Research Centre for the Subatomic Structure of Matter, Adelaide, Australia, and particularly its Director, A.W. Thomas, for hospitality while part of this book was being written. Finally, we would like to thank the National Science Foundation for its partial support while this work was carried out. Research was supported under NSF contracts PHY-9722076 and DMR-9423088. Summer undergraduate students were supported under NSF Research Experiences for Undergraduates (REU) programs at the Indiana University Cyclotron Facility.

Bloomington, IN, September 1999

J. Timothy Londergan
John P. Carini
David P. Murdock

Contents

1. Introduction 1
1.1 The Purpose of This Book 1
1.2 An Overview of the Text 3

2. Bound States in Low-Dimensional Systems 7
2.1 Localized Modes in Constrained Two-Dimensional Systems .. 9
2.1.1 Bulges and Bound States in Tubes 11
2.1.2 Existence of Bound States in Curved Tubes of Constant Width 15
2.1.3 Bound States in Curved Tubes of Arbitrary Shape 18
2.1.4 Transfer-Matrix Formalism for Curved Tubes 23
2.1.5 Example: One-Dimensional Reduction Applied to the L-Shaped Tube 31
2.2 Bound States in Three-Dimensional Tubes 33

3. Transmission and Conductance in Tubes 37
3.1 Transmission and Reflection in a Long Tube 37
3.1.1 Example: Transmission in the L-Shaped Tube 40
3.2 Transmission and Quantum Probability Flow 47
3.3 Behavior of Electrons in Quantum Heterostructures 54
3.4 Electron Conductance in Quantum Wires 58
3.4.1 Conductance for a Many-Channel System 61
3.5 Electron Conductance Through a Straight 2-D Channel 64
3.5.1 Qualitative Features of Conductance in a 2-D Channel 66

4. Waveguide Measurements of the Properties of Curved Tubes 71
4.1 EM Fields in Thin Resonating Cavities 72
4.2 Mapping EM Energy Densities in Waveguide Cavities 73
4.3 Microwave Measurements with Curved Waveguides 75
4.3.1 Confined Mode Studies in Waveguides 76
4.3.2 Waveguide Experiments Above the Lowest Cutoff Frequency 78

5. Binding and Transmission in Wires and Waveguides 81
5.1 Tube with a Circular Bend 82
5.1.1 Bound States in the Limit of Small Curvature..... 84
5.1.2 Bound State Properties for a Circular Bend..... 86
5.1.3 Transmission in a System with a Circular Bend 91
5.2 Tube with a Single Sharp Bend 95
5.2.1 Bound States for Structures with a Sharp Bend 98
5.2.2 Sub-Cutoff Confined Modes in Curved Waveguides ... 99
5.3 A Tube with a "T-Stub" 102
5.3.1 Transmission in Structures with T-Stubs 104
5.4 Structures with Two Coupled Cells 113
5.4.1 Bound States in Systems with Two Coupled Cells 114
5.4.2 Transmission Through a System with Two Coupled Cells 123
5.4.3 Electron Conductance in Double-Bend Quantum Wires 126

6. Two-Dimensional Systems with Finite Periodic Structure . 145
6.1 Bound States in Periodic 2-D Systems 146
6.2 Origin of Band Structure in Periodic Systems 154
6.3 Transmission and Conductance in Periodic 2-D Systems 157
6.3.1 Transmission in a "Staircase" System 157
6.3.2 Transmission in the "Quantum Dot Superlattice" 163
6.4 Defects in Quantum Wire "Crystals" 173
6.4.1 Trapped Modes in Band Gaps 175

7. Localized Modes in Photonic Crystals 181
7.1 Maxwell's Equations in a Dielectric Medium 182
7.1.1 Band Structure in a Photonic Crystal 184
7.2 "Waveguides" in Photonic Crystals 187
7.3 "Bound States" in Photonic Crystal Waveguides..... 189
7.3.1 Bound States in Local Constrictions 190
7.3.2 Bound States
in Curved Photonic Band Gap Waveguides 193

8. Epilogue 197

A. Comparison of Various Approximate Quantum Wells 199
A.1 Effects of a Diffuse Surface 200
A.2 Potentials of Finite Depth 201
A.3 Effect of Sharp Boundaries on Transmission..... 202

B. Conducting Sphere on a Grounded Surface 203

References 209

Index 219

1. Introduction

1.1 The Purpose of This Book

In the past decade remarkable progress has been achieved in our understanding of the properties of electrons in mesoscopic systems. It is now possible to fabricate mesoscopic structures in which at least one of the transverse dimensions is of the order of the de Broglie wavelength for cold electrons. Conductance of low-temperature electrons in such systems will be dominated by electron wave effects. "*Quantum wires*" are quantum heterostructures where the electron motion is confined primarily to two dimensions. Hundreds of papers in the past decade have discussed the basic and applied physics of quantum heterostructures.

In this book, we do not attempt to duplicate the exhaustive work on electron properties in mesoscopic systems, particularly since there are now several excellent monographs on this topic. The interested reader may want to consult Datta's [1] account of electron transport in mesoscopic conductors, or Ferry and Goodnick's [2] comprehensive review of both theory and experiment in mesoscopic systems. The recent book by Mitin, Kochelap and Stroscio [3] contains a detailed review of the properties of electrons in quantum heterostructures. There are also very good summaries of earlier work in this field [4, 5, 6, 7, 8], as well as more recent topical conferences in this area [9, 10]. Much experimental and theoretical progress has been made in the study of structures which are well approximated as quasi two-dimensional, one-dimensional or zero-dimensional systems. A very nice recent review of the physics of low-dimensional semiconductors, at a level suitable for first-year graduate students, is given by Davies [11]. Detailed discussions of low-dimensional systems are also provided in books by Weisbuch and Vinter [12] and Kelly [13].

This book will focus on physical situations which can be well approximated as quasi-two dimensional (2-D) systems, and more specifically those where the 2-D motion is confined to a finite area. Our aim is to consider the simplest theoretical models capable of describing some aspects of this confined two-dimensional motion. In most circumstances, the model we choose is that of a sharp 2-D surface with zero (or constant) potential inside, and infinite hard wall boundaries. For time-independent scattering the resulting

J. T. Londergan, J. P. Carini and D. P. Murdock: LNPm 60, pp. 1 - 5, 1999
© Springer-Verlag Berlin Heidelberg 1999

mathematical problem is the Helmholtz equation with Dirichlet boundary conditions.

We will call a bounded 2-D surface with perfect hard wall conditions a *tube*. In some circumstances we will use the term *wire* as a synonym, particularly when we refer to those applications which involve the motion of electrons in quasi-2-D quantum heterostructures. Occasionally these terms will be used to describe three-dimensional [3-D] systems, but unless explicitly identified as a 3-D system, all references to tubes and wires in this book will imply 2-D motion. Despite the extreme simplicity of this idealized picture, hard wall tubes display a wide variety of phenomena: bound states, "*virtual bound state*" resonances, non-trivial transmission and reflection phenomena, effects of discrete symmetries, the relation of S-matrix singularities to transmission properties, and the origin of "miniband "structure in finite periodic systems.

Perhaps surprisingly, for systems which have been so widely studied, new results for constrained 2-D motion in these tubes have been obtained in the past few years. For example, under a rather general set of conditions [14], such tubes will always possess at least one bound state [15, 16, 17, 18, 19, 20, 21, 22, 23, 24]. There is also a one-to-one correspondence between particles in hard wall tubes and TE modes in electromagnetic waveguides. Consequently one can make analogies between properties of electrons in quantum wires and EM modes in conventional waveguides. Even in waveguides, systems which have been investigated for several decades, there are some surprises: for example, the existence proofs for bound states in bent tubes also predict confined EM modes below cutoff frequency in curved waveguides. To the best of our knowledge, such states were not known to exist until the past few years.

Recently, there has been much research into the properties of *photonic crystals*. In photonic crystals a lattice of dielectric materials is used to control the optical properties of a system. Recent progress in the field of photonic crystals is summarized in a book by Joannopoulos, Meade and Winn [25]. We review briefly the properties of 2-D photonic crystals and show how they can be used to control the propagation of light. Our primary interest is in the use of cavities to produce "waveguides" in photonic crystals. Scattering and "binding" properties in photonic crystal cavities are compared and contrasted with analogous states in both quantum wires and conventional waveguides.

The material presented here should be accessible to an upper-level undergraduate student in physics. It requires only a background in basic quantum mechanics and electromagnetism, and some elementary condensed matter physics. Many of the results obtained for simple 2-D geometries would fit nicely into an introductory quantum mechanics course (if there were time to consider 2-D problems, following a section on one-dimensional [1-D] models and before moving on to the physics of three-dimensional systems). This book focuses on qualitative descriptions of motion in two dimensions, and is aimed at the general reader. Our discussion of bound state and scattering properties lacks the rigor associated with mathematical physics theorems, and our

assumptions regarding quasi-two dimensional motion in semiconductors are seriously oversimplified for anyone wishing to construct a working quantum heterostructure device. On the other hand, our goal is to convey the richness of the physical phenomena one can explore in these systems, and to demonstrate that the analogy between tubes and waveguides can lead to an increased understanding of electronic, electromagnetic and optical systems.

The focus of this book is on binding and transport phenomena in simple two-dimensional systems. In particular, we are interested in comparing and contrasting analogous phenomena which occur in quantum wires, conventional waveguides, and photonic crystals. As a result, this book will not include a number of conditions which produce important effects in quantum heterostructures. First, we do not consider the effects of strong external magnetic fields in mesoscopic semiconductors. For example, neither magnetic edge states nor Aharonov–Bohm effects in quantum wires are covered here. A second topic which is not included in this book concerns effects which arise from shifts in electron trajectories around impurities in quantum heterostructures. Changes in the trajectories of electrons can arise from variation of Fermi energies in semiconductors, due to changes in external fields. Such shifts in electron trajectories can lead to universal conductance fluctuations in a mesoscopic device. Finally, this book will only consider quantum wires which have two leads. The resulting formulas for conductance will greatly simplify, but important physical effects such as the integer and fractional Quantum Hall Effect will not be discussed. Detailed discussion of all of these effects, together with references to books and review articles describing these phenomena, can be found in the books by Datta [1], Ferry and Goodnick [2], and Davies [11].

1.2 An Overview of the Text

This book is organized in the following way. In Chap. 2, the conditions for bound states are reviewed, for a free particle moving in a 2-D tube with perfect hard walls. Two qualitative mechanisms leading to a bound state are contrasted: a bulge in an otherwise straight tube, and a bend in a tube of constant width. We show how each situation produces an effective attraction which necessarily supports at least one bound state [18, 26]. These arguments can also be extended to three-dimensional tubes. The transfer matrix formalism is presented, and 1-D reductions are introduced. In many situations, 1-D approximations give remarkably accurate descriptions of 2-D binding and scattering, as well as considerable insight into the important physics. Our review of transfer matrix techniques follows closely the methods used in a series of papers by Sprung, Wu and Martorell [27, 28, 29, 30, 31].

Chapter 3 discusses transmission and conductance for particles in tubes, and examines the features which produce structure in transmission. We show the relation between the probability current and transmission, and discuss

the role of vortices and fixed points in determining quantum probability flow. A remarkable formula is presented for the conductance in such quantum systems; this formula was first derived by Landauer [32, 33]. The temperature dependence of conduction in such systems is discussed.

Chapter 4 reviews the correspondence between particles in 2-D tubes and electromagnetic fields in rectangular waveguides with the same geometry. This correspondence allows us to draw on the rich literature of the physics of waveguides [34] and acoustic phenomena [35]. Because of the similarity in the underlying equations, quantum wire and heterostructure systems have been termed "*quantum waveguides*" [19, 36]. The existence of bound states for particles in curved 2-D tubes implies the presence of confined "*evanescent*" sub-cutoff EM modes in waveguides with the same shape [37]. Experimental microwave experiments, which led to the observation of confined EM modes in curved waveguides [21, 22], are discussed. We show how electromagnetic energy densities in the waveguide can be mapped out by measuring resonant frequency shifts resulting from insertion of a small metal sphere.

In Chap. 5 bound states and scattering are examined in detail for a few simple physical systems. The emphasis is to demonstrate some rather fundamental aspects of binding, transmission, and resonances with simple but illustrative models. The systems examined have just one or two structures, or "*cells.*" We examine conditions for bound states, and investigate the dependence of binding energy on geometry. Basic properties of transmission are analyzed for these systems. The resonance structure of 2-D systems is studied, and we demonstrate that substantial physical insight into the mechanisms of transmission can be obtained from a transfer-matrix analysis of electron transport. It is shown that studies of the quantum probability current also provide useful information regarding the nature of transmission in 2-D systems. Experiments with conventional waveguides are also used to illustrate properties of bound states in curved tubes.

Of particular interest are structures which have a single T-stub protruding from one or both sides of a tube. In these systems the low-energy transmission is shown to be a periodic function of the stub length. In principle, this periodicity could be used to create a "*quantum transistor*" [38]. In such a system one could produce complete (or zero) transmission at predetermined energies, by varying the effective length of a stub in a quantum heterostructure.

Chapter 6 extends our discussion to 2-D tubes containing a periodic series of identical structures or cells. It is shown that miniband structure, analogous to the band structure characteristic of infinitely periodic systems, arises in finite periodic structures. It is demonstrated that the Bloch phase for a single cell allows one to separate allowed and forbidden regions for a periodic tube. Finally, we review briefly the effects of changing a single cell in an otherwise perfectly periodic system: this is the analog of adding a single "*defect*" to a crystal. Some general properties of defects, and their effects on the mode structure in finite periodic tubes, are briefly summarized.

In Chap. 7 photonic crystals are discussed. These are systems where a lattice of different dielectric media is used to control the propagation of light. Our focus is on the physics of 2-D photonic crystals. We show how "*waveguides*" can be produced in photonic crystal cavities, and we investigate the similarities and differences between modes in photonic crystal cavities, and those in bent tubes or conventional waveguides.

2. Bound States in Low-Dimensional Systems

In this book we will be concerned with the properties of particles moving in confined regions. For example, there has been much research recently on the motion of electrons in quantum heterostructures (a *heterostructure* refers to a semiconductor composed of a series of different materials). For the systems discussed in this book, the motion of electrons in one dimension is restricted. Frequently the electron motion in one dimension can be confined to a single quantum state, so that the electron behavior in this direction is well understood. In this and similar cases the motion of the particles is well approximated as a quasi-low-dimensional system.

In most of this book, the focus will be on particles whose motion occurs primarily in two dimensions. Furthermore, within the effective plane of motion the particle is constrained to a finite area by some effective potential. We define a *tube* to be a two-dimensional system where a particle is confined to a finite region by a potential. This chapter and Chap. 3 are devoted to an intuitive picture of the properties of particles in idealized tubes.

Consider a particle moving in a tube with some external boundary $\mathcal{S}$, under the simplifying assumption that the potential vanishes inside the tube (or maintains a constant value there), and that the potential is infinite outside the tube. The "*perfect hard wall*" boundary condition requires that the particle wave function vanish on (and outside) the boundary $\mathcal{S}$, so that one has Dirichlet boundary conditions. Although the perfect hard wall condition is often only approximately satisfied in physical systems, such systems are relatively simple ones to study. There has been much research regarding binding and scattering properties in hard wall tubes.

This book will consider only tubes which have two external leads, with a central section of arbitrary shape. Given the width W of the external leads, it will be shown that an energy threshold exists. Above this threshold energy, a continuum of states exists, so that a solution to the scattering conditions can be found for any energy above the threshold. For energies below the threshold, generally one cannot find a wave function which satisfies the differential equation and boundary conditions. For a given geometry, there may be a certain number of discrete energies below the continuum threshold where a solution can be found to the differential equation. Such energies are called *bound state energies*. For some systems, no bound states will exist below

J. T. Londergan, J. P. Carini and D. P. Murdock: LNPm 60, pp. 7 - 35, 1999
© Springer-Verlag Berlin Heidelberg 1999

threshold; in other systems, there will be a finite number of discrete energies where bound states will be found [1]. In a long tube, for energies below continuum threshold, the bound states will decrease exponentially at large distances, while the continuum states will possess oscillatory behavior. So for bound states to exist in such a system requires the presence of states below the continuum threshold energy. This in turn requires an *energy gap* between the bound state energies, and the threshold energy.

In this book we will primarily be concerned with deformations involving a bend or bulge in a tube, or a combination of the two. This chapter reviews the following question: under what conditions will bound states exist in these quasi two-dimensional systems? Once the bound state conditions have been proved, the properties of the resulting bound states will be studied. Many of the bound state existence theorems proved here have straightforward extensions to three-dimensional [3-D] systems; these extensions are presented in Sect. 2.2. Chapter 3 discusses the general properties of transmission and conductance in these tubes.

As we will show, in recent years some rather powerful theorems have been proved regarding the existence of bound states in perfect hard wall tubes, under rather general circumstances. Furthermore, important general features regarding transmission and conductance can also be derived for particles moving in hard wall tubes. These idealized conditions are used to illustrate qualitative features of electron motion in quantum heterostructures. The assumption of hard-wall tubes with potential-free interiors gives a drastically oversimplified (although often surprisingly accurate) picture of electron motion in mesoscopic systems. There has been a great deal of research on quantum wires over the past decade. Excellent reviews of electron motion in such systems are given in the books by Datta [1] and Ferry and Goodnick [2]. The recent book by Davies [11] also gives a thorough discussion of the properties of electrons in quantum wires. We refer the reader to these books for a review of the literature on this subject. Section 3.4 gives a brief review of the physics of electron motion in quantum heterostructures, and the extent to which this approximate model must be modified to treat realistic quantum wire systems.

There are many similarities between the motion of electrons in perfect hard wall tubes, and electromagnetic modes in waveguides with a similar geometry. Consider a 2-D surface in the $x - y$ plane, bounded by a curve $\mathcal{S}$. We call this the tube defined by $\mathcal{S}$. Construct a rectangular waveguide by raising the tube defined by $\mathcal{S}$ upwards in the z direction. We call this three-dimensional object the waveguide constructed from $\mathcal{S}$. The 2-D surface bounded by the curve $\mathcal{S}$ is sometimes called a "*quantum waveguide*" [19, 36, 39], because of the one-to-one relation between electron motion in a

[1] We are assuming that the tube in question contains a finite number of structures or cells. If the tube possesses an infinite number of cells then in principle the number of sub-threshold states could increase without limit.

2-D tube and transverse electric [TE] modes in a rectangular waveguide with the same cross-section. This correspondence is reviewed in Chap. 4, where we show the relationship between particle bound states in curved tubes and confined electromagnetic modes in curved waveguides. Because of this relationship, if a particle bound state exists in a hard wall tube defined by a curve S, then a stable electromagnetic mode will exist below the cutoff frequency in the rectangular waveguide constructed from S. For waveguides, the "perfect hard wall" approximation is in very good agreement with experimental conditions. In later chapters microwave experiments in waveguides are used to simulate the properties of electrons in quantum wires. Once again, this uses the analogy between the wave function for particles in tubes, and the electric field in a conventional waveguide.

This chapter summarizes existence theorems for bound states in deformed tubes with hard walls. It will be seen that, under rather general conditions, a tube with a localized bend or bulge will possess at least one bound state. Hard wall tubes have a minimum or threshold energy above which a continuum of states is available. The bound state is a confined mode which exists below the continuum threshold. Section 2.1 reviews the proofs of such confined modes in two-dimensional [2-D] tubes, since the focus of this book is on two-dimensional systems. However, Sect. 2.2 does provide extensions of the bound state existence proofs to three-dimensional [3-D] tubes. Most of the theorems presented here can be extended straightforwardly to three-dimensional systems. The treatment presented here is impressionistic and intuitive, with an emphasis on the qualitative features of the bound state proofs. We caution the interested reader to consult the mathematical physics literature cited, for descriptions of the precise restrictions on tube geometry and boundary conditions [2] necessary for the validity of these existence proofs.

2.1 Localized Modes in Constrained Two-Dimensional Systems

The motion of particles in simple curved two-dimensional tubes has many interesting features. One of the more surprising aspects of these curved tubes, and one which has been understood relatively recently, is the variety of conditions under which a particle will possess at least one bound state. This chapter gives a qualitative review of the conditions which lead to bound states in hard wall tubes. We refer the reader to the manuscript by Duclos and Exner [14], which reviews a series of theorems on the existence and nature of bound states in curved 2-D and 3-D tubes. Duclos and Exner summarize the boundary conditions, and properties of differentiability and compactness, necessary for bound states to occur.

[2] For example, the existence proofs presented here are generally valid only for systems obeying Dirichlet boundary conditions.

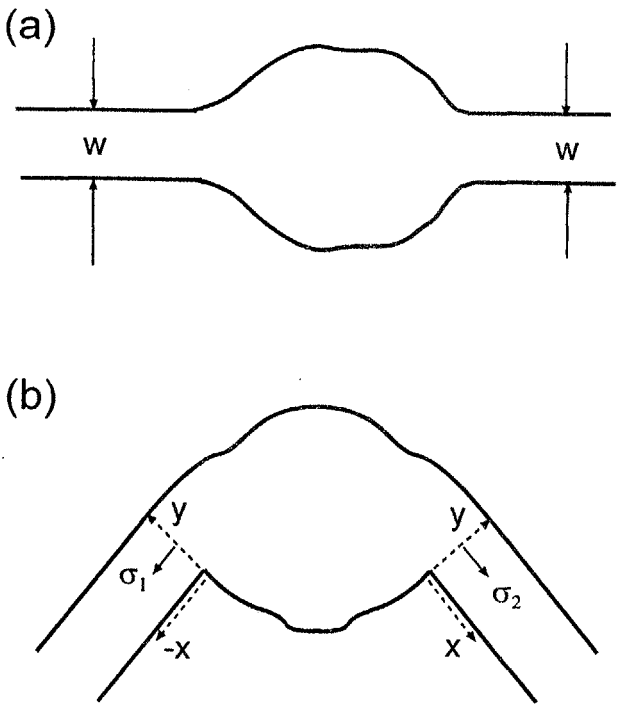

Fig. 2.1. (a) Schematic picture of a "quantum waveguide". This tube has hard walls and straight external leads of width W, with a central "bulge". (b) A tube with straight external leads, normalized to unit width, which join to a central deformed region of arbitrary shape. Boundary surfaces with outward normal vectors σ_1 and σ_2 separate the interior region from the straight leads

First, consider a very long tube with two external leads (finite-length systems will be considered later). At each end, the tube is straight with width W, as shown in Fig. 2.1a. In the middle, the tube is allowed to bend in an arbitrary fashion. Let the curve $\mathcal{S}$ define the outer boundary of the tube. Because the potential is infinite at, and outside, the tube boundary, the particle wave function must vanish on the tube boundary.

Section 2.1.1 discusses the physics of an otherwise straight 2-D tube of constant width which contains a finite "bulge." We will review the proof that such a tube always possesses at least one bound state. In Sect. 2.1.2 an existence proof is presented for bound states in a bent 2-D tube of constant width. In Sect. 2.1.3 these results are extended to consider bound states in deformed 2-D tubes of more general shapes. In Sect. 2.1.4 we outline the transfer-matrix method which is used extensively throughout this book. A major virtue of this method is that reasonably accurate results can often be obtained by truncating the transfer matrix, including only the open modes at a given energy. This "*open mode*" scheme is summarized in Sect. 2.1.4.

For simple geometries, the open-mode scheme can often provide analytic approximations for binding and low-energy scattering. Section 2.2 discusses the extension of the bound state existence proofs to curved 3-D tubes.

2.1.1 Bulges and Bound States in Tubes

In this section we review the qualitative features produced by a localized bulge in an otherwise straight tube. First, consider the case of a long straight 2-D tube of width W. For a perfect hard wall tube, the potential is assumed to be zero inside the tube, and infinite at the boundary. Consider a particle which satisfies the time-independent Schrödinger (or Helmholtz) equation inside the tube

$$\left[\frac{\partial^2}{\partial x^2} + \frac{\partial^2}{\partial y^2} + k^2\right] \psi(x,y) = 0. \tag{2.1}$$

In (2.1), the wave number is related to the energy by

$$k^2 = \frac{2m^* E}{\hbar^2}, \tag{2.2}$$

where m^* is the mass of the particle (for an electron in a mesoscopic system, m^* will generally be the effective mass, which is a function of the conducting material [3]). The hard wall boundary condition requires $\psi|_{\mathcal{S}} = 0$, where $\mathcal{S}$ is the outer boundary of the tube. The tube dimensions parallel and transverse to the tube walls are defined as x and y, respectively, where $y = 0$ and $y = W$ denote the tube walls.

The dimensions in this system obey simple scaling laws. If the width of the legs of the tube are scaled by some factor η, $W' = \eta W$, then the system will remain invariant if the momenta scale as $k' = k/\eta$, and the energy scales as $E' = E/\eta^2$. Without loss of generality, observables can be calculated at any convenient scale, and the units can be rescaled to fit any physical device. All of the tubes in this review have two external leads of equal width W, so for simplicity the external leads are rescaled to unit width. We will also use units where $\hbar^2/2m^* = 1$, except when making reference to energies or length scales appropriate to realistic quantum heterostructures. With these units the energy is related to the wave number by $E = k^2$.

With the tube width rescaled to one, the eigenfunctions of (2.1) can be expanded in terms of normalized transverse eigenfunctions ϕ_n with energies ϵ_n, and longitudinal wave number α_n,

$$\begin{aligned} \psi_n(x,y) &= \exp(\pm i\alpha_n x)\phi_n(y) \quad , \\ \phi_n(y) &= \sqrt{2}\sin(n\pi y) \quad , \quad \epsilon_n = (n\pi)^2 \\ \alpha_n &= \sqrt{k^2 - (n\pi)^2} \quad . \end{aligned} \tag{2.3}$$

[3] The justification for using an effective mass for electrons in heterostructures is given by Davies [11]. A more complete derivation is given in the book by Bastard [40].

For a particle in the n^{th} transverse mode, the Schrödinger equation requires

$$\begin{aligned} k^2 &= \alpha_n^2 + \epsilon_n \\ &= \alpha_n^2 + (n\pi)^2 \quad . \end{aligned} \tag{2.4}$$

Equation 2.4 shows that for a given energy, the longitudinal momentum α_n is real when $k > n\pi$ and imaginary when $k < n\pi$. When α_n is real, the longitudinal solutions for the n^{th} transverse mode will be oscillatory, and when α_n is imaginary the solutions will be exponential. Whenever $k > \pi$, there will always be at least one transverse channel with oscillatory longitudinal wave functions. For a given wave number k, there will be a transverse mode $N = \text{Int}[k/\pi]$ such that for all channels $n > N$, the longitudinal wave function is exponential. Here Int$[x]$ is the largest integer less than x.

The two-dimensional surfaces considered in this book will have two external leads, which can be renormalized to unit width, connected to an internal section of arbitrary shape. At very large distances we will require that the surfaces become straight sections. Solution of the differential equation and boundary conditions thus requires matching the wave functions and normal derivatives at the boundary of the straight sections with the internal regions. When $k < \pi$, all of the longitudinal momenta are pure imaginary, so that the longitudinal wave function is exponential in every transverse channel. In order that the wave function be normalizable, only the decreasing exponential term $\exp(-|\alpha_n x|)$ can be present in the straight sections, so the longitudinal terms which behave like increasing exponentials must be discarded. Thus, at these energies one discards half of the terms in the longitudinal wave function in the straight sections of the tube. As a result, it is generally not possible to satisfy the continuity of both the wave function and normal derivative at the boundary between the straight sections and the internal region.

When $k > \pi$, oscillatory solutions for the longitudinal wave function exist in at least the lowest transverse channel. Both solutions $\exp(\pm i\alpha_n x)$ are allowed in the straight sections. As a result, for wave numbers $k > \pi$ one can always satisfy the boundary conditions between the straight and internal sections of the tube. Thus, a *continuum* of allowed solutions to the scattering equation starts at $k_{th} = \pi$ ($E_{th} = \pi^2$), and a new transverse mode opens up whenever $k = N\pi$ ($E = (N\pi)^2$), where $N \geq 2$. The discrete transverse energies follow from the quantization of the transverse wavelength, $\lambda_n = 2/n$. Below the threshold for the n^{th} transverse mode, the wave number α_n is imaginary, *i.e.*

$$\alpha_n = i|\alpha_n| = i\sqrt{(n\pi)^2 - k^2} \quad \text{when } k < n\pi \quad . \tag{2.5}$$

In the rare cases where a state with $k^2 < \pi^2$ satisfies the boundary conditions for the wave function, the tube will have a bound state or confined mode at that energy.

Since the transverse channel eigenmodes are integer (squared) multiples of the continuum threshold, quantum effects will be easily seen in any system

where the particle energy is comparable to the continuum threshold energy. For an electron in a tube with $W = 20$ nm and $m^* = 0.067\ m_e$ (these values are reasonably typical for quantum wires in GaAs/AlGaAs systems, which comprise the majority of quantum heterostructure systems), the continuum threshold energy is $\epsilon_1 \approx 15$ meV, which is comparable to the energy of a cold electron in these structures.

As an example, consider an otherwise straight tube with hard walls and (renormalized) width $W = 1$ at the ends, but a localized outward "bulge" of arbitrary shape in the middle, as shown schematically in Fig. 2.1a. It would seem plausible that this tube should possess a bound state, as it could accommodate a state with increased transverse wavelength (and hence an energy lower than the continuum threshold) in the bulge. The wave function for this state would be "confined" to the vicinity of the bulge, and would decay exponentially outside this region.

We first give a heuristic proof that a tube with hard walls and a gentle bulge possesses at least one bound state. By a "gentle" bulge, we mean that all derivatives of $W(x)$ are so small that they can be neglected. The wave function ψ for such a tube satisfies the Hamiltonian of (2.1). Define the width of the system at the point x as $W(x)$, where for large $|x|$, $W(x) = 1$, and $W(x) > 1$ in the bulge region. Choose a trial wave function ψ_t of the form

$$\psi_t(x, y) = f(x) \sin\left[\frac{\pi y}{W(x)}\right] . \tag{2.6}$$

Inserting this function into (2.1), and enforcing the adiabatic condition that all derivatives of $W(x)$ can be neglected, the Schrödinger equation reduces to the one-dimensional equation

$$-\frac{d^2 f(x)}{dx^2} + \frac{\pi^2}{W(x)^2} f(x) \approx k^2 f(x) \ . \tag{2.7}$$

In the adiabatic limit of gentle curvature, the problem reduces to a one-dimensional equation with an effective potential $V_{\text{eff}}(x) = \pi^2/W(x)^2$. In the external straight sections of the tube the effective potential has the value $V_{\text{eff}}(x) = \pi^2$; in the region of the bulge where $W(x) > 1$, the effective potential has a local minimum. As is well known, for the Schrödinger equation in one dimension any local minimum in a potential produces at least one bound state. Therefore under adiabatic constraints (gentle curvature), any finite "bulge" in a tube with hard walls, regardless of its size or extent, should produce an effective local attractive force and hence a bound state. The magnitude of the effective attraction increases as the bulge increases in size. Conversely, an adiabatic local constriction in a tube will produce an effective local repulsion.

The general proof, that any outward bulge in an otherwise straight tube with hard walls produces a bound state, was given in 1997 by Bulla, Gesztesy, Renger and Simon [26]. We summarize their variational solution here, and refer the reader to the original paper for detailed conditions.

As has been mentioned, the threshold energy for a straight tube of unit width is $k_{th}^2 = \pi^2$. Since the minimum energy of the eigenvalue spectrum can only decrease as the boundary is moved outward [4], it suffices to demonstrate the existence of a state with energy $E = k^2 < \pi^2$ for a specific deformation all of whose points lie inside the bulge. Consider a long tube whose walls are defined by $y = 0$ and $y = 1$, respectively. Without loss of generality, assume that the bulge occurs around the point (0,1). There must exist positive numbers (a, b) such that all points in the triangle defined by $(-a, 1)$, $(+a, 1)$ and $(0, 1 + b)$ lie inside the bulge.

Define the energy functional

$$E[\hat{\psi}] = \frac{\int d^2x |\nabla\hat{\psi}|^2}{\int d^2x |\hat{\psi}|^2} \ . \tag{2.8}$$

It is straightforward to show that there will be a bound state if a trial function ψ_t can be found such that $E[\psi_t] < \pi^2$. For the Helmholtz equation with Dirichlet boundary conditions, the exact energy will always be less than or equal to the energy corresponding to the trial wave function [41]. Consequently, once a trial function is found with $E[\psi_t] < \pi^2$, then a bound state must exist. Choose the following trial function $\hat{\psi}$, a function of the parameters β and γ,

$$\hat{\psi}_{\beta,\gamma}(x,y) = \begin{cases} \sin(\pi y)\exp(-\gamma(|x|-a)), & |x| > a, \quad 0 < y < 1, \\ \sin\left(\frac{\pi y}{1+\beta\left(1-\frac{|x|}{a}\right)}\right), & |x| \le a, \quad 0 < y < 1+\beta\left(1-\frac{|x|}{a}\right), \\ 0, & \text{otherwise} \quad , \end{cases} \tag{2.9}$$

where $0 < \beta < b$. It is straightforward to show that

$$E[\hat{\psi}_{\beta,\gamma}] = \pi^2(1 - 2a\gamma\beta) + \mathcal{O}(\beta^2\gamma) + \mathcal{O}(\gamma^2) \ . \tag{2.10}$$

By careful choice of γ and β it can be demonstrated that the energy is always smaller than π^2. This proves that any bulge, no matter how small, always produces at least one bound state.

In the schematic diagram of a tube with a bulge, Fig. 2.1a, the straight sections of the tube are oriented in the same direction. This is not necessary for the bound state proof, which still holds even if the straight sections of the tube are bent with respect to one another. Also, in the case we have considered the deformation or bulge is always outward or positive. In the existence proof for the bound state it is not necessary that the deformation of the tube be positive everywhere; the deformation could be outward in some places and inward in others, provided that the *net* area of the deformation was positive. Exner and Vugalter [42, 43] showed that under certain conditions

[4] This statement will be justified in Sect. 2.1.3

the bound state existence proof could be extended to the "critical" case where the deformation had a net area of zero [5].

2.1.2 Existence of Bound States in Curved Tubes of Constant Width

In Sect. 2.1.1 it was demonstrated that any bulge in an otherwise straight 2-D tube will produce at least one bound state. In this section we show that a bent tube of constant width always possesses at least one bound state. For a detailed proof and set of conditions the reader is referred to the comprehensive review on this topic by Duclos and Exner [14]. Various authors had previously analyzed the problem of constrained motion on curves, and their work implictly contained bound state solutions [44, 45, 46, 47, 48, 49]. In addition, there was work which showed that wave functions on surfaces tend to be largest in regions of maximum curvature [50]. For sufficiently gentle bends, Exner and Seba [19, 20] showed in 1989 that such bends produce an effective attraction which leads to binding. In 1992 Goldstone and Jaffe [18] gave the general proof that any bend in a tube of constant width must produce at least one bound state. Their variational method is reviewed in this section. In the past several years many groups have examined how bound states arise in such systems, and how these bound states can affect measurable properties such as conductance in quantum heterostructures, or transmission in bent waveguides. The literature regarding confined modes in specific geometries will be reviewed in later sections.

First we give an adiabatic proof of the existence of bound states in a bent tube of constant width. Consider a curved 2-D tube with constant width (scaled to unity), as shown schematically in Fig. 2.2. Define curvilinear coordinates s and u such that s is always directed along one wall of the tube, and u is the transverse coordinate normal to s; u takes on values $0 \leq u \leq 1$. A requirement for the existence of bound states is that the curvature vanish asymptotically; a sufficient condition is that the curvature go to zero at least as fast as $1/|s|$ [14]. Goldstone and Jaffe imposed the stronger condition that there exists a point s_0 such that $\kappa(s) = 0$ for $|s| > s_0$, where $\kappa(s)$ is the curvature at any point s. From Fig. 2.2, $\kappa(s)$ is related to the radius of curvature (measured to the outer edge of the curve) by

$$\begin{aligned} &\kappa(s) = 1/R(s) \quad , \\ &\text{so } 0 \leq |\kappa(s)| < 1 \quad . \end{aligned} \tag{2.11}$$

The wave function ψ satisfies the Hamiltonian of (2.1), with hard wall boundary condition $\psi|_{\mathcal{S}} = 0$. In these curvilinear coordinates the differential element of length is

[5] These authors also found a condition under which no bound state would exist in the critical case.

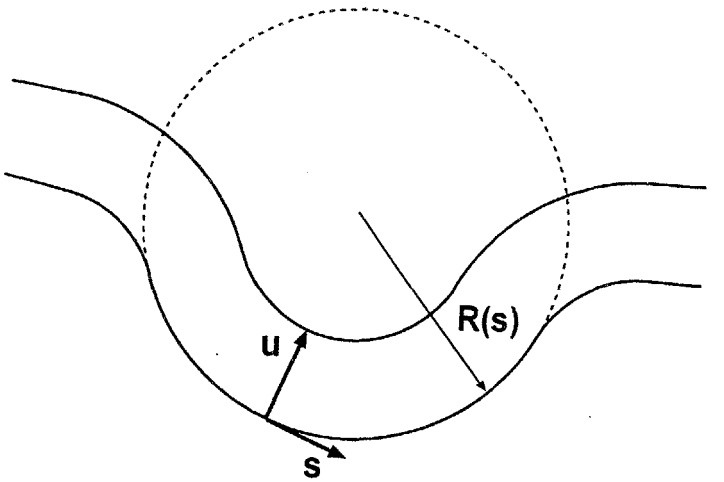

Fig. 2.2. Two-dimensional tube of constant (unit) width. The coordinate s is measured along one wall of the tube, and $0 \leq u \leq 1$ is normal to s. The radius of curvature to the outer tube wall is $R(s) = 1/\kappa(s)$

$$dr = [1 - \kappa(s)u]ds\hat{\mathbf{s}} + du\hat{\mathbf{u}}, \tag{2.12}$$

so the wave function ψ satisfies the differential equation

$$\left(\frac{1}{1-\kappa(s)\,u}\right) \left[\frac{\partial}{\partial s}\left(\frac{1}{1-\kappa(s)\,u}\frac{\partial\psi(s,u)}{\partial s}\right) + \frac{\partial}{\partial u}\left(1-\kappa(s)\,u\right)\frac{\partial\psi(s,u)}{\partial u}\right] + k^2\psi(s,u) = 0. \tag{2.13}$$

The wave function $\psi(s,u)$ can be redefined in terms of the function ϕ where

$$\psi(s,u) = \frac{1}{\sqrt{1-\kappa(s)\,u}}\phi(s,u). \tag{2.14}$$

The function ϕ then satisfies the equation

$$\frac{1}{(1-\kappa(s)\,u)^2}\frac{\partial^2\phi}{\partial s^2} + \frac{2\kappa'(s)u}{(1-\kappa(s)\,u)^3}\frac{\partial\phi}{\partial s} + \frac{\partial^2\phi}{\partial u^2} + \left[k^2 - V(s,u)\right]\phi = 0, \tag{2.15}$$

where

$$V(s,u) = -\frac{\kappa(s)^2}{4(1-\kappa(s)\,u)^2} - \frac{\kappa''(s)\,u}{2(1-\kappa(s)\,u)^3} - \frac{5(\kappa'(s))^2\,u^2}{4(1-\kappa(s)\,u)^4}. \tag{2.16}$$

First, we give a plausibility argument that a bound state will exist in the adiabatic limit of a tube where the curvature is both small and slowly varying. Define a trial wave function for the tube,

$$\psi(s,u) = \frac{\xi(s)\sin(\pi u)}{\sqrt{1-\kappa(s)\,u}} \quad . \tag{2.17}$$

Inserting this wave function into the differential equation (2.13), expanding to lowest order in κ and neglecting derivatives of κ, one obtains the effective one-dimensional equation

$$-\frac{d^2\xi(s)}{ds^2} + \left[\pi^2 - \frac{\kappa(s)^2}{4} - k^2\right]\xi(s) \approx 0 \quad . \tag{2.18}$$

From (2.18) it is clear that at any point in the bent tube, the curvature $\kappa(s)$ produces an effective attractive potential, where the magnitude of the attraction is approximately $-\kappa(s)^2/4$. Marcus [44] first pointed out that the effective attraction was proportional to the square of the curvature. This is apparent if one neglects derivatives of the curvature in the effective potential $V(s,u)$ of (2.16) [6]. Since in one dimension a local attraction always produces at least one bound state, any tube with a sufficiently gentle bend, no matter how small, will possess at least one confined mode.

Goldstone and Jaffe [18] provided a variational proof for the general case. In their proof the tube is required to be straight beyond some point s_0 [7]. They chose the following trial wave function

$$\hat{\psi}(s,u) = \begin{cases} \exp(-\lambda(|s|-s_0))\sin(\pi u), & |s| > s_0, \quad 0 \le u \le 1, \\ \psi_t(s,u), & |s| \le s_0, \quad 0 \le u \le 1, \end{cases} \tag{2.19}$$

with a variational parameter $\lambda > 0$. Inserting this trial wave function into the energy functional of (2.8), the integrals over the straight sections can be done analytically. The condition for a bound state then becomes

$$E[\hat{\psi}] = \frac{\lambda/2 + \pi^2/(2\lambda) + \int_c d^2x|\nabla\psi_t|^2}{1/(2\lambda) + \int_c d^2x|\psi_t|^2} < \pi^2 \, . \tag{2.20}$$

In (2.20), $\int_c$ means integration over the curved region of the tube, inside the limits $|s| \le s_0$. A bound state will occur if a function ψ_t in the curved region can be found which obeys the boundary conditions, such that

$$I[\psi_t] > \frac{\lambda}{2} > 0 \quad , \text{ where } \quad I[\psi] \equiv \int_c d^2x\,\left[\pi^2\psi^2 - |\nabla\psi|^2\right] \quad . \tag{2.21}$$

If we adopt the trial function $\psi_t(s,u) = \sin(\pi u)$ in the curved region, it can be shown that $I[\psi_t] = 0$. However, ψ_t is not an extremum of $I[\psi]$, since

[6] The higher terms in the effective potential can be neglected for either a sufficiently slowly varying curvature, or for a sufficiently thin tube with fixed κ.

[7] Renger and Bulla [51] have extended this proof, and shown that it holds for more general curvatures and under weaker conditions than imposed by Goldstone and Jaffe.

$$\nabla^2\psi_t(s,u) + \pi^2\psi_t(s,u) \neq 0 \quad . \tag{2.22}$$

Thus there must exist a wave function ϕ such that $I[\phi] > 0$, and therefore (2.21) will be satisfied, for λ sufficiently small. Thus every bent tube of constant width will have at least one bound state, *i.e.* a state with energy below the continuum threshold $E_{th} = \pi^2$. The wave function for the bound state will be large in the vicinity of the bend, and will decay exponentially along the straight sections outside the bend.

The demonstration that a state exists with energy below the original threshold ($E_{th} = \pi^2$) proves the existence of a bound state, unless the curvature of the tube depresses all energy states so as to lower the continuum threshold. If the curvature is required to vanish sufficiently fast asymptotically, this will ensure that the continuum threshold is unchanged. Goldstone and Jaffe enforce this by requiring that the curvature vanish beyond a certain distance. As we mentioned earlier, it is sufficient to require that the curvature go to zero faster than $1/|s|$ (a logarithmic spiral) [14].

To see how exceptions can arise, consider an infinitely long non-intersecting spiral tube, with hard walls and a constant curvature κ. The effective attraction arising from the bending is constant everywhere. If the curvature occurs over a finite region, there are a finite number of bound states with different energies. In the limit as the curved region becomes infinitely long, the number of bound states increases without limit, and the energy of every state approaches the same value. This point becomes an accumulation point for the bound states. Furthermore, in this limit new states descend to fill the gap between the old continuum and this point. The net effect is that the continuum threshold is lowered to this new value. The infinite spiral tube thus has no bound states, and its continuum threshold is lower than the threshold energy of a straight tube [8]. In Sect. 5.1.2 this effect will be observed when considering bound states in tubes with a circular bend.

2.1.3 Bound States in Curved Tubes of Arbitrary Shape

The bound state theorem for bent tubes is rather remarkable. Under the rather general conditions we have cited, at least one bound state must appear for a particle in any bent 2-D tube with constant width and hard walls. Dunne and Jaffe [53] showed that bound states also occur in any bent tube of constant width threaded by an Aharonov–Bohm magnetic flux line. Section 2.2 will consider extensions of this theorem to three-dimensional tubes.

Duclos and Exner derive an upper bound to the number of bound states possessed by a sufficiently thin curved tube [14]; they also derive an expansion for the bound state energy of a bent tube in the adiabatic limit of small curvature, when the curvature extends over a fixed length of the tube. One

[8] We do not consider here the detailed properties of the spectrum for a periodically curved quantum waveguide. This issue is addressed by Yoshitomi [52]

replaces the curvature function $\kappa(s)$ by $\beta\gamma(s)$, where $\gamma(s)$ is a fixed function of s and $\beta > 0$ is a variable parameter. The length of the curved section is related to the integral of $|\gamma(s)|$ over the whole tube, defined as $||\gamma||$. In the limit $\beta \to 0$ Duclos and Exner obtain

$$\sqrt{\pi^2 - E(\beta)} = \frac{\beta^2}{8}\left[||\gamma||^2 + c_1\right] + \mathcal{O}(\beta^3) \ . \tag{2.23}$$

In (2.23), the quantity c_1 is a contribution arising from higher transverse modes; c_1 involves derivatives of the curvature along the tube. We define the binding energy as the difference between the bound state energy and the continuum, π^2. Thus for tubes containing sufficiently gentle bends of fixed length, the binding energy should vary as the square of the right hand side of (2.23). Hence the binding energy in such tubes will vary as the fourth power of the scale parameter β. The reader is referred to the mathematical review by Duclos and Exner [14] for additional theorems on bound states in bent tubes.

Up to this point bound state existence proofs have been given for two general classes of curved tubes: otherwise straight tubes which contain an outward "bulge," and tubes of constant width which contain at least one bend. The bound state existence proofs which we have presented can be extended to a much larger class of curved tubes. We give a heuristic proof here, which can be made more rigorous using the "bracketing" inequalities of spectral analysis [54]. Consider a 2-D tube with hard walls and any shape, which possesses at least one bound state. The wave function for this tube obeys the Schrödinger or Helmholtz equation of (2.1). Asymptotically the tube boundaries become straight and for convenience the dimensions are renormalized so the width of the tube approaches one. The presence of a confined mode ensures that the lowest energy eigenstate for the tube is $E_0 < \pi^2$, with the corresponding bound state wave function ψ_0. Consider any other tube obtained by making an outward deformation of the original tube over a finite area. The new tube will also possess at least one bound state, and the lowest energy state in the deformed tube cannot be higher than E_0.

To prove this statement, take the following trial wave function for the deformed tube:

$$\hat{\psi}_t = \begin{cases} \psi_0, & \text{in the original tube} \\ 0, & \text{in the deformation} \end{cases} . \tag{2.24}$$

The trial wave function in (2.24) is continuous in the new tube, and vanishes at the tube boundaries [9]. Inserting $\hat{\psi}_t$ into the variational equation (2.8) gives a trial energy E_0, thus the deformed tube must have at least one bound state with energy no greater than E_0. This technique can be used to prove the existence of bound states in tubes with vastly different geometries. For any given tube, provided that one can inscribe a smaller tube which is known to

[9] The function $\hat{\psi}_t$ does not have a continuous first derivative everywhere but this is not a necessary condition for the trial wave function.

have a bound state, then at least one bound state must exist in the larger tube. Furthermore, the energy of the lowest bound state in the larger tube cannot be greater than the bound state energy E_0 in the smaller tube.

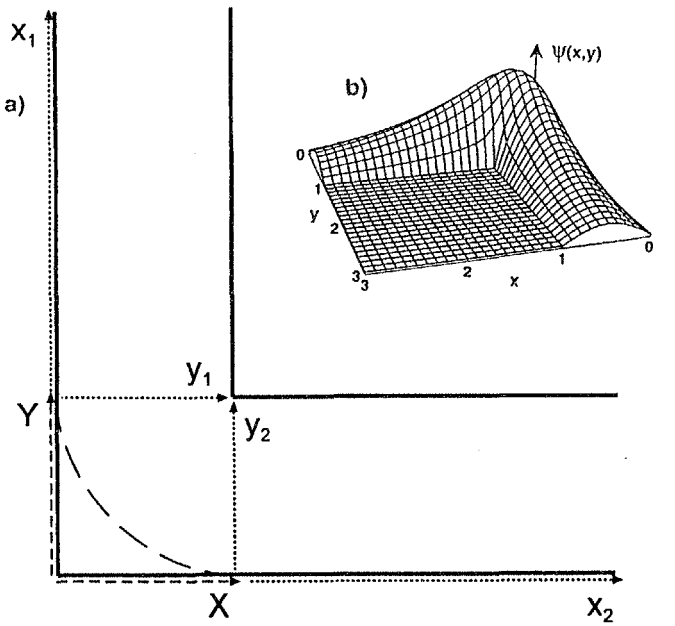

Fig. 2.3. (a) The L-shaped tube: a tube with a sharp bend of angle $\theta = 90°$. External leads are described by coordinates (x_1, y_1) and (x_2, y_2); the central square has coordinates (X, Y). The dashed line shows an inscribed arc of a circle of unit radius. (b) The exact bound state wave function ψ in tube of part (a), from [21]

As an example of the existence theorem for deformed tubes of general shapes, consider a tube which possesses a "kink," formed by joining two long straight sections of unit width at some angle $\theta \neq 0$. Figure 2.3a shows the L-shaped bent tube, where $\theta = \pi/2$. It was rather surprising when Lenz *et al.* [17], and later Schult, Ravenhall and Wyld [15], Peeters [16], and Exner, Seba and Stovicek [55] showed that the L-shaped tube possessed a bound state, by solving the Helmholtz equation for this geometry.

Based on our discussion of bound states, bends and bulges, it should not be surprising that tubes with a kink should have at least one bound state. In the vicinity of the kink, the tube has both a bend and a bulge, and we have shown that each effect separately is sufficient to produce binding. In Fig. 2.3a the dashed curve is an arc of a circle with constant width, inscribed inside the L-shaped tube and centered at the inside corner of the bend. We

could similarly inscribe a tube of constant width with a circular bend, inside a tube with a kink, for any bend angle. Consequently, our bound state theorems prove that a tube with a kink must contain at least one bound state, a fact which was pointed out by Avishai *et al.* [23]. As the tube becomes straight (as the exterior angle between the two straight sections $\theta \to 0$), the binding energy of the confined mode (the distance from the confined mode to the continuum threshold) goes to zero as the fourth power of the bend angle θ. The proof by Bulla *et al.* [26], reviewed in Sect. 2.1.1, also shows that a tube with an outward bulge of any kind possesses a bound state, and a tube with a kink is covered under this proof.

In Sect. 2.1.1 we showed that the effective adiabatic potential for a tube could be written in terms of the width $W(s)$ as $V_{\text{eff}}(s) = \pi^2/W(s)^2$. While a local increase in width corresponded to an effective local attraction, a constriction would correspond to an effective repulsion which would raise the energy of a state. What are the properties of a tube which simultaneously bends (producing a local attraction), and constricts? One can combine the effective potentials for bulges and bends ((2.7) and (2.18)) to obtain an adiabatic effective interaction for sufficiently gentle curved tubes,

$$V_{\text{eff}}(s) \approx \frac{\pi^2}{W(s)^2} - \frac{\kappa(s)^2}{4} \quad . \tag{2.25}$$

We have already shown that a tube which simultaneously bends and bulges will produce a larger attraction than either effect alone. The relation (2.25) shows that if a bend is combined with a constriction, the former produces an effective attraction, while the latter produces a local repulsion. This raises the possibility that one could combine the attraction arising from a bend with the repulsion from constriction, so as to effectively cancel each other. Adiabatically this can be produced for any system in which the width and curvature are correlated so that $V_{\text{eff}}(s)$ of (2.25) remains constant.

One potential application of this relation might be to minimize reflection in a bent waveguide. The presence of a bend at any point in a tube tends to produce reflection. It has long been known, for example, that any bend in a conventional waveguide produces reflection [34]. It would be interesting to examine the extent to which a correlated bend and constriction could minimize the reflection in a bent waveguide. Equation (2.25) suggests that it might be possible to produce a bent waveguide with nearly perfect transmission in some frequency range [10].

Subsequent chapters will consider the case of tubes which contain several identical structures, or "*cells*," in series. There are various techniques which one can use to solve for the states in a system composed of a series of identical cells. Some general techniques are given in the quantum mechanics textbook

[10] Since the "bend-squeeze" compensation from (2.25) requires essentially total cancellation of competing effects, it is possible that higher-order terms would destroy this cancellation [56].

by Merzbacher [57]. Ashcroft and Mermin [58] show how to solve periodic systems which give rise to band structure in condensed matter physics. Several approximate methods which are useful for problems in low-dimensional systems are given in the book by Davies [11].

In Sect. 5.4 we will review in detail the situation which arises for two cells in series. Chapter 6 discusses the case of the "*quantum superlattice*", where one studies a finite periodic sequence of identical cells. Here we will review some of the qualitative features of confined modes in a series of identical cells. If an individual cell will support one bound state, its bound state wave function will be localized in the vicinity of the cell, and will decrease exponentially in the connecting sections [11]. In the limit where the separation between cells grows without limit, the wave functions in neighboring cells do not interact. A system of N identical cells, separated by very large distances, would then possess N degenerate bound states. As the cells move closer together, the bound states interact, with a few states being pushed down in energy while the remaining states get pushed up. As the distance between cells decreases, the number of "true" bound states tends to decrease as some of the higher modes move into the continuum.

The constrained two-dimensional systems considered in this monograph are interesting examples of systems in which quantum wave conditions produce an energy spectrum quite distinct from classical conditions. A classical particle in such a tube is confined in the transverse direction but completely free in the longitudinal direction. The classical continuum will thus start at zero energy. However, the quantum boundary conditions (vanishing of the wave function on the tube boundaries) give an effective confining potential which produces a minimum (cutoff) energy for continuum solutions (bands of propagating states). When states exist with energy below continuum threshold, their wave functions decay exponentially in the longitudinal direction. The situation where boundary conditions on Schrödinger wave functions give rise to binding has been termed "*quantum confinement*" [10]. In this book we will confine our attention to quantum wires, conventional waveguides and photonic crystals. However, similar models have been used to describe other physical systems, for example chemical rearrangement processes [59, 60]. In addition, there has been considerable work on analogous problems in areas like fluid dynamics or acoustics, which generally have Neumann boundary conditions. Parker and Stoneman [61] review a number of situations where acoustic resonances are observed, and Evans, Levitin and Vassiliev [62] prove existence theorems for trapped modes in 2-D acoustic waveguides. As we have mentioned, many previous studies of scattering and transmission in two and three-dimensional curved tubes did not predict the existence of bound states in the spectrum.

[11] In all systems considered in this book, each cell will support one bound state, and the straight sections connecting adjacent cells are required to have the same width as the external leads of the system.

The existence of bound states in bent tubes has several implications for low-dimensional electron systems with similar boundary conditions. These have been discussed at length in previous papers [63, 64]. Lasing action has been observed from electrons bound at a T junction in a quantum wire [65]. Bound states of electrons in quantum heterostructures are observed most directly in electron transport experiments as subthreshold peaks in conductance due to resonant tunneling through the confined mode(s) [66, 67].

2.1.4 Transfer-Matrix Formalism for Curved Tubes

Calculation of scattering properties for particles in tubes of arbitrary shape requires numerical solution of the 2-D Helmholtz equation in order to extract the transmission amplitudes. Many methods have been developed to solve this equation. For simple geometries, particularly involving square or perfectly rounded corners, wave function matching techniques are quite effective [15, 23, 68, 69].

Transmission and reflection coefficients in two-dimensional systems can also be calculated using Green function techniques [70, 71, 72]. Here the transmission amplitude is obtained by projecting the Green function onto the desired transverse mode in the asymptotic part of the external lead. Lent and Kirkner [73] introduced a "*quantum transmitting boundary method*," similar to a method of Frohne *et al.* [74], which was capable in principle of solving two-dimensional transmission problems with an arbitrary number of external leads and for arbitrary internal geometries. For quantum heterostructures, Datta [1] gives a thorough review of Green function techniques, and Ferry and Goodnick [2] review many of these numerical techniques, in particular lattice Green function methods. We refer the reader to those texts for comprehensive references.

In this monograph, transfer matrix techniques will be utilized for solving transmission and bound state properties in deformed tubes. Transfer matrix methods have two major advantages for our purposes. First, for the simple geometries chosen in this book, the transfer matrix is straightforward to calculate, since the transverse eigenfunctions can be calculated analytically, as can the matrix elements which appear in the resulting coupled algebraic equations. Our primary objective is to obtain a qualitative understanding of the physics of binding and transmission. In particular, the major focus of these investigations will be at low energies, either below the threshold for continuum transmission, or in the region between threshold and the second transverse mode. In this case, as we will demonstrate, the resulting infinite-dimensional equations can often be truncated with reasonable accuracy by including only contributions from one or a few modes. This reduction can provide a great deal of insight into the origin of physical effects. In fact, for low energy scattering in the "*single mode approximation*," where only the lowest transverse mode is retained, analytic results can be derived for most geometries investigated in this book.

The second advantage of transfer matrix techniques is their application to tubes composed of a series of identical cavities or cells [75, 31]. In such systems, transmission through a series of identical cells can be calculated by repeated multiplication of the transfer matrix for a single cell. Wu, Sprung and collaborators have examined the qualitative features of binding and transmission in 2-D tubes, in a series of papers [27, 28, 29, 30, 31]. They have shown that an excellent qualitative understanding of transmission and conductance through such tubes, particularly at low energies, can be obtained by truncating the expansion of the scattering amplitude to the lowest transverse mode. In this truncated expansion one can straightforwardly derive a number of predictions for binding and transmission, and these features are in excellent agreement with results of exact calculations of scattering through 2-D tubes. Our introduction to the transfer matrix approach follows the paper by Wu, Sprung and Martorell [30]. In the remainder of this chapter, this method is applied to bound state problems. In Chap. 3, the transfer matrix formalism is extended to calculate transmission and conductance in the continuum.

The transfer matrix equations are valid for any 2-D system with an internal deformed surface coupled to two straight external leads, shown schematically in Fig. 2.1b. The two leads are denoted 1 and 2, respectively, and the boundaries between the inner surface and the leads as σ_1 and σ_2, respectively (with outward unit vectors $\boldsymbol{\sigma}_1$ and $\boldsymbol{\sigma}_2$). The orthonormalized solutions for the external transverse modes and their eigenvalues are given by $\phi_n(y)$ and ϵ_n, which are given by (2.3) after rescaling the external leads to unit width.

In the internal region, define auxiliary wave functions χ_{n0} and χ_{0n} which satisfy the Schrödinger equation under the following boundary conditions. On one of the boundary surfaces, the auxiliary functions χ_{n0} and χ_{0n} reduce to the channel wave function $\phi_n(y)$ for the external leads, *i.e.*

$$\begin{aligned} \chi_{n0}(x,y)|_{\sigma_1} &= \chi_{0n}(x,y)|_{\sigma_2} = \phi_n(y) \\ \chi_{n0}(x,y)|_{\sigma_2} &= \chi_{0n}(x,y)|_{\sigma_1} = 0 \ . \end{aligned} \tag{2.26}$$

On all of the internal surfaces of the cell, the auxiliary functions vanish. The wave functions in the leads, and in the interior, are then expanded in their respective sets of basis functions

$$\begin{aligned} \psi_\Gamma(x,y) &= \sum_n \left(C_{\Gamma n} \exp(i\alpha_n x) + \widetilde{C}_{\Gamma n} \exp(-i\alpha_n x) \right) \phi_n(y), \\ \alpha_n &= \sqrt{k^2 - (n\pi)^2} \ , \\ \psi_{in}(x,y) &= \sum_n D_n \chi_{n0}(x,y) + E_n \chi_{0n}(x,y) \ . \end{aligned} \tag{2.27}$$

In (2.27), $\Gamma = 1, 2$ denotes the two external leads. In the external leads, the longitudinal wave function is expanded in terms of traveling waves in the open transverse channels, and exponentially increasing and decreasing terms for the closed transverse modes. The function ψ_{in} denotes the wave function

inside the cell. To solve (2.27), one requires continuity of the wave function and its normal derivatives at the boundaries. Upon imposing these boundary conditions, the interior expansion coefficients D_n and E_n in (2.27) can be eliminated to obtain an equation relating the coefficients of the external leads on either side of the cell,

$$\mathbf{U}\mathbf{S}_1 = \mathbf{V}\mathbf{S}_2 \quad . \tag{2.28}$$

In (2.28), $\mathbf{S}_j$ (j=1,2) is the column array

$$\mathbf{S}_j = \begin{pmatrix} \mathbf{C}_j \\ \widetilde{\mathbf{C}}_j \end{pmatrix} \quad , \tag{2.29}$$

where $\mathbf{C}_j$ ($\widetilde{\mathbf{C}}_j$) are column arrays with elements $C_{j,n}$ ($\widetilde{C}_{j,n}$). The matrices $\mathbf{U}$ and $\mathbf{V}$ appearing in (2.28) have the form

$$\begin{aligned} \mathbf{U} &= \begin{pmatrix} \mathbf{B}+i\alpha & \mathbf{B}-i\alpha \\ \mathbf{A}' & \mathbf{A}' \end{pmatrix} \quad , \\ \mathbf{V} &= \begin{pmatrix} \mathbf{A} & \mathbf{A} \\ \mathbf{B}'-i\alpha & \mathbf{B}'+i\alpha \end{pmatrix} \quad . \end{aligned} \tag{2.30}$$

In (2.30), α denotes a diagonal matrix with elements α_n, and $\mathbf{A}$, $\mathbf{A}'$, $\mathbf{B}$ and $\mathbf{B}'$ are auxiliary matrices defined by

$$\begin{aligned} \mathbf{A}_{nm} &= -\int_0^1 dy\, \phi_n(y)\, (\nabla \chi_{0m} \cdot \boldsymbol{\sigma}_1)\,|_{\sigma_1} \quad , \\ \mathbf{A'}_{nm} &= -\int_0^1 dy\, \phi_n(y)\, (\nabla \chi_{m0} \cdot \boldsymbol{\sigma}_2)\,|_{\sigma_2} \quad , \\ \mathbf{B}_{nm} &= \int_0^1 dy\, \phi_n(y)\, (\nabla \chi_{m0} \cdot \boldsymbol{\sigma}_1)\,|_{\sigma_1} \quad , \\ \mathbf{B'}_{nm} &= \int_0^1 dy\, \phi_n(y)\, (\nabla \chi_{0m} \cdot \boldsymbol{\sigma}_2)\,|_{\sigma_2} \quad . \end{aligned} \tag{2.31}$$

The matrices $\mathbf{B}$ and $\mathbf{B}'$ are real and symmetric, and the matrices $\mathbf{A}$ and $\mathbf{A}'$ are real and obey the relation $\mathbf{A}' = \mathbf{A}^T$. In principle (2.28) represents an infinite-dimensional coupled channel problem. However, at any given energy, only a finite number of transverse channels are open. In the closed channels the wave function decreases exponentially in the longitudinal direction because the longitudinal momentum is imaginary. Consequently, the transfer matrix can be truncated without loss of accuracy at some finite number of channels, denoted by the integer J. Following this truncation, the matrices $\mathbf{A}$ and $\mathbf{B}$ become $J \times J$ square matrices, and the transfer matrix $\mathbf{M}$ is a $2J \times 2J$ square matrix. When the cell is symmetric with respect to the two leads, one obtains the relations $\mathbf{B} = \mathbf{B}'$ and $\mathbf{A} = \mathbf{A}'$. All examples used in this text will be symmetric with respect to the external leads; consequently at various points in the text we will assume this symmetry. It is straightforward to extend the resulting equations to solve the general case of asymmetric cells.

The relation (2.28) can be straightforwardly generalized to the case where one has a series of N cells. In this case the wave function coefficients at the cell boundaries can be numbered sequentially, from left to right, and one can define the column matrices $\mathbf{S}_j$, where $j = 1, 2, \ldots, N+1$. The transfer matrix relates the wave function coefficients across any cell, so (2.28) can be rewritten to relate the wave function on both sides of the j^{th} cell, as

$$\mathbf{S}_j \equiv \mathbf{M}_j \, \mathbf{S}_{j+1} = (\mathbf{U}_j)^{-1} \mathbf{V}_j \, \mathbf{S}_{j+1} \quad , \tag{2.32}$$

where $j = 1, 2, \ldots, N$. In (2.32), $\mathbf{M}_j$ is the transfer matrix for the j^{th} cell. The transfer matrix $\mathbf{M}^{(N)}$ for transmission through the N-cell system links the wave functions on the right and left sides of the entire system,

$$\mathbf{S}_1 \equiv \mathbf{M}^{(N)} \, \mathbf{S}_{j+1} = \mathbf{M}_1 \, \mathbf{M}_2 \ldots \mathbf{M}_N \, \mathbf{S}_{j+1} \quad . \tag{2.33}$$

From (2.33) it is clear that the transfer matrix for transmission through a series of N cells is given by the product of the individual transfer matrices for each cell,

$$\mathbf{M}^{(N)} = \mathbf{M}_1 \, \mathbf{M}_2 \ldots \mathbf{M}_N \quad . \tag{2.34}$$

In the case that the cells are identical, the net transfer matrix is obtained by multiplying the transfer matrix across an individual cell N times,

$$\mathbf{M}^{(N)} = (\mathbf{M})^N \quad . \tag{2.35}$$

In later chapters we will consider tubes which contain a repeated pattern of cells. Each cell will contain a bend or cavity, and will be separated from neighboring cells by a straight section of length l. Although in principle the straight section could be included as part of the "cell," it is generally much easier to obtain analytic formulae for auxiliary wave functions such as χ_{n0} if the straight section is treated separately. In this case the cell is divided into two parts, a deformed cavity and a straight section. In all examples considered in this text, the width of the interior straight sections is kept identical to the width of the external leads (and the dimensions are renormalized so the external leads have unit width). It is straighforward to account for propagation through a straight section: a wave traveling to the right through a straight section of length l, acquires a phase $\mathbf{P} = \exp(i\alpha l)$. Adding the phase acquired from the straight section requires re-defining the matrices $\mathbf{U}$ and $\mathbf{V}$ from (2.30). The matrices $\mathbf{U}$ and $\mathbf{V}$, which describe propagation through a cell described by the auxiliary matrices of (2.31) coupled to a straight section of length l, are given by

$$\begin{aligned} \mathbf{U} &\rightarrow \begin{pmatrix} (\mathbf{B} + i\alpha)\mathbf{P} & \mathbf{B} - i\alpha \\ \mathbf{A}'\mathbf{P} & \mathbf{A}' \end{pmatrix} \quad , \\ \mathbf{V} &\rightarrow \begin{pmatrix} \mathbf{A} & \mathbf{A}\mathbf{P} \\ \mathbf{B}' - i\alpha & (\mathbf{B}' + i\alpha)\mathbf{P} \end{pmatrix} \quad . \end{aligned} \tag{2.36}$$

It should be mentioned that there are technical difficulties with the transfer matrix formalism. The longitudinal momenta α_n in the closed channels are imaginary, so wave propagation decays exponentially in closed channels. The matrices which appear in (2.30) are singular, so attempts to invert them can cause numerical instability [31]. It is not clear *a priori* how many closed channels, or evanescent states, need to be included to obtain the desired numerical accuracy. It is frequently necessary to vary the number of channels included, in order to determine by trial and error when the desired precision is reached. Furthermore, other numerical methods may provide more efficient ways to calculate scattering in these systems. In terms of the length L of a given step in numerical integrations, the transfer matrix requires a computational cost proportional to L^3. For comparison, recursive Green function methods have a computational cost proportional to L^4, while the boundary element method of Frohne *et al.* [74] has a computational cost proportional to L^2. Despite these drawbacks, the transfer matrix equations can always be converted to equivalent linear equations which minimize these difficulties. Furthermore, our main interest in the transfer matrix formalism is to provide a guide to the relevant physics. The transfer matrix method clarifies the relation between transmission through a single "cell" (a tube with a single bend or cavity), and a series of cells (tubes with regularly repeated structures).

Wu, Sprung and collaborators [31, 27, 28, 29] have emphasized the advantages of the "*open mode*" approximation scheme, where one includes only those transverse modes which are energetically accessible at a given energy. In the closed channels, wave functions tend to die off exponentially with distance in the external leads, so contributions from closed channels to transmission and reflection are generally small, except for energies quite close to channel thresholds. The open-mode approximation gives results which are often quite close to the exact scattering through a system [12]. Moreover, this approximation gives analytic expressions for certain geometries, and provides considerable insight into the physics of more complicated systems.

For bound states, and low-energy scattering in the region below the second transverse excitation mode, at most one of the longitudinal wave numbers α_n is real. In this energy regime, the open mode approximation neglects all modes $n > 1$. In this case (defined as the "*single-mode approximation*" [SMA]) the matrices $\mathbf{A}$ and $\mathbf{B}$ of (2.31) simply become numbers, and the transfer matrix $\mathbf{M}$ of (2.32) is a 2×2 Hermitian matrix with determinant one. Since the SMA is frequently easy to calculate, and often straightforward to interpret, we will review in some detail the properties of SMA matrix elements for scattering and bound states. Note that since only a single transverse channel is retained, there is no interference between different modes in SMA. Consequently, the single-mode approximation is a one-dimensional reduction

[12] For bound states, where no channels are open, reasonable estimates are often obtained in the "single-mode approximation," where one includes only the lowest transverse channel.

of the 2-D scattering problem. Many powerful techniques have been developed to solve 1-D problems, and these can be applied to this situation.

For a symmetric cell it is straightforward to show that in single-mode approximation the diagonal elements of the matrix M of (2.32) have the form

$$M_{11} = \exp(-i\alpha l)\left(\frac{B}{A} - i\frac{A^2 - B^2 + \alpha^2}{2\alpha A}\right)$$
$$M_{22} = \exp(i\alpha l)\left(\frac{B}{A} + i\frac{A^2 - B^2 + \alpha^2}{2\alpha A}\right) \quad . \tag{2.37}$$

In (2.37), $A = \mathbf{A}_{11}$, etc, and $\alpha = \alpha_1$. By inspection, above continuum threshold (2.37) has the property

$$M_{22} = M_{11}^* \quad . \tag{2.38}$$

Transmission and reflection coefficients will be discussed in more detail in Sect. 3.1. For now, consider transmission through a single cell, in single-mode approximation. Consider the case where one has an incident wave of unit magnitude on the left side of the cell. There is a reflected wave with amplitude r_1 on the left side, and on the right hand side there is no incident wave and a transmitted wave with amplitude t_1. The transfer matrix can then be written as

$$\begin{pmatrix} 1 \\ r_1 \end{pmatrix} = \begin{pmatrix} M_{11} & M_{12} \\ M_{21} & M_{22} \end{pmatrix} \begin{pmatrix} t_1 \\ 0 \end{pmatrix} \quad . \tag{2.39}$$

By inspection, the SMA transmission and reflection amplitudes are related to the transfer matrix elements through

$$t_1 = 1/M_{11}$$
$$r_1/t_1 = M_{21} \quad . \tag{2.40}$$

A useful quantity is the *Bloch phase* ϕ for a periodic system, which for a symmetric cell in SMA is related to the transfer matrix through the relation

$$\cos(\phi) = Tr(\mathrm{M})/2$$
$$= \frac{B}{A}\cos(\alpha l) - \frac{A^2 - B^2 + \alpha^2}{2\alpha A}\sin(\alpha l) \quad . \tag{2.41}$$

For energies above continuum threshold one has $\cos(\phi) = Re(M_{11})$ [13]. Below continuum threshold, the longitudinal momentum in the lowest transverse channel becomes imaginary, *i.e.* $\alpha \to i|\alpha|$ and the SMA relation for the Bloch phase then takes the form

[13] In earlier papers by Sprung *et al.* it was asserted that this relation holds below threshold as well. From (2.37) it can be seen that $\cos(\phi) \neq Re(M_{11})$ below continuum threshold. These and other relations of scattering amplitudes below continuum threshold are reviewed in a recent addendum by Wu, Sprung and Martorell [76].

$$\cos(\phi) = \frac{B}{A}\cosh(|\alpha|l) - \frac{A^2 - B^2 - |\alpha|^2}{2|\alpha|A}\sinh(|\alpha|l) \quad . \tag{2.42}$$

An "*allowed*" region is defined by $|\cos(\phi)| < 1$, and a "*forbidden*" region by $|\cos(\phi)| > 1$. Allowed regions are those characterized by free propagation through the system. In allowed regions the Bloch phase gives the phase shift arising in the transition across a single cell. In forbidden regions, where the Bloch phase is complex, the magnitude of the wave function decreases exponentially when crossing a cell.

The single-mode approximation provides an estimate for the bound state energies in a bent tube. A bound state is a stationary state existing below continuum threshold, for some $k_b < \pi$. For the bound state all longitudinal momenta are imaginary, i.e. $\alpha_n = i\sqrt{(n\pi)^2 - k_b^2}$. For energies below the continuum, the traveling wave terms in the external straight sections from (2.3) become exponentially increasing and decreasing solutions. For a bound state to exist, the wave function must decrease exponentially in the straight sections. If the exponentially increasing terms are retained, the wave function cannot be normalized. Therefore, the coefficients of the exponentially increasing terms from (2.27) are set to zero. In SMA the resulting equation for the bound state can be written

$$\begin{pmatrix} 0 \\ r_1 \end{pmatrix} = \begin{pmatrix} M_{11} & M_{12} \\ M_{21} & M_{22} \end{pmatrix} \begin{pmatrix} t_1 \\ 0 \end{pmatrix} \quad . \tag{2.43}$$

It is seen by inspection of (2.43) that the condition for a bound state is $M_{11} = 0$. From (2.37) one can obtain the SMA estimate for the bound state in a single symmetric cell,

$$A^2 = (B + |\alpha|)^2 \quad . \tag{2.44}$$

For transmission through N identical cells in series, one needs the matrix $\mathbf{M}^{(N)}$. In SMA the transfer matrix $\mathbf{M}$ is a unimodular 2×2 matrix. For such a matrix one can derive the relation [30]

$$\mathbf{M}^{(N)} = \frac{1}{\sin(\phi)}\left[\sin(N\phi)\mathbf{M} - \sin((N-1)\phi)\mathbf{I}\right] \quad . \tag{2.45}$$

In (2.45) the matrix $\mathbf{I}$ is the unit matrix. Thus in single-mode approximation the transmission and reflection amplitudes through N identical cells, t_N and r_N respectively, can be written directly in terms of the elements of M and the Bloch phase,

$$\begin{aligned} \left(M^{(N)}\right)_{11} &= 1/t_N = \frac{1}{\sin(\phi)}\left[\sin(N\phi)M_{11} - \sin((N-1)\phi)\right] \\ &= \frac{1}{\sin(\phi)}\left[\sin(N\phi)/t_1 - \sin((N-1)\phi)\right] \\ \left(M^{(N)}\right)_{21} &= r_N/t_N = \frac{\sin(N\phi)}{\sin(\phi)}M_{21} = \frac{\sin(N\phi)}{\sin(\phi)}(r_1/t_1) \quad . \end{aligned} \tag{2.46}$$

Equation (2.46) shows that in this approximation, the transmission and reflection amplitudes can be written in terms of t_1 and r_1 through a single cell, and the Bloch phase. In particular, the ratio of reflection to transmission amplitudes for N identical cells has a particularly simple relationship to the corresponding result through a single cell [14]. In Chap. 6, when we discuss tubes composed of a series of identical cells, it will be demonstrated that (2.46) provides a qualitative understanding of many of the features of scattering through a finite periodic series of cells.

It is straightforward to show [28] that, in single-mode approximation, the transmission probability through a symmetric curved tube obtained using (2.37) is identical to the transmission probability through a one-dimensional square well with width w and depth V [78]. Since in SMA only a single transverse channel is considered, one can drop channel indices and adopt the notation $A = A_{11}$, $B = B_{11}$, and $\alpha = \alpha_1$. The wave numbers outside and inside the square well are α and $\gamma = \sqrt{A^2 - B^2}$, respectively, and the width and depth of the "*effective square well*" potential are related to the tube parameters through

$$w = \frac{1}{\gamma}\cos^{-1}(\frac{B}{A}) = \frac{1}{\sqrt{A^2 - B^2}}\cos^{-1}(\frac{B}{A}) \ ,$$
$$V = \gamma^2 - \alpha^2 = A^2 - B^2 - \alpha^2 \ . \tag{2.47}$$

Therefore, in single-mode approximation, the transfer matrix for any symmetric quantum wire with two external leads is identical to that of an effective one-dimensional square well, whose parameters are given by (2.47). The matrix elements A_{11} and B_{11} depend explicitly on the energy, so both the width and depth of this effective potential are energy dependent. Nevertheless, the square well approximation derived by Wu, Sprung and Martorell [28] is useful for understanding a number of scattering and binding problems in two-dimensional tubes. In Chaps. 5 and 6 the effective SMA square-well potential will be used to investigate binding and scattering phenomena in tubes with two cells and many cells, respectively.

For certain geometries, the open-mode truncation gives analytic expressions for the effective potential width and depth, and provides analytic approximations for the bound states and transmission coefficients. Bound state energies can be estimated by applying the single-mode approximation at low energies, and the SMA result of (2.44) provides a first estimate for the binding energy. Wu, Sprung and collaborators have applied these estimates to several systems of interest [27, 28, 79, 80]. In later sections we will give several examples of the power of this approximation, particularly for systems composed of a finite periodic series of identical cells.

[14] Vezzetti and Cahay [77] had previously shown that, for an effective one-dimensional problem, (2.46) held for the transmission probability (the square of the transmission amplitude). The more general result (2.45) was proved in [30].

In approximations where only the lowest transverse channel is considered, the resulting scattering is quasi-one-dimensional. There are a number of approximation schemes for 1-D problems which can be applied to obtain analytic formulas for the transmission and conductance. One method which has been widely used is called the "*current conservation method*," which was first introduced by Griffith [81, 82]. In this scheme the continuity of normal derivatives of wave functions at junctions is enforced in the same way as current conservation in circuits via Kirchhoff's laws. This method has subsequently been applied by several other groups [83, 84, 85, 86, 87]. Shi and Gu [88] derived algorithms which allow one to assign an impedance to any "circuit element" (stub, Aharonov–Bohm ring, etc.) connected in series or parallel, and gave rules for combining impedances in any 1-D system. One-dimensional systems have also been studied widely in optics [89].

These 1-D models help us to evaluate the nature of the phenomena seen in quantum wires. To the extent that the single-mode approximation reproduces exact scattering results, the dominant physics is quasi-1D. Certainly at energies above the second transverse channel threshold, such an approximation will no longer be valid, and 1-D models also fail to reproduce the quasi-bound state which will be seen just below the second transverse channel threshold. Nevertheless, these 1-D models generally give very good qualitative agreement (and often quantitative agreement) with low-energy bound state and transmission properties of quantum wires. Such models provide powerful insight into the physics governing the behavior of these systems, and they enable us to separate quasi-1D effects from true two-dimensional phenomena.

2.1.5 Example: One-Dimensional Reduction Applied to the L-Shaped Tube

As an example of the transfer matrix method, consider the L-shaped tube shown in Fig. 2.3a. After it was demonstrated that this system possesses a bound state [15, 16, 17, 55], binding and low-energy scattering in tubes with a single bend were studied by several groups [21, 22, 23, 27, 28]. The transverse eigenfunctions in the straight leads are given by (2.3). As the tube is symmetric with respect to reflection about its center, it is necessary to consider only the interior function χ_{0n} of (2.26), which can be calculated analytically

$$\begin{aligned}
\chi_{0n}(X,Y) &= \sqrt{2}\sin(n\pi Y)\frac{\sin(\alpha_n X)}{\sin(\alpha_n)} \\
\nabla\chi_{0n}\cdot\boldsymbol{\sigma}_1|_{\sigma_1} &= \sqrt{2}n\pi\,(-1)^n\frac{\sin(\alpha_n X)}{\sin(\alpha_n)} \\
\nabla\chi_{0n}\cdot\boldsymbol{\sigma}_2|_{\sigma_2} &= \sqrt{2}\alpha_n\sin(n\pi Y)\cot(\alpha_n)\ . \qquad (2.48)
\end{aligned}$$

The coefficients of the matrices **A** and **B** can also be calculated exactly,

$$A_{nm} = \frac{2nm\pi^2\,(-1)^{n+m}}{(n\pi)^2 - \alpha_m^2} \approx \frac{2\pi^2}{\pi^2 - \alpha_1^2}$$
$$B_{nm} = \alpha_n \cot(\alpha_n)\delta_{nm} \approx \alpha_1 \cot(\alpha_1) \quad . \tag{2.49}$$

In (2.49), the second values given are the elements A_{11} and B_{11} (only these elements are used in the single-mode approximation). From (2.44), the SMA estimate for the bound state energy is $k_s^2 = 0.946\,\pi^2$; if the full matrices A and B are included (rather than just the lowest mode terms), the exact bound state energy can be calculated, with the result $E_b = k_b^2 = 0.929\,\pi^2$. We define the *binding energy* BE as the difference between the continuum and the bound state energy, *i.e.*

$$BE = E_{th} - E_b$$
$$= \pi^2 - k_b^2 \quad . \tag{2.50}$$

The single-mode approximation to the binding energy for the L-shaped tube is not particularly precise ($BE_s = 0.054\,\pi^2$ vs. the exact value $BE = 0.071\,\pi^2$); the exact binding energy is about 30% larger than the SMA value, for this geometry. The single-mode result will give a lower limit to the binding energy since every transverse channel produces an effective attractive potential, so the SMA (which includes only the lowest transverse mode) underestimates the binding potential. Figure 2.3b shows the exact bound state wave function. The wave function is large in the vicinity of the bend, vanishes at the tube boundary, and decays exponentially along the straight legs of the tube. The bound state wave function has no zeroes inside the tube, and a single maximum in the bend region. In later sections we will encounter systems which have more than one bound state. In such systems, the higher-energy states must be orthogonalized to the lower energy states. As a result, the higher energy bound states in such systems will have nodes in their wave functions.

The effective square well potential for this geometry can be obtained from (2.47). One can obtain reasonable results by assuming that α_1 is small; if the single-mode values for A_{11} and B_{11} in (2.49) are expanded to lowest order in α_1, the approximate values for a tube of unit width are

$$A_{11} \approx 2\,, \qquad B_{11} \approx 1\,, \qquad \gamma \approx \sqrt{3}$$
$$w \approx \frac{\pi}{3\sqrt{3}}\,, \qquad V \approx 3 \quad . \tag{2.51}$$

The bound state energy in the square well (sw) approximation is $k_{sw}^2 = 0.938\,\pi^2$. The effective square well prediction is somewhat closer to the exact binding energy than the SMA estimate. For bent waveguides composed of several successive L-shaped bends, the effective potential for such a system can be considered as a series of effective square wells. If successive bends are separated by a distance l then the square well width is given by (2.51), with separation l between adjacent square wells [15]. In Chap. 5 this approximation

[15] Clearly, for a tube with a series of successive cells, the SMA estimate of the effective potential as a series of identical square wells will not make sense if the

will be extended to treat the case of two cells in series, and Chap. 6 it will be applied to series connections of many identical cells.

2.2 Bound States in Three-Dimensional Tubes

In this chapter we have focused our attention on the properties of bound states in 2-D tubes. However, most of the bound state existence proofs given here can be straightforwardly extended to three-dimensional [3-D] tubes. For example, a 3-D tube with a bulge will always possess at least one bound state, provided only that the deformed tube has a greater volume than the original tube. This was proved by Bulla *et al.* [26], and is a direct extension of the arguments used in the two-dimensional existence proof.

A 3-D tube of constant normal cross-section will also have at least one bound state if it has a local curvature over a finite part of its length. This was demonstrated in the adiabatic limit by Exner [90], and proved generally by Goldstone and Jaffe [18]. Again, adiabatically the curvature produces an effective "potential" $-\kappa^2/4$, and the torsion appears as a gauge field. Here we briefly review the variational 3-D proof of Goldstone and Jaffe.

First, construct the tube and a convenient coordinate system from a curve C parametrized as $\mathbf{x}(s)$ and a disc D of arbitrary shape. Begin with the Frenet frame vectors $\widehat{\mathbf{t}}$, $\widehat{\mathbf{n}}$ and $\widehat{\mathbf{b}}$ which satisfy

$$\widehat{\mathbf{t}}' = \kappa(s)\widehat{\mathbf{n}} \qquad \widehat{\mathbf{n}}' = -\kappa(s)\widehat{\mathbf{t}} + \tau(s)\widehat{\mathbf{b}} \qquad \widehat{\mathbf{b}}' = \tau(s)\widehat{\mathbf{n}} \ . \tag{2.52}$$

In (2.52), $\kappa(s)$ and $\tau(s)$ are the curvature and torsion of $\mathbf{x}(s)$, and the prime signifies differentiation with respect to s. From these frame vectors one defines two new vectors

$$\begin{aligned} \widehat{\mathbf{N}} &= \cos[\theta(s)]\widehat{\mathbf{n}} + \sin[\theta(s)]\widehat{\mathbf{b}} \\ \widehat{\mathbf{B}} &= -\sin[\theta(s)]\widehat{\mathbf{n}} + \cos[\theta(s)]\widehat{\mathbf{b}} \ , \end{aligned} \tag{2.53}$$

with $\theta(s)$ defined by

$$\theta(s) = -\int_{-\infty}^{s} ds'\,\tau(s') \ . \tag{2.54}$$

From the definition (2.53) for the new frame vectors, the vectors $\widehat{\mathbf{N}}$, $\widehat{\mathbf{B}}$ and $\widehat{\mathbf{t}}$ can be shown to satisfy the relations

$$\begin{aligned} \widehat{\mathbf{N}}' &= -\kappa(s)\cos[\theta(s)]\widehat{\mathbf{t}} \\ \widehat{\mathbf{B}}' &= \kappa(s)\sin[\theta(s)]\widehat{\mathbf{t}} \\ \widehat{\mathbf{t}}' &= \kappa(s)\{\cos[\theta(s)]\widehat{\mathbf{N}} - \sin[\theta(s)]\widehat{\mathbf{B}}\} \ . \end{aligned} \tag{2.55}$$

width w of an individual well from (2.51) is greater than the separation l between adjacent cells.

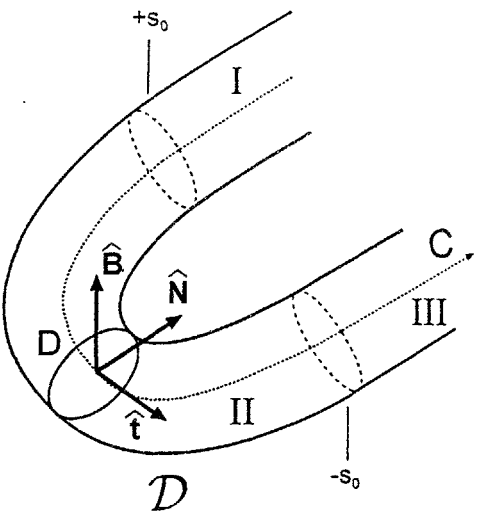

Fig. 2.4. Schematic picture of a three-dimensional tube constructed from a disk D moving along the curve C. The vectors in the "parallel transport frame" are shown. The tube can have non-zero curvature up to the points $s = \pm s_0$

The new triad (the "*parallel transport frame*" [91]) is used to construct the tube; the disc D is moved along C rigidly in a reference frame such that $\widehat{\mathbf{N}}$ and $\widehat{\mathbf{B}}$ are at rest, so that its boundary sweeps out the tube $\mathcal{D}$. The unit vectors for such a coordinate system are shown schematically in Fig. 2.4. If the points inside $\mathcal{D}$ are parametrized by

$$\mathbf{x}(s,\xi,\eta) = \mathbf{x}(s) + \xi\widehat{\mathbf{B}} + \eta\widehat{\mathbf{N}} \ , \tag{2.56}$$

then one can show that the volume element is

$$d^3x = (1 - \kappa(s)\{\eta\cos[\theta(s)] - \xi\sin[\theta(s)]\})ds\,d\xi\,d\eta \ . \tag{2.57}$$

From here on, the variational argument for the existence of a bound state is similar to that of the two-dimensional case. The tube is divided into straight sections labeled I and III with $|s| > s_0$, and a central curved section II with $|s| < s_0$, as shown in Fig. 2.4. Suppose $\chi(\xi,\eta)$ is the lowest eigenfunction of the Dirichlet problem on the disc D; if its eigenvalue is $-k_0^2$, the transverse coordinates ξ and η can be rescaled so that $k_0^2 = 1$. Then consider the trial function

$$\psi(s,\xi,\eta) = \begin{cases} \chi(\xi,\eta)e^{-\lambda(|s|-s_0)} & \text{for } |s| > s_0 \\ \psi_{\rm II}(s,\xi,\eta) & \text{for } |s| < s_0 \end{cases} \ . \tag{2.58}$$

Inserting the trial function from (2.58) into the energy functional of (2.8), the condition for a bound state reduces to

$$\int_{\rm II} d^3x\,(\psi_{\rm II}^2 - |\nabla\psi_{\rm II}|^2) > 4\lambda \ . \tag{2.59}$$

Since λ was an arbitrary positive number, it is only necessary to show that the integral in (2.59) is *positive* for some trial function $\psi_{\rm II}$ in the curved region, which satisfies the boundary conditions $\psi_{\rm II}(\pm s_0, \xi, \eta) = \chi(\xi, \eta)$.

In fact, choosing $\psi_{\rm II} = \chi(\xi, \eta)$ it is possible to show [18] that

$$\int_{\rm II} d^3x(\psi_{\rm II}^2 - |\nabla\psi_{\rm II}|^2) =$$
$$\int_{-s_0}^{s_0} ds \int_D d\eta\, d\xi\, [1 - \kappa(\eta\cos\theta - \xi\sin\theta)]\,(\chi^2 - |\nabla_\perp\chi|^2) = 0 \quad . \quad (2.60)$$

There will exist a function $\phi_{\rm II}$ which *does* satisfy the condition given in (2.59) unless the choice $\psi_{\rm II} = \chi(\xi, \eta)$ is an extremum for the variational problem on region II, subject to the boundary condition. It is clear that this is not the case, since then it would satisfy $\nabla^2\psi_{\rm II} + \psi_{\rm II} = 0$. It does not, so a suitable function $\phi_{\rm II}(\mathbf{x})$ on II must exist, which satisfies (2.59) for a suitably small positive number λ. This completes the bound state existence proof in three dimensions.

In their review article on bent tubes and bound states, Duclos and Exner [14] discuss the extension of the bound state existence proofs to three dimensions. As in the 2-D case, it is not necessary that the torsion vanish at a certain distance, as required by Goldstone and Jaffe. Duclos and Exner summarize the limits on the torsion and its derivatives necessary to produce binding. They separate the relative contributions of bending and torsion to binding in a three-dimensional tube. Just as for the 2-D case, they produce lower bounds on the number of bound states in a bent 3-D tube, and an adiabatic approximation for the bound state energy in such a tube. Takagi and Tanzawa [92] consider the quantum mechanics of a particle in a gently twisted and curved loop.

3. Transmission and Conductance in Tubes

Chapter 2 summarized the properties of bound states in constrained two-dimensional structures. In this chapter we discuss transmission and conductance through these 2-D systems. Section 3.1 considers the physics of transmission and reflection through long curved tubes. Some general formulas are derived for such systems, and examples of transmission in simple geometries are studied. In later chapters these formulas are applied to tubes with various geometries.

In Sect. 3.2, the probability current is introduced. It is shown that plots of the probability current density give considerable insight into the physics of particle transmission through bent tubes. In this case one follows the stream lines of the quantum probability current $\mathbf{j}$. The properties of stream lines in the flow are reviewed. We also demonstrate the importance of vortices in the probability flow, and fixed points which form boundaries between different regions of flow. It is shown that deep minima in the transmission are generally associated with substantial vortex formation in the probability flow.

Section 3.3 briefly reviews the physics of electron quantum heterostructures. We focus on the extent to which the analogy of single particles moving in 2-D tubes is an accurate description of electron motion in quantum wires. Section 3.4 presents a qualitative derivation of the Landauer formula for electron conductance in quantum heterostructures. In Sect. 3.5 the conductance is derived for the simple case of a straight conducting channel between two reservoirs. The qualitative features of the conductance are reviewed, and the dependence of conductance on electron temperature is studied.

3.1 Transmission and Reflection in a Long Tube

Consider a long curved tube of the type shown schematically in Fig. 2.1b. The tube has two straight leads of unit width labeled 1 and 2, connected by a center region of arbitrary shape. Coordinates in regions 1 and 2 are defined as shown; the longitudinal and transverse directions are defined as x_j and y_j respectively in lead j, with the boundary to the deformed region defined as $x_j = 0$. In the straight sections the wave functions are expanded in terms of transverse eigenfunctions $\phi_m(y)$ with eigenvalues ϵ_m. The wave functions in the straight sections $\Gamma = 1, 2$ are expanded using (2.3) and (2.27),

J. T. Londergan, J. P. Carini and D. P. Murdock: LNPm 60, pp. 37 - 70, 1999
© Springer-Verlag Berlin Heidelberg 1999

$$\begin{aligned}\psi_\Gamma(x,y) &= \sum_m \left[C_{\Gamma,m}\exp(i\alpha_m x) + \widetilde{C}_{\Gamma,m}\exp(-i\alpha_m x)\right]\phi_m(y)\\ \phi_m(y) &= \sqrt{2}\sin(m\pi y)\\ \alpha_m &= \sqrt{k^2-\epsilon_m}\ , \quad \epsilon_m = (m\pi)^2\ .\end{aligned} \tag{3.1}$$

Elastic threshold begins at energy $k_{th}^2 = \pi^2$. For a given energy above threshold, there are a certain number of open channels. If transverse channel n is open, then $k > \epsilon_n$, and the longitudinal wave number α_n is real. Channels for which $\epsilon_m > k$ are closed channels, which have imaginary longitudinal wave numbers $\alpha_m = i\beta_m$, where $\beta_m = \sqrt{\epsilon_m - k^2}$. To solve this problem, the wave functions in the internal region of the tube are expanded in a complete set of channel eigenfunctions defined in (2.26), which satisfy the boundary conditions in that region. The expansion coefficients are fixed by requiring the wave functions and normal derivatives to be continuous on the region boundaries σ_1 and σ_2 shown in Fig. 2.1b.

The scattering problem is solved by finding the reflected and transmitted waves resulting from an incident wave in transverse channel n of lead 1. In this case, the boundary conditions require that external lead 1 have an incoming wave in channel n and reflected waves in all channels; in lead 2 there are only outgoing transmitted waves in all channels. Normalized to the incident flux, the expansion coefficients of (3.1) then have the form

$$\begin{aligned}C_{1m}^{(n)} &= \frac{\delta_{nm}}{\sqrt{\alpha_m}}\\ \widetilde{C}_{1m}^{(n)} &= \frac{\mathcal{R}_{nm}}{\sqrt{\alpha_m}}\\ \widetilde{C}_{2m}^{(n)} &= 0\\ C_{2m}^{(n)} &= \frac{\mathcal{T}_{nm}}{\sqrt{\alpha_m}}\ .\end{aligned} \tag{3.2}$$

In (3.2) there is a unit incident wave in channel n of lead 1, and no incident waves in lead 2. The quantity $\mathcal{R}_{nm}$ is the *reflection amplitude* in channel m of lead 1, arising from an incident wave in channel n, and $\mathcal{T}_{nm}$ is the *transmission amplitude* in channel m of lead 2. By normalizing to the flux in each channel (the $\sqrt{\alpha_m}$ factor in the denominator of each term in (3.2)), we normalize the various channel states so that they carry equal current; with this definition the resulting transmission and reflection amplitudes do not require additional renormalization to account for unequal current densities in the various transverse channels.

In general, the transmission and reflection amplitudes are complex quantities. The reflection and transmission *coefficients* are non-negative real numbers which are given by the absolute square of the reflection and transmission amplitudes, respectively,

$$R_{nm} = |\mathcal{R}_{nm}|^2$$
$$T_{nm} = |\mathcal{T}_{nm}|^2 \quad . \tag{3.3}$$

The total reflection and transmission *probabilities* give the total probability that a wave incident in channel n is reflected (or transmitted) into all channels. The reflection (transmission) probability is given by the sum of the reflection (transmission) coefficients

$$R_n = \sum_m{}' R_{nm}$$
$$T_n = \sum_m{}' T_{nm} \quad , \tag{3.4}$$

where the sum in (3.4) is taken only over open channels.

A special case occurs when the two-dimensional system possesses longitudinal symmetry with respect to reflection about the center of the tube, as was discussed in Sect. 2.1.4. For this case one can consider separately those states which are symmetric or antisymmetric with respect to reflection. The symmetric state is obtained by averaging the states obtained for an incident wave in channel n from lead 1, and from lead 2, of the system. In the external leads of the tube the symmetric wave function has the form

$$\psi_S^{(n)}(x,y) = \sum_m [\exp(-i\alpha_m|x|)\delta_{nm} + (\mathcal{T}_{nm} + \mathcal{R}_{nm})\exp(i\alpha_m|x|)] \frac{\phi_m(y)}{\sqrt{\alpha_m}} \quad , \tag{3.5}$$

where the symmetric state is identical in both external leads of the wire. The antisymmetric wave function is obtained by taking the wave function incident from lead 1 in channel n and subtracting the one incident from lead 2. In this case the wave function in lead 2 can be written

$$\psi_{A,2}^{(n)}(x,y) = \sum_m [-\exp(-i\alpha_m x)\delta_{nm} + (\mathcal{T}_{nm} - \mathcal{R}_{nm})\exp(i\alpha_m x)] \frac{\phi_m(y)}{\sqrt{\alpha_m}} \quad . \tag{3.6}$$

The antisymmetric wave function in external lead 1 has the form

$$\psi_{A,1}^{(n)}(x,y) = -\psi_{A,2}^{(n)}(-x,y) \quad . \tag{3.7}$$

In Chap. 2 we defined the transfer matrix M; this matrix gave the coefficients of waves on the left side of a cell as a function of the coefficients on the right side. The transfer matrix is directly related to the transmission or T-matrix. For example, it was shown in (2.40) that in single-mode approximation the elastic transmission amplitude is given by $\mathcal{T}_{11} = 1/M_{11}$. An alternative quantity is the scattering or S-matrix. This matrix expresses the coefficients of the outgoing waves on either side of a cell in terms of the incoming waves. Elementary definitions of the scattering matrix and its

properties can be found in the quantum mechanics textbook by Merzbacher [57]. More detailed discussion can be found in the monographs by Newton [93] or Goldberger and Watson [94]. One can therefore define symmetric and antisymmetric S-matrix elements in terms of the transmission and reflection amplitudes,

$$\begin{aligned} \mathcal{S}^S_{nm} &= (\mathcal{T} + \mathcal{R})_{nm} \\ \mathcal{S}^A_{nm} &= (\mathcal{T} - \mathcal{R})_{nm} \quad . \end{aligned} \tag{3.8}$$

The various symmetries of the scattering problem require that the S-matrix obey certain relations. One of the most important conditions is that the symmetric and antisymmetric S-matrix are *unitary*. Unitarity follows from the invariance of the S-matrix under time reversal. Loosely speaking, if one took a movie of a microscopic interaction, time reversal invariance would mean that there would be no distinguishable difference between running the movie forward, or backward. For spinless particles, the operation of time reversal changes the sign of the longitudinal momentum, and interchanges the initial and final channel labels. More detailed discussions of time-reversal invariance can be found in the books by Schiff [78] or Newton [93].

The unitarity condition requires that

$$\begin{aligned} (\mathcal{S}^S)^\dagger \mathcal{S}^S &= \mathbf{I} \\ (\mathcal{S}^A)^\dagger \mathcal{S}^A &= \mathbf{I} \quad . \end{aligned} \tag{3.9}$$

The unitarity condition (3.9) is a matrix relation, where the matrix $\mathbf{I}$ is the unit matrix. The elements of the adjoint of a matrix are related to the elements of the original matrix by

$$A^\dagger_{mn} = (A^*)_{nm} \quad . \tag{3.10}$$

The dimension of the S-matrix in (3.9) is limited to those channels which are open at a given energy.

For a symmetric tube, the unitarity conditions (3.8) and (3.9) impose two conditions on the transmission and reflection matrices

$$\begin{aligned} \mathcal{T}^\dagger \mathcal{T} + \mathcal{R}^\dagger \mathcal{R} &= \mathbf{I} \\ \mathcal{T}^\dagger \mathcal{R} + \mathcal{R}^\dagger \mathcal{T} &= 0 \quad . \end{aligned} \tag{3.11}$$

Equation (3.11) expresses the unitarity constraints on transmission and reflection amplitudes which follow from the symmetry of the system. The first of (3.11) includes the conservation of probability, *i.e.* $R_n + T_n = 1$, where T_n and R_n are respectively the total transmission and reflection probabilities given by (3.4).

3.1.1 Example: Transmission in the L-Shaped Tube

As an example of transmission in a curved tube, consider the L-shaped tube shown in Fig. 2.3a. From our discussion in Chap. 2, the L-shaped tube contains both a bend and a bulge in the vicinity of the right-angle corner. The

coefficients $C_{\Gamma,m}$ and $\widetilde{C}_{\Gamma,m}$ are obtained by solving the resulting linear equations, (2.28), where $\Gamma = 1, 2$ refers to the wave function on the left and right hand side of the bend, respectively.

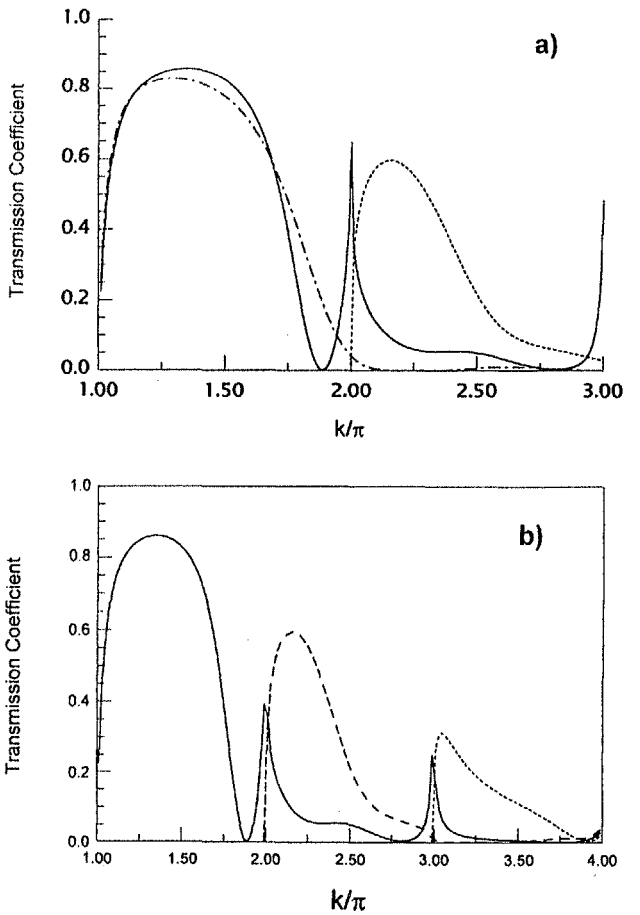

Fig. 3.1. (a) Dot-dashed curve: single-mode approximation to transmission probability T_1 for the L-shaped tube, vs. the wave number k, from [27]. Solid curve: T_1, dotted curve: T_2 calculated using four transverse modes. (b) Transmission coefficients T_{11} (solid curve), T_{12} (dashed curve) and T_{13} (dotted curve) from (3.3), calculated using 20 transverse modes

In Sect. 2.1.5 it was shown that the "single-mode approximation" (SMA) gave a reasonable prediction for the bound state energy in the L-shaped tube. We apply the SMA to estimate the transmission amplitude in this tube, for energies from threshold to the opening of the second transverse channel. In this case the sum over transverse modes is truncated at $N = 1$, the matrices

A and **B** defined in (2.31) become numbers which are given in (2.49), and using (2.37) and (2.40) one obtains an analytic expression for the transmission probability,

$$T_1(\alpha_1) = \frac{1}{|M_{11}|^2} = \left[\frac{B^2}{A^2} + \left(\frac{A^2 - B^2 + \alpha_1^2}{2\alpha_1 A}\right)^2\right]^{-1}$$
$$= \left[1 + \left(\frac{u^2 - 1}{2u\sin(\alpha_1)}\right)^2\right]^{-1} , \tag{3.12}$$

where the quantity u in (3.12) is given by

$$u = \frac{2\pi^2 \sin(\alpha_1)}{(\pi^2 - \alpha_1^2)\,\alpha_1} . \tag{3.13}$$

The dot-dashed curve in Fig. 3.1a shows the SMA estimate for the transmission probability T_1 in the L-shaped tube vs. the wave number k, as calculated by Martorell *et al.* [27]. The solid curve shows the transmission probabilities T_1 and T_2, from (3.4), when four channels are included in the expansion. The transmission probability rises rapidly from zero at threshold ($k/\pi = 1$) to a maximum transmission $T_1 \approx 0.85$. Upon reaching a maximum, the transmission probability remains roughly constant until shortly before the opening of the second transverse channel, when it decreases and is nearly zero for $k/\pi \sim 1.88$. Figure 3.1b shows the transmission coefficients T_{11} (solid curve), T_{12} (dotted curve), and T_{13} (dashed curve) calculated by Trinkle [95], when 20 transverse channels are included. The single-mode approximation gives a reasonable estimate of T_{11}, until energies slightly below the second transverse channel (k/π =2). However, the single-mode approximation cannot reproduce the destructive quasi-bound state at $k/\pi \sim 1.88$, since this is an interference effect arising from the effect of higher transverse modes excluded from the SMA.

We can deduce some general features of the transmission amplitudes, and hence the transmission probabilities. Note that the transmission probability of (3.12) is a function of the longitudinal momentum α_1. In our constrained 2-D systems, the transmission amplitude depends only on the longitudinal momentum. There is a direct relation between the longitudinal momentum α_n in the n^{th} transverse channel and the overall wave number k, as given in (2.3), however the transmission amplitudes will be explicit functions of the longitudinal momenta.

Many of our examples will involve low-energy binding or scattering. In this regime the single-mode approximation, or SMA, often gives accurate approximations to the exact results. In the SMA the transfer matrix is a 2×2 matrix. We can write the transmission and reflection amplitudes as functions of the longitudinal momentum $\alpha_1 \equiv \alpha$,

$$\mathcal{T}_{11}(\alpha) = t(\alpha)$$
$$\mathcal{R}_{11}(\alpha) = r(\alpha) . \tag{3.14}$$

In SMA, the general form of the transfer matrix which is consistent with time reversal is

$$\mathrm{M}_{SMA}(\alpha) = \begin{pmatrix} \frac{1}{t(\alpha)} & \frac{r(-\alpha)}{t(-\alpha)} \\ \frac{r(\alpha)}{t(\alpha)} & \frac{1}{t(-\alpha)} \end{pmatrix} \quad . \tag{3.15}$$

The relation (3.15) is valid both above and below the continuum threshold. Above threshold, the transmission and reflection amplitudes obey the relation

$$\begin{aligned} t^*(\alpha) &= t(-\alpha) \\ r^*(\alpha) &= r(-\alpha) \quad . \end{aligned} \tag{3.16}$$

Consequently, above continuum threshold the transfer matrix in SMA can be written in the following form,

$$\mathrm{M}_{SMA}(\alpha) = \begin{pmatrix} \frac{1}{t(\alpha)} & \frac{r^*(\alpha)}{t^*(\alpha)} \\ \frac{r(\alpha)}{t(\alpha)} & \frac{1}{t^*(\alpha)} \end{pmatrix} \quad . \tag{3.17}$$

Because of the conservation of probability which holds for energies above continuum threshold but below the threshold for the second transverse channel,

$$|t(\alpha)|^2 + |r(\alpha)|^2 = 1 \quad , \tag{3.18}$$

it is straightforward to show that the transfer matrix of (3.17) has determinant one.

The near-threshold behavior of the transmission can be understood by considering how the bound state influences the low-energy transmission amplitude $\mathcal{T}_{11}$. From Sect. 2.1.5, the L-shaped tube has a bound state which occurs at energy $E_b = 0.929\,\pi^2$. One can define the magnitude of the longitudinal wave number appropriate for the bound state $|\alpha_b| = \sqrt{\pi^2 - E_b}$. As the bound state wave function is symmetric with respect to reflection, the bound state appears as a pole in the symmetric S-matrix $\mathcal{S}^S$ defined in (3.8), at the point $\alpha = i\alpha_b$. From (3.8), the transmission amplitude near continuum threshold can be written as

$$\mathcal{T}_{11}(\alpha_1) = \frac{\mathcal{S}^S_{11}(k) + \mathcal{S}^A_{11}(k)}{2} = \frac{1}{2}\left[\frac{\alpha_1 + i\alpha_b}{\alpha_1 - i\alpha_b} + f_b(\alpha_1)\right] \quad . \tag{3.19}$$

The first term in (3.19) is the contribution from the pole in $\mathcal{S}^S$. Unitarity or conservation of probability, expressed in the conditions (3.11), requires that for energies above continuum threshold, the magnitude of the transmission amplitude cannot exceed one. The pole term is written in a form which, for real values of α_1, does not violate the unitarity condition on $\mathcal{T}_{11}$. The pole term is also consistent with the relation (3.16). The second term $f_b(\alpha_1)$ in (3.19) is the antisymmetric S-matrix contribution to $\mathcal{T}_{11}$. In general, $f_b(\alpha_1)$ will be a slowly varying background term, relative to the pole contribution, for energies near the continuum threshold at $\alpha_1 = 0$. The requirement that the transmission amplitude be zero at threshold means that

$$f_b(\alpha_1 = 0) = 1 \ . \tag{3.20}$$

A reasonable approximation for the scattering amplitude near threshold can be obtained by assuming that the background term is constant, *i.e.*

$$\mathcal{T}_{11}(\alpha_1) \approx \frac{\alpha_1 + i\alpha_b}{2(\alpha_1 - i\alpha_b)} + \frac{1}{2} = \frac{\alpha_1}{\alpha_1 - i\alpha_b} \ . \tag{3.21}$$

As α_1 increases from zero near threshold, the transmission amplitude $\mathcal{T}_{11}$ will start at zero and undergo a clockwise circular rotation with radius 1/2, centered about the point $\mathcal{T}_{11} = 1/2$. This will continue until the transmission probability (the absolute square of the transmission amplitude) is nearly one. The transmission probability will thus increase rapidly from its threshold value of zero, to a maximum value close to one. Using the approximation of (3.21), we obtain the prediction for the transmission probability

$$\begin{aligned} &T_1 = |\mathcal{T}_{11}(\alpha_1)|^2 \approx 0.5 \\ &\text{when} \qquad \alpha_1 = \alpha_b, \\ &\text{or} \qquad\quad k = \sqrt{\pi^2 + \alpha_b^2} \ . \end{aligned} \tag{3.22}$$

For the L-shaped bend, where $\alpha_b = 0.266\,\pi$, (3.22) predicts that the transmission probability should reach 0.5 when $k/\pi \approx 1.035$. Figure 3.1a shows that this estimate gives a good approximation to the low-energy transmission probability. Because the binding energy for particles in curved tubes is frequently quite small, the transmission probability will therefore increase very rapidly as the energy crosses the continuum threshold. The smaller the binding energy, the faster T_1 will rise just above threshold.

Just before the second transverse channel opens, at $k/\pi \approx 1.88$, the transmission probability goes almost to zero. At this energy, the second transverse mode is almost accessible. Just as in the lowest transverse mode, there is an attractive effective potential in this closed transverse channel, produced from all the higher transverse channels. The effective attraction produces a quasi-bound, or "*virtual bound state*" resonance[1]. If the (closed) second transverse mode was not coupled to the open first transverse mode, there would be a bound state just below the opening of the second transverse mode. Because the coupling between the channels is relatively weak, the width of the resulting resonance is small. This effect can be understood in terms of the time delay associated with resonance formation. If an incident wave in the first transverse mode makes a virtual transition to a very weakly coupled closed channel, the system will spend a long time in the second transverse mode before finally making a transition back to the energetically allowed first transverse mode. There will therefore be a pole of the $\mathcal{S}$-matrix, at a complex value of the longitudinal momentum α_1, which corresponds to

[1] Bayman and Mehoke [96] studied the properties of quasi-bound resonances in a 2-D tube.

this virtual bound state. The long time delay will mean a small resonance width. Since the first transverse mode is an open channel, this quasi-bound resonance pole will appear on an unphysical Riemann sheet of the complex k-plane. A detailed discussion of the properties of resonance poles can be found in Newton's book on scattering theory [93].

The quasi-bound state resonance produces a rapid change in the symmetric S-matrix element $\mathcal{S}^S_{11}$. This manifests itself as a zero in the transmission coefficient T_{11} just below the opening of the second channel. In two-dimensional tubes, a quasi-bound state will appear as a deep minimum in the transmission coefficient for each open channel just below the opening of a new transverse channel. For waves in tubes, this is the analog of the highly inelastic multi-channel resonances, familiar in nuclear and particle physics, which show up as nearly total destructive interference. For example, in $\pi + \pi$ S-wave elastic scattering, there is a sudden drop in the cross section just below $K\overline{K}$ threshold due to a virtual bound state resonance, the a_0, in the latter channel [97].

Lin and Jaffe [98] explained why these states always appear as destructive resonances in symmetric curved tubes, and why the resulting minimum in the transmission is nearly zero. Consider an energy which is slightly below the opening of the second transverse channel. In this region, the transmission amplitude $\mathcal{T}_{11}$ for a simple curved tube will generally be large, with magnitude close to one. The attractive potential resulting from the bend will produce a quasi-bound state just below the second transverse mode. This quasi-bound state appears as a pole in the symmetric S-matrix, and hence in the transmission amplitude $\mathcal{T}_{11}$, at a complex value of the longitudinal momentum $\alpha_1 = q_1 + i\gamma_1$. As we will see, the quantity γ_1 gives a measure of the width of the resonance as a function of energy; as γ_1 gets smaller, the ensuing resonance becomes progressively sharper. The real part q_1 of the pole position gives the point of maximum change in the transmission coefficient. The quasi-bound resonance occurs just below the opening of the second transverse mode $k \sim 2\pi$, which from (2.3) means that $q_1 \approx \sqrt{3}\pi$.

In the vicinity of this pole, the scattering amplitude in channel 1 can then be written

$$\mathcal{T}_{11}(\alpha_1)|_{k\sim 2\pi} \approx \frac{\alpha_1 - q_1 + i\gamma_1}{2\,(\alpha_1 - q_1 - i\gamma_1)} + f_b(\alpha_1) \quad , \tag{3.23}$$

where $f_b(\alpha_1)$ in (3.23) is a background term which varies smoothly over the resonance region. Equation (3.23) shows that for any symmetric curved tube which has an effective attractive potential arising the higher modes, the quasi-bound state pole in the S-matrix will produce an anticlockwise circular rotation in the transmission amplitude $\mathcal{T}_{11}$ with a radius of $1/2$, shortly below the second channel threshold [2]. The extent of the rotation and its speed will

[2] The resonant behavior in the $\mathcal{T}$ matrix becomes apparent in an *Argand diagram*, where one plots the Real part of the transmission amplitude *vs.* the imaginary part. In Sect. 5.1.3, the transmission amplitude for a tube with constant width

depend on the effective (quasi)binding, which is proportional to the square of γ_1, the coupling of this state to the lowest channel. The precise behavior of the transmission amplitude will depend on the binding energy and width, relative to the location of the second channel threshold. For example, if the resonance width γ_1 is sufficiently small, the transmission amplitude will exhibit an extremely rapid energy dependence. $\mathcal{T}_{11}$ will move through almost a complete counterclockwise circle of radius 1/2 just below the second channel threshold. Since by unitarity the magnitude of the transmission amplitude cannot exceed one, the magnitude of the transmission has to decrease, requiring that the quasi-bound state appear as a destructive resonance.

Consider a hypothetical case where there is zero reflection at energies just below the quasi-bound resonance, *i.e.*, $|\mathcal{T}_{11}| = 1$, and assume also that γ_1 is sufficiently small that the transmission amplitude undergoes almost a complete counterclockwise rotation of radius 1/2 as governed by (3.23). Unitarity requires that the transmission amplitude can never move outside a circle of unit magnitude. In order to avoid violating unitarity, $\mathcal{T}_{11}$ must move so that the quasi-bound resonance circle is tangent to the unitarity circle. In this case, the transmission amplitude (a circle of radius 1/2 tangent to the unit circle) has to pass exactly through zero.

In order that the transmission amplitude from the quasi-bound resonance pass exactly through zero, it was necessary to assume that the transmission amplitude was right on the unitarity circle at energies below the resonance, and any energy dependence of the background term had to be neglected. In general, these conditions are not satisfied, so $\mathcal{T}_{11}$ does not have to vanish identically. Nevertheless, in many situations involving a two-dimensional tube with an effective attractive potential (arising from a bend or cavity), these conditions will be approximately satisfied, and the scattering amplitude will become very small at energies just below the opening of the second transverse channel.

If the quasi-bound state has a stronger coupling to the lowest transverse mode, *i.e.* a larger value of γ_1 in (3.23), then the transmission amplitude will not vary as rapidly with energy. In this case $\mathcal{T}_{11}$ may not move in a complete resonant circle before the second transverse mode opens up. Alternatively, the background term $f_b(\alpha_1)$ in (3.23) may vary substantially across the resonance. This is the case for the L-shaped tube. As can be seen from Fig. 3.1, the zero in the transmission probability T_1 occurs fairly far below the second channel threshold, and T_1 does not vary particularly rapidly with energy, because the resonance width is rather large for this geometry.

We have shown that the transmission amplitude will exhibit a sharp dip for energies just below the opening of the second tranvserse channel. Similar behavior will occur at energies just below the opening of each subsequent transverse channel, where a quasi-bound state will appear as a destructive

and a circular bend is reviewed in detail. The quasi-bound state can be seen clearly in Fig. 5.8.

resonance. The transmission amplitude for each open channel will decrease sharply, as that amplitude undergoes an anticlockwise rotation in (approximately) a circular motion. For higher channels, however, the presence of more than one open mode means that the transmission amplitude does not have to go almost through zero. Otherwise the behavior will be qualitatively similar to that seen just below the threshold for the second transverse mode.

The destructive quasi-bound resonance will appear in theoretical calculations of transmission through a single circular bend, in Sect. 5.1.3; in this case the resulting resonance is extremely narrow. This very rapid decrease of the transmission amplitude just below each transverse mode is characteristic of theoretical calculations of transmission through a curved channel. The Landauer formula, which will be introduced in Sect. 3.4, relates the electron conductance in quantum heterostructures to the transmission amplitudes. These quasi-bound resonances should appear as sharp minima in the electron conductance just before a transverse mode opens up. The decrease can occur over such a small energy region that it may be impossible to observe in quantum heterostructures, with the relatively poor energy resolution available in those systems[3]. In Sect. 4.3.2 we will demonstrate that microwave measurements in waveguides show evidence for this dramatic decrease in the transmission coefficient just below the threshold for a new transverse mode.

3.2 Transmission and Quantum Probability Flow

Lent [99] pointed out that plots of the probability current density gave useful insight into the physics of particle transmission through curved tubes. This was also studied for various geometries by Berggren and collaborators [100, 101, 102, 103, 104], and by Wu and Sprung [105]. The probability current can be related to quantum probability flow, so consideration of this quantity can provide a useful qualitative picture of the motion of quantum particles in two-dimensional tubes. Wu and Sprung [105] pointed out that the relevant physics could be clarified using the quantum mechanical formulation emphasized by Bohm [106, 107]. Their arguments are reviewed in this section.

The motion of particles in a two-dimensional tube can described by the time-independent Schrödinger equation with a real scalar potential V,

$$-\frac{\hbar^2\nabla^2}{2m^*}\psi(\mathbf{r}) + V(\mathbf{r})\psi(\mathbf{r}) = E\psi(\mathbf{r}) \quad . \tag{3.24}$$

The results quoted here will be only true in the case of a scalar potential; in the presence of a vector potential $\mathbf{A}$, the resulting probability flow will be

[3] It will be demonstrated that sharp structure in the conductance also disappears with increasing electron temperature. The curves shown in Sect. 5.1.3 are appropriate for zero temperature electrons.

qualitatively different. The wave function $\psi(\mathbf{r})$ in (3.24) can be written in terms of two real quantities, the magnitude R and phase S defined by

$$\psi(\mathbf{r}) = R(\mathbf{r}) \exp(iS(\mathbf{r})/\hbar) \quad . \tag{3.25}$$

Inserting (3.25) into (3.24) gives two equations, for the real and imaginary parts respectively,

$$\begin{aligned} E &= \frac{1}{2} m^* v^2 + V - \frac{\hbar^2}{2m^*} \frac{\nabla^2 R}{R} \quad , \\ \nabla \cdot \mathbf{j} &= 0 \quad , \quad \text{where} \\ \mathbf{j} &= R^2 \mathbf{v} = \frac{\hbar}{2im^*} [\psi^* \nabla \psi - \psi \nabla \psi^*] \quad , \\ \mathbf{v} &= \frac{\nabla S}{m^*} \quad . \end{aligned} \tag{3.26}$$

In Bohm's formulation of quantum mechanics, the Schrödinger equation (3.24) is rewritten to resemble a classical fluid flow problem, in (3.26). The particle moves in the external potential V plus what is called the "*quantum potential*"

$$Q(\mathbf{r}) = -\frac{\hbar^2}{2m^*} \frac{\nabla^2 R(\mathbf{r})}{R(\mathbf{r})} \quad . \tag{3.27}$$

In analyzing quantum mechanical scattering, physicists tend to concentrate their attention on the properties of $R(\mathbf{r})$, the norm of the wave function. Plots of the probability density emphasize the wave aspects of quantum mechanical systems, since the zeroes and the period of $|R(\mathbf{r})|^2$ reflect the wave nature of the system. The probability current $\mathbf{j}$ is more sensitive to the particle nature of quantum transport, and it was this aspect of quantum mechanical systems which was stressed by Bohm [106, 107].

For the time-independent Schrödinger problem the current conservation equation requires that the divergence of the probability current $\mathbf{j}$ vanish. The *stream lines* of the probability flow are lines tangent to $\mathbf{j}$. Since for a scalar potential V the velocity $\mathbf{v}$ is proportional to the gradient of S, $\mathbf{v}$ is normally irrotational. The only exceptions are nodes of the wave function, *i.e.* points where $R(\mathbf{r}) = 0$, where S does not have continuous second derivatives. Therefore, it is possible to form *vortices* centered at the nodes of the wave function. This was first pointed out by Dirac [108], and was later discussed by Hirschfelder [109].

Vortex formation in tubes is often associated with standing waves, since standing waves possess a regularly-spaced series of wave function zeroes. Vortices can then form around the zeroes of the wave function. Also, a standing wave is formed from equal amplitude waves traveling in both directions, therefore one can imagine equal flow of probability current in both directions, as can be seen for flow around a single vortex. By expanding about a point where $R = 0$, it can be shown that in the vicinity of wave function nodes, the quantum potential Q for a two dimensional system has the form [105]

$$Q(r,\theta) \propto \frac{f(\theta)}{r^2} \ . \tag{3.28}$$

It follows that the stream lines around a "*quantum vortex*" form circles for sufficiently small r. In addition, the change of S around a vortex is quantized, i.e. for a closed path around a single vortex [4],

$$\Delta S = \oint m^* \mathbf{v} \cdot d\mathbf{r} = \pm h \ . \tag{3.29}$$

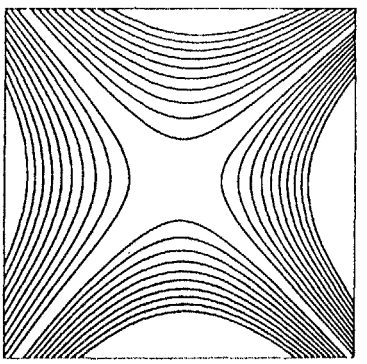

Fig. 3.2. Velocity stream lines around a node of the quantum probability current. The stream lines form hyperbolae, with the asymptotes meeting at right angles

In addition to the vortices, other significant points in the quantum probability flow are the *velocity nodes*, points where $\mathbf{v} = 0$. If the equation of motion

$$m^* \frac{d\,\mathbf{v}}{dt} = -\nabla(V + Q) \ , \tag{3.30}$$

is expanded about a fixed point, it can be shown that the resulting stream lines around the fixed point are hyperbolae whose asymptotes form right angles [105]. Since stream lines do not cross, the stream lines around a fixed point are shown schematically in Fig. 3.2. Flow which approaches a fixed point in the direction of one axis separates into two streams which depart along opposite directions. Thus the fixed points separate different regions of flow.

The flow of quantum probability current in a curved tube can then be classified into three different types. First are stream lines which come from infinity, and either pass through the tube or are reflected back. If the stream lines are traced back in the direction of the incident flux, the former give rise to the transmitted flux, and the latter the reflected flux. The second type are closed lines. These must enclose at least one vortex. The third class consists

[4] (3.29) assumes that the wave function has a simple zero at the point in question.

of lines which connect hyperbolic points; these lines form boundaries between different regions of flow.

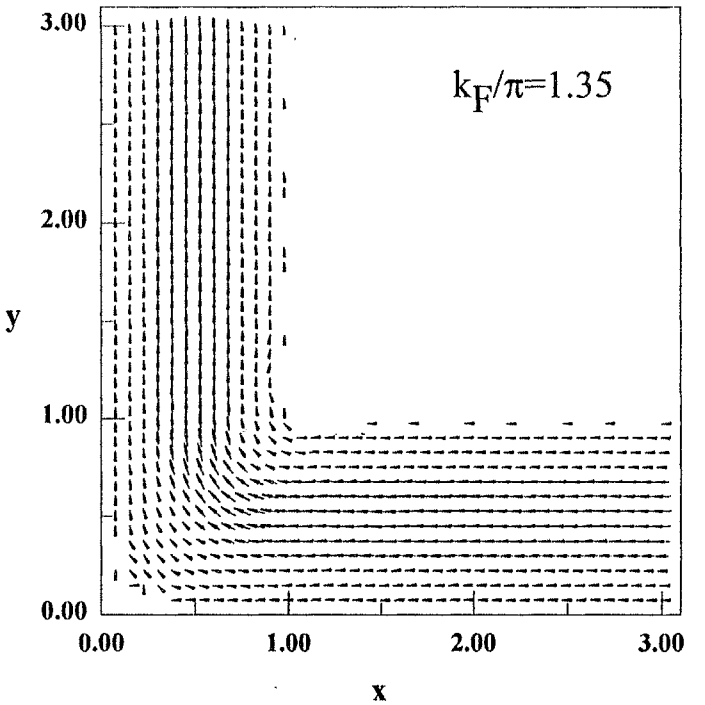

Fig. 3.3. Schematic picture of stream lines of the quantum probability current **j** of (3.26), for the L-shaped tube of Fig. 2.3a. The magnitude and direction of the arrows show the relative magnitude of **j**. Wave number $k = 1.35\pi$, corresponding to the peak in transmission probability T_1 of Fig. 3.1. The probability flow is laminar at this energy

Using the L-shaped tube as an example, we will show how analysis of the probability current density **j** can provide a clear qualitative picture of the mechanism for transport of quantum particles through this two-dimensional system. Figure 3.3 plots the probability current **j** for a long L-shaped tube. The direction of the arrows is the direction of **j**, and the relative magnitude of the probability current is determined by the length of the arrows. The particle is incident from the lower right of the figure, and travels around the bend in the tube. Figure 3.3 corresponds to $k = 1.35\,\pi$. From Fig. 3.1, this energy corresponds to a maximum in the transmission through the tube. The transmitted wave function has a simple structure at this energy. The wave function has no nodes; consequently, there are no fixed points and no vortices.

The flow is clearly laminar, and corresponds to roughly 85% transmission through the tube.

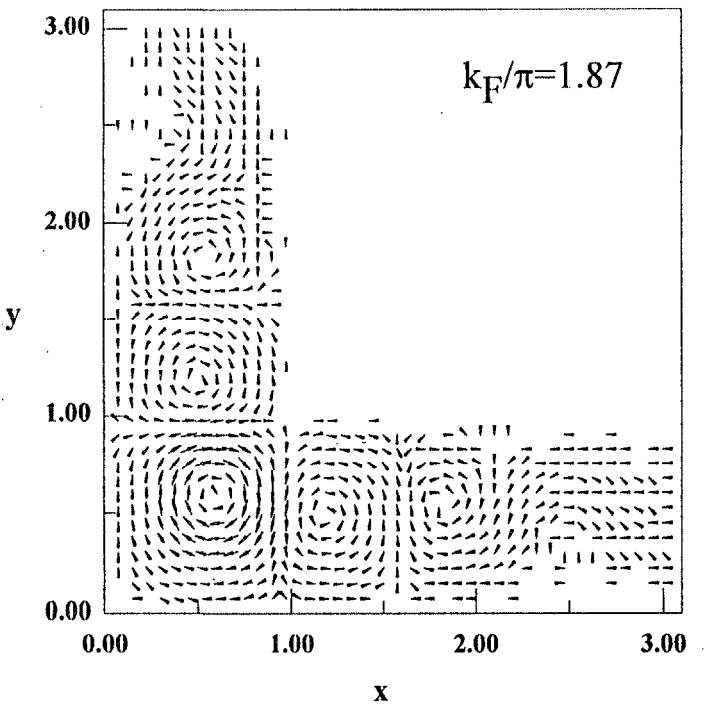

Fig. 3.4. Quantum probability current j of (3.26), for the L-shaped tube of Fig. 2.3a. Wave number $k = 1.87\pi$, just below the zero in T_1 (see Fig. 3.1). Large vortices completely fill the tube, blocking the flow

Figure 3.4 plots the probability current in the L-shaped tube for $k = 1.87\,\pi$, corresponding to an energy very near the zero in the transmission. The transmission minimum occurs where a standing wave is set up in the tube. The regularly-spaced nodes in the wave function form the centers for a series of large vortices, which essentially fill up the space in the tube. The fixed points can also be seen at the boundaries of the tube. As one crosses the energy where the transmission vanishes, the direction of rotation about each vortex changes sign. We can give a qualitative argument why the vortex rotation should abruptly change sign across a zero in the transmission probability. There is some energy E_0 where the transmission amplitude vanishes. At this energy the probability current j in the interior of the tube essentially goes to zero. For $E < E_0$ a vortex will exist about a given wave function node, with a quantized vorticity given by (3.29). Right at the energy E_0 the circulation will be undefined since the probability current vanishes. The vor-

ticity in the vicinity of this point can be represented by a step function in the energy, with argument $(E - E_0)$. When the energy increases and the current is no longer zero, the vortices will reappear and their direction of rotation about a given zero in the wave function must therefore change sign.

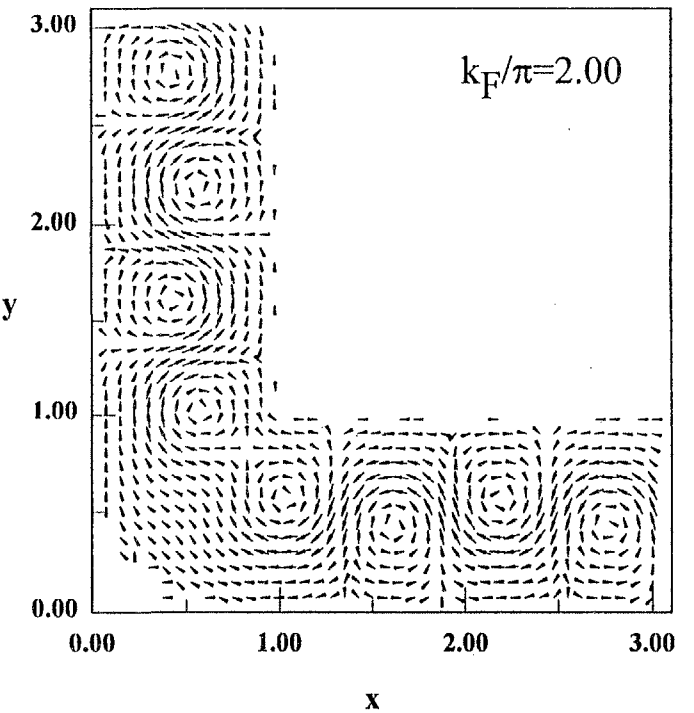

Fig. 3.5. Quantum probability current j of (3.26), for the L-shaped tube of Fig. 2.3a. Wave number $k = 2.00\pi$, just below a maximum in T_1. Although large vortices persist, probability can flow along a "street" surrounding the vortices.

Figure 3.5 corresponds to wave number $k/\pi = 2.00$. From Fig. 3.1, this is near a maximum in the transmission. For energy sufficiently far above the zero in transmission, the vortices eventually disappear and the flow once again becomes laminar. At this energy, significant vortices are still present in the probability current. However, Fig. 3.5 shows that a "*street*" is present, which provides an allowed path for flux around the vortices. The resulting transmission probability is substantial, $T_1 \sim 60\%$.

Note, in the vector plots of Figs. 3.3 through 3.5 the probability currents have been renormalized so that the lengths of the longest arrows are equal in each figure. If we wish to compare the absolute values of the probability currents in these three figures, the probability current densities should be multiplied by the respective values $1 : \frac{1}{5} : 4$.

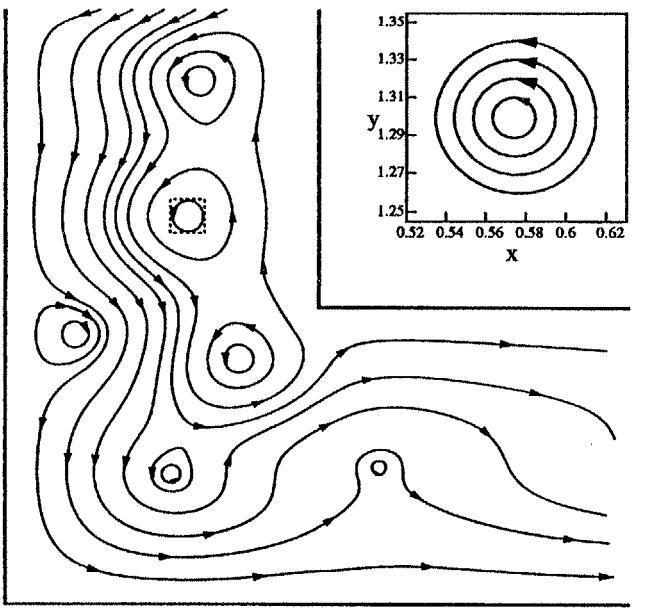

Fig. 3.6. Stream lines of the quantum probability current **j** for the L-shaped tube, for wave number $k = 2.5\pi$. Solid curves represent stream lines connected to nodes in the velocity **v** defined in (3.26). The particle enters from the top in the lowest transverse mode, and is transmitted to the lower right. Three vortices, separated by two velocity nodes, form a cluster which blocks transmission through the tube. The inset is a magnification of velocity lines around one vortex, showing the circular nature of lines near the vortex. From [105]

Finally, Fig. 3.6 from Wu and Sprung [105] plots the stream lines of the quantum probability current for the L-shaped tube, for wave number $k = 2.5\pi$. Here the particle enters the tube from the top, in the lowest transverse mode, and leaves at the bottom right (as opposed to the previous figures where the direction of flow is reversed). The solid curves represent stream lines connected to velocity nodes. At this energy six velocity nodes are present (the nodes are centered at the closed loops in the velocity stream lines). Three of the vortices form a cluster, separated by two velocity nodes (the points where the velocity stream lines intersect). This cluster tends to block the flow of probability current through the tube, and reduces the transmission probability, which at this energy is $T_1 = 0.264$. The inset at upper right is a magnification of the velocity stream lines in the vicinity of a single vortex. The circular nature of the stream lines near the vortex, as predicted from (3.28), is evident in this case.

In the following sections, graphs of the probability current density will be used to provide an intuitive understanding of transmission and reflection phenomena in 2-D systems. Minima in the transmission through curved tubes are generally associated with substantial vortex formation in the probability current. The ensuing large vortices fill up the space in the tube, preventing the transmission of flux. From unitarity, transmission minima are necessarily associated with maxima in the reflection. Reflection maxima produce the conditions for zeroes in the wave function (equal incident and reflected amplitudes), and vortices can form around these zeroes. The presence of large vortices does not always imply small transmission, as there are occasionally cases where maxima in transmission are associated with substantial vortex formation. This was seen in Fig. 3.5. Another example where a transmission maximum was associated with large vortex formation was given by Lent [99]. We will encounter another such case in Sect. 5.3. The size and location of the vortices are the crucial ingredients in determining the quantum probability flow through the tube.

3.3 Behavior of Electrons in Quantum Heterostructures

Quantum wires are a particular type of *quantum heterostructure*. A heterostructure refers to a semiconductor composed of more than one material. The majority of quantum wire experiments involve GaAs/AlGaAs systems. "AlGaAs" is an acronym for the alloy $Al_xGa_{1-x}As$. Here we review their properties and compare electron motion in these systems with our idealized picture of 2-D motion in a tube with perfect hard walls. Detailed reviews of the physics of quantum wires, and the behavior of electrons in these systems, are given in the books by Datta [1] and Ferry and Goodnick [2]. The book by Davies [11] gives a brief summary of the properties of heterostructures and compares various methods for constructing them.

Figure 3.7a gives a schematic picture of the most common quantum wire system, a GaAs/AlGaAs heterostructure. The source of electrons is the n-type doped AlGaAs layer. Electrons which leave their donors and migrate into the GaAs layer lose energy. Because of the offset in conduction bands between the two materials, the electrons are unable to climb the energy barrier and return to the AlGaAs. The positively charged donors provide an electrostatic attractive force for the electrons. Therefore, the electrons which have migrated into the GaAs tend to collect right at the boundary to the AlGaAs layer.

Figure 3.7b shows the resulting conduction band profile. The plus signs denote the doped AlGaAs layer, followed by the undoped AlGaAs spacer layer and then the GaAs substrate. Electrons from ionized donors in the doped AlGaAs layer transfer to the lower-energy GaAs layer. Due to the band offset between the AlGaAs and GaAs layers, the electrons are localized along the infinite plane formed at the interface. In this way one can create

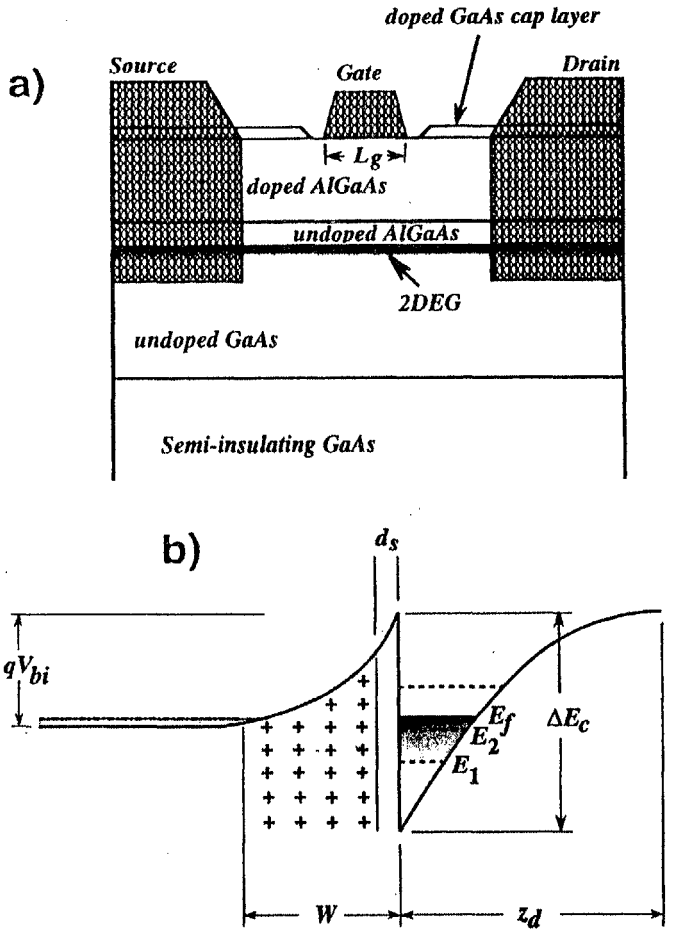

Fig. 3.7. (a) Schematic picture of the cross-section of a split-gate GaAs/AlGaAs quantum heterostructure used to produce quantum wires. Shown (from top down) are the gate, GaAs cap layer, doped AlGaAs donor layer, undoped AlGaAs spacer layer, 2DEG layer, and undoped GaAs substrate. (b) Conduction band profile through the quantum heterostructure shown in (a). From left to right (top to bottom) are the donor layer (pluses), spacer layer, 2DEG layer and substrate

a very narrow layer of electrons which are relatively free to move in this plane, and which form a "*two-dimensional electron gas*" (2DEG). Because the doped layer is separated from the substrate by the undoped spacer layer, the electron scattering from impurities is greatly reduced, so that one can obtain very high electron mobilities (of the order of 10^7 cm^2/V s).

The electrons near this interface experience an effective confining potential in the vertical direction, which is shown schematically in Fig. 3.7b. Mitin, Kochelap and Stroscio [3] give a detailed derivation of this effective poten-

tial for quantum heterostructures. It is possible that nearly all the electrons will be in the same quantum state in this binding potential. In this case the electron wave function can be separated into a confined vertical, or z dependence, and free motion in the plane normal to the interface. This constitutes the 2DEG state. To create a quantum wire, it is necessary to further restrict the electron motion in the plane. One way to accomplish this is by depositing a split metal gate atop the cap layer, as shown in Fig. 3.7a. Such structures are sometimes called *quantum point contacts*, in analogy with earlier experiments which were carried out in metallic systems [110, 111]. When the metal electrodes are negatively biased, the 2DEG region under the electrodes is depleted, as the carriers are emptied from the region. In Fig. 3.7a electrons will be expelled from the region directly beneath the electrodes, leaving electrons which are relatively free to move in a finite region in x and an infinite region in y (into the page). This constitutes the *quantum wire*. As a general rule, the metal gate structure runs over a small volume. Thus, in a typical quantum wire one has a narrow "wire" underneath the split gate, connected on both sides of the wire by a much larger 2DEG reservoir. The reservoir serves as a source of electrons which can enter the wire from either side. In the next section we review how the conductance in such a structure is related to the transmission amplitudes for electron scattering.

Two-dimensional structures in semiconductors can also be grown directly by application of etching and lithographic techniques. Structures grown in this way can be more precisely controlled than "wires" whose width is determined by metal gates. There is a practical limit on the transverse dimensions which can be achieved using metal gates. Also, the gates must be placed a certain distance above the electrons, which limits the sharpness of the electrostatic potential seen by the electrons. Thus, with metal gates one necessarily produces quantum wires with a fairly diffuse boundary. However, the methods for direct growth of wires in semiconductors are very slow processes, and with metal gates one can produce quantum wires with much more complicated geometries than with the direct growth techniques.

The calculations presented in this book assume a constant potential for electrons inside the wire, with hard wall boundary conditions. This approximation can be compared with self-consistent calculations for electrons in GaAs quantum wires by Laux, Frank and Stern [112]; similar calculations have also been performed by Kojima *et al.* [113] and Martorell *et al.* [114]. Figure 3.8 plots the self-consistent potentials vs. distance x for various bias voltages. For relatively low voltages, the potentials look quite similar to the hard-wall potential. They are rather constant across the wire and rise very rapidly at the surface. As the bias voltage becomes more negative, the effective potential more closely resembles a parabolic confining potential. From Fig. 3.8 it is clear that the effective channel width decreases as the gate bias potential becomes more negative. In this way the width of the channel can be controlled by varying the gate potential. In the next section it will be

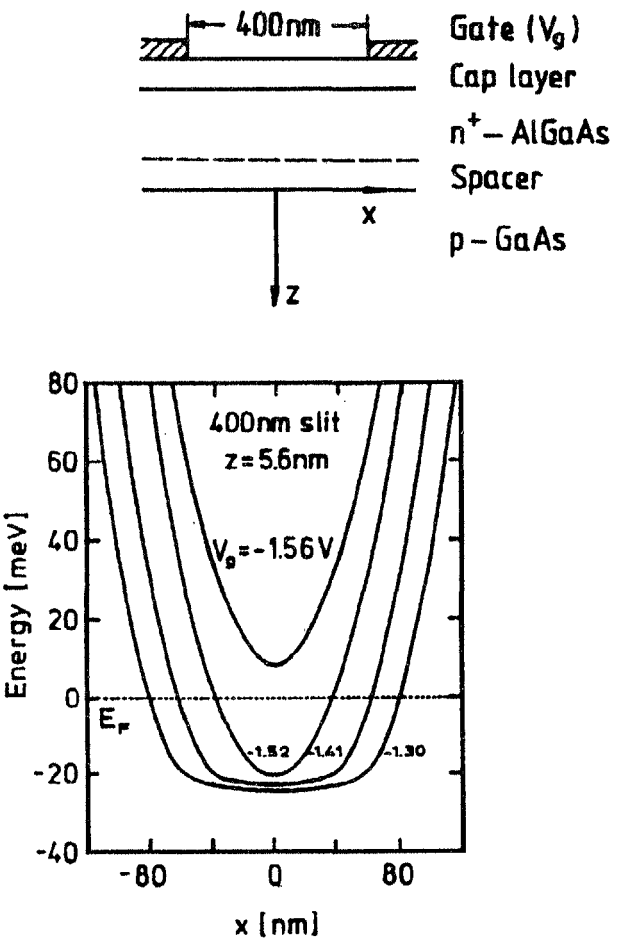

Fig. 3.8. Numerical self-consistent potential for a split-gate GaAs/AlGaAs structure, as a function of gate voltage V_g, from Laux *et al.*, [112]

demonstrated that experimental measurements of conductance show quite dramatically how variation of the gate potential changes the effective width.

Our model for electron motion in quantum heterostructures assumes hard wall one-body potentials for electrons. It should be emphasized that it is a dramatic oversimplification to treat electron behavior in quantum heterostructures as a one-body problem. The effective potential shown in Fig. 3.8 arises from self-consistent calculations which average over a very large number of electron states. It gives the Hartree–Fock field for one additional electron at the Fermi surface, and neglects effects of impurities which would perturb the resulting field locally. We use the effective potential for its simplicity. However, it would be a mistake to take this one-electron picture too

seriously. In later sections we will compare qualitative results in electron heterostructures with states which appear in conventional waveguides, which are systems well approximated by hard wall boundaries.

For reasons of space, we will restrict our attention to those properties of quantum wires which have a direct analogy to electromagnetic [EM] states in waveguides. Consequently we will not consider those cases involving strong magnetic fields in quantum heterostructures. Thus in this book we will not discuss important topics such as magnetic edge states or Aharonov–Bohm rings. Comprehensive reviews of these topics can be found in the literature [1, 2, 5, 6, 115]. In addition, we only consider wires with two external leads and cells of very simple geometry. Extensions to several external leads and topologically more complicated structures have been considered by several groups [1, 2, 73, 88, 116, 117].

In addition, we will frequently assume geometries with sharp corners, rather than more realistic rounded shapes. This allows us to obtain analytic results for many observables, but for geometries which differ from those in more realistic systems. In Appendix A we review some of the qualitative differences we expect for energies and wave functions arising from our use of perfect hard wall boundary conditions, in contrast to various other approximate boundary potentials we could use to describe the physics of electrons in quantum wires.

3.4 Electron Conductance in Quantum Wires

The quasi-two-dimensional systems produced in quantum heterostructures typically possess conducting surfaces in which a narrow conducting path connects two reservoirs of electrons in thermal equilibrium. Each reservoir can be described as a two-dimensional electron gas (2DEG). If a voltage bias is produced between the reservoirs, electrons will move through the connecting conductor. In such systems, electrons can enter the conducting surface from either end. One measures the conductance as a function of the electron temperature and external gate voltage, which controls the depth to which electrons move along the conducting path.

Several different length scales govern the motion of electrons in these systems. The first is the electron *mean free path*, which is largely determined by elastic scattering from residual impurities in the channel. The second length scale is the *phase coherence length*, the length over which quantum coherence occurs. The third length scale is the *Fermi wavelength*, since transport occurs at the Fermi surface in these two-dimensional systems. In typical quantum heterostructures, the Fermi wavelength is of the order of tens of nanometers, which is comparable to the transverse dimensions of these systems. The mean free path (mfp) can be two orders of magnitude larger than the transverse dimensions of the system (the mfp is also substantially larger than the lon-

gitudinal dimensions of the system), and the phase coherence length can be another order of magnitude larger still.

Under these conditions, the conductance of the electrons can differ dramatically from the "normal" motion of electrons in a conductor. The resistance does not arise from myriad electron collisions in the conductor, but instead the wires act like electron waveguides. The factors governing conductance in disordered systems were originally considered by Landauer [32, 33, 118, 119], and have since been studied by many authors [70, 120, 121]. Here we give a heuristic derivation of Landauer's conductance formula for electrons in a quantum wire. In this book we restrict our attention to systems with only two external leads, so the resulting conductance formula is considerably simpler than the general case with many leads. A more complete discussion is provided in the monographs by Datta [1] and Ferry and Goodnick [2]. We will review the derivation given by Davies [11].

Consider a conductor connecting two 2DEG reservoirs, as shown schematically in Fig. 3.9a. The system is biased so that the left hand and right hand contacts are at Fermi energies μ_L and μ_R, respectively [5]. The conductor has straight external leads normalized to unit width connecting to the 2DEG on the left and right ends of the wire, and an arbitrary shape in the interior.

Since the width of a quantum wire is comparable to the electron de Broglie wavelength, only a small number of transverse modes are energetically available for the electron. We first derive the Landauer formula for a system with only a single transverse mode. We will then extend the derivation to consider systems with several transverse modes. The conductance is given by

$$G = \frac{I}{V} \quad , \tag{3.31}$$

where I in (3.31) is the current across the conductor and V is the applied voltage. Since electrons can enter the conductor from the 2DEG on either side, the current is obtained by calculating the net current arising from electrons from either the left or right sides of the conductor. The current arising from electrons from the left has the form

$$\begin{aligned} I_L &= 2e \int \frac{dk}{2\pi} v(k) T(k) f(E(k), \mu_L) \\ &= \frac{2e}{h} \int_{U_L}^{\infty} dE \, T(E) f(E, \mu_L) \quad . \end{aligned} \tag{3.32}$$

In (3.32), the factor of 2 accounts for the two spin states of the electron. The current density is obtained by multiplying $ev(k)$ by the Fermi function

[5] The following additional assumptions are made in deriving Landauer's formula. First, assume zero voltage drop inside the contacts, and that the entire voltage drop occurs at the interface between the 2DEG and the conductor. Next, make the assumption of "*reflectionless contacts*," *i.e.*, that an electron in either 2DEG can enter the conducting lead with a negligible probability of reflection [1].

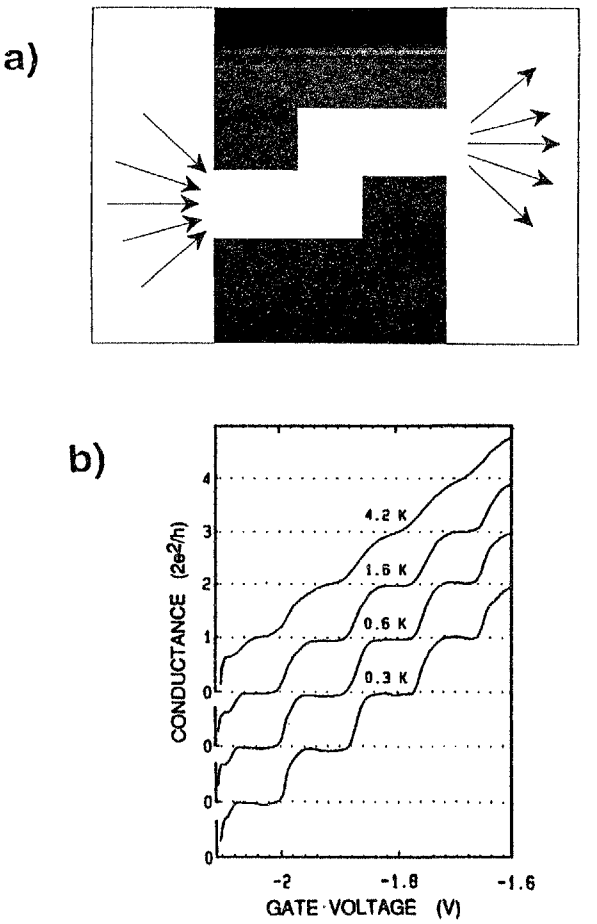

Fig. 3.9. (a) Schematic picture of electron conductance through a (finite) quantum wire. Electrons enter the wire, averaged over all incident angles, from 2DEG reservoirs at either end of the wire. (b) Experimental temperature dependence of the electron conductance in a quantum point contact structure, vs. gate voltage, from van Wees *et al.*, [122]

$f(E(k), \mu_L)$ which gives the probability that the given state is occupied. This is multiplied by the probability $T(k)$ that the incident electron will be transmitted through the conductor. The second equation in (3.32) is obtained by changing the integration variable from the wave number to the energy. The quantity U_L is the energy corresponding the the bottom of the conduction band on the left side of the conductor.

The net current, obtained by summing the currents from the left and right sides of the conductor, is given by

$$I = \frac{2e}{h} \int_U^\infty dE\, T(E)\,[f(E,\mu_L) - f(E,\mu_R)]$$
$$= \frac{2e^2 V}{h} \int_U^\infty dE\, T(E) \left(-\frac{\partial f}{\partial E}\right) \quad . \tag{3.33}$$

In (3.33), the quantity U is the larger of the quantities U_L and U_R, the energies at the bottom of the conduction band. The second equation in (3.33) is obtained in the limit that the applied voltage $V = (\mu_L - \mu_R)/e$ is very small. In this case one can expand the Fermi function to first order in a Taylor series as a function of μ. The derivative with respect to energy E follows since the Fermi function is a function only of $E - \mu$. Inserting (3.33) into (3.31) gives the relation for the conductance

$$G = \frac{2e^2}{h} \int_U^\infty dE\, T(E) \left(-\frac{\partial f}{\partial E}\right) \quad . \tag{3.34}$$

In the limit of extremely low temperatures, the Fermi function is essentially a step function. We can then replace the derivative of the Fermi function in (3.34) by

$$-\partial f/\partial E \approx \delta(E - \mu) \quad , \tag{3.35}$$

where μ in (3.35) is the average of the Fermi energies μ_L and μ_R of the 2DEG on the left and right sides of the quantum wire, respectively. The low-temperature limit of the conductance is obtained by inserting (3.35) into (3.34) to obtain

$$G_{T\sim 0} = \frac{2e^2}{h} T(\mu) \quad . \tag{3.36}$$

3.4.1 Conductance for a Many-Channel System

Equation (3.36) gives the form of the conductance for a one-dimensional system, with a single mode and in the low-temperature limit. The conductance is proportional to the transmission probability of the electrons. The more common form of Landauer conductance formula [32, 33, 70] is obtained by extending our discussion to systems which contain many modes or channels. The transverse energy in the n^{th} channel is ϵ_n. For a given total electron energy E, those channels with $E > \epsilon_n$ will have propagating states. Equation (3.36) can be modified to include the effects of additional channels. The corresponding equation becomes

$$G = \frac{2e^2}{h} \sum_n \theta(E - \epsilon_n) T_n(E - \epsilon_n)$$
$$= \frac{2e^2}{h} \sum_n \sum_m |\mathcal{T}_{nm}|^2$$
$$= \frac{2e^2}{h} \sum_m \sum_n \mathcal{T}^\dagger_{mn} \mathcal{T}_{nm} = \frac{2e^2}{h} \mathrm{Tr}[\mathcal{T}^\dagger \mathcal{T}] \quad . \tag{3.37}$$

In (3.37), $\mathcal{T}$ is the transmission matrix whose coefficients were defined in (3.2), and we substitute (3.4) for the transmission probability. The sum is over all open channels for a given electron energy.

To get a qualitative impression of the conductance in such a system, consider the hypothetical case of a conductor with 100% transmission in each open channel, and examine the behavior of the conductance as the electron energy is varied. For electron energies below the lowest transverse channel energy $E < \epsilon_1$, no channels are energetically accessible to the electrons, so the conductance should be zero [6]. Once the energy is greater than the continuum threshold, (3.37) predicts that the conductance G will jump discontinuously by $2e^2/h$. G will remain constant until the electron energy passes the threshold for the second transverse channel, at which time another discontinuous jump of $2e^2/h$ will occur.

In a system with perfect transmission, the conductance for each open mode will be governed by the quantity $G_0 \equiv 2e^2/h$, the "*quantum*" of conductance. Expressed in units of G_0, (3.37) shows that the conductance vs. electron energy (or wave number) for a zero temperature electron in a tube will exhibit sharp "steps" of unit height every time the energy crosses the threshold for a new transverse mode [7]. As the energy increases between thresholds for transverse modes, the conductance remains constant in this ideal system. The characteristic "*staircase*" behavior of the conductance vs. wave number follows because the conductance (in units of G_0) jumps by one unit every time a new channel opens up. For a tube with external leads normalized to unit width, a channel threshold occurs whenever $k = n\pi$.

The features of sharp increase in the conductance just above transverse channel thresholds, and some evidence of "*plateaus*" in the conductance between channel thresholds, are seen in both calculations and experiments for quantum wires. However, in quantum heterostructures the physical conditions differ considerably from our idealized picture. The electron energy (the Fermi energy) is essentially fixed. The effective dimensions of the system can be changed by varying the gate voltage, as described in the previous section. In the quantum heterostructure, the conductance is typically measured for fixed electron energy as a function of the gate voltage. Figure 3.9b shows the experimental conductance in a *quantum point contact* structure, from van Wees *et al.* [122], at four different electron temperatures. A quantum point contact structure behaves like a quantum wire with a very short length. The electrons travel through a narrow gap between two 2DEG reservoirs, where the effective width of the gap is controlled by the bias voltage from metal

[6] For the time being we neglect the possibility of sub-threshold quantum tunneling of electrons through the conductor. This possibility will be considered later.

[7] In obtaining this relation for the conductance, the potential difference between the 2DEG reservoirs is neglected, relative to the Fermi energy; if this quantity is not negligible, including the potential drop along a quantum wire will decrease the magnitude of the 'steps' in conductance [123, 124].

gates on the surface of the heterostructure. This produces a narrow conducting path which is well approximated as a quasi-one-dimensional system.

Figure 3.9b shows the experimental conductance for four values of the electron temperature. If one considers the lowest electron temperature, 0.3 K, the conductance is observed to increase in regular jumps, each of magnitude $G_0 = 2e^2/h$, as the gate voltage changes from roughly -2.1 V to -1.6 V. From the preceding discussion, each of these jumps occurs when the effective width changes so that $k_F = n\pi/W_{\text{eff}}$, where k_F is the (fixed) electron wave number in the 2DEG. Figure 3.9b demonstrates that the effective width is essentially a linear function of the gate voltage. For higher electron energies it is no longer accurate to neglect the form of the Fermi function, so we must evaluate (3.34). We will discuss the temperature dependence of the conductance in the next section.

Up to this point we have neglected the effects of reflection on the conductance. For energies where N transverse channels are open, the maximum possible value of the conductance is $G_{max} = NG_0 = 2Ne^2/h$. In the case of a reflectionless wire, the conductance would jump by G_0 each time the energy permitted a new transverse channel to open up. The conductance would reach a "plateau" after each new channel opened, and would then jump upwards by G_0 with the opening of each new transverse mode. In the presence of reflection, the conductance will be smaller than the maximum permitted amount. If the transmission amplitudes contain sharp structure, the conductance will exhibit narrow upward or downward fluctuations, superimposed on the jumps and plateaus which occur at transverse mode thresholds. In later sections we will try to provide simple physical pictures for the sharp structure predicted for the transmission probabilities. One will find elastic resonances which produce sharp conductance peaks, inelastic resonances which produce deep minima in conductance, and for curved tubes with a "*quasi-periodic*" repeated structure, allowed and forbidden "*minibands*" in the conductance.

The presence of electron bound states for tubes with bends or bulges can lead to nonzero conductance below the threshold for continuum transmission. Here electrons quantum mechanically "*tunnel*" through the bound state(s) in the system. As the bound state wave function for these electrons is largest in the bend regions, and decays exponentially in the straight sections, this tunneling will give rise to sharp subthreshold conductance peaks, whose properties are strongly dependent on the system geometry. For finite temperature electrons, one averages over contributions from a range of energies near the top of the Fermi sea. This averaging will tend to wash out the sharp features of the conductance for zero temperature electrons, hence the sharp features characteristic of zero temperature conductance will disappear rather rapidly for electrons with sufficiently high temperature. This is qualitatively what is observed in Fig. 3.9b.

3.5 Electron Conductance Through a Straight 2-D Channel

The previous sections reviewed the physics of quantum wires, where narrow conducting structures connect two reservoirs of electrons, which are incident from various directions on both sides of the wire. To calculate the conductance one averages over all possible directions for the incident electrons, for a given electron temperature.

In this section we calculate electron conductance in a finite-length structure. Our derivation is based on the treatment of electron conductivity in 2-D systems carried out by Kirczenow [125], and by Szafer and Stone [126]. Later Wu and collaborators [28], and Berggren, Wang and collaborators [100, 102, 103, 104, 127, 128], also calculated conductivity in the ballistic regime for a number of different geometries.

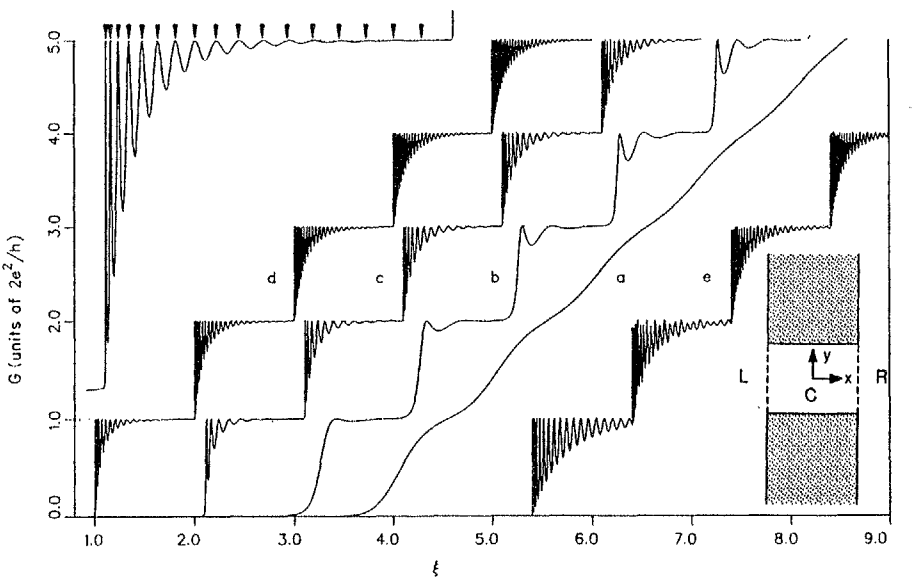

Fig. 3.10. Conductance G, in units $G_0 = 2e^2/h$, vs. effective channel momentum $\xi = k_F/\pi$, for straight tube shown in inset at right. Tube has width W, length $2d$. Curve a: $\widehat{d} \equiv 2d/W = 0$; curve b: $\widehat{d} = 1$; curve c: $\widehat{d} = 5$; curve d: $\widehat{d} = 10$. Left inset: maxima in the $\nu = 1$ conductance plateau of curve d; arrows denote the predicted peaks using (3.50). Figure from [125]

The simplest problem which can be considered involves the transmission of zero-temperature electrons through a straight quantum wire of finite length, as shown schematically in the inset at the bottom right of Fig. 3.10. Electrons with Fermi momentum k_F are incident from the 2DEG reservoir on either side, travel through a quantum wire of width W and length $2d$, and exit into

region R. We first rescale all system lengths and momenta to dimensionless quantities by dividing or multiplying by the channel width W, as described in Sect. 2.1.1. For example, the rescaled dimensionless Fermi momentum is given by

$$k_F^2 \equiv \frac{2m^* W^2 E_F}{\hbar^2} \quad , \tag{3.38}$$

where E_F is the Fermi energy of the electrons in the conducting material.

For electrons incident from the left in Fig. 3.10, the wave function in region L has incident and reflected terms while the transmitted wave function in region R has only outgoing waves. Inside the channel the wave function $\psi_k^c(x,y)$ is expanded in eigenfunctions ϕ_n from (3.1), giving

$$\begin{aligned}
\psi_L(x,y) &= e^{ikx+iKy} + \int_{-\infty}^{+\infty} \frac{dK'}{2\pi} a_{K'}^L e^{-ik'x} e^{iK'y}, \quad [x \le -d] \\
\psi_k^c(x,y) &= \sum_n \phi_n(y)[a_n^+ e^{iq_n x} + a_n^- e^{-iq_n x}], \quad [-d \le x \le d, 0 \le y \le 1], \\
\psi_R(x,y) &= \int_{-\infty}^{+\infty} \frac{dK''}{2\pi} a_{K''}^R e^{ik''x} e^{iK''y} \quad [x \ge d] \ .
\end{aligned} \tag{3.39}$$

In (3.39), the incident wave function in region L has horizontal momentum k and transverse momentum K.

Continuity of $\psi_{\mathbf{k}}$ and $\partial\psi_{\mathbf{k}}/\partial x$ at the channel boundaries gives the relations

$$\begin{aligned}
\sum_n \left[(T_{mn} - q_n\delta_{mn})a_n^- e^{iq_n d} + (T_{mn} + q_m\delta_{mn})a_n^+ e^{-iq_n d}\right] &= 2ke^{-ikd}\phi_m(-K) \\
\sum_n \left[(T_{mn} - q_m\delta_{mn})e^{iq_n d}a_n^+ + (T_{mn} + q_m\delta_{mn})e^{-iq_n d}a_n^-\right] &= 0
\end{aligned} \tag{3.40}$$

where

$$\begin{aligned}
\phi_m(Q) &\equiv \int_{\infty}^{+\infty} e^{-iQy}\phi_n(y)dy \\
T_{mn} &\equiv \int_{-\infty}^{+\infty} \frac{dK'}{2\pi} k'\phi_m(-K')\phi_n(K')
\end{aligned} \tag{3.41}$$

Using (3.40), the coefficients a_n^+ and a_n^- can be calculated by truncating the infinite dimensional expansions to N basis functions (for relatively low electron energies, $N = 10$ was found to give sufficient numerical accuracy).

The conductance can be written in terms of the electron current, averaged over all possible transverse directions for the electron. Thus one integrates over all momenta K using the relation $k_F = \sqrt{k^2 + K^2}$, to obtain

$$\begin{aligned}
G(E_F, W, T=0) &= \frac{2m^* e}{h^2} \int_{-k_F}^{k_F} \langle\psi_{\mathbf{k}}|j_x|\psi_{\mathbf{k}}\rangle \frac{dK}{k} \\
&= \frac{e}{h} \int_{-k_F}^{k_F} \frac{dK}{2\pi i k} \int_0^1 dy \left(\psi_{\mathbf{k}}^* \frac{\partial\psi_{\mathbf{k}}}{\partial x} - \psi_{\mathbf{k}} \frac{\partial\psi_{\mathbf{k}}^*}{\partial x}\right)
\end{aligned} \tag{3.42}$$

Combining (3.40) and (3.42), the conductivity can be found from:

$$G(E_F, W, T=0) = \left[\frac{2e^2}{h}\right] \int_{-k_F}^{k_F} \left[\sum_{n \text{ open}} q_n (|a_n^+|^2 - |a_n^-|^2) + i \sum_{n \text{ closed}} |q_n| [(a_n^-)^* a_n^+ - (a_n^+)^* a_n^-] \right] \frac{dK}{2\pi k} \quad (3.43)$$

Equation (3.43) is appropriate for zero-temperature electrons. In this case one treats the left side of the wire in the inset to Fig. 3.10 as a reservoir of free electrons with motion described by plane waves, filling momentum states up to $|\mathbf{k}| = k_F$. The same is true for the conducting material on the right side. Only the electrons at the top of the Fermi sea contribute to the current; the electron currents from these states are summed to give the conductance G. To include the effect of finite temperature T one sums over contributions from a small range of energies around the top of the Fermi sea. Assume a Fermi distribution for the electrons

$$f(E) = [1 + \exp((E-\mu)/k_B T)]^{-1} \ , \quad (3.44)$$

where k_B is the Boltzmann constant and μ is the electron Fermi energy. The finite T conductance is obtained by averaging the zero temperature value over a range of energies in the vicinity of the Fermi energy,

$$\begin{aligned} G(\mu, W, T) &= -\int_0^\infty \left(\frac{df}{dE}\right) G(E, W, T=0)\, dE \,, \\ &= \int_0^\infty \frac{e^{(E-\mu)/k_B T}}{[1 + e^{(E-\mu)/k_B T}]^2} G(E, W, T=0) \frac{dE}{k_B T} \,. \end{aligned} \quad (3.45)$$

3.5.1 Qualitative Features of Conductance in a 2-D Channel

In the previous section formulas were derived for the conductance of electrons traveling through a straight two-dimensional channel. Figure 3.10 plots the conductance (in units of $G_0 = 2e^2/h$) vs. effective momentum for various channel widths (the dimensionless effective momentum is defined as

$$\xi = k_F/\pi \ , \quad (3.46)$$

where k_F in (3.46) is given by (3.38)). The conductance was calculated by Kirczenow [125]. The curves labeled a, b, c, d correspond to renormalized channel widths $\widehat{d} = 2d/W = 0, 1, 5, 10$, respectively. There is no conductance below the threshold $\xi = 1$. For a straight channel there are no bound states, and hence no sub-threshold conductance.

For $d = 0$, the conductance rises roughly linearly with effective momentum. However, for nonzero channel width $2d$, the conductance exhibits sharp jumps of almost exactly one unit in height (expressed in units of G_0) at integer values of ξ. These jumps correspond to the opening of new transmission modes when the electrons have enough energy to support an additional transverse oscillation. They can be seen in the experimental low temperature quantum point contact conductance measurements shown in Fig. 3.9b.

For the straight channel, the origin of the "staircase" behavior of the conductance is straightforward. Note from (3.43) that the conductance $G(E_F)$ contains no contributions from coupling between modes. Because the channel is straight, the modes do not couple. The total conductance is thus given by a sum over individual modes, evaluated at a shifted energy, *i.e.*

$$G(E) = \sum_n G_n = \frac{2e^2}{h} \sum_n T_n(\alpha_n)\theta(E - \epsilon_n) \quad . \tag{3.47}$$

The quantity T_n in (3.47) is the transmission probability in the n^{th} transverse mode, and α_n is the longitudinal wave number in that mode,

$$\alpha_n = \sqrt{E - \epsilon_n} = \sqrt{E - (n\pi)^2} \quad . \tag{3.48}$$

The conductance is the sum over all open modes of a series of contributions from each separate mode. The staircase behavior in the conductance thus results from the shifted energy for each mode (given in (3.48)), and the lack of interference between different transverse modes [79]. In order to produce more structure in the conductance, one requires coupling between the various modes, and one way to accomplish this is to have bends or cavities in the channel.

The other striking feature of zero temperature conductance through a straight channel is the occurrence of very sharp maxima and minima at certain energies. For small values of $\widehat{d}$ (*e.g.*, curve b in Fig. 3.10), there are relatively few maxima. The conductance rises rather sharply as each transverse channel opens, and rapidly reaches a fairly constant plateau until the next transverse channel opens. This is similar to the low-temperature conductance shown in Fig. 3.9b, which was obtained with "quantum point contacts," which are quantum wires of extremely short length. Thus quantum point contacts possess well defined conductance plateaus, but they do not show any evidence for other sharp structure in the conductance. However, for large values of $\widehat{d}$, there are a series of very sharp minima and maxima in conductance, as the overall value of the conductance rises to each plateau. In curve c of Fig. 3.10, as the integer ν representing the transverse channel increases, the number of sharp maxima in that plateau increases.

The upper left inset of Fig. 3.10 shows 17 maxima in the first ($\nu = 1$) conductance plateau for the case $\widehat{d} = 10$. These maxima are the analog of acoustic resonances in an organ pipe open at both ends. In an organ pipe of

length L and sound velocity v, resonances will occur for sound of frequency $f_j = jv/2L$ for any integer j [8]. Analogously, for transmission through the straight channel of Fig. 3.10, a maximum in the conductance will occur whenever the longitudinal momentum obeys the condition $k_j = j\pi/2d$. The arrows show the maxima predicted by Kirczenow [125]. He included an effective channel length

$$d_{\text{eff}} = \widehat{d}\gamma \quad , \tag{3.49}$$

with γ in (3.49) an adjustable parameter. This accounts for end effects, well known in acoustics, which can make the effective length differ from the actual length of the channel. An excellent fit to the position of all maxima in Fig. 3.10 was obtained for $\gamma = 1.044$.

Expressed in terms of the dimensionless momentum ξ of (3.46), the conductance should reach a maximum for all ξ_{nj} obeying the relation

$$\xi_{nj} = \sqrt{n^2 + \left(\frac{j}{\widehat{d}\gamma}\right)^2} \quad , \tag{3.50}$$

where j and n take on all possible integer values. This is the condition for the j^{th} longitudinal standing wave, when the wave passing through the channel has n transverse oscillations. For the ν^{th} conductance plateau one has $1 \leq n \leq \nu$. For a given n, maxima occur when j takes on integer values bounded by

$$\widehat{d}\gamma\sqrt{\nu^2 - n^2} \; < \; j \; < \; \widehat{d}\gamma\sqrt{(\nu+1)^2 - n^2} \quad . \tag{3.51}$$

It is straightforward to show that as ν increases, the number of maxima in that plateau increases. For the case shown in Fig. 3.10 ($\nu = n = 1$, $\widehat{d}\gamma = 10.44$), (3.51) predicts there should be 17 maxima in the first plateau. With a single adjustable parameter γ, one obtains remarkably good agreement with the calculated maxima in the conductance.

The preceding discussion is valid for zero temperature electrons. Figure 3.11 shows the expected temperature dependence of the conductance. For this case, Kirczenow [125] kept E_F and d fixed but varied the width W of the channel. He chose $\widehat{d} = 5$ when the Fermi level was at the bottom of the $n = 11$ sub-band. Figure 3.11 shows the $\nu = 3$ plateau, for three temperatures. For $T = 0$, the very sharp maxima in the conductance are observed just after the opening of the third transverse channel. For temperature $kT/\mu = 0.001$, the magnitude of the maxima are greatly reduced near channel threshold, but the conductance closely resembles the $T = 0$ result at the top of the plateau. When $kT/\mu \geq 0.005$, the oscillations in the conductance have complely disappeared; only the average slope of the conductance is observed. This is essentially what is seen experimentally in Fig. 3.9b, where the sharp

[8] Although acoustic waves obey Neumann boundary conditions, as opposed to Dirichlet conditions in our tubes, in both cases resonances arise when integer numbers of half waves can be accommodated within the tube.

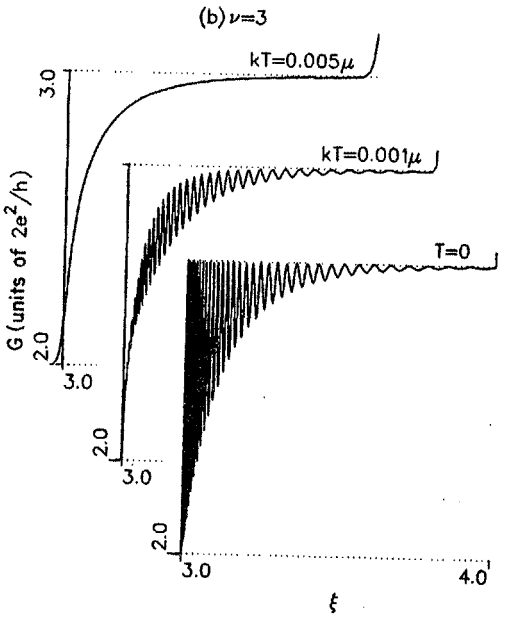

Fig. 3.11. Temperature dependence of conductance vs. the effective channel momentum ξ, for the straight tube shown in the right inset of Fig. 3.10. The $\nu = 3$ conductance plateau is shown at three different electron temperatures. From [125]

structure in the conductance becomes rounded and finally disappears as the electron temperature increases.

Figure 3.12 plots the theoretical conductance, in units of $2e^2/h$, for zero temperature electrons in an L-shaped tube with unit width and external leads of length three. As discussed in Sect. 2.1.5, the L-shaped tube has a bound state, so the conductance exhibits a sharp peak just below the threshold for conductance $k/\pi = 1$. Since the bound state wave function decreases exponentially in the external leads, this peak is very sensitive to the length of the leads. As this length increases, the subthreshold conductance peak becomes extremely narrow. In experiments, unless the external leads of a curved tube are quite short, it is likely that the resulting conductance peak due to a bound state will be so sharp that it cannot be observed.

There is a minimum in the conductance just below the opening of each new transverse channel at $k/\pi = N$. This results from the destructive quasi-bound resonances which were discussed in the preceding chapter. Sharp jumps in conductance are observed after each new transverse channel opens up. The resulting "plateaus" do not jump by integer values of G_0, because there is quite a bit of reflection due to the sharp bend in the channel. Finally, narrow maxima are seen in the conductance at certain values of the channel wave number. These maxima are the analog of the "organ-pipe" resonances seen

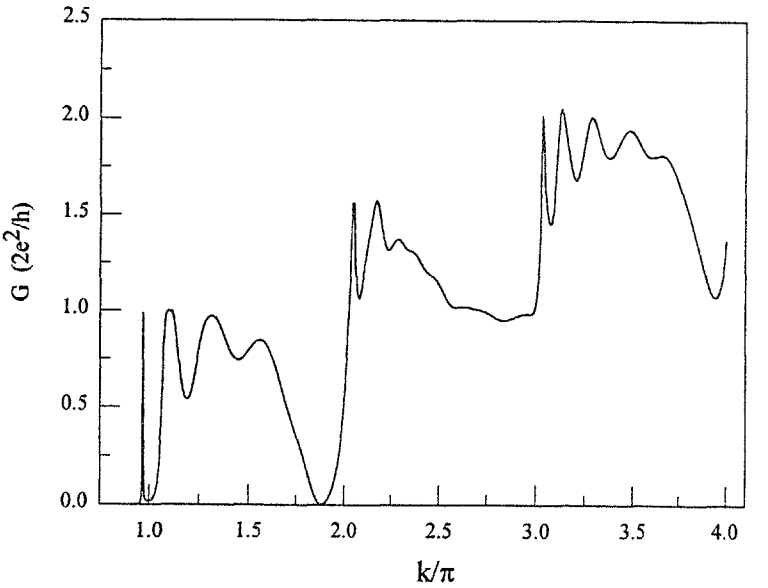

Fig. 3.12. Theoretical conductance G in units $G_0 = 2e^2/h$ vs. the effective momentum k/π for an L-shaped tube of unit width and legs of length 3. The subthreshold peak in G is due to the bound state in the tube. The zero in G at $k/\pi = 1.88$ results from destructive interference from a quasi-bound resonance

so dramatically in the straight channel. They occur at momenta where the tube can accommodate an integer number of standing waves.

In Chap. 5 and 6, the conductance will be studied for tubes with more complicated geometries. First, conductance will be investigated in tubes containing single "cells" (bends or cavities) of various types, and later in systems made up of a series of identical cells.

4. Waveguide Measurements of the Properties of Curved Tubes

Until now our attention has been focused on the properties of particles moving in curved 2-D tubes. In Chap. 2 it was proved that a broad category of curved tubes with hard walls must possess at least one bound state. This includes any tube with either a bulge or (for a tube of constant width) a bend. As the conditions for the existence of a bound state were proved relatively recently, the location and properties of these confined or "*trapped*" modes is a subject of considerable interest. As was discussed, such trapped modes should appear in any two-dimensional wave system with this geometry, which satisfies the Helmholtz equation with Dirichlet boundary conditions. These include elastic waves on a membrane with fixed boundaries, TE_{n0} electromagnetic waves with conducting boundaries, and low-energy quantum particles in narrow channels with high transverse barriers.

Experimental techniques have been developed which enable the bound states in quantum heterostructures to be located and studied [65, 66]. Such techniques require extremely precise measurements in nanometer-scale devices. However, there is an alternative way to identify and measure these bound states. This makes use of the one-to-one correspondence between confined TE modes in curved waveguides, and bound states in hard wall tubes of similar shape. There are two interesting consequences of the relationship between hard wall tubes and waveguides. First, as was pointed out by Exner and Seba [37], the presence of bound states for electrons in curved tubes implies the existence of confined modes in curved electromagnetic waveguides. Second, as will be demonstrated, the use of waveguide structures allows these states to be studied in "*table-top*" experiments using microwave cavities. Such experiments on curved waveguides can demonstrate the presence of confined sub-cutoff EM modes; they can also predict the structure of bound state wave functions for electrons in curved quantum heterostructures with similar geometries.

In Sect. 4.1 we review the analogy between EM modes in waveguides and states in 2-D tubes. Section 4.2 describes how electromagnetic energy densities can be mapped out by moving a small metal sphere inside a waveguide. The energy densities are directly related to the electron bound state wave functions and their gradients. Section 4.3 discusses experimental properties of the waveguides and microwave measuring apparaus, which were used to

J. T. Londergan, J. P. Carini and D. P. Murdock: LNPm 60, pp. 71 - 80, 1999
© Springer-Verlag Berlin Heidelberg 1999

locate and map out the confined modes. Further details of waveguide experiments will be provided in later chapters.

4.1 EM Fields in Thin Resonating Cavities

Here we review briefly the equations satisfied by electromagnetic fields inside a resonating cavity. More details can be found in Jackson's text on classical electrodynamics [129]. Consider a thin cavity with conducting walls constructed so that the height h (measured along the z direction) is small compared with any important dimension of the base shape, a 2-dimensional surface in the $x-y$ plane. The EM fields inside the cavity satisfy Maxwell's equations in vacuum

$$\begin{aligned} \nabla \times \mathbf{E} &= -\frac{1}{c}\frac{\partial \mathbf{B}}{\partial t} = i\frac{\omega}{c}\mathbf{B} \\ \frac{i\omega}{c}\nabla \times \mathbf{B} &= -\nabla^2 \mathbf{E} = \frac{\omega^2}{c^2}\mathbf{E} \ , \end{aligned} \tag{4.1}$$

where both $\mathbf{E}$ and $\mathbf{B}$ in (4.1) are divergenceless. The $\mathbf{E}$ and $\mathbf{B}$ fields in the interior are harmonic in time with angular frequency ω. The boundary condition requires that $E_{\|}$ and $B_{\perp}$ be continuous at the conducting walls.

The requirement that B_z vanish at $z = 0$ and $z = h$ insures that the lowest frequency state has $B_z = 0$. The lowest energy state in a thin cavity will be a TE mode where the $\mathbf{E}$ field has only a z component, which requires that $B_z = 0$. So

$$\mathbf{E} = E_z(x, y, z)e^{-i\omega t}\hat{\mathbf{k}} \ , \tag{4.2}$$

where the EM fields are given by the real part of the complex expressions.

Since $\mathbf{E}$ has only a z component, which in the lowest TE mode has no z dependence, then Maxwell's equations for this mode can be written

$$\left(\frac{\partial^2}{\partial x^2} + \frac{\partial^2}{\partial y^2} + \frac{\omega^2}{c^2}\right) E_z(x, y) = 0 \ , \tag{4.3}$$

where $E_z(x, y)$ is required to vanish at the lateral boundaries of the waveguide. By inspection, E_z of (4.3) and the wave function ψ of the related quantum mechanical problem for the curved tube (2.1) satisfy the same differential equation and boundary conditions. Let a curved tube in the $x-y$ plane have an outer boundary defined by a curve $\mathcal{S}$. Construct a rectangular waveguide by raising the boundary curve $\mathcal{S}$ upward in the z direction. If the curved tube possesses a bound state with energy $E = k^2$ and wave function $\psi(x, y)$, then the waveguide will have a confined TE mode below the cutoff frequency. The frequency of the confined mode and the electric field $E_z(x, y)$ are related to the corresponding quantities in the tube by

$$k^2 = \omega^2/c^2$$
$$E_z(x,y) \propto \psi(x,y) \quad . \tag{4.4}$$

The electric field E_z for the confined EM mode will be identical to the bound state wave function ψ, to within an overall constant. These confined electromagnetic modes in curved waveguides were predicted in 1990 by Exner and Seba [37], and were measured by Carini *et al* [21, 22]. Before this time, to the best of our knowledge, scientists were unaware of the existence of sub-cutoff confined modes in curved waveguides[1].

4.2 Mapping EM Energy Densities in Waveguide Cavities

The following section reviews the procedures for constructing curved waveguides and locating their confined modes. The waveguides used were constructed with a height of a few cm, for which the resonant frequencies are in the GHz range, appropriate for microwave measurements. To locate confined EM modes, microwave power was sent into the waveguides through coaxial lines, and the ratio of reflected power to incident power was measured as the microwave frequency was varied. A bound state appears as a sharp decrease in reflected power below the waveguide cutoff frequency.

Once the confined mode frequency is determined, the electromagnetic energy density distribution for the confined mode can be mapped out using the cavity perturbation method originally introduced by Maier and Slater [130], and later reviewed by Amato and Herrmann [131]. This method makes use of the fact that at resonance in a cavity, the time-averaged electric and magnetic field energy are equal. Inserting a small object (such as a metal ball) into the cavity will make these energies unequal. The resonant frequency shifts to a new value to equalize the field energies. For small shifts, the change in the resonant frequency is proportional to the product of the volume of the ball times a function of the difference between $U_{\mathrm{el},0}$ and $U_{\mathrm{mag},0}$, the electric and magnetic field densities for the unperturbed bound state, at the location of the ball. We review briefly the relation between the resonant frequency shift and the EM energy densities.

The cavity resonator is equivalent to an LC circuit, and hence has a resonant frequency

$$f_0^2 = \frac{1}{(4\pi^2 LC)} \quad . \tag{4.5}$$

At resonance equal amounts of energy are stored in the electric and magnetic fields ,

[1] In Chap. 2 it was proved that either bulges or bends could produce bound states in a tube. It was well known that a bulge in a waveguide would support a confined mode [34], but it was apparently not realized that bending alone would produce a stable confined EM mode.

$$U_{\mathrm{el},0} = U_{\mathrm{mag},0} \ . \tag{4.6}$$

Perturbations in the fields caused by the steel ball will change the resonant frequency f_0, since the steel ball changes the effective L and C of the cavity. It can be shown that the resulting change in f_0 has the form

$$\frac{\Delta f_0}{f_0} = \frac{1}{2}\frac{dU_{\mathrm{el}}}{U_{\mathrm{el}}} - \frac{1}{2}\frac{dU_{\mathrm{mag}}}{U_{\mathrm{mag}}} \ . \tag{4.7}$$

The electric field energy shift dU_{el} is obtained from the energy shift for a conducting sphere of radius r placed in an (initially) uniform electric field (Eq. (4.93) in [129]). The magnetic energy shift is obtained from the magnetization for a sphere in a constant magnetic field [2] (Eq. (5.150) in [129]). The resulting electric and magnetic energy shifts have the form

$$\begin{aligned} dU_{\mathrm{el}} &= -\frac{1}{2}r^3E^2 \ , \\ dU_{\mathrm{mag}} &= -\frac{1}{4}r^3B^2 \ . \end{aligned} \tag{4.8}$$

Here, E and B stand for the root-mean-square values of the electric and magnetic fields.

Inserting the energy shifts of (4.8) into (4.7) and renormalizing to the total energy in the cavity gives the relation

$$\frac{\Delta f_0}{f_0} = -\frac{r^3}{2U_{\mathrm{Tot}}}\left[E^2 - \frac{B^2}{2}\right] \ , \tag{4.9}$$

where U_{Tot} is the total energy of the electromagnetic field. The square of the B field can be obtained from Maxwell's equations, (4.1),

$$|\mathbf{B}|^2 = \frac{c^2}{\omega^2}|\nabla \times \mathbf{E}|^2 = \frac{1}{k^2}|\nabla E_z|^2 \ . \tag{4.10}$$

From the preceding discussion, the quantum mechanical bound state wave function $\psi(x,y)$ in a 2-D tube is proportional to $E_z(x,y)$ of the standing EM wave. Using the normalization of ψ and the relation between E^2 and the energy density of the cavity one can show that they are related by:

$$|\psi|^2 = \frac{Dw^2}{4\pi U_{\mathrm{Tot}}}E^2 \ . \tag{4.11}$$

where D and w are respectively the depth and width of the waveguide. Therefore the fractional change in resonant frequency $\Delta f_0/f_0$, which occurs when a metal ball is placed at a point inside the waveguide, is related to the bound state wave function and its gradient at that point through

[2] Equation (4.8) for the magnetic energy shift is valid when the EM field oscillates sufficiently rapidly, as is true for GHz frequency microwaves in a waveguide.

$$\frac{\Delta f_0}{f_0} = -\frac{r^3}{2U_{\mathrm{Tot}}}\left[c_0 E^2 - \frac{c^2}{2\omega^2}|\nabla E|^2\right]$$
$$= -\frac{2\pi r^3}{Dw^2}\left[c_0|\psi(x,y)|^2 - \frac{1}{2k^2}|\nabla\psi(x,y)|^2\right] . \qquad (4.12)$$

The relation (4.12) shows how the EM energy densities can be mapped out by measuring the position dependence of resonant frequency shifts obtained when a small metal ball is moved through the waveguide. Resonant frequency shifts will be negative (positive) where the electric field (magnetic field) is large. Regions of the waveguide with the largest electric field values will produce the most negative frequency shifts, and conversely the most positive frequency shifts will denote regions where the magnetic field density is greatest.

In (4.12), since the conducting sphere is in contact with the lower conducting surface of the waveguide, the initial expression $dU_{\mathrm{el}} = -r^3 E_0^2/2$ of (4.8) is a poor approximation for the electric energy shift. In Appendix B it is shown that an improved induced dipole calculation gives the electric energy shift a multiplicative factor

$$c_0 = 2\zeta(3) \approx 2.404 \ , \qquad (4.13)$$

where $\zeta(n)$ in (4.13) is the Riemann Zeta function of argument n (Chap. 23 of [132]), and the factor c_0 has been incorporated in (4.12).

4.3 Microwave Measurements with Curved Waveguides

This section describes the experimental features of the curved waveguides which were constructed for microwave experiments. Additional details can be found in [21, 22, 133]. The width and depth of the waveguides were chosen to produce a cutoff frequency for the lowest TE_{10} mode (determined by the waveguide width w) which was accessible with conventional network analyzers, and also well separated from the cutoff frequency for the TE_{01} mode (governed by the waveguide depth D). The experiments discussed here used waveguides of width $w = 1.905$ cm (3/4"), which gives a cutoff frequency of $c/(2w) = 7.87$ GHz for the TE_{10} mode, and waveguide depth $D = 0.635$ cm (1/4"), for which the TE_{01} cutoff frequency is $c/(2D) = 23.61$ GHz.

Figure 4.1 shows waveguide sections which were used in a study of properties in a tube with a single sharp bend [21, 22]. The waveguide is formed from parallel aluminum bars held between two large aluminum plates (not shown). Both the inner and outer bars could be moved to change the angle of the bend, which for this structure could be varied from roughly 60° to 120°. Results of experiments carried out with this system are described in the following section and in Sect. 5.2.

In addition to waveguides with single bends, waveguides with multiple bends were also studied. An example of this second type is shown in the

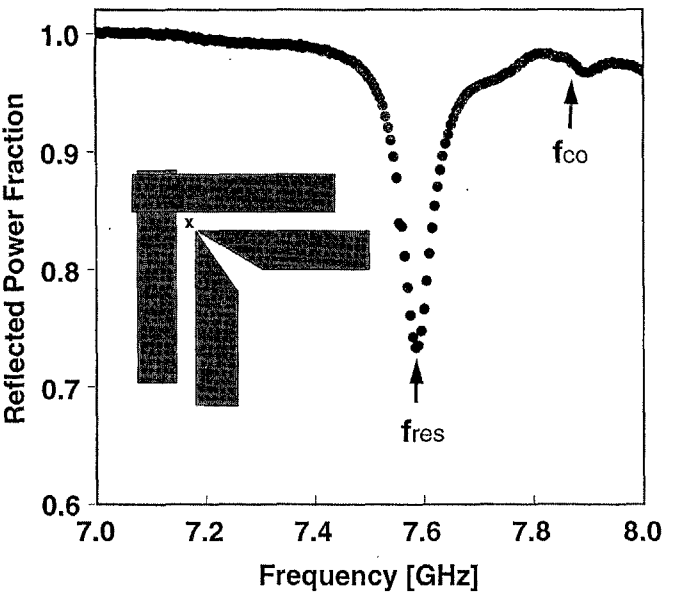

Fig. 4.1. Inset: top view of geometry for waveguide sections, formed from parallel aluminum bars held between two large aluminum plates (not shown). "x" marks the location of a coaxial conductor through which microwaves were radiated into the waveguide. Data: measured ratio of reflected power to incident power, as a function of the incident frequency in GHz, for 90° waveguide bend. Arrows denote frequencies of the confined mode f_{res} and cutoff f_{co}. Data from [21]

inset to Fig. 5.30 (this is the first color plate). This is a tunable double-bend waveguide designed by Yung *et al.* [133, 134]. Two identical aluminum plates were constructed, each having the shape shown as the upper plate in the inset to Fig. 5.30. The shaded section is raised, with the remainder of the plate cut to a depth of $1/4''$. When two identical plates were assembled as shown (the lower graph in the inset to Fig. 5.30), this produced a double-bend waveguide where the aspect ratio (the distance between bends) was continuously variable by sliding the plates relative to each other. An aluminum plate was placed atop the structure and the system was clamped together. Experiments carried out with this system are reviewed in the following section and also in Sect. 5.4.

4.3.1 Confined Mode Studies in Waveguides

Microwave transmission was used to locate confined or trapped sub-cutoff modes in curved waveguides, which are the analog of bound states in curved tubes. Microwaves were radiated into the structure from an antenna placed

through holes in the waveguide walls near the bend region. The antenna consisted of the protruding center conductor of a semi-rigid coaxial cable, which was either straight (oriented parallel to the polarization of the ac electric field in the waveguide and located toward the center of the waveguide), or looped (oriented perpendicular to the polarization of the ac magnetic field in the waveguide and located toward the edge of the waveguide).

With a single antenna and for frequencies close to the confined mode, the equivalent microwave circuit is a transmission line terminated by a resonator coupled through a variable capacitance or inductance. This is shown schematically in Fig. 4.1. The position marked "x" shows the location where a coaxial line with a protruding center conductor was inserted through a hole in the top aluminum plate. When power was sent toward the antenna and the reflected power was measured, nearly 100% of the power was reflected except at resonance, where a sharp dip in the reflected power occurred. In Fig. 4.1, the resonant frequency is labeled $f_{\rm res}$, where a dramatic dip is seen in the fraction of reflected power. The cutoff frequency $f_{\rm co}$ marks the onset of the continuum for transmission through the straight sections of the waveguide. In the limit of vanishing coupling, the frequency of the sub-cutoff confined EM mode (which corresponds to the bound state in a curved tube) equals the frequency of the dip.

Experiment and theory were compared using the dimensionless ratio between the confined mode frequency and the cutoff frequency for the straight waveguide sections. The $\rm TE_{10}$ cutoff frequency was determined experimentally by turning a portion of the straight section into a transmission line resonator with a length L and measuring the first few standing wave resonant frequencies for the $\rm TE_{mnp}$ modes with $m = 1$ and $n = 0$, $f(m = 1, n = 0, p)$. The measured frequencies were fit to the rectangular cavity formula

$$f^2(m = 1, n = 0, p) = f_{\rm co}^2(m = 1, n = 0) + p^2 \left(\frac{c}{2L}\right)^2 \quad , \tag{4.14}$$

and the cut-off frequency was extracted as the intercept of a linear fit.

The electromagnetic energy distribution was mapped out by inserting a small metal sphere inside the waveguide, and measuring the resonant frequency shift, using (4.12). Note that placing the ball in a region of large electric field density decreases the resonant frequency, while inserting it in a region of relatively large magnetic field density increases the resonant frequency. In Appendix B it is demonstrated that a single metal surface in contact with the ball will increase the magnitude of the frequency shift due to the electric field energy, by the factor c_0 of (4.13). The precise coefficient depends on the ratio of the size of the ball to the height of the waveguide. The quantity c_0 was treated as a variable parameter which was initially set at 2.40, and then varied slightly to best fit the observed resonant frequency shifts.

Sridhar [135] adapted the perturbation method into a powerful field-mapping technique. The steel ball can be manipulated through the top plate

using a strong magnet. By moving the ball between points on a grid and measuring the resulting frequency shift, the energy density can be mapped out with a spatial resolution of about 1 mm. Using Sridhar's method, several experiments have mapped out the electromagnetic energy density in waveguide structures with one or more bound states [21, 22, 133, 134]. Figure 5.30 compares an experiment which measured the frequency shift as a function of ball position within a double-bend waveguide structure, with a theoretical calculation for the frequency shift using (4.12). Red represents regions of negative frequency shift (where the electric field energy is relatively large), while blue represents regions of positive frequency shift (with large magnetic field energy). The most negative frequency shift measured was -152 MHz (theory predicted -127 MHz using the enhancement factor $c_0 = 2.46$, as mentioned above) while the most positive frequency shift measured was 34 MHz (theory predicted 23 MHz, although errors due to the uncertainty in the position of the ball become very great close to the inner corners, where the magnetic field strength diverges).

The contours are scaled exactly the same way in each graph, which demonstrates good overall agreement between theory (Fig. 5.30a) and experiment (Fig. 5.30b) where the total field energy is largest (close to the bend region). Away from the bend region, the electromagnetic field energy becomes much smaller (it decreases exponentially along the straight sections of the waveguide), so experimental uncertainties become relatively greater. This is most noticeable along the side walls of the waveguide away from the bend.

4.3.2 Waveguide Experiments Above the Lowest Cutoff Frequency

Experiments in the frequency range above the lowest cutoff frequency primarily focus on studies of the transmission of waves through waveguide structures. There are two principal approaches, shown schematically in Fig. 3.9a and the inset to Fig. 4.2. In quantum heterostructures, finite structures typically connect two electron gases. Electrons are incident from all directions on both sides of the structure, and the conductance of the structure depends on the transmission coefficient for the electrons averaged over all directions, as is depicted in Fig. 3.9a. It is difficult to mimic this technique in microwave experiments, where one would need to measure the transmission coefficient from every possible pair of angles for the incoming and outgoing waves. The second approach measures point-to-point transmission in a structure, which is easy to accomplish with microwaves, since they can be introduced through small holes in the structure, but difficult with electrons in quantum wires. In the point-to-point method, shown schematically in the inset to Fig. 4.2, microwaves are radiated in all directions within the structure, which simulates the averaging over incident directions that occurs in electronic structures. Both approaches can yield information about the effect of the geometry of the tube on the transmission of waves.

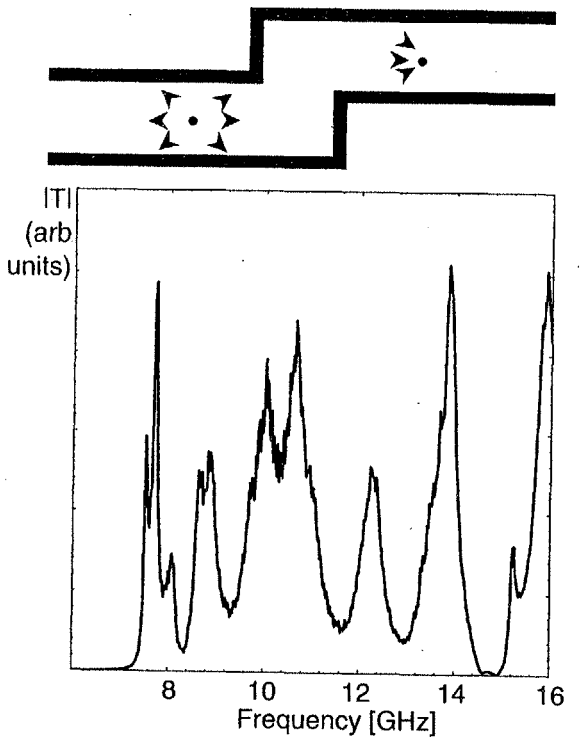

Fig. 4.2. [Inset: schematic illustration of transmission through curved waveguide. This illustrates point-to-point transmission through a waveguide, when the signal is inserted at a single point within the waveguide. Contrast with Fig. 3.9a, which shows conductance of electrons through a curved quantum wire connecting two 2DEG reservoirs.] Transmission of microwaves through a double-bend waveguide structure shown in inset to Fig. 5.30. Total transmission probability $|T|$ through waveguide, vs. microwave frequency in GHz. Waveguide aspect ratio was $R = 6.0$ and nominal cutoff frequency was $f_{co} = 7.87$ GHz. Two sharp peaks below cutoff frequency represent the two subthreshold confined modes. The deep minimum at about 15 GHz is caused by the quasi-bound destructive resonance

Figure 4.2 shows the results of a transmission experiment through a double bend structure [136]. The transmission is negligible below the lowest cutoff frequency (nominally 7.87 GHz) except at the frequencies of the confined EM modes, *i.e.* the bound state frequencies. Other features include the abrupt dip in transmission immediately below the TE_{20} cutoff frequency. This is the deep minimum seen at about 15 GHz. It is associated with the destructive "quasi-bound" resonance which was discussed in Sect. 3.1.1. The other noteworthy feature of the measured transmission is the sharp oscillations caused by the formation of standing waves in the central section of the structure. These are analogous to the "organ-pipe" resonances described in Sect. 3.5.1. All of

these features of transmission through curved tubes will be encountered in later sections of this review.

5. Binding and Transmission in Wires and Waveguides

In this chapter we will review bound state and transmission properties in wires and waveguides. For simplicity, we will restrict ourselves to the study of systems with very simple geometries. Thus, our focus will be on the properties of tubes with two straight external leads connected to one or a series of internal structures or "cells". A single cell will consist of either a bend, or a rectangular cavity. After the properties of a single cell are reviewed, systems consisting of two identical cells in series will be studied. Despite the great simplicity of the shapes of the structures considered here, it will be shown that the bound state and scattering features observed in these systems display all the phenomena described in Chaps. 2 and 3.

This chapter will discuss in detail the qualitative features which occur when studying tubes with one or two cells (bends or cavities). The study of binding and transmission in wires or waveguides will be completed in Chap. 6 by considering the limit of tubes constructed from a series of identical cells. It was shown in Chap. 2 that at low energies, the effect of a single bend or cavity can be approximated by a simple attractive square well. When a tube is formed by coupling together a series of identical cells, the scattering problem is analogous to that for transmission through a regularly spaced series of identical potentials. One of the more dramatic features which will appear in this limit is the emergence of the band structure which is well known from solid state physics.

The discussion begins in Sect. 5.1 with a system which possesses a very simple shape. This is a tube of constant width, where straight external leads are coupled to a central section with constant curvature. The interior section of the tube is thus a portion of a spiral. This structure displays a rich variety of the phenomena discussed in previous chapters: bound states, quasi-bound resonances just below channel thresholds, and substantial vortex formation at certain energies. In Sect. 5.2 scattering behavior is examined in a tube with a single sharp bend. By comparing binding and scattering in this system with analogous features for a circular bend, one can see the relative importance of bends and bulges on these phenomena. Sect. 5.3 describes the physics of a tube with a single "*T-stub*" junction. Transmission in these systems shows interesting selectivity in wave number, which in principle could be exploited in the fabrication of devices which preferentially transmit, or reflect, specific

J. T. Londergan, J. P. Carini and D. P. Murdock: LNPm 60, pp. 81 - 144, 1999
© Springer-Verlag Berlin Heidelberg 1999

predetermined wave numbers. In particular, the "*cross*" geometry (a pair of stubs placed symmetrically on either side of a tube) is the basis for the "*quantum dot*" configuration, which has been extensively studied. Sect. 5.4 considers structures with two coupled bends. One of the interesting features which arise in double-bend systems is sharp resonance formation, which will be associated with the ability to set up standing waves inside the tube.

5.1 Tube with a Circular Bend

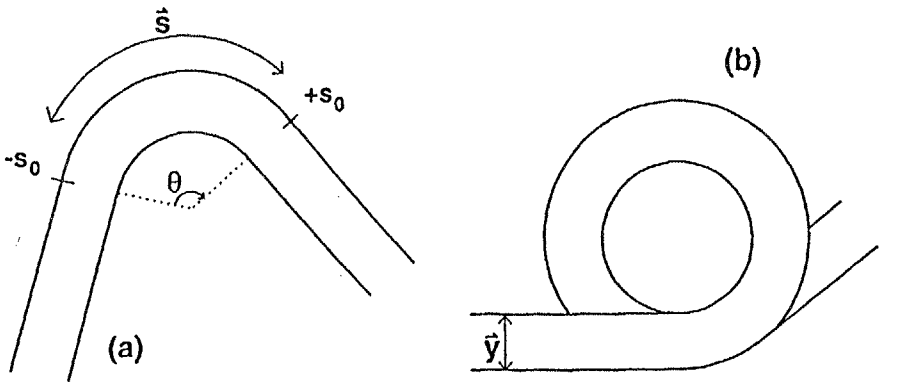

Fig. 5.1. Schematic picture of a tube with a circular bend, from [98]. The structure has constant (unit) width, with long straight sections at the ends, and a middle region with constant curvature κ and total bend angle θ (in our notation, $\theta = 2\Theta$). (a) $2\Theta < \pi$. (b) $2\Theta > 2\pi$ (the tube does not cross itself)

This section discusses binding and scattering properties for a simple geometry, shown schematically in Fig. 5.1. This is a tube of constant width, normalized to one, with long straight sections at both ends, and a central region of constant curvature κ. The curvature κ is defined with respect to the outer boundary of the tube, so $\kappa = 1/R$ relative to the outer radius of curvature R [1]. The system is then completely defined by specifying the two quantities κ, where $0 < \kappa \leq 1$, and the total bending angle 2Θ. The total bend angle 2Θ can be greater than 2π; in this case the tube does not cross itself, but forms part of a nonintersecting spiral, as shown in Fig. 5.1b.

From the theorem outlined in Sect. 2.1.2, such structures will have at least one bound state [14]. The bending produces an effective attraction which

[1] Note, in the article by Duclos and Exner [14], reviewed in Chap. 2, the curvature was defined with respect to the center line of the tube.

adiabatically approaches the value $-\kappa^2/4$, and which is constant through the bend region. As the curvature increases, the attractive potential increases roughly as the square of the curvature. Binding and scattering in circular-bend tubes has been studied by several groups [24, 45, 98, 137, 138]. We will review in considerable detail the location and properties of the bound state(s), the transmission through a tube with a circular bend, and the flow of probability current. The properties of tubes with circular bends can be contrasted with L-shaped systems, which were studied in Sect. 2.1.5 and Sect. 3.1.1. Many of the qualitative features found in circular-bend tubes are also seen in systems with more complicated geometries.

In the straight sections of the tube, the channel wave functions can be expanded in terms of the transverse channel eigenmodes, as given in (2.3)

$$\psi_n(x,y) = \exp(\pm i\alpha_n x)\sqrt{2}\sin(n\pi y) \ . \tag{5.1}$$

In the circular section, define polar coordinates $R-1 \leq r \leq R$ and $-\Theta \leq \theta \leq \Theta$. The wave function in this region satisfies the equation

$$\frac{\partial^2\psi}{\partial r^2} + \frac{1}{r}\frac{\partial\psi}{\partial r} + \frac{1}{r^2}\frac{\partial^2\psi}{\partial\theta^2} + k^2\psi = 0. \tag{5.2}$$

Equation (5.2) has solutions

$$\begin{aligned} \psi_s(r,\theta) &= Z_\nu(kr)\cos(\nu\theta) \ , \\ \psi_a(r,\theta) &= Z_\nu(kr)\sin(\nu\theta) \ . \end{aligned} \tag{5.3}$$

Since the system is symmetric with respect to reflection about its center, $\theta \to -\theta$, and the differential equation is invariant under this reflection, the wave function ψ_s (ψ_a) in (5.3) will be symmetric (antisymmetric) with respect to reflection about the center of the tube. The r-dependent solutions in (5.3) must vanish at the boundary of the tube, *i.e.* at $r = R-1$ and $r = R$. As the resulting equation is Bessel's differential equation, they can be written as linear combinations of Bessel functions. Up to an overall normalization factor, the resulting functions $Z_\nu(kr)$ in (5.3) have the form

$$Z_\nu(kr) = J_\nu(kr)Y_\nu(kR) - J_\nu(kR)Y_\nu(kr) \ . \tag{5.4}$$

In (5.4), J_ν and Y_ν are the Bessel and Neumann functions, respectively, of order ν. The boundary conditions on the r-dependent solutions are

$$Z_\nu(kr)|_{r=R} = Z_\nu(kr)|_{r=R-1} = 0 \ . \tag{5.5}$$

By construction, $Z_\nu(kr)$ of (5.4) satisfies the first of (5.5). The remaining radial boundary condition places a condition on the allowed modes for the system. For a given wave number k and radius of curvature R, the allowed modes ν are those satisfying the second constraint of (5.5). Once the allowed modes are obtained from the boundary condition, the exact solutions

are obtained by matching the wave functions and normal derivatives at the boundary of the straight and curved sections. In the limit of large curvature, Lin and Jaffe [98] found that straightforward matching at the boundary did not converge. We refer the reader to their paper which outlines the matching techniques they employed in this limit.

5.1.1 Bound States in the Limit of Small Curvature

An interesting limit is obtained when the curvature of the tube is very slight, or alternatively when the radius of curvature is very large. In this case ($\kappa \to 0$ or $R \to \infty$), the system still possesses a bound state although the binding energy approaches zero as the curvature goes to zero. Sprung, Wu and Martorell [138] derived an approximation for the binding energy in the limit of small curvature. Following Jensen and Koppe [45], one makes the transformation

$$\psi(r,\theta) = \frac{\chi(r,\theta)}{\sqrt{r}}, \tag{5.6}$$

then (5.2) takes the form

$$\frac{\partial^2\chi}{\partial r^2} + \frac{1}{r^2}\frac{\partial^2\chi}{\partial\theta^2} + \left[k^2 + \frac{1}{4r^2}\right]\chi = 0. \tag{5.7}$$

In the limit of very large R, the quantity r^2 can be replaced by some average value $\overline{R^2}$ in the denominator of (5.7). Sprung *et al.* found that the best result was obtained by using the r value at the center of the bend,

$$\overline{R} = R - 1/2 \ . \tag{5.8}$$

Replacing $r^2 \to \overline{R}^2$ in (5.7) produces separable solutions. These involve the quantity $x = \overline{R}\theta$, the distance along the center line of the bend, with limits $-\overline{R}\Theta \le x \le \overline{R}\Theta$. Equation (5.7) then has the form

$$\begin{aligned} \chi_n(r,\theta) &= \Phi_n(\overline{R}\theta)\sin(n\pi(r+1-R)) \quad , \\ \frac{d^2\Phi_n(x)}{dx^2} &+ \left[\alpha_n^2 + \frac{1}{4\overline{R}^2}\right]\Phi_n(x) = 0 \quad . \end{aligned} \tag{5.9}$$

The equation satisfied by Φ_n in (5.9) is just that for motion in a one-dimensional square well of depth

$$V_0 = \frac{\hbar^2}{2m^*}\frac{1}{4\overline{R}^2} \quad , \tag{5.10}$$

and width $2\overline{R}\Theta$. In (5.9) the longitudinal channel energy in the n^{th} transverse channel is $\alpha_n^2 = k^2 - (n\pi)^2$. In addition, the $\sqrt{r}$ term in (5.6) can be treated as a constant; then the channel wave functions decouple and the problem becomes truly one-dimensional.

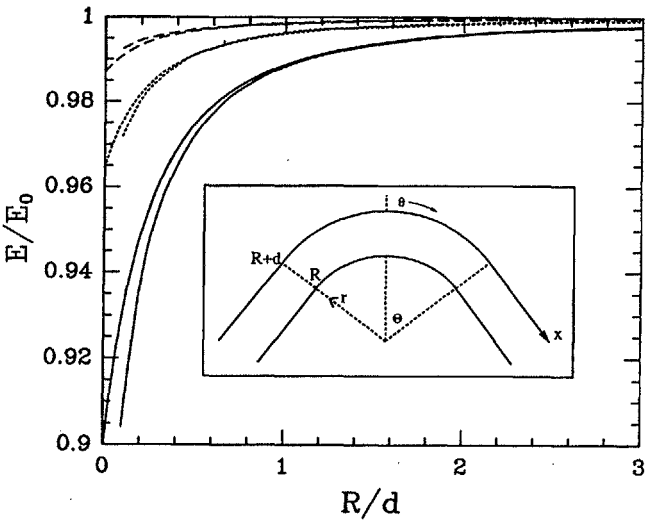

Fig. 5.2. Bound state energy vs. radius of curvature for circular bend tubes. Dashed curves: $\Theta = \pi/4$. Dotted curves: $\Theta = \pi/2$. Energy in units E/E_0, where E_0 is the continuum threshold, vs. inner radius of curvature R/d, where d is the width of the tube. Exact numerical results of [24] are compared with the approximate results of [138]; the latter are the curves which extend to $R = 0$

The approximation of Sprung *et al.* leads to the following analytic estimates for the lowest allowed mode ν and the bound state wave number k_b^2:

$$\begin{aligned} \tan(\nu\Theta) &= \sqrt{\frac{1}{4\nu^2} - 1} \\ k_b^2 &= \pi^2 - \frac{1 - 4\nu^2}{4\overline{R}^2} \quad . \end{aligned} \tag{5.11}$$

Figure 5.2 plots the bound state energy vs. the radius of curvature for two bent tubes. The dashed curve is for a right-angle bend, *i.e.* $\Theta = \pi/4$, and the dotted curves are for a 180° bend, $\Theta = \pi/2$. As would be expected, as the total bend angle increases for a given radius of curvature, the binding energy increases. The solid curve in Fig. 5.2 shows the binding energy in the limit as the bend angle becomes infinite. In this limit the width of the effective square well potential approaches infinity, so that the bound state energy moves to the bottom of the effective square well. The vertical axis is

in units E/E_0, where E_0 is the threshold energy for the continuum (when the tube is normalized to unit width, $E/E_0 = k^2/\pi^2$). The lines which terminate for small R are the numerical results of Sols and Macucci [24]; the other curves are the approximate results of Sprung *et al.*[2] [138].

For a tube with a very gentle circular bend (a large value of R), an accurate estimate of the bound state energy can be obtained by neglecting the r dependence of (5.7), and taking $r \approx \overline{R}$. From Fig. 5.2 it is evident that this approximation works even for rather small values of R, where the assumption that r is roughly constant should not be valid.

5.1.2 Bound State Properties for a Circular Bend

The bound state energies for the circular bend tube have been studied by Lin and Jaffe [98]. In accordance with the existence proofs given in Sect. 2.1.2, any bending of the tube always gives at least one bound state. In the limit as the curvature $\kappa \to 0$ the effective attraction approaches zero, so in this limit the binding energy will go to zero for any fixed bend angle Θ. On the other hand, since the effective attraction is constant through the bend, if the bend angle is made large enough for fixed curvature, the net attraction will become large, and the system could support more than one bound state.

Figure 5.3 plots the bound state wave numbers $\bar{k}_j$ vs. total bend angle, for curvature $\kappa = 0.8$, *i.e.* outer radius of curvature $R = 1.25$ [3] [98]. With increasing total bend angle 2Θ, the eigenvalue $\bar{k}_j$ decreases monotonically, *i.e.* for fixed curvature, the binding energy of the j^{th} bound state increases monotonically with the length of the bend region.

As Θ is increased for a given κ, for some bend angle a second bound state can be supported. Figure 5.4 shows the total bend angle $\theta_2(\kappa)$ at which the second bound state appears, as a function of the curvature κ. In the limit of zero curvature ($\kappa \to 0$), the minimum total bend angle necessary to produce a second bound state is 2π radians. To understand this result, return to the coordinate system discussed in Sect. 2.1.2, where the coordinates s and u are defined along and perpendicular to the walls of the tube, respectively [98]. After some distance $|s| = s_0$, the tube is straight. In the limit $\kappa \to 0$ the wave function in the bent region can be written

$$\psi(s,u) \xrightarrow[\kappa \to 0]{} \sin(\pi u)\sin(\nu_1 \kappa s) \ ,$$

$$\text{where from (2.18)}, \quad \nu_1^2\kappa^2 + \pi^2 - \frac{\kappa^2}{4} - k^2 = 0 \ . \tag{5.12}$$

The smallest bend angle occurs when $k = \pi$, and from (5.12) this requires $\nu_1 = 1/2$. The wave function in the bend region must match onto a decreasing exponential in the straight region, which requires that

[2] In Fig. 5.2, the quantity labeled R is $R - 1$ in our notation, and our scaling of the tube width sets $d = 1$.

[3] In Fig. 5.3, θ represents the total bend angle, which equals 2Θ in our notation.

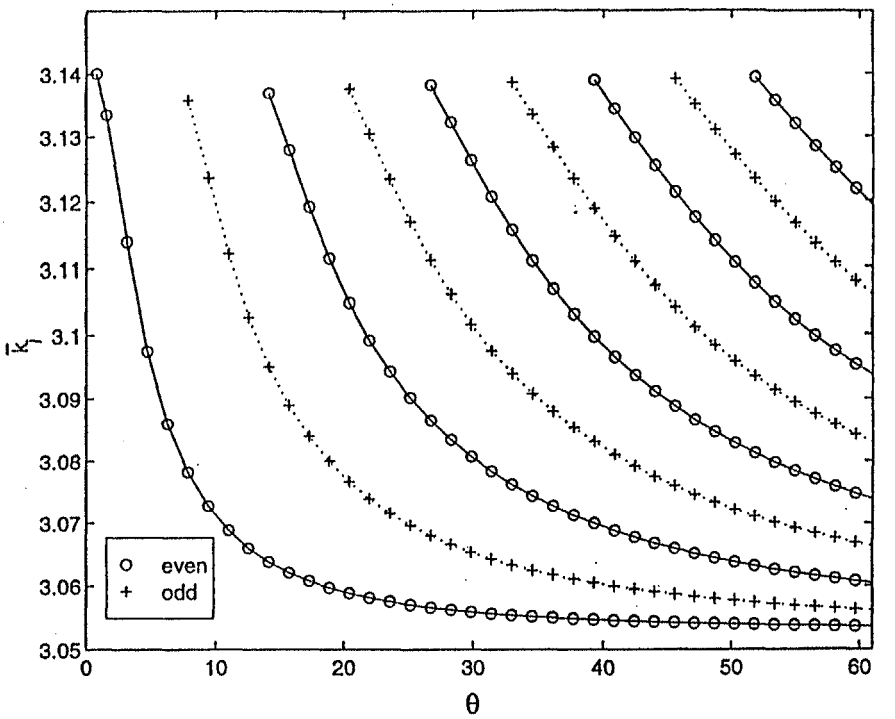

Fig. 5.3. Bound state eigenvalues $\bar{k}_j$ vs. total bend angle $\theta = 2\Theta$ for the circular bend tube of Fig. 5.1, with curvature $\kappa = 0.8$. Solid curves, circles: bound states which are even under reflection; dashed curves, x's: bound states which have odd reflection symmetry

$$\frac{\partial \psi}{\partial s} < 0 \ . \tag{5.13}$$

This requires that

$$\begin{aligned} \nu_1 \kappa s_0 \ &= \nu_1 \Theta \geq \frac{\pi}{2} \ , \\ \text{or} \quad 2\Theta &\geq 2\pi \ . \end{aligned} \tag{5.14}$$

In (5.14) we have used the relation $s_0 = \Theta/\kappa$. Thus the total bend angle $\theta_2(\kappa = 0) = 2\pi$, as shown in Fig. 5.4 [98].

It was proved in Sect. 2.1.2 that greater curvature produces greater binding, so one would naively expect θ_2 to decrease as κ increases. This is opposite the behavior shown in Fig. 5.4. The reason for this is that θ_2 depends on s_0 and $s_0 = \theta/(2\kappa)$. For a fixed value of θ, s_0 is much larger for small κ. Thus the attractive potential acts over a much larger distance when κ is small, and this effect dominates the determination of the binding energy.

For $\kappa = 0.8$, a second bound state occurs whenever $2\Theta > 6.57$ radians. The lowest bound state is symmetric with respect to reflection about the

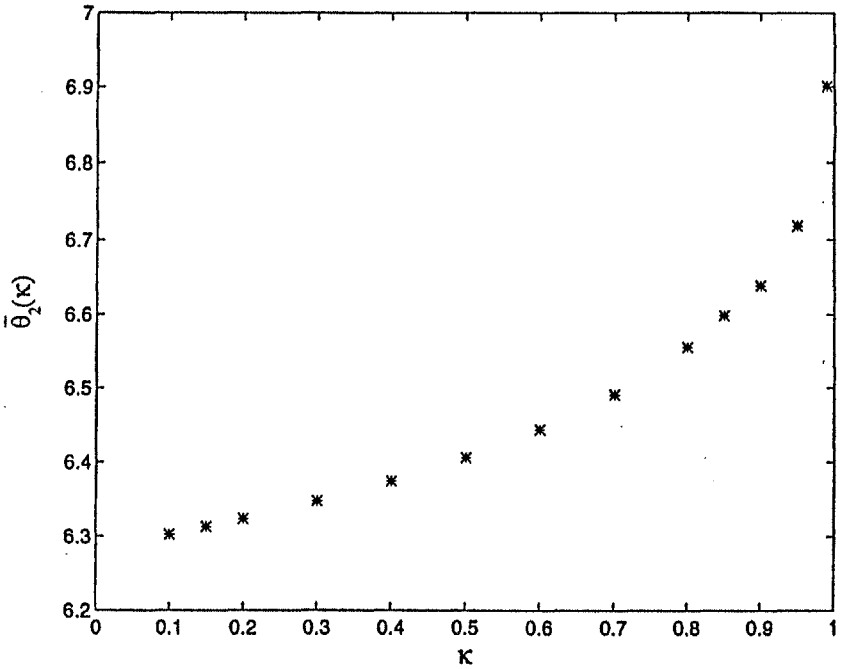

Fig. 5.4. Total bend angle θ_2 at which a second bound state (antisymmetric) appears, vs. the curvature κ of a circular bend tube. As $\kappa \to 0$, $\theta_2 \to 2\pi$

center of the tube ($\theta = 0$), while the second bound state is antisymmetric in θ. From (5.3), the wave function of the lowest state will behave like $\cos(\nu_1\theta)$, and the second bound state will look like $\sin(\nu_2\theta)$, where ν_j (j=1,2) are the lowest allowed modes for the eigenfunctions in the bend, satisfying (5.5). The eigenvalue $\overline{k}_2$ of the second state also decreases monotonically with increasing bend angle Θ. Further increases in Θ will support more bound states. The reflection symmetry of each successive bound state is opposite that of the state below it.

A remarkable feature of Fig. 5.3 is that, for very large Θ, the number of bound states increases and all eigenvalues $\overline{k}_j$ approach the same value. This value, which depends on the curvature κ, is called $\overline{k}_\infty$ by Lin and Jaffe. This can be understood in the following way. In the limit $\Theta \to \infty$, the curved region becomes infinitely long and (for bound states) the external straight region is negligible. In this limit one can accommodate a wave function with any number of oscillations in θ, without changing the energy of the state. From (5.3), the longitudinal (θ) dependence of the wave function will be sinusoidal [4]. This will contribute roughly $(\nu/\overline{R})^2$ to the energy, so that if

[4] For symmetric states the wave function will have an angle dependence $\cos(\nu\theta)$, while the antisymmetric states will vary like $\sin(\nu\theta)$.

$\nu \to 0$ the contribution of the longitudinal oscillations to the energy will be negligibly small.

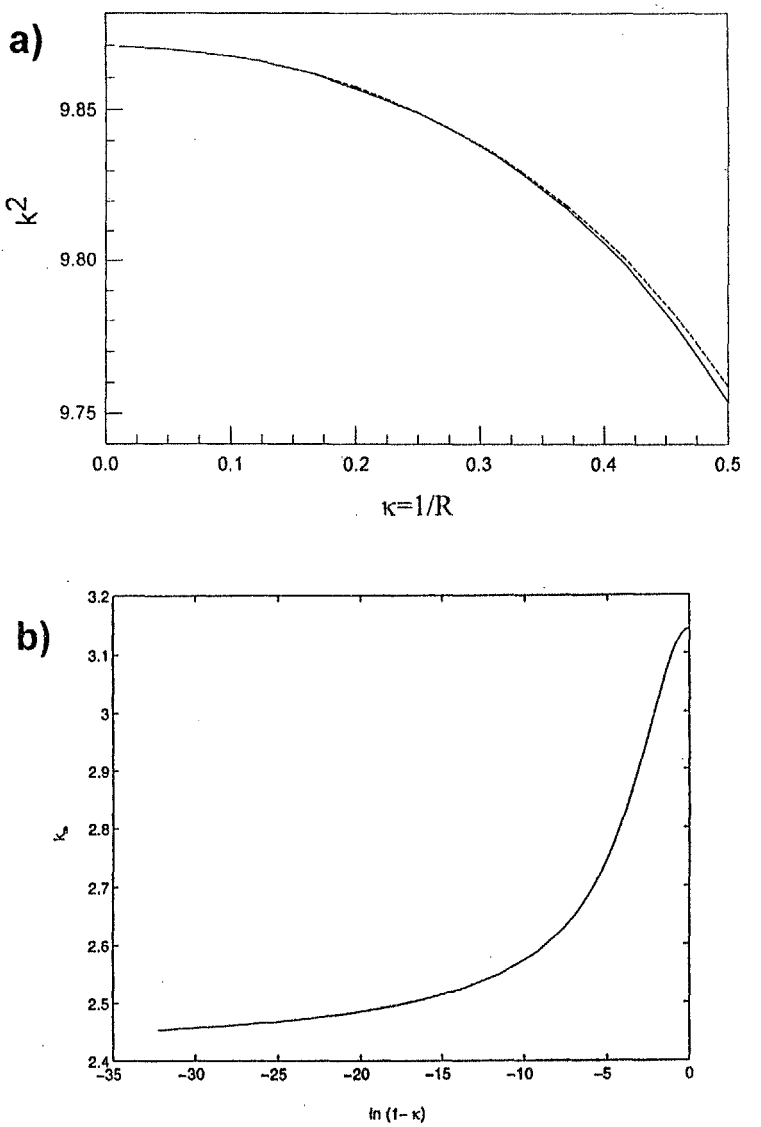

Fig. 5.5. (a) Plot of $\overline{k}_\infty^2$ vs. curvature $\kappa = 1/R$ for a circular bend tube as the bend angle $\Theta \to \infty$. Solid curve is the solution of (5.15). Dashed curve uses the approximation from [138], given in (5.16). (b) Plot of $\overline{k}_\infty$ vs. $\ln(1-\kappa)$

The behavior of bound states in the limit of large bend angle can also be deduced from (5.11), which gives the approximate relation between the bend angle Θ and mode ν. This suggests that as $\Theta \to \infty$ for a given radius of curvature R, all modes $\nu_j \to 0$. Thus as $\Theta \to \infty$, an increasing number of bound state energies will accumulate at the value $\overline{k}_\infty$, and the value of the mode ν for each state will approach zero. The value of $\overline{k}_\infty(R)$ is determined by solving the transcendental boundary value condition, (5.5) by setting $\nu = 0$,

$$J_0(\overline{k}_\infty(R-1))Y_0(\overline{k}_\infty R) - J_0(\overline{k}_\infty R))Y_0(\overline{k}_\infty(R-1)) = 0 \quad . \tag{5.15}$$

The solid curve in Fig. 5.5a plots $\overline{k}_\infty^2$ vs. $\kappa = 1/R$. In the limit $\kappa \to 0$ (*i.e.*, $R \to \infty$), we have $\overline{k}_\infty^2 \to \pi^2$. This is the continuum threshold for a straight tube, which has no bound state. For finite radius of curvature, the energy vs. curvature plot is a parabola. In the limit of an infinitely long curved section the effective attractive potential $-\kappa^2/4$ is constant everywhere. The net result is that the energy simply shifts by this amount, so one expects to find

$$\overline{k}_\infty^2 \approx \pi^2 - \frac{\kappa^2}{4} \approx \pi^2 - \frac{1}{4\overline{R}^2} \quad . \tag{5.16}$$

This result could also be obtained from the approximation of Sprung *et al.*, (5.11). In this picture the circular bend is approximated by a square well potential of depth $1/4\overline{R}^2$ and width $2\overline{R}\Theta$. As $\Theta \to \infty$, the square well becomes infinitely wide, and the bound state energy moves to the bottom of the well. The dashed curve in Fig. 5.5a plots the quantity $\pi^2 - 1/(4\overline{R}^2)$, where $\overline{R} = R - 1/2$. This gives an excellent fit to the calculated values of $\overline{k}_\infty^2$ for all cases where the radius of curvature $R > 2$.

As $\kappa \to 1$, the system develops a "kink" at the inner corner, as $R - 1 \to 0$. In this limit, (5.16) no longer gives a reasonable estimate for $\overline{k}_\infty$. This can be seen by inspection of (5.15). In the limit as $R \to 1$, $J_0(k(R-1))$ goes to zero, and $Y_0(k(R-1))$ blows up. The mode equation then reduces to

$$J_0(\overline{k}_\infty(\kappa = 1)) = 0 \quad , \tag{5.17}$$

i.e., $\overline{k}_\infty(\kappa = 1) = 2.405\ldots$, the first zero of the Bessel function J_0. Figure 5.5b plots $\overline{k}_\infty$ vs. $\ln(1-\kappa) = \ln((R-1)/R)$. As $\kappa \to 1$, the curve for $\overline{k}_\infty$ is seen to approach the first zero of the zeroth order Bessel function. This gives the limit of $\overline{k}_\infty$ as $\kappa \to 1$, *i.e.* $\ln(1-\kappa) \to -\infty$ in Fig. 5.5b [98].

In the limit $\Theta \to \infty$, the curved region is infinitely long, so the straight section can be neglected, and the system becomes an infinite non-intersecting spiral. The curvature produces a constant attractive potential everywhere; it produces an infinite number of bound states all of which accumulate at the point $\overline{k}_\infty(\kappa)$. Since the effective potential is constant everywhere, the continuum states from the straight tube are all shifted downwards by this constant amount. They fill the gap between the original continuum threshold

(for the straight tube) and $\overline{k}_\infty$. The net result is that the continuum threshold simply shifts downwards to $\overline{k}_\infty$. The net result is that the infinite spiral has a lower continuum threshold than the straight tube and no bound states, as was predicted in Sect. 2.1.2.

5.1.3 Transmission in a System with a Circular Bend

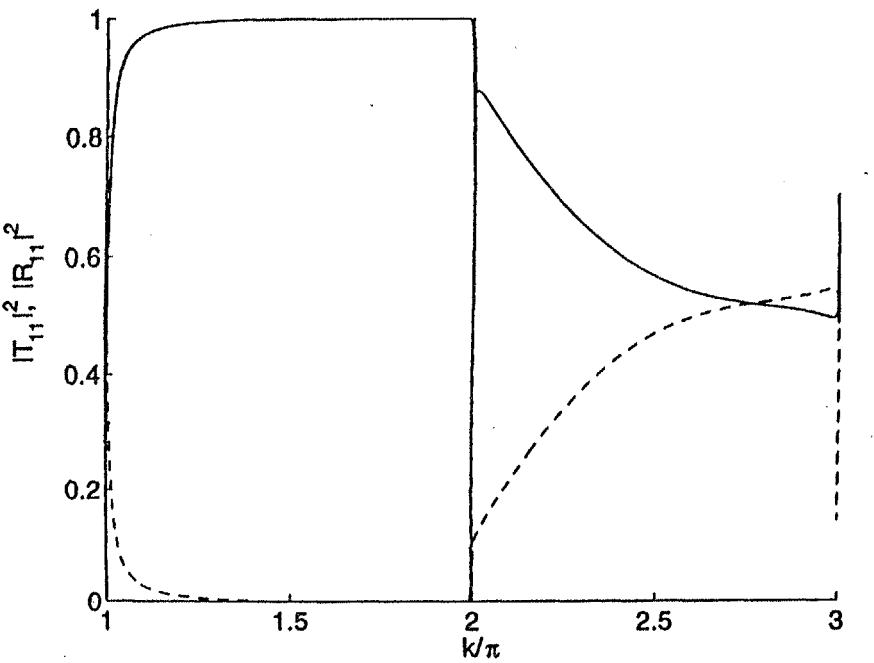

Fig. 5.6. Transmission and reflection coefficients $|\mathcal{T}_{11}|^2$ (solid curve) and $|\mathcal{R}_{11}|^2$ (dashed curve) vs. k/π, for a circular bend tube with $\kappa = 0.9$ and $2\Theta = \pi/2$. From [98]

Transmission through a tube with a circular bend has been studied by Lent [137], Sols and Macucci [24], Sprung *et al.* [138], and Lin and Jaffe [98]. Figure 5.6 plots the transmission coefficients vs. k/π, as calculated by Lin and Jaffe [98]. The solid curve is the transmission coefficient $|\mathcal{T}_{11}|^2$, and the dashed curve is the reflection coefficient $|\mathcal{R}_{11}|^2$, as defined in (3.2). The parameters of the system are $\kappa = 0.9$ ($R = 1.11$), $2\Theta = \pi/2$. For this geometry the system has only a single bound state.

The transmission coefficients have the following qualitative features. For a tube of unit width the threshold for continuum scattering is $k/\pi = 1$, and inelastic thresholds (higher transverse modes) open up whenever $k/\pi =$

$N \geq 2$. The transmission is zero at threshold. $|\mathcal{T}_{11}|^2$ rises very rapidly to a value very close to one, and remains close to unity until just below the first inelastic threshold. In this region, these ideal circular bends introduce almost no resistance to the current flow, so there is almost zero reflection. Just before the opening of the second transverse mode, the transmission drops extremely sharply towards zero, then rises abruptly again above inelastic threshold. Below the threshold for the second transverse mode ($k = 2\pi$), unitarity requires $|\mathcal{T}_{11}|^2 + |\mathcal{R}_{11}|^2 = 1$.

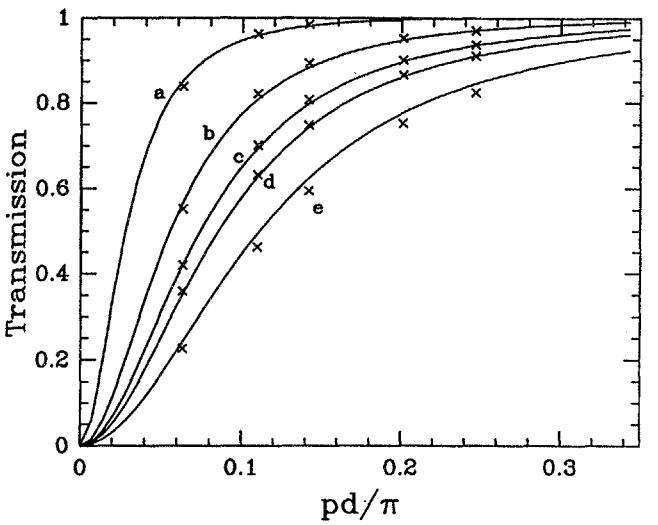

Fig. 5.7. Near-threshold transmission probability $|\mathcal{T}_{11}|^2$ for a right-angle circular bend tube with $2\Theta = \pi/2$, plotted vs. longitudinal wave number pd/π. Curves correspond to single-mode approximation of Sprung *et al.*, [138], for outer radius of curvature (a) $R = 2.5$; (b) $R = 1.5$; (c) $R = 1.25$; (d) $R = 1.15$; (e) $R = 1.0$. Crosses mark transmission probability calculated by Lent [137]

The single-mode approximation of Wu *et al.* [28], presented in Sect. 2.1.4, gives a good fit to transmission near threshold. Figure 5.7 plots the transmission probability $|\mathcal{T}_{11}|^2$ for a 90° circular bend. The results are plotted vs. the longitudinal wave number pd/π. When the system dimensions are rescaled to unit width, we have $pd = \alpha_1 = \sqrt{k^2 - \pi^2}$. The curves correspond to outer radius of curvature (a) $R = 2.5$; (b) $R = 1.5$; (c) $R = 1.25$; (d) $R = 1.15$; and (e) $R = 1.0$. The crosses are the exact results of Lent [137], and the solid curves are the single-mode approximation of Sprung *et al.* [138]. It is clear that the single-mode approximation successfully reproduces not only the bound state energies but low-energy scattering as well. Equation (3.21)

predicts that the transmission probability near continuum threshold should have the form

$$|\mathcal{T}_{11}(\alpha_1)|^2 \sim \frac{\alpha_1^2}{(\alpha_1^2 + \alpha_b^2)} \quad . \tag{5.18}$$

In (5.18), $|\alpha_b| = \sqrt{\pi^2 - E_b}$ is the magnitude of the longitudinal wave number at the bound state which occurs at energy E_b. From (5.18), one expects that the transmission probability $|\mathcal{T}_{11}|^2 \approx 0.5$ when $\alpha_1 = \alpha_b$. For fixed bend angle, the bound state energy E_b increases, and hence α_b decreases, as the radius of curvature R increases. Equation (5.18) thus predicts that the transmission probability should rise more rapidly as R increases, and this is observed in Fig. 5.7.

The low-energy transmission for the circular bend can be compared with that for the L-shaped system shown in Fig. 3.2. The L-shaped tube has substantial additional space at the bend, relative to the circular bend, so for a given bend angle the bound state energy E_b (effective momentum α_b) for an L-shaped tube is significantly smaller (larger) than the corresponding quantities for the circular bend tube. As a result the transmission probability for the circular tube rises much faster than for the L-shaped system at low energies, as predicted by (3.21). When the transmission reaches a maximum, the circular bend gives nearly 100% transmission, since it produces almost no reflection in this region. The maximum transmission probability for the L-shaped tube, $|\mathcal{T}_{11}|^2 \approx 0.85$ (see Fig. 3.1), is substantially less than for the circular bend tube, since the sharp corners in the L-shaped structure produce substantially more reflection.

The transmission amplitude $\mathcal{T}_{11}$ for the circular bend tube displays all of the qualitative features which were predicted in Sect. 3.1. Figure 5.8 shows the Argand diagram for $\mathcal{T}_{11}$, in the energy region from threshold to the second transverse mode, i.e $\pi < k < 2\pi$, from the calculation of Lin and Jaffe [98]. The system parameters are those given in Fig. 5.6. The circles in Fig. 5.8 denote equal k intervals. The salient qualitative features of the transmission are:

- At elastic threshold, $\mathcal{T}_{11} = 0$.
- Just above elastic threshold, $\mathcal{T}_{11}$ moves clockwise in a circle of radius 1/2, centered about the point $\mathcal{T}_{11} = 1/2$, until it reaches $|\mathcal{T}_{11}| \approx 1$. This can be understood from (3.21), which showed that the existence of a symmetric bound state and the vanishing of the transmission at threshold required

$$\mathcal{T}_{11}(\alpha_1 \approx 0) \sim \frac{\alpha_1 + i\alpha_b}{2(\alpha_1 - i\alpha_b)} + \frac{1}{2} \quad . \tag{5.19}$$

  This produces the motion of $\mathcal{T}_{11}$ (a semicircle of radius 1/2 in the clockwise direction, centered about the point $\mathcal{T}_{11} = 1/2$) observed near threshold.
- After the initial clockwise circular rotation near threshold, $\mathcal{T}_{11}$ continues to move clockwise with increasing energy, almost on the unit circle. In

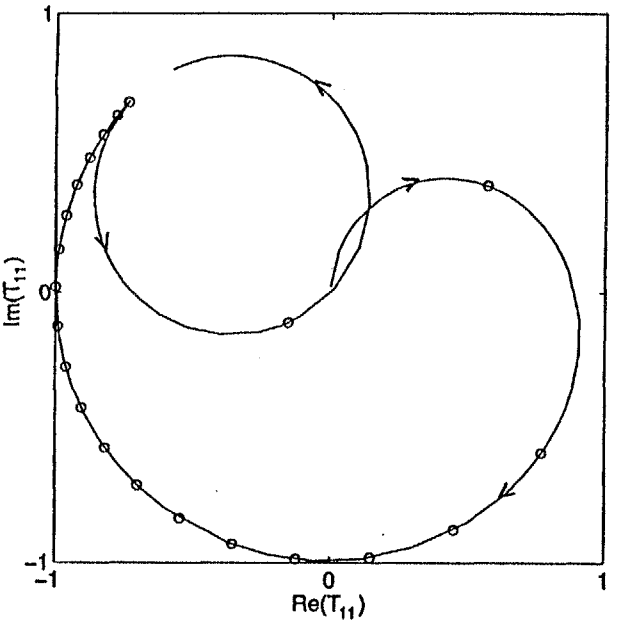

Fig. 5.8. Argand diagram for $\mathcal{T}_{11}$, a plot of the Real vs. Imaginary parts of the transmission amplitude, for a circular bend tube with $\kappa = 0.9$ and $2\Theta = \pi/2$. Here, $\pi < k < 2\pi$; arrows indicate direction of increasing k; circles mark equal intervals in k. From [98]

this energy region, the circular bend provides almost no resistance to the electron motion.

- As the energy increases, the system continues to have nearly perfect transmission, until energies just below the second transverse mode. In this region $\mathcal{T}_{11}$ moves rapidly counterclockwise in a circle of radius 1/2. As $\mathcal{T}_{11}$ moves along this resonant circle, the transmission amplitude decreases in magnitude very rapidly. In fact, at its lowest value the transmission coefficient almost exactly vanishes.

These features of the transmission are understood in terms of the quasi-bound state just below the second transverse mode threshold, which was discussed in Sect. 3.1. From (3.23), this quasi-bound state appears as a pole in the transmission amplitude $\mathcal{T}_{11}$ at a complex value of the longitudinal momentum $\alpha_1 = q_1 + i\gamma_1$, just below the second transverse mode, so that $q_1 \approx \sqrt{3}\pi$. From (3.23), the structure of the quasi-bound pole requires that the transmission amplitude undergo an anticlockwise circular rotation with a radius of 1/2, shortly below the second channel threshold.

For the circular bend, the width of the quasi-bound state, which is proportional to the square of the coupling γ_1 to the lowest mode, is extremely small. This has three observable consequences. First, the transmission am-

plitude $\mathcal{T}_{11}$ varies extremely rapidly for energies near this resonance. Second, $\mathcal{T}_{11}$ completes almost a complete counterclockwise circle of radius 1/2, before the second transverse mode opens. Third, since the transmission amplitude is almost exactly on the unit circle for energies below the resonance, in order to avoid violating unitarity $\mathcal{T}_{11}$ must move so that the quasi-bound resonance circle is tangent to the unitarity circle. This requires that the transmission amplitude pass almost exactly through the origin. This behavior is seen in both Figs. 5.6 and 5.8.

In Sect. 3.1 it was shown that a quasi-bound state should appear before the opening of every new transverse mode. Figure 5.9 shows the Argand diagram for the transmission amplitudes $\mathcal{T}_{12}$ and $\mathcal{T}_{22}$, in the range $2\pi < k < 3\pi$. The qualitative features are identical with those for the lowest mode transmission amplitude $\mathcal{T}_{11}$: just above threshold the amplitude $\mathcal{T}_{22}$ rotates clockwise through a semicircle of radius roughly 1/2 [5]. $\mathcal{T}_{22}$ then moves clockwise on a roughly circular path with magnitude approximately unity, until just below the third transverse mode when $\mathcal{T}_{22}$ moves rapidly counterclockwise in a circle of radius roughly 1/2, producing a very rapid dip in the transmission probability $|\mathcal{T}_{22}|^2$.

The destructive quasi-bound state resonances which appear just below the opening of each transverse mode produce resonances whose line shape cannot be described by the standard Lorentzian form

$$T(E) \sim \frac{1}{[(E - E_R)^2 + \Gamma^2/4]} \quad . \tag{5.20}$$

Resonances with a non-Lorentzian line shape are generically referred to as "*Fano resonances*" [139], which were originally identified in atomic and molecular reactions. An analysis of the analytic properties of the transmission amplitudes provides us with a detailed description of the quasi-bound Fano resonances in curved 2-D systems.

5.2 Tube with a Single Sharp Bend

The preceding section discussed the physics of particles traveling through a tube with a circular bend. In this section we analyze the case of a 2-D structure with a "*kink*": two straight sections of unit width joined at some interior angle $0 < \theta < \pi$. This is shown schematically in the inset to Fig. 5.10. In Sect. 2.1.3 it was shown that such a system always has at least one bound state for all $\pi > \theta \geq 0$, and Sect. 2.1.5 reviewed the properties of the L-shaped tube, where $\theta = \pi/2$. A tube with a circular bend can always be inscribed inside any tube with a kink (see the dashed curve in Fig. 2.3a), so

[5] Above inelastic threshold the sum of the transmission and reflection coefficients in channel 2 is no longer required to equal 1, because of the coupling of this mode to channel 1.

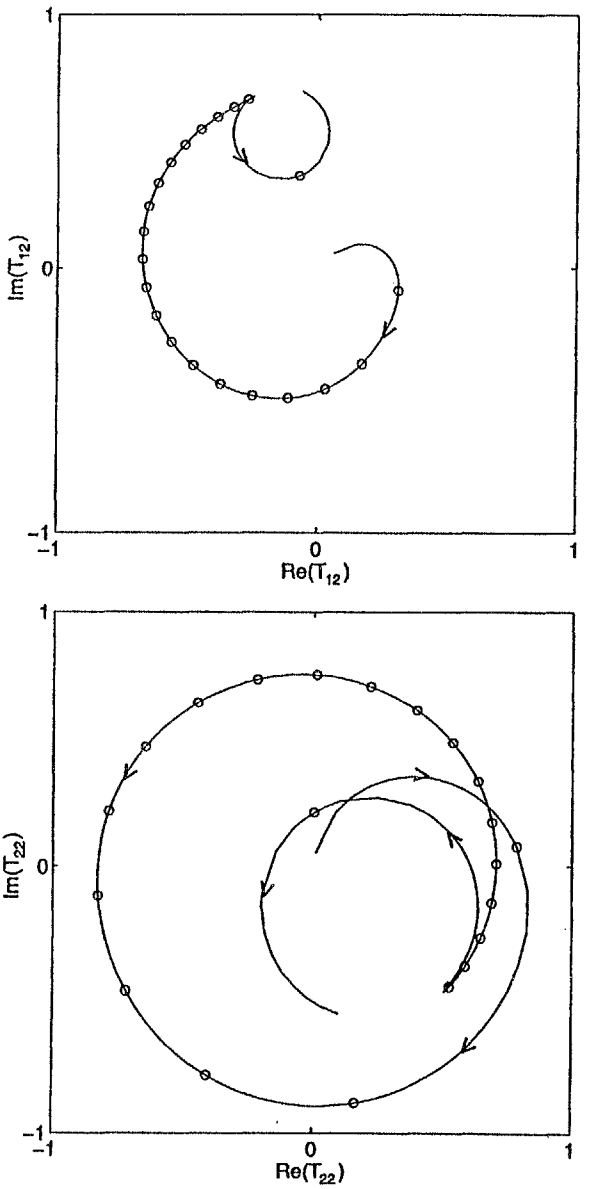

Fig. 5.9. Argand diagrams for $\mathcal{T}_{12} = \mathcal{T}_{21}$ and $\mathcal{T}_{22}$, for circular bend tube with parameters given in Fig. 5.8. Energy range is $2\pi < k < 3\pi$

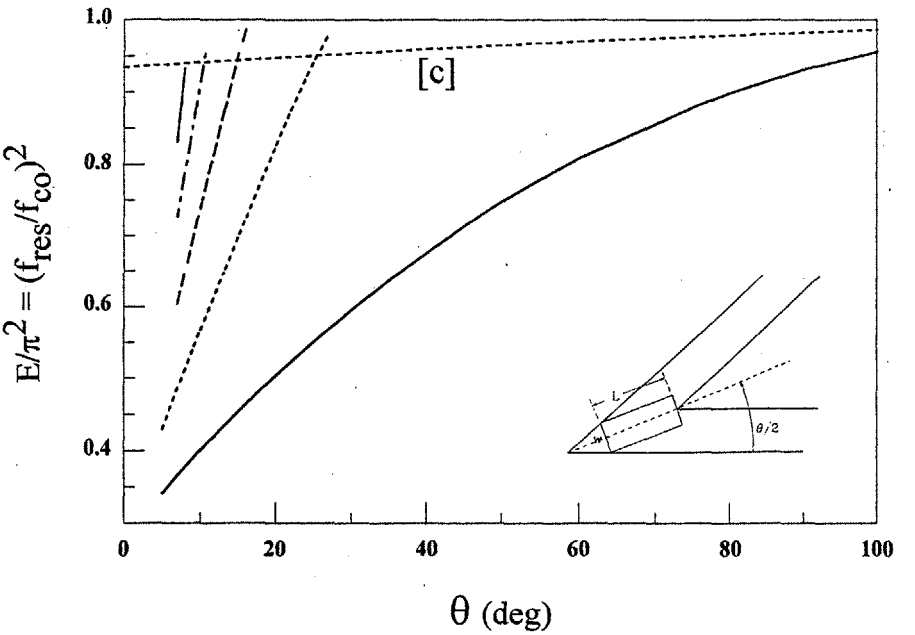

Fig. 5.10. [Inset: schematic of bent tube formed from joining two straight sections of unit width and internal angle θ. A rectangle of length L and width W is inscribed in the central bend.] The bound state energies for the system are shown in the inset, as a function of the internal bend angle θ. Solid curve: lowest-energy ($m = 1$) state; dotted curve: ($m = 2$) state; dashed curve: ($m = 3$) state; dot-dashed curve: ($m = 4$) state; solid curve:($m = 5$) state. Dashed curve [c] is the bound state energy for the circular bend tube with identical total bend angle ($\pi - \theta$)

by comparing a system with a kink to the corresponding circular bend tube with the same total bend angle, one can understand the relative importance of bends and "bulges" in binding and scattering phenomena.

As the internal bend angle $\theta \to \pi$, the binding energy goes to zero (the eigenvalue $k^2 \to \pi^2$), although at least one bound state exists for any $\theta \neq \pi$. With decreasing θ, the extra space contained in the "bulge" in the sharp bend (the difference in area between this system and the inscribed circular bend tube) increases dramatically. In the limit $\theta \to 0$, the structure approaches the case of a straight tube of width two which breaks up into two tubes of unit width (the additional area in the corner of the system grows without limit). Thus for small values of θ, one expects to have more than one bound state. Furthermore, in the limit $\theta \to 0$ the number of bound states should become infinite, and the energy of every bound state should approach $\pi^2/4$. At $\theta = 0$, the continuum threshold would be lowered to $E_{th} = \pi^2/4$.

This is analogous to the situation found in the preceding section, for a system with a circular bend. For sufficiently large circular bend angle Θ the tube had more than one bound state, and in the limit $\Theta \to \infty$, the number of bound states increased without limit, the energy of all bound states approached the same asymptotic value, and the continuum threshold was lowered by this amount.

We give an intuitive estimate of bound state energies for a tube with a sharp bend of internal bend angle θ. In the interior of the bend, inscribe a rectangle with length L and width W, as shown in the inset to Fig. 5.10. Consider the energy eigenvalues for a scalar field which satisfies the Helmholtz equation inside the rectangle and vanishes on the sides of the rectangle. The energy of such states is easily calculated,

$$E_{nm} = \pi^2 \left[\frac{n^2}{W^2} + \frac{m^2}{L^2} \right] , \tag{5.21}$$

for nonzero integer values (n, m). The lowest energy state (the ground state) of the system corresponds to the values $n = m = 1$. The length of the inscribed rectangle is related to the width by

$$L = \csc(\theta/2)[1 - W \cos(\theta/2)/2] \ . \tag{5.22}$$

It is a straightforward exercise to calculate the dimensions of the inscribed rectangle which has the lowest ground-state energy, for a given bend angle θ. Using these dimensions, it can be demonstrated that for small θ in the limit as $W \to 2$,

$$E_{nm} \to \frac{\pi^2}{4} \left[n^2 + \left(2n^2 + m^2\right) \theta^{2/3} + \ldots \right] \ . \tag{5.23}$$

Since the rectangle is inscribed in the tube, its eigenenergies provide an upper limit for the bound state energies of the system. It is apparent from (5.23) that as $\theta \to 0$, the inscribed rectangle has more and more bound states, and the energies for all of these approach $\pi^2/4$ for sufficiently small θ (in (5.23), such states have $n = 1$ and any value for m).

These simple arguments agree with the results of numerical calculations. For sufficiently small values of θ multiple bound states occur; the number of bound states increases rapidly at very small θ, and the energy $\pi^2/4$ is an accumulation point for such states in the limit $\theta \to 0$.

5.2.1 Bound States for Structures with a Sharp Bend

Carini *et al.* [22] calculated bound state energies for scalar fields inside a system containing a single sharp bend, using two different techniques. First, they used a relaxation method to give lower limits on the binding energy. They also used a series expansion method to calculate bound state wave functions. This approximation is essentially that of Tang *et al.* [59], who used

it to solve a simple model for chemical reactions which could be reduced to the bent tube problem. This method makes use of the fact that the bound state wave functions for the bent system are symmetric upon reflection across the diagonal at the bend, so the normal derivative of the wave function must vanish on the diagonal.

Thus, one searches for solutions on half the structure, with Neumann boundary conditions on the diagonal (vanishing of the normal derivative there). The channel is divided into two adjacent regions: a semi-infinite straight section and a central triangular region. The bound state energy is found by matching the wave functions and normal derivatives at the region boundary, and finding an eigenstate whose wave function decays exponentially in the straight section.

The theoretical predictions for bound states are shown in Fig. 5.10. The bound state eigenvalues (divided by π^2) are shown for the first five bound states, as a function of the interior bend angle θ. The bound state energies decrease monotonically as θ is decreased. As $\theta \to 0$, all bound state energies tend towards $\pi^2/4$. For very sharply bent tubes, the number of bound states increases rapidly with decreasing θ. For interior bend angles $\theta > 27.5°$, there is only a single bound state; below this angle one has at least two bound states. A third bound state appears at $\theta \approx 18°$, followed by a fourth around 11° and a fifth at about 9°. In Fig. 5.10, the dashed curve labeled [c] shows the ground state energy of a circular bend with the same bend angle as a tube with a kink. The sharply bent systems have much greater binding energy than the circular bend tubes. The sharply bent system contains the same overall bend angle as the circular bend tube which can be inscribed inside it. The system with a kink contains an additional "bulge" in the corner. Fig. 5.10 shows that the bulge in the sharply bent tube plays a dominant role in determining the bound state energies, relative to the curvature.

5.2.2 Sub-Cutoff Confined Modes in Curved Waveguides

Experimental measurements of bound states in sharply bent tubes were made with bent waveguides [21, 22], using the correspondence between wires and waveguides outlined in Chap. 4. An adjustable waveguide is shown schematically in Fig. 4.1, and was described in Sect. 4.3. A second waveguide was constructed with a fixed internal angle $\theta = 22.5°$. The calculated cutoff frequency for the waveguide sections is $f_{co} = c/2w$, approximately 7.87 GHz for width $w = 1.905$ cm.

Microwave power was sent into the bend region through a coaxial line. The bound state then appears as a sharp decrease in reflected power $R(f)$, *i.e.*, as a resonant absorption of power for microwave frequencies below cutoff frequency. Figure 5.11 shows $R(f)$ for the 22.5-degree bend with a low coupling strength between the coaxial line and the waveguide. For this bend angle, the waveguide should have two sub-cutoff confined EM modes, as can

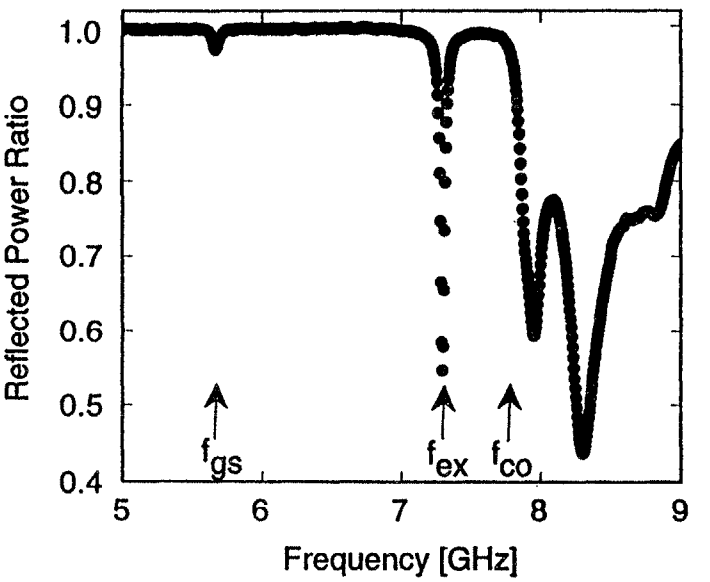

Fig. 5.11. Ratio $R(f)$ of reflected power to incident power, vs. microwave frequency in GHz, for a waveguide with interior bend angle $\theta = 22.5°$. Arrows denote the low-coupling resonant frequencies f_{gs} and f_{ex} for the ground and first excited confined modes, and the cutoff frequency f_{co} for the straight waveguide sections

be seen from Fig. 5.10. The lower energy bound state appears as the prominent minimum in $R(f)$ at 5.666 GHz, shown by the arrow marked f_{gs}. This corresponds to a bound state energy $E_1 = (0.530 \pm 0.002)\pi^2$ in a tube of unit width, in excellent agreement with the theoretical prediction shown in Fig. 5.10. The first excited state appears at frequency $f_{ex} = 7.305$ GHz, indicated by the arrow marked f_{ex}, and equivalent to bound state energy $E_2 = (0.882 \pm 0.004)\pi^2$. Both resonances occurs well below the calculated cutoff frequency, indicated by the arrow f_{co}.

As discussed in Chap. 4, the "bound states" in the waveguide are stable confined EM modes located below the waveguide cutoff frequency. The measurements of Carini *et al.* [21] mark the first known determination of these sub-cutoff confined states, which were first predicted in 1990 [55].

As was demonstrated in Sect. 4.2 and Sect. 4.3, the electromagnetic energy densities in the waveguide can be mapped out by measuring the shift in resonant frequency when a small metal sphere is inserted in the waveguide. The frequency shift will be positive at points where the magnetic field (gradient of the wave function) is relatively large, and negative where the electric field (wave function) is large. Figure 5.12b shows theoretical contour plots of the frequency shifts in a waveguide with internal bend angle $\theta = 22.5°$. Figure 5.12b shows contour plots for the higher-energy bound state. Shaded

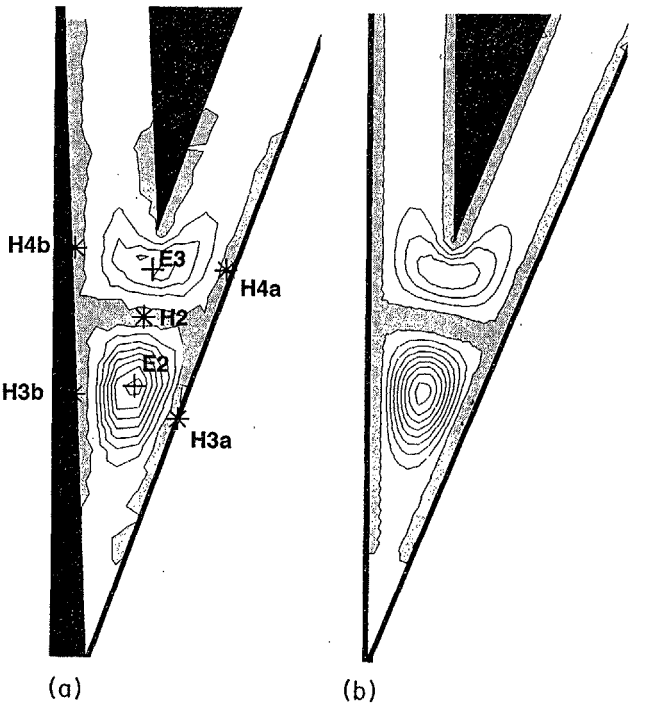

Fig. 5.12. (a) Experimentally measured contour plot of the frequency shift for the first excited state of a bent waveguide with interior angle $\theta = 22.5°$. Points $E2$ and $E3$ denote maximum measured negative frequency shifts; points $H2$, $H3a$, $H3b$, $H4a$ and $H4b$ represent local maxima in the frequency shifts. (b) Theoretical calculations of the frequency shift for the same quantity shown in (a)

areas denote regions of positive frequency shift, while unshaded areas denote negative frequency shifts. For the higher frequency sub-cutoff mode, the E field is predicted to have a maximum and minimum value, separated by a node. Thus there should be two regions of maximum negative frequency shift along the middle of the bend region, with a line of maximum positive frequency shift between them. The B fields are predicted to be large along both the inner and outer waveguide walls, where the E fields vanish.

Figure 5.12a displays the experimental measurements of frequency shift [22]. The qualitative agreement between theory and experiment is quite good, especially in the vicinity of the maximum E field. Away from this region, the frequency shifts become so small that the experimental measurement is dominated by noise. The maximum positive and negative frequency shifts are denoted by asterisks and crosses, respectively. Quantitatively, the experimental frequency shifts at the antinodes in magnetic field agree remarkably well

with theory. Near the antinodes of E, however, the measured frequency shift is only about 75% of the theoretical value. Similarly good results are found for the lowest-energy bound state in this waveguide [22].

These measurements clearly demonstrate the extent to which waveguide experiments can locate confined modes in bent waveguides, and can map out the electromagnetic field densities. These "table top" measurements can give useful qualitative information regarding electron bound state wave functions in quantum heterostructures with the same geometry. If sufficiently accurate measurements were available for electron wave functions in quantum wires, they could be compared with waveguide measurements to highlight the different boundary conditions in quantum heterostructures and waveguides, which were discussed in Sects. 3.3-3.4.

5.3 A Tube with a "T-Stub"

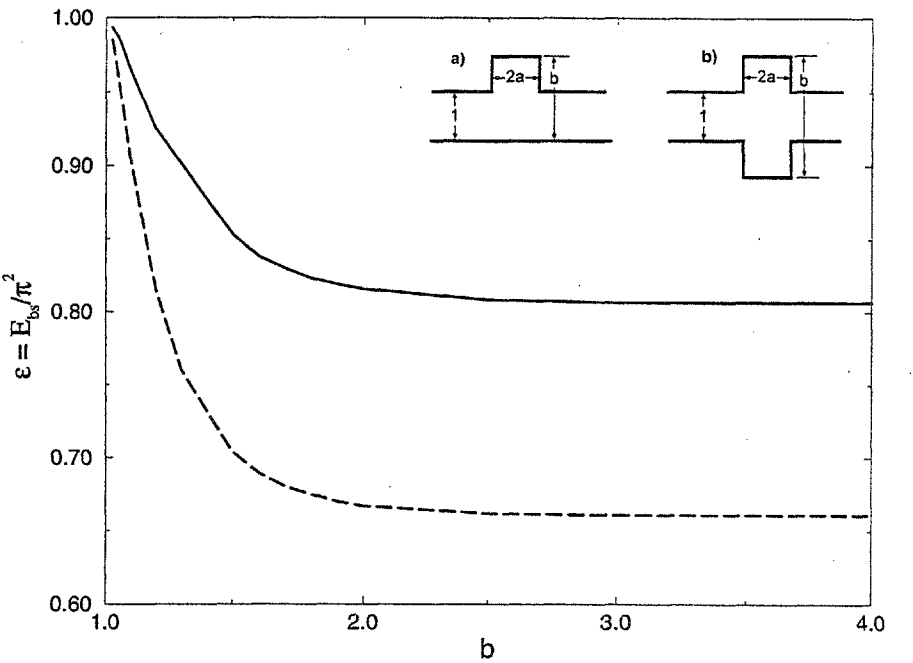

Fig. 5.13. [Inset: schematic picture of tubes with stubs. (a) Tube with a T-stub, a single stub of width $2a$ and height b, for a tube with external legs of unit width. (b) A structure with a cross or "quantum dot", stubs of width $2a$ and total height b projecting from both sides of a tube.] Bound state energy $\epsilon = E_b/\pi^2$ vs. stub height b, for tube with unit channel width and stub width $2a = 1$. Solid curve: bound state energy for T-stub shown in (a); dashed curve: bound state energy for quantum dot shown in (b)

This section examines the physics of tubes containing stubs. Structures of this shape provide a rich field for both theoretical and experimental studies. We will give just a brief review of the physics of these structures, relying heavily on our discussion of systems with different geometries. Graph (a) in Fig. 5.13 shows a schematic picture of a tube with a single T-stub of finite length. The width of the stub is defined to be $2a$, and the height of the tube at the stub is b, when dimensions are scaled so the external legs have unit width. Graph (b) in Fig. 5.13 shows a "cross," a tube with a single junction which extends symmetrically on both sides of the straight legs. Structures with a series of identical T-stubs or crosses will be considered in the next chapter. Theoretical analyses of these systems have been carried out by several groups [38, 66, 99, 116, 128, 140, 141, 142, 143]. Experiments on these systems were carried out by Haug, Lee and Hong [144, 145].

Any tube with either a T junction or a cross will have at least one bound state. The number of bound states, and the shape of the bound state wave functions, will depend sensitively on the width $2a$ of the stub, and somewhat less sensitively on the height b. First, by varying the width of the stub, relative to the width of the external legs, one can ensure that the resulting bound state wave function will be large either in the straight section of the tube, or in the stub. For the case $2a < 1$, the wave function in the stub must have a higher transverse energy than in the straight section. Consequently, the particle's probability density will be largest in the straight section of the tube, except at those energies where a standing wave can fit across the stub. When $2a > 1$, the bound state energy will decrease substantially as the stub width increases. In this case the transverse energy is lower in the stub than in the straight channel, so the bound state wave function tends to be concentrated in the stub. For larger values $2a \geq 2$, one has the possibility of producing a substantial number of bound states, with rather interesting probability distributions for some confined modes. For stubs with large width, the number of bound states and their structure depends sensitively on the geometry of the system.

In this monograph we will confine our attention to systems with stubs where the width of the external legs and the stub are required to be identical, *i.e.* $2a = 1$. In this case the the tube and the stub are said to be "*well matched*," in the sense that the transverse energy is the same in the external legs, and in the stub. In the well matched geometry, a tube with either a stub or a cross will have just one bound state, regardless of the length of the stub. The bound state wave function will be localized in the region of the junction, and will be concentrated primarily in the straight channel of the tube. Figure 5.13 shows the bound state energy $\epsilon = E_b/\pi^2$ for a structure with a stub of width $2a = 1$, vs. the height b of the stub. The solid curve is the bound state energy for the T-stub, and the dashed curve is the energy for the cross. It is clear that by the time the stub height reaches $b = 2$, the bound state energy has nearly reached its asymptotic value for infinite stub

length. Because the bound state wave function is essentially zero except in the immediate vicinity of the junction, further increases in stub height have essentially no effect on the bound state energy. The bound state probability density in a single T-stub is shown in Fig. 6.2a; in this case the stub height is $b = 2.2$. With increasing b, the bound state eigenvalue and probability density remain essentially unchanged. In the limit $b \to \infty$, the bound state energy for the cross approaches the value calculated originally by Schult, Ravenhall and Wyld [15] and Peeters [16].

5.3.1 Transmission in Structures with T-Stubs

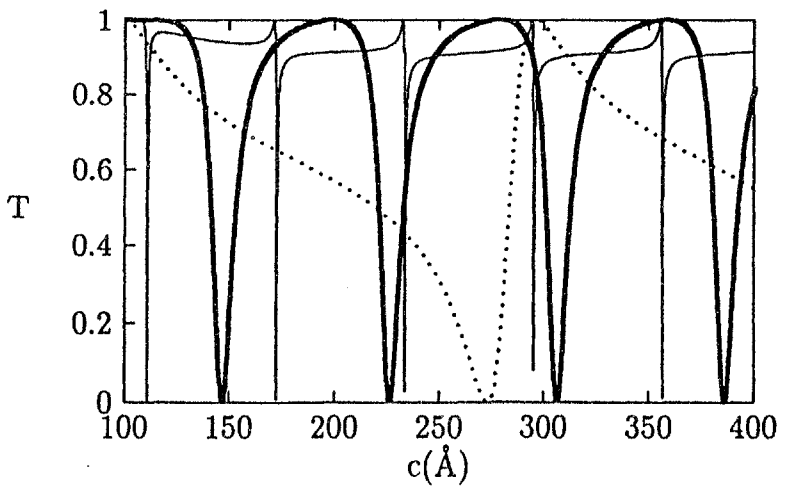

Fig. 5.14. Transmission coefficient vs. stub height c for the T junction (graph (a) of Fig. 5.13). Calculation by Sols *et al.*, [38], for a quantum wire with channel width and stub width $w = 2a = 100$ Å. Electron energies correspond to $E = 1.27E_1$ (dotted curve), $E = 2.56E_1$ (heavy solid curve), and $E = 3.64E_1$ (light solid curve), where E_1 is the continuum threshold

Structures with T-stubs possess interesting transmission properties, which have the possibility of producing practical nanoscale devices. Figure 5.14 plots the transmission coefficient $T_{11} = |\mathcal{T}_{11}|^2$ for the T-stub as a function of the stub length c [6], for the well-matched case $2a = 1$. This was originally calculated by Sols *et al.* [38, 140], for a quantum wire of channel width 100 Å (equal to the stub width). The results are shown for three different electron energies. Relative to the threshold energy E_1 for transmission, the dotted line is for

[6] Note that the quantity labeled c in Fig. 5.14 is the total height of the stub, which we have denoted as b.

$E = 1.27\,E_1$, the heavy solid curve for $E = 2.56\,E_1$, and the light solid line corresponds to $E = 3.64\,E_1$. The transmission coefficients have two striking features. First, as the height of the stub is varied, the transmission coefficient for a given energy fluctuates from one to zero. Second, these fluctuations are periodic. The difference in stub height δb between successive transmission maxima is constant, and is identical to the difference between successive transmission minima. The quantity δb is seen to be a function of the electron energy.

Sols *et al.* suggested that the dependence of the transmission coefficient on the stub length could be utilized to produce a "*quantum modulated transistor*" [38, 140]. One could fabricate a quantum wire whose shape resembled the T-stub, and vary the effective length of the stub by applying an external gate voltage. In this way, for a given electron energy one could ensure either total transmission or total reflection, by varying the stub length according to Fig. 5.14. Lent *et al.* [146] pointed out the possibility of transistor action in transmission through a constriction in a quantum waveguide. Datta [147] listed a number of devices which could be produced in quantum heterostructures, and whose actions would essentially reproduce those in conventional semiconductor systems. Kouwenhoven *et al.* [142] observed conductance fluctuations in a one-dimensional crystal containing a series of equally-spaced stubs.

The periodicity in the transmission probability can be understood using a simple 1-D model. Consider a long straight channel coupled to a T-stub, in the limit where the channel width is negligible relative to the length b of the stub. Xia [83] derived an analytic formula for the transmission amplitude in such a 1-D system,

$$t(k) = [1 + \frac{i}{2}\cot(kb)]^{-1} \quad . \tag{5.24}$$

In (5.24), k is the wave number. The transmission amplitude $t(k)$ varies between 0 and 1 at regular intervals,

$$t(k) = \begin{cases} 0 & \text{whenever } \; kb = n\pi, \quad n = 1, 2, \ldots \\ 1 & \text{whenever } \; kb = \frac{(n-1)\pi}{2} \quad n = 1, 2, \ldots \end{cases} \tag{5.25}$$

Porod *et al.* [148, 149] carried out numerical studies of systems involving T-stubs, and note that the regular oscillations in the T-matrix between 0 and 1 are not found in 1-D resonant tunneling between double potential barriers. From (5.24), $t(k)$ has poles at the points

$$kb = n\pi - i\ln(3)/2 \quad , \tag{5.26}$$

for integer values of n. Note that this 1-D example appears not to possess a bound state. In the case of a 2-D tube of width w, the transverse energy is π^2/w^2 (in units where $\hbar^2/(2m^*) = 1$). Consequently, the threshold for transmission is $k_{th} = \pi/w$, as there is a minimum amount of energy which

appears in the transverse channel. However, in the limit where the channel width is neglected, the continuum starts at $k = 0$.

The scattering matrix here is an interesting example of a non-Lorentzian "Fano resonance" [139], introduced in Sect. 5.1.3. For a Lorentzian resonance with no background, the transmission coefficient is a maximum when the longitudinal wave number is equal to the real part of the pole position. Note that the real parts of the pole positions (5.26) for this 1-D model occur at the location of the *zeroes*, and not the maxima, in the transmission amplitude [148]. From (5.25) we predict that as the length of the stub is varied for fixed energy (or k), the distance between successive maxima (or minima) in the transmission will be

$$\delta b = \pi/k \quad . \tag{5.27}$$

The relation (5.24) was derived for strictly 1-D problems in the limit of zero channel width, so it is not particularly accurate in predicting the absolute location of zeros and maxima in T for Fig. 5.14, where the channel width is of the same order as the stub height. But (5.24) is very good at predicting the *spacing* between successive maxima or minima. In the lowest transverse mode, an electron of wave number k has longitudinal momentum $\alpha_1 = \sqrt{k^2 - \pi^2}$ [7]. Choose a stub height b at which the transmission probability is a maximum. For this geometry the wave reflected in the stub has maximal constructive interference with the wave traveling straight through the main channel. If the height of the stub is increased by δb, such that this additional height provides exactly one additional half wavelength in the stub, then the reflected wave in the stub will once again give maximal constructive interference and produce a peak in the transmission probability.

Exactly the same change in stub length will take a minimum in the transmission to another minimum. Therefore, the transmission probability $T_{11}(\alpha)$, as a function of the height of the stub, is a periodic function with period

$$\delta b = \frac{\pi}{\sqrt{k^2 - \pi^2}} \quad . \tag{5.28}$$

Equation (5.28) has been calculated for channel width $W = 1$; it scales to arbitrary width W by rescaling $k \to Wk$ and $\delta b \to W\delta b$. For $W = 100$ Å and $k^2 = 2.56\pi^2$, the conditions corresponding to the heavy solid curve in Fig. 5.14, one calculates $\delta b \approx 80$ Å. Figure 5.15, from Ref [79], shows plots of the electron density $|\phi|^2$ in a system with a single stub, at this energy. The channel width and stub width are 100 Å. Figure 5.15a and 5.15c both correspond to $T_{11} = 0$; they have stub height $b = 146$ Å and $b = 226$ Å, respectively. The incident electron is coming from the right. Clearly, the wave function in Fig. 5.15c has exactly one additional half wavelength in the stub, relative to Fig. 5.15a. Similarly, both Fig. 5.15b and 5.15d have transmission probability $T_{11} = 1$. They correspond to stub heights $b = 200$ Å and $b = 280$ Å. Again,

[7] Because the stub has the same width as the channel, this is also the longitudinal momentum in the stub.

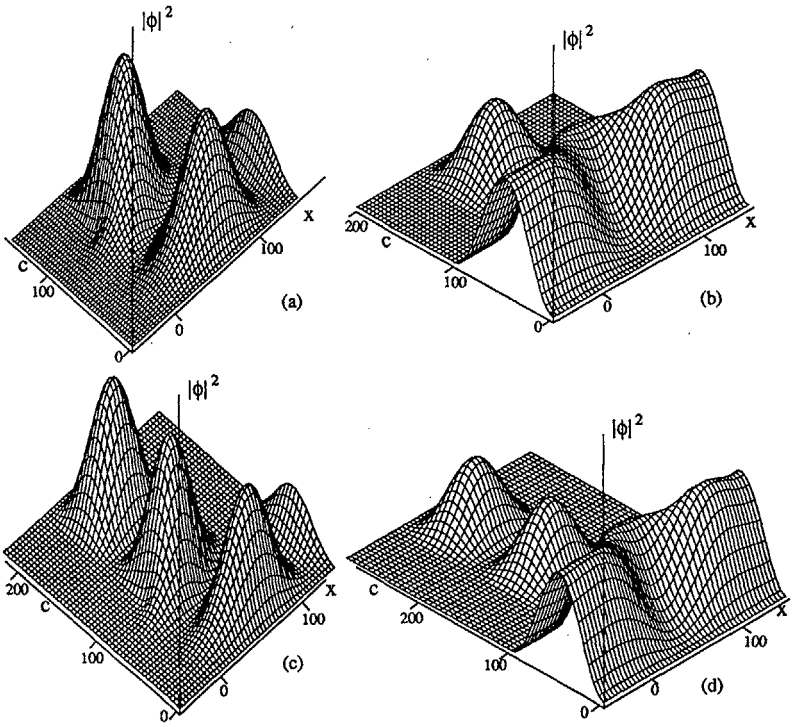

Fig. 5.15. Electron probability density $|\phi|^2$ for T-stub, graph (**a**) of Fig. 5.13. The electron energy corresponds to $E = 2.56E_1$, and the dimensions are the same as in Fig. 5.14. The incident wave comes from the right. (**a**) $c = b = 146$ Å (in the notation of Fig. 5.13), and transmission probability $T = 0$. (**b**) $b = 200$ Å, and $T = 1$. (**c**) $b = 226$ Å, and $T = 0$. (**d**) $b = 280$ Å, and $T = 1$. The wave functions in (**c**) and (**d**) have one extra half wavelength in the stub compared to (**a**) and (**b**), respectively. From [79]

the wave function in Fig. 5.15d has one additional half wavelength relative to Fig. 5.15b. The difference in stub length between successive zeroes and maxima in the transmission is in excellent agreement with the calculated value $\delta b = 80$ Å.

A geometry frequently encountered in quantum heterostructures is shown schematically in Fig. 5.16. In such a system, a bulge in a 2-D quantum wire is connected to 2DEG reservoirs through a constriction on either side of the bulge. Note that the geometry of the cavity coupled to the reservoirs is essentially that of the "cross" configuration, graph (b) in Fig. 5.13. We review

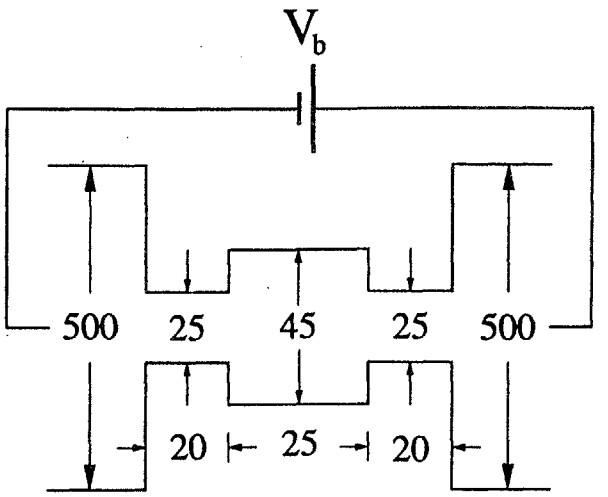

Fig. 5.16. Schematic diagram of a "*quantum-dot*" structure, a cavity coupled to 2DEG reservoirs on either side. The cavity has the same structure as the "cross", graph (b) of Fig. 5.13. The structure has realistic dimensions (given in nm), and a bias potential V_b between the two reservoirs. From [150]

the physics of such systems briefly, since this is the archetypal design used to create an isolated system called a *quantum dot structure*. The dimensions given in Fig. 5.16 are realistic dimensions in nanometers. In such a geometry, one can effectively create a one-dimensional electron state in the bulge region between the two constrictions in the cavity. Electrons are able to tunnel from the 2DEG into the cavity region, and then out again.

From our discussion of confined modes in structures containing bends or cavities, it is clear that at least one bound state will exist in a very long tube with such a cavity. When the cavity is coupled to the external reservoir, one expects that sharp peaks should be seen in the transmission through this structure, when the Fermi energy in the 2DEG coincides with quasi-bound states in the central cavity (dot) region. Figure 5.17 shows the electron probability density for transmission from left to right through the quantum-dot structure of Fig. 5.16 at two electron energies. Fig. 5.17a is essentially at the peak of the resonance, and Fig. 5.17b is "off" resonance. The formation of a quasi-bound resonance in the central cavity is quite clear in this figure, calculated by Weisshaar *et al.* [150].

Figure 5.18 shows the transmission probability vs. electron energy for the quantum dot structure shown in Fig. 5.16. Two dramatic features are evident in the transmission. First, there is the familiar plateau which occurs once the electron energy exceeds the transmission threshold through the constriction.

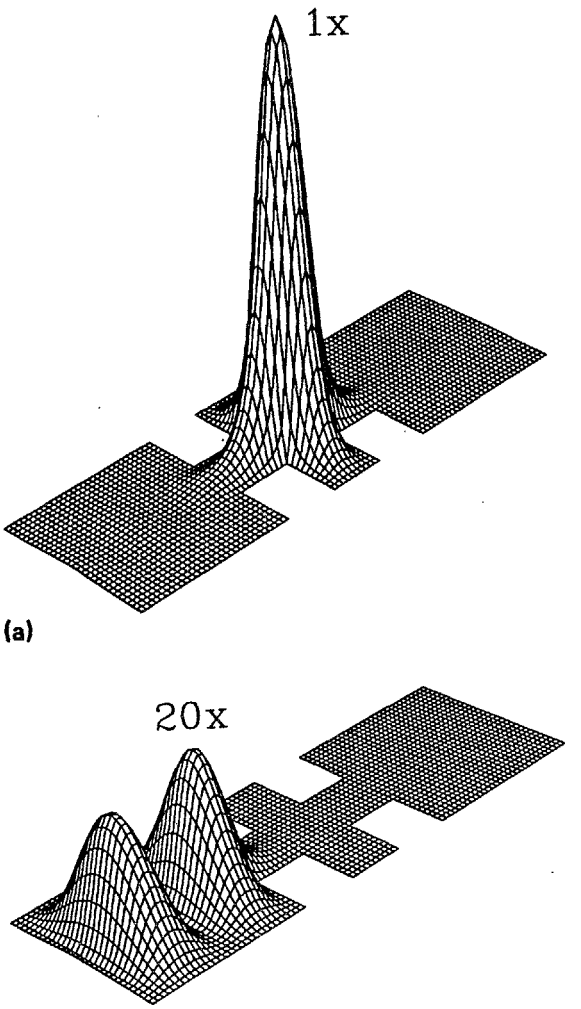

Fig. 5.17. Electron probability density $|\psi|^2$ inside the quantum-dot structure shown in Fig. 5.16. (**a**) On resonance ($E = 37.25$ meV); (**b**) off resonance ($E = 30$ meV). The resonant structure of the probability density inside the quantum dot is evident. From [150]

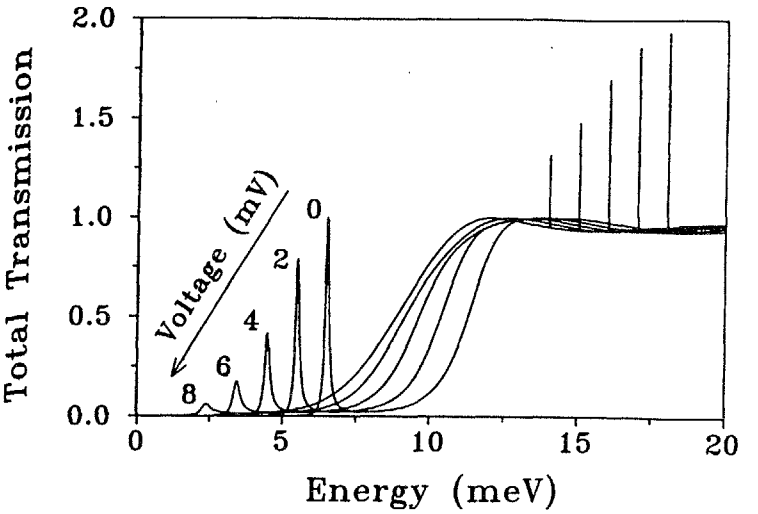

Fig. 5.18. Total transmission probability as a function of energy and bias voltage for the single quantum-dot structure of Fig. 5.16. From [150]

The second feature is a sharp resonance peak below the plateau, due to tunneling of the electrons through a quasi-bound state in the central cavity. In this case one provides a bias voltage between the two 2DEG reservoirs, shown in Fig. 5.16 as V_b. As V_b is varied, the position and height of the sub-threshold transmission peak changes. The transmission is calculated assuming that the bias voltage appears as a linear drop distributed across each of the constrictions.

The literature on quantum dot phenomena is extensive, and exceeds the scope of this book. We refer the reader to the extensive review in the book by Ferry and Goodnick [2], and the recent monograph on quantum dots by Jacak, Hawrylak and Wojs [151], and references cited there. One interesting feature of this structure, as pointed out by Weisshaar *et al.* [150], is that the current-voltage characteristics of this quantum-dot structure exhibit a region of *negative differential resistance* [NDR], which is similar to that achieved in resonant tunneling diodes. However, at present experimental fabrication techniques prevent the NDR effects from being strong, and they are observed only at very low electron temperatures.

Bound state and transmission properties for a quantum dot structure (graph (b) in Fig. 5.13) can be analyzed by constructing the transfer matrix for this system, as defined in Sect. 2.1.4. The "*unit cell*" is a rectangular cavity of width $2a$ and total height b, coupled to straight sections of length l, with width normalized to one. The origin of the system is placed at the center of the cavity. Since the system is symmetric with respect to reflection

about the mid axis of the tube (which is defined to be the x axis), the even and odd parity transverse modes do not mix. Thus the two lowest even parity modes correspond to transverse channel indices $n = 1$ and $n = 3$, respectively [8]. Consequently, the "single-mode approximation" for the even parity modes should be valid from the continuum threshold energy up to the opening of the $n = 3$ channel. One can independently construct a single-mode approximation for the odd parity modes, which would be valid from the $n = 2$ channel threshold until the opening of the $n = 4$ transverse channel.

To construct the transfer matrix, one first constructs the auxiliary matrices **A** and **B** for the quantum dot geometry. The internal cavity solutions $\chi_{0n}(x, y)$ and $\chi_{n0}(x, y)$ defined in (2.26) in Sect. 2.1.4 were calculated by Wu, Sprung and Martorell [30]

$$\begin{aligned} \chi_{0n}(x,y) &= \sum_{m=1}^{\infty} R_{nm} \frac{\sin[K_m(x+a)]}{\sin(2K_m a)} \sqrt{\frac{2}{b}} \sin\left[\frac{m\pi}{2}\left(\frac{2y}{b}+1\right)\right] \\ \chi_{n0}(x,y) &= \chi_{0n}(-x,y) \\ \text{where} \quad k^2 &= K_m^2 + \left(\frac{m\pi}{b}\right)^2 \quad . \end{aligned} \tag{5.29}$$

In (5.29) the expansion coefficients R_{nm} are given by

$$R_{nm} = \begin{cases} \frac{4n(-1)^{(m+1)/2}}{\pi\sqrt{b}} \frac{\cos[m\pi/(2b)]}{(m/b)^2-n^2} & (n, m \text{ odd}) \\ \frac{4n(-1)^{m/2}}{\pi\sqrt{b}} \frac{\sin[m\pi/(2b)]}{(m/b)^2-n^2} & (n, m \text{ even}) \\ 0 & \text{otherwise} \quad . \end{cases} \tag{5.30}$$

Whereas the interior cavity matrix elements for the right angle bend are expressed as a single term (*viz.*, (2.48)), those for the quantum dot are expanded in an infinite series. The **A** and **B** matrix elements are straightforwardly calculated from the cavity functions using (2.31). One obtains

$$\begin{aligned} A_{nm} &= \sum_{r=1}^{\infty} R_{nr} R_{mr} \frac{K_r}{\sin(2K_r a)} \\ B_{nm} &= \sum_{r=1}^{\infty} R_{nr} R_{mr} \frac{K_r}{\tan(2K_r a)} \quad . \end{aligned} \tag{5.31}$$

With the matrices **A** and **B** given by (5.31), the transfer matrix **M** can be constructed from the steps derived in Sect 2.1.4. The bound state and transmission properties can then be calculated using the transfer matrix elements. In the next chapter the transmission properties will be studied in detail for the case of the "*quantum dot superlattice*," which results when a number of identical quantum dots are connected in series.

[8] Note that modes which have even parity correspond to odd transverse channel indices, and vice versa.

If one examines the quantum probability current $\mathbf{j}$ defined in (3.26) for a quantum dot, one expects to see substantial vortex formation associated with sharp structure in the transmission probability. This should be especially noticeable in the vicinity of zeroes in the transmission. Lent [99] showed that a system with a cross, or a single quantum dot, showed strong vortex formation at the minima in the transmission. Berggren *et al.* [100] examined quantum probability flow in a tube with a quantum dot, and found regions of laminar flow, as well as regions where the flow was dominated by formation of large vortices. As has been shown in Sect. 3.2, the vortex structure can be quite complex, and the direction of rotation around a vortex tends to change sign as one passes through a deep minimum in transmission. This was observed by Berggren *et al.* [100] in studies of vortex behavior for the quantum dot.

However, Berggren and collaborators also found that significant vortex formation, and rapid reversal of flow around the vortices, was occasionally associated with a maximum in the conductance through a single quantum dot. This behavior had previously been observed by Lent [99]. An example of this is shown in Fig. 5.31 (this is the second color plate), which plots the probability density for a state which is associated with a prominent and very sharp peak in the conductance. The dimensions of the quantum dot are $w = 2a = 100$ nm, and $b = 200$ nm. In this figure, the region with highest probability is colored dark red and the lowest probability region is colored magenta. At this energy, a standing wave with 2 1/2 wavelengths forms in the cross, as is evident from Fig. 5.31. The inset at right shows the conductance vs. energy for this structure. The energy corresponding to this plot, $E = 3.935$ meV, is denoted by the boundary between the red and blue regions. The formation of the standing wave produces a very narrow resonant peak in the conductance.

Figure 5.32 plots the quantum probability current of (3.26) (this is the third color plate). The energy is $E = 3.934$ meV, which for the dimensions of this wire is just below the conductance peak. The directions of the arrows denote the direction of $\mathbf{j}$ at each point. The current enters the quantum dot at the left of the figure, and exits to the right. The largest value of $\mathbf{j}$ is denoted by violet, and the smallest value of $\mathbf{j}$ is denoted by blue. Eight vortices can be seen in the probability current; the vortices form symmetric pairs on opposite sides of the central axis of the wire. Comparing Fig. 5.32 with Fig. 5.31, it is seen that the vortices are centered at the zeroes of the probability density. Despite the significant number of vortices and stationary points in Fig. 5.32, the transmission is quite large. The figure shows that a significant amount of the flux is transmitted around the vortices and through the center of the wire.

In Fig. 5.33, the fourth color plate, the energy $E = 3.937$ meV is just above the conductance peak. Although the increase in energy from Fig. 5.32 to Fig. 5.33 is only 0.003 meV, the direction of flow around each vortex has reversed. Thus, for some states very large vortex formation can be associated with

conductance maxima. Just as for vortex flow across a zero in conductance, the direction of flow around each vortex reverses itself over a very small energy interval. The reversal in vortex flow occurs as the energy passes the position of the sharp resonance. The detailed behavior of the vortices is quite complicated in this region. With very small increase in energy, new vortices with opposite direction of rotation appear, producing the pattern seen in Fig. 5.33. Note that at this higher energy, the transmitted flux flows around the top and bottom of the "cross," and then is squeezed to the center of the wire in passing around the two vortices furthest to the right in this figure.

5.4 Structures with Two Coupled Cells

We have now discussed binding and scattering through a variety of 2-D systems with a single cell (*i.e.*, a bend or cavity). From the discussion in Sect. 2.1.4, one can describe scattering in a structure with two identical cells in series, by first calculating the transfer matrix for a single cell, and then multiplying this transfer matrix for each of the two cells. In the following chapter this procedure will be extended to study binding or transmission processes for a series of N identical cells.

This section will investigate systems with two coupled cells; as an example, we first consider systems with two coupled bends. It will be shown how the same qualitative arguments which were applied to structures with a single bend can predict the number of bound states, their binding energies and properties of the eigenfunctions in double bend systems. In this way one can obtain a qualitative pictures of transmission and probability flow in double bend systems. To test these results, we will construct waveguides with double bends, find the frequencies of the confined EM modes, and map out the EM energy densities, using the methods outlined in preceding sections. The properties determining the electron conductance in double bend quantum wires of finite length are reviewed, and theoretical predictions will be compared with experimental measurements by Wu *et al.* [66, 152].

Many of the properties of bound states and transmission could be predicted from analogy with other physical systems. For example, if one has a pair of identical bends or cavities connected by a very long straight section, then one would expect the number of bound states, and their energies, to be nearly identical to those for an isolated cell. Sharp resonance structure will also be observed in double-bend systems, for energies which accommodate an integral number of standing waves inside the tube. Such resonances are analogous to the standing-wave resonances for sound waves in a tube open at both ends.

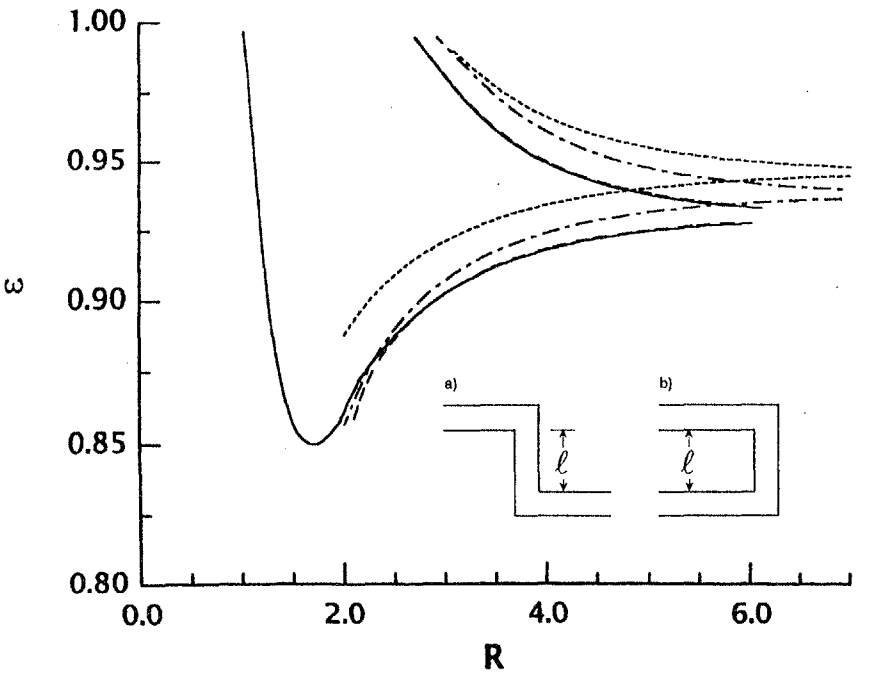

Fig. 5.19. [Inset: schematic picture of systems with two right-angle bends, separated by a distance l. (a) "Step" double bend tube. (b) U-shaped double bend. (Note: for structures with unit channel width, the aspect ratio $R = \ell + 2$).] Bound state energies for a double bend as a function of the aspect ratio R. Upper curves are for antisymmetric bound states; lower curves are for symmetric bound states. Solid lines: exact energies $\epsilon = E_b/\pi^2$ for bound states in step double bend tube. Dashed lines: exact bound state energies for U-shaped double bend system. Dot-dashed lines: energies predicted by square-well approximation. Dotted lines: SMA approximation to bound state energies

5.4.1 Bound States in Systems with Two Coupled Cells

In this section, we examine the number of bound states in a tube with two identical cells in series. We will limit ourselves to the case where each cell will support a single bound state. As specific examples, we examine the case of tubes which contain two right angle bends, shown schematically in Fig. 5.19. Graph (a) shows the case of the "step" double bend case, while graph (b) shows the "U" shape double bend system. The next chapter will consider the case of systems composed of a number of identical cells in series. Following the notation of [28], we call a structure with a series of steps a "*staircase*" configuration, and a system with a series of U bends will be called a "*snake*" tube. In Sect. 2.1.5 and Sect. 3.1.1 the bound state and transmission prop-

erties, respectively, were derived for a system with a single right angle bend. When the external leads are rescaled to unit width, the binding energy for a tube with two right-angle bends depends only on the aspect ratio R, the ratio of the total height of the tube to the width of the legs. When the external legs of the system are rescaled to unit width, the aspect ratio R is related to the quantity l, the length of the straight section between unit square bends shown in Fig. 5.19, by

$$R = l + 2 \ . \tag{5.32}$$

The transfer matrix for the double bend system is obtained by multiplying the transfer matrices for each component cell. The transfer matrix for a given cell can be written as

$$\mathbf{M} = \mathbf{U}^{-1}\mathbf{V}\mathbf{F} \ , \tag{5.33}$$

where the matrices $\mathbf{U}$ and $\mathbf{V}$ are given in (2.36). For the snake tube, $\mathbf{F}$ in (5.33) is the unit matrix. For the staircase system, the matrix $\mathbf{F}$ has the form

$$\mathbf{F} = \begin{pmatrix} f & 0 \\ 0 & f \end{pmatrix} ; \quad f_n = (-1)^{n+1} \ . \tag{5.34}$$

In Sect. 2.1.5, the transfer matrix equations were derived for two-dimensional systems. It was shown that, for bound states and low-energy transmission, useful insight could be obtained using the single-mode approximation [SMA], which truncates the expansion in transverse modes to include only the lowest channel. As an example of the validity of this approximation, SMA estimates will be derived for the location of bound states in a structure with two right angle bends. The "*unit cell*" in this case is a unit square coupled to a straight section of length l. Since this cell is symmetric about its center, all observables can be written in terms of two auxiliary matrices, since $B' = B$ and $A' = A$ in (2.31) [9]. In the SMA, the transmission matrix $\mathbf{M}^{(2)}$ through two identical cells in series can be related to the transmission matrix $\mathbf{M}$ through a single cell by

$$\mathbf{M}^{(2)} = \frac{1}{\sin(\phi)} \left[\sin(2\phi)\mathbf{M} - \sin(\phi)\mathbf{I}\right] \ . \tag{5.35}$$

Equation (5.35) follows since the matrix $\mathbf{M}^{(2)}$ is formed by multiplying the matrix $\mathbf{M}$, a 2×2 matrix with unit determinant, by itself.

From (5.35) the transmission amplitude $t^{(2)}$, for elastic scattering through two cells in the lowest transverse channel, is related to the scattering matrix for a single cell by

$$\left[\mathbf{M}^{(2)}\right]_{11} = \frac{1}{t^{(2)}} = \frac{1}{\sin(\phi)} \left[\sin(2\phi)\mathbf{M}_{11} - \sin(\phi)\right]$$

[9] The following equations assume that the cells are symmetric with respect to reflection about a line through their center. The extension to asymmetric cells is straightforward.

$$= 2\cos(\phi)\mathrm{M}_{11} - 1 = \frac{2\cos(\phi)}{t^{(1)}} - 1 \ ,$$

$$\text{where} \quad \mathrm{M}_{11} = \exp(-i\alpha\, l)\left[\frac{B}{A} - \frac{i\,(A^2 - B^2 + \alpha^2)}{2\,\alpha\, A}\right] \ . \qquad (5.36)$$

In (5.36), $\left[\mathbf{M}^{(2)}\right]_{11}$ and $\mathrm{M}_{11} = 1/t^{(1)}$ are the (11) elements of the transfer matrix for two cells in series and a single cell, respectively. B and A denote the matrix elements $\mathbf{B}_{11}$ and $\mathbf{A}_{11}$, respectively, and $\alpha = \alpha_1$. Note that in SMA, both the "*step*" and "*U*" double bend systems have the same transmission amplitude, since when one includes only the lowest transverse mode, $\mathbf{F}$ is just the 2×2 unit matrix. The quantity ϕ in (5.36) is the *Bloch angle*, which is related to the transfer matrix and the auxiliary matrices by

$$\cos(\phi) = \frac{1}{2}\mathrm{Trace}[\mathbf{M}] = \cos(\alpha\, l)\frac{B}{A} - \sin(\alpha\, l)\frac{(A^2 - B^2 + \alpha^2)}{2\,\alpha\, A} \ . \qquad (5.37)$$

The condition for bound states in a system of two cells is

$$\left[\mathbf{M}^{(2)}\right]_{11} = 0 \ . \qquad (5.38)$$

The bound states of (5.38) will occur below continuum threshold, where the longitudinal momentum in the lowest channel is imaginary, *i.e.*

$$\alpha = i|\alpha| = i\sqrt{\pi^2 - k^2} \ . \qquad (5.39)$$

From (5.36) and (5.37) it is straightforward to show that the bound state SMA condition, for two cells connected in series and separated by a straight section of length l, is

$$(B + |\alpha|)^2 - A^2 = \pm\exp(-|\alpha|\, l)\,|A^2 + |\alpha|^2 - B^2| \ . \qquad (5.40)$$

As the tube is symmetric with respect to reflection about its midpoint, the lower-energy bound state, corresponding to the (+) root in (5.40), will have a wave function which is symmetric with respect to reflection, while the higher energy bound state (the (−) root in (5.40)) will be antisymmetric.

The SMA estimate for the bound state energies can be calculated directly in certain limiting cases. In the limit $l = 0$, (5.40) gives

$$(B + |\alpha|)^2 - A^2 = \pm|A^2 + |\alpha|^2 - B^2| \ . \qquad (5.41)$$

For the case of a tube consisting of two right angle bends, it was shown in Sect. 2.1.5 that the matrices A and B for a right angle bend system could be given analytically in the SMA, *e.g.* from (2.49),

$$A = \frac{2\pi^2}{\pi^2 - \alpha^2} \ ; \quad B = \alpha\cot(\alpha) \ . \qquad (5.42)$$

In this case the bound state energies can be easily calculated, and one finds that when $l = 0$ the SMA predicts a symmetric bound state with energy $\epsilon_s^{(1)} = E_s/\pi^2 = 0.887$. The SMA predicts that the antisymmetric state is not bound, as its energy gets pushed up into the continuum, and (5.41) has no solution when the right hand side is negative.

In the limit as $l \to \infty$, when the straight section joining the bends grows without limit, (5.40) gives the bound state condition

$$(B + |\alpha|)^2 - A^2 = 0 \ . \tag{5.43}$$

This condition is identical for both symmetric and antisymmetric states; furthermore, it is the same condition as (2.44) for a single cell. Thus, as the length of the straight section increases, the symmetric and antisymmetric bound state energies both should approach the energy for a single bend. In the limit of large l, the bound state wave functions are small everywhere except in the bends. The only difference between the symmetric and antisymmetric bound state wave functions, in the large l limit (or equivalently, the limit of large R) is that for the antisymmetric state the wave function will have opposite sign in the two bends. As $l \to \infty$, the symmetric and antisymmetric bound state energies should approach asymptotically the energy of the bound state for the L-shaped system, or $E_b = 0.929\,\pi^2$.

Figure 5.19 plots the bound state energies for the double bend structures, as a function of the aspect ratio R. The energies are plotted as ratios of the bound state energy to the continuum threshold, $\varepsilon = E_b/\pi^2$. The lower (upper) solid lines are the exact results for the symmetric (antisymmetric) bound states for the step double bend. The dashed lines are the exact results for the U double bend. The lower (upper) dotted curves are the symmetric (antisymmetric) bound state predictions in single-mode approximation, for $l > 0$ ($R > 2$) [10]. From Fig. 5.19 one sees that all qualitative features of the SMA predictions are fulfilled. The exact bound state energies for the step and U systems are very similar. With increasing l, the symmetric and antisymmetric bound state energies approach the same result, the bound state energy for a single right angle bend. For $l = 0$, the exact symmetric bound state energy is $\epsilon_s(l = 0) = 0.861$, as compared to the SMA estimate $\epsilon_s^{(1)}(l = 0) = 0.887$. For small values of the straight section, $l < 0.6$ ($R < 2.6$), the antisymmetric state is pushed into the continuum, just as predicted by the SMA. The antisymmetric state then becomes a quasi-bound state. For systems with many bends, if the straight sections between the bends are sufficiently short, several of the states will be pushed up into the continuum. This will be seen in Chap. 6.

Although the "U" double bend is only defined for $l > 0$, the "step" double bend is defined for $l > -1$. However, for $l < 0$ (alternatively, $R < 2$)

[10] In the single-mode approximation, the step and U double bend bound state energies are identical.

neither the SMA estimate nor the effective square well interaction give reliable quantitative estimates for bound state energies in this geometry. For these cases, Sprung [153] has shown that one can produce effective potentials with other geometries than square wells. For example, one could produce an effective potential of triangular shape which gives a good approximation to a tube with a single L-bend. When applied to a system with two steps and $1 \leq R < 2$, reasonable estimates of bound state energies can be obtained by combining two of the triangular effective interactions.

Although qualitatively the SMA predictions for the double bend system are in excellent agreement with exact results, the SMA estimates shown in Fig. 5.19 are not quantitatively correct. The SMA predicts a higher value than the exact result for the bound state energy in the single bend L-shaped structure. For a tube with a single bend, the difference between the SMA prediction $\epsilon^{(1)}$ and the exact bound state energy ϵ_b is

$$\delta\epsilon = \epsilon^{(1)} - \epsilon_b = 0.946 - 0.929 = 0.017 \ . \tag{5.44}$$

The SMA predictions for bound state energies in the double-bend system are also too high, for all values of l. However, if the SMA estimates for the double-bend system are corrected by subtracting off $\delta\epsilon$, the energy overestimate for the single-bend structure, there is very good quantitative agreement between the SMA and exact results in the double-bend system, for all values $l > 0$ and for both symmetric and antisymmetric states. This can be seen by shifting downward the dotted curves in Fig. 5.19 so that the curves line up with the solid curves in the limit of large R.

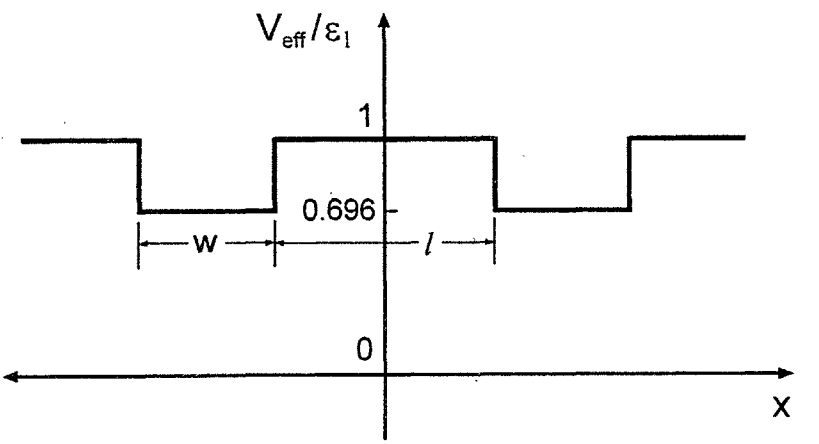

Fig. 5.20. Effective one-dimensional potential for the double-bend system, using the single-mode approximation of [138]. The potential is renormalized so that it has the value 1 in the straight sections of the tube. The effective square well potential is the same for both step and U geometries (inset in Fig. 5.19)

In Sect. 2.1.4 it was demonstrated that a bend in a system produces an effective potential which can be approximated by an attractive square well. Thus, in a tube with two right angle bends, each corner can be regarded as the site of an effective one-dimensional square well. The effective square well model of Wu, Sprung and Martorell [28] provides a convenient qualitative picture of binding in such systems. Figure 5.20 shows the effective one-dimensional square well potential for the double bend system. The potential parameters in single-mode approximation are given in (2.51). In each bend there is a square well of depth 3, and the effective potential has the value π^2 in the straight sections of the tube. Renormalizing the potential to have unit magnitude in the straight sections, the potential in each bend is $1-3/\pi^2 \approx 0.696$. The two wells are separated by distance $l = R-2$, in terms of the aspect ratio R for the double bend system [11]. The effective square well model also predicts the same binding for the "step" and "U" double bend structures, just as the SMA.

The lower (upper) dot-dashed curves in Fig. 5.19 are the effective square well approximations for the symmetric (antisymmetric) bound state energies. The square well approximation gives a reasonably accurate prediction for the bound states; however, at large aspect ratio R the square well predictions are too large. The difference between the square well prediction for the single bend L-shaped tube and the exact bound state energy is

$$\delta\epsilon_{sw} = \epsilon_{sw} - \epsilon_b = 0.938 - 0.929 = 0.009 \quad . \tag{5.45}$$

If the square well predictions are shifted down by $\delta\epsilon_{sw}$, they give rather accurate quantitative values for the double bend bound state energies. After shifting the square well energies, the effective square well predicts that for $R < 2.6$ the antisymmetric state will move into the continuum, in good quantitative agreement with the exact results.

Figs. 5.21b and 5.21c show contour plots of the exact symmetric and antisymmetric bound state wave functions for the case $R = 3$, calculated by Carini *et al.* [133]. From Fig. 5.19, the bound state energies differ significantly for this aspect ratio. The contour plots are lightest in regions where the wave function is large and positive. The shading becomes darker as the value of the wave function decreases. In 5.21b the wave function is always positive, and goes to zero at the transverse boundaries of the tube, and at large distances from the bends of the system. In both cases the wave function has a peak at each bend. The antisymmetric bound state wave function has a node in the center of the structure, so the two peaks have opposite sign, in contrast to the symmetric state where the peaks have the same sign in both bends. As the aspect ratio R decreases, the interaction between the bound states pushes the antisymmetric bound state energy up rapidly, relative to the symmetric

[11] When $l = 0$ the two square wells touch, producing an effective square well with the same depth and twice the width of each single well.

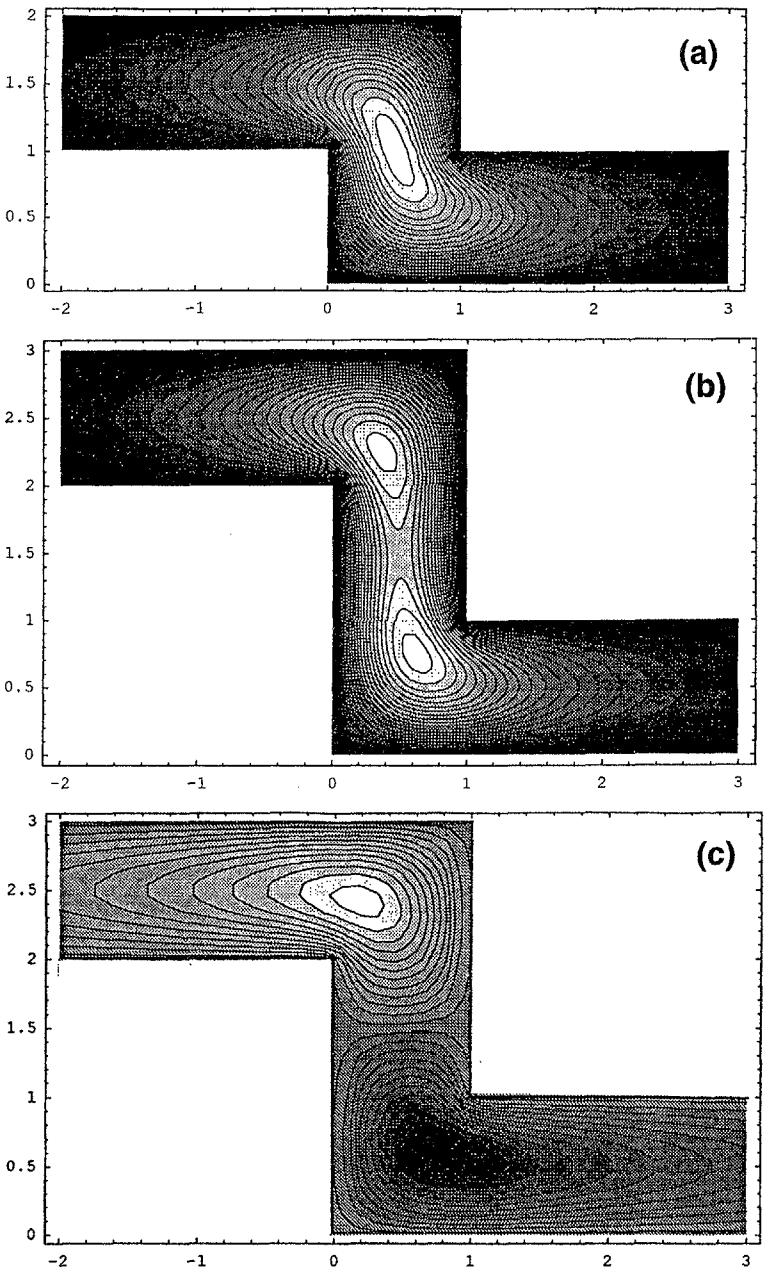

Fig. 5.21. Calculated contour plots for bound state wave functions in a long step double bend tube. (a) Bound state wave function (symmetric), for aspect ratio $R = 2$. (b) Symmetric bound state, with aspect ratio $R = 3$. (c) Antisymmetric bound state, with aspect ratio $R = 3$. Maximum positive values have lightest shading. The shading becomes progressively darker as the value of the wave function decreases

bound state, so that for $R \approx 2.6$, the antisymmetric state becomes a quasi-bound state and moves into the continuum.

For $1 < R < 2.6$ the step double bend structure has only one symmetric bound state. Figure 5.21a shows a contour plot of the bound state wave function for $R = 2$. This has only a single peak in the center of the structure. Figure 5.19 shows that as R is decreased from 2, the eigenenergy of the symmetric bound state continues to decrease until it reaches a minimum energy $E_b = 0.852\,\pi^2$ at $R = 1.69$. With further decrease in R, the bound state energy increases (*i.e.*, the binding energy decreases), and as $R \to 1$ the bound state energy approaches the continuum threshold value $E_1 = \pi^2$.

As was discussed in Sect. 4.3, the bound state energies in curved tubes can be located by constructing a curved waveguide with the same geometry and finding the sub-cutoff confined EM modes. A double bend waveguide structure was constructed with a shape shown schematically in Fig. 5.30 [133]. Using this apparatus, the aspect ratio $R = H/W$ could be varied continuously over the range $1 < R < 6$. This device was used to measure the frequencies corresponding to the confined modes (bound states), and map the electromagnetic energy densities for these confined modes. The confined modes occur at frequencies corresponding to sharp drops in the reflected power, as was discussed in Sect. 4.3.

Figure 5.22 plots the experimental values for the symmetric and antisymmetric waveguide confined mode frequencies (*i.e.*, bound state eigenvalues) as a function of the aspect ratio R [133]. The experimental results are shown by data points, and the curve represents the theoretical predictions from Fig. 5.19. A symmetric bound state is seen below the cutoff frequency (f_{co}, indicated by the solid horizontal line) for all values $R > 1$. Antisymmetric bound states are observed for $R \geq 3$ [12]. For large values of R the symmetric and antisymmetric frequencies approach each other closely, as predicted in Fig. 5.19. The symmetric confined mode frequency has a minimum at $R \approx 1.7$ (compared with the theoretical prediction $R = 1.69$), and then rapidly increases to the cutoff frequency as $R \to 1$. The shapes of the theoretical curves and a line drawn through the data points in Fig. 5.22 are nearly identical.

The field distribution for the bound states was mapped out for a few representative values of R, using the two-dimensional mapping technique of Maier and Slater [130], as reviewed in Sect. 4.3. The resonance was perturbed with a 1/8" diameter steel ball located at a known position within the waveguide bend. The relative change in the resonant frequency of the confined mode, $\Delta f(x,y)/f_0(x,y)$, was measured as a function of the position of the ball, and compared with the theoretical prediction of (4.12).

Figure 5.30 shows results of field mapping for the symmetric bound state, in a step double bend waveguide with aspect ratio $R = 3$. Red shading de-

[12] The antisymmetric state could not be located for $R < 3$ (numerical calculations predict antisymmetric bound states for $R \geq 2.6$). However, the observed bound state energies are in good agreement with theoretical predictions.

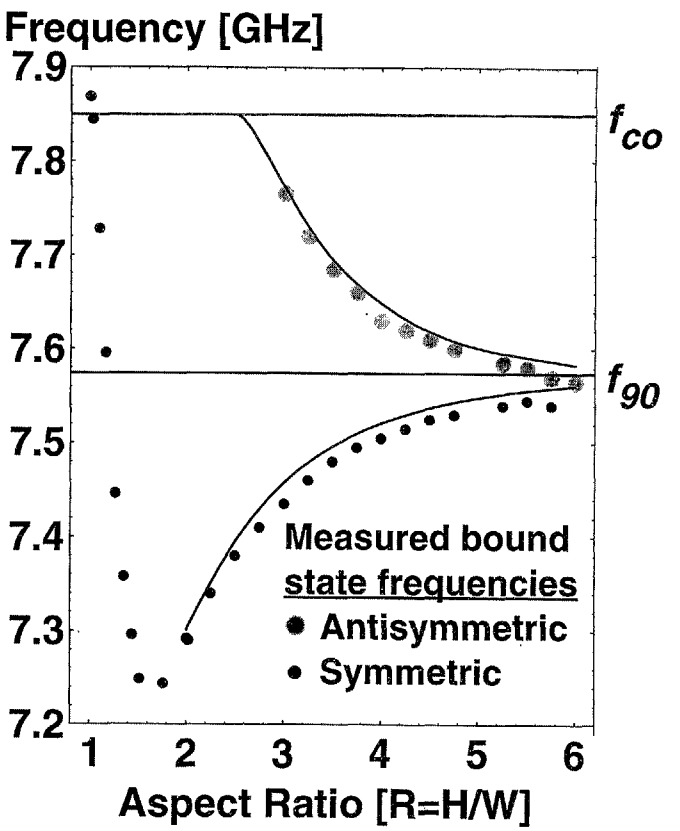

Fig. 5.22. Bound state frequencies as a function of aspect ratio $R = H/W$ in the step double bend waveguide (graph (a) of Fig. 5.19). The symbols represent the experimental results for the symmetric (black circles) and antisymmetric bound states (gray circles). The lines represent the theoretically determined resonant frequencies calculated from the bound state energies from Fig. 5.19 and the threshold energy E_{th} for free propagation: $f_{\mathrm{bd}} = f_{\mathrm{co}}\sqrt{E_b/E_{th}}$

notes negative frequency shift (large electric energy density), and blue denotes positive frequency shift (large magnetic energy). The E-field for this mode has a peak in each bend, and decreases exponentially along the legs of the waveguide, as is shown in Fig. 5.21b. The largest magnetic energy density occurs where the surface current densities are greatest near the adjacent side walls of the waveguide, and also near the location of the antenna, on the left waveguide section. Figure 5.30b shows the experimental results. Figure 5.30a shows the theoretical calculations for the resonant frequency shift using (4.12) with $r^3/(DW^2) = 1/576$ and choosing the adjustable parameter $c_0 = 2.46$. There is generally excellent quantitative and qualitative agreement

between theory and experiment. Equally good agreement was obtained for the antisymmetric bound state with this geometry [22].

5.4.2 Transmission Through a System with Two Coupled Cells

In this section we will review transmission properties for particles passing through a structure with two identical cells in series. As an example, we will examine the case of a tube with two coupled bends. The following section will compare theoretical calculations with experimental measurements of electron conductance in quantum heterostructures. This discussion will focus on the qualitative features of the amplitudes $\mathcal{T}$ for transmission through a 2-D tube with two cells.

A good qualitative picture is obtained from the single-mode approximation to the transfer matrix, for two identical cells in series. From Sects. 2.1.4 and 5.4.1, in SMA the transmission amplitude $\mathbf{M}^{(N)}$ through N identical cells has the form

$$\mathbf{M}^{(N)} = \frac{1}{\sin(\phi)} \left[\sin(N\phi)\,\mathbf{M} - \sin((N-1)\phi)\,\mathbf{I}\right] \quad . \tag{5.46}$$

From (5.46), it is straightforward to calculate the SMA approximation to the transmission and reflection amplitudes for a structure with N identical cells,

$$\begin{aligned} \left[\mathbf{M}^{(N)}\right]_{11} &= \frac{1}{t^{(N)}} = \frac{1}{\sin(\phi)} \left[\sin(N\phi)\,\mathbf{M}_{11} - \sin((N-1)\phi)\right] \quad , \\ \left[\mathbf{M}^{(N)}\right]_{21} &= \frac{r^{(N)}}{t^{(N)}} = \frac{\sin(N\phi)}{\sin(\phi)}\mathbf{M}_{21} = \frac{\sin(N\phi)}{\sin(\phi)} \left(\frac{r^{(1)}}{t^{(1)}}\right) \quad . \end{aligned} \tag{5.47}$$

In (5.47), $t^{(N)}$ and $r^{(N)}$ are respectively the transmission and reflection amplitudes through N identical cells, in the lowest transverse channel. Similarly, $t^{(1)}$ and $r^{(1)}$ are the transmission and reflection amplitudes for a single cell. The quantities $\left[\mathbf{M}^{(N)}\right]_{11}$ and $\mathbf{M}_{11}$ in (5.47) are the (11) transfer matrix elements for N cells and one cell, respectively, and ϕ is the Bloch angle given by (5.37). For a system with two cells ($N = 2$), (5.47) reduces to

$$\begin{aligned} \frac{1}{t^{(2)}} &= 2\cos(\phi)\,\mathbf{M}_{11} - 1 \quad , \\ \frac{r^{(2)}}{t^{(2)}} &= \frac{\sin(2\phi)}{\sin(\phi)} \frac{r^{(1)}}{t^{(1)}} \\ \frac{1}{T^{(2)}} - 1 &= \frac{|\sin(2\phi)|^2}{|\sin(\phi)|^2} \left(\frac{1}{T^{(1)}} - 1\right) \quad . \end{aligned} \tag{5.48}$$

In (5.48), $T^{(1)}$ ($T^{(2)}$) are the transmission probabilities through a single cell and two cells, respectively, for energies below the opening of the second transverse mode. From (5.48) one can make a number of predictions regarding

transmission through two identical cells. Although these results are only true in SMA, they will be seen to give generally reliable results, until the energy approaches the opening of the second transverse mode.

- Whenever there is 100% transmission through a single cell ($T^{(1)} = 1$), there will also be 100% transmission through two cells at the same wave number. If a single cell is completely transparent, then it makes sense that no reflection will occur when a number of identical cells are combined in series.
- There will also be 100% transmission through two cells for any wave number where $\sin(2\phi) = 0$. This is just the condition that allows the structure to accommodate an integer number of standing waves. In SMA, there will be complete transparency whenever this condition is satisfied. This is the analog of the condition for sound wave resonances in a tube open at both ends.
- If the transmission through a single cell is zero, ($T^{(1)} = 0$), the transmission through two cells will be zero at the same wave number. This can be seen by inspection from (5.48). This stands to reason since if there is complete reflection through a single cell at some energy, there will be no incident flux left to transmit through any additional cells coupled in series.
- Whenever $|\cos(\phi)| > 1$, one has $T^{(2)} < T^{(1)}$. For these wave numbers, there is no allowed path for a particle through the system. The wave function will be exponentially damped in crossing a single cell, therefore the probability of transmission through two cells will be less than the transmission probability for a single cell. In fact, from (5.48) we can make the stronger statement that $T^{(2)} < T^{(1)}$ whenever $|\cos(\phi)| > 1/2$, that is, the transmission orobability through two cells will be smaller than transmission through a single cell in parts of the "allowed" region as well.
  The only exceptions to this statement occur at points where there is 100% transmission through a single cell ($T^{(1)} = 1$), or 100% reflection through a single cell ($T^{(1)} = 0$). In both of these cases, $T^{(2)} = T^{(1)}$; we have reviewed these special cases in the preceding bullet points.

Figure 5.23 shows the transmission probability through a system with two right angle bends. The "cell" in this case is a unit square coupled to a straight section with length $l = 4$. The upper curve in Fig. 5.23 is the Bloch phase $\cos(\phi)$. The solid curve in Fig. 5.23 is the exact calculation of Wu and Sprung [80], and the dotted line is the single-mode approximation. As was the case for the single bend, the SMA gives very good qualitative agreement with the exact transmission, except for energies near to the opening of the second transverse mode ($k = 2\pi$)[13].

Figure 5.23 confirms the qualitative features predicted in SMA. First, the transmission through a single cell vanishes at $k \approx 1.88\pi$, and $T^{(2)}$ vanishes

[13] In our calculations, we set $d = 1$ in Fig. 5.23. Also, the quantity T in that figure is $T^{(2)}$ in our notation.

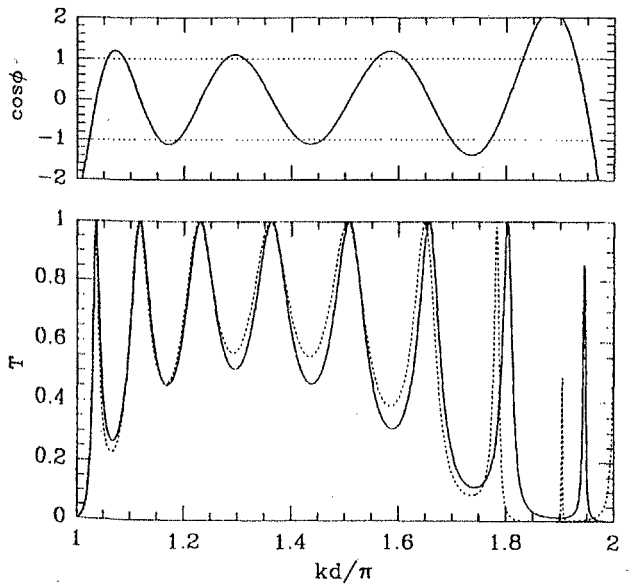

Fig. 5.23. Upper figure: cosine of Bloch phase ϕ from (2.41) vs. k/π. Lower figure: transmission probability T vs. wave number k/π for the step double bend tube with $l = 4$. Solid curve: exact result; dotted curve: single-mode approximation. From [80]

at that same point. Furthermore, minima in $T^{(2)}$ occur when $|\cos(\phi)| > 1$, as predicted. In single-mode approximation, the transmission probability $T^{(2)}$ must be one whenever the single-cell transmission probability is one. For a single right-angle bend, the transmission probability below the second transverse mode is never one, as can be seen from Fig. 3.1. Figure 5.23 confirms that the transmission probability $T^{(2)}$ for the double bend is one whenever $\cos(\phi) = 0$.

These maxima in transmission arise due to formation of longitudinal standing waves in the tube. One way to see this is to rewrite the Bloch phase as [80]

$$\begin{aligned} \cos(\phi) &= \rho \cos(\alpha_1 l + \theta) \\ \rho &= \frac{\sqrt{(2\alpha B)^2 + (A^2 - B^2 + \alpha^2)^2}}{2\alpha |A|} \\ \tan(\theta) &= \frac{A^2 - B^2 + \alpha^2}{2\alpha B} \quad . \end{aligned} \tag{5.49}$$

The condition for a zero in $\cos(\phi)$, and hence for a maximum in $T^{(2)}$ in SMA, is

$$\alpha l + \theta = (n + 1/2)\pi \quad , \tag{5.50}$$

i.e. that an integral number of half-waves can be accommodated in the tube at that energy. The SMA is generally valid up to the opening of the second transverse mode, which occurs at $\alpha = \sqrt{3}\pi$. Consequently, the number of additional maxima in the transmission through two cells, due to vanishing of the cosine of the Bloch phase in this energy region, should be

$$N_{\max} = \mathrm{Int}[\sqrt{3}\, l + \Delta\theta/\pi] \ . \tag{5.51}$$

$N_{\max}$ in (5.51) is the largest integer less than the quantity in brackets, where $\Delta\theta$ is the change in the angle θ defined in (5.49) between threshold and the opening of the second transverse mode. If (5.51) is applied to the double bend tube with geometry corresponding to Fig. 5.23, one has $l = 4$, and one can straightforwardly calculate the phase change $\Delta\theta \sim 3\pi/2$. Therefore, the SMA predicts eight maxima in the transmission through two cells up to the second transverse mode. Fig. 5.23 shows that the number of transmission maxima agrees with exact calculations, and for $k/\pi < 1.8$ the locations of the maxima are very close to the SMA predictions.

5.4.3 Electron Conductance in Double-Bend Quantum Wires

The conductance G for electrons through a curved quantum wire is given by the Landauer formula of (3.37), which was derived in Sect. 3.4,

$$G = \frac{2e^2}{h} {\sum}' \mathrm{Tr}(\mathcal{T}^\dagger \mathcal{T}) \ , \tag{5.52}$$

the sum being over the open channels. In the Landauer formula for the conductance, the transmission probability $\mathcal{T}^\dagger\mathcal{T}$ is summed over all energetically accessible channels. Consequently, one should be able to understand the major features of electron conductance through wires with two or more cells, in terms of the transmission amplitudes discussed in the preceding sections. For systems with a single cell, the conductance was observed to have subthreshold peaks arising from tunneling through the bound states in the wire. The conductance exhibited sharp structure associated with the opening of each new transverse mode, and (to the extent that coupling between channels could be ignored) tended to possess "plateaus" in units of $G_0 = 2e^2/h$ after the opening of a given transverse mode. In this section we first review theoretical calculations of electron conductance in simple models of quantum heterostructures, and then compare theoretical predictions with experimental data.

Theoretical calculations of electron conductance typically compute G as a function of the electron energy for fixed geometry. Several groups [66, 104, 127, 154, 155, 156, 157, 158] have examined the conductance for a quantum wire with two right angle bends. Figure 5.24 shows the conductance for a double bend structure (shown in the inset) calculated by Wang [104]. The figure shows G, in units of $2e^2/h$, vs. electron energy E_F in meV, for zero

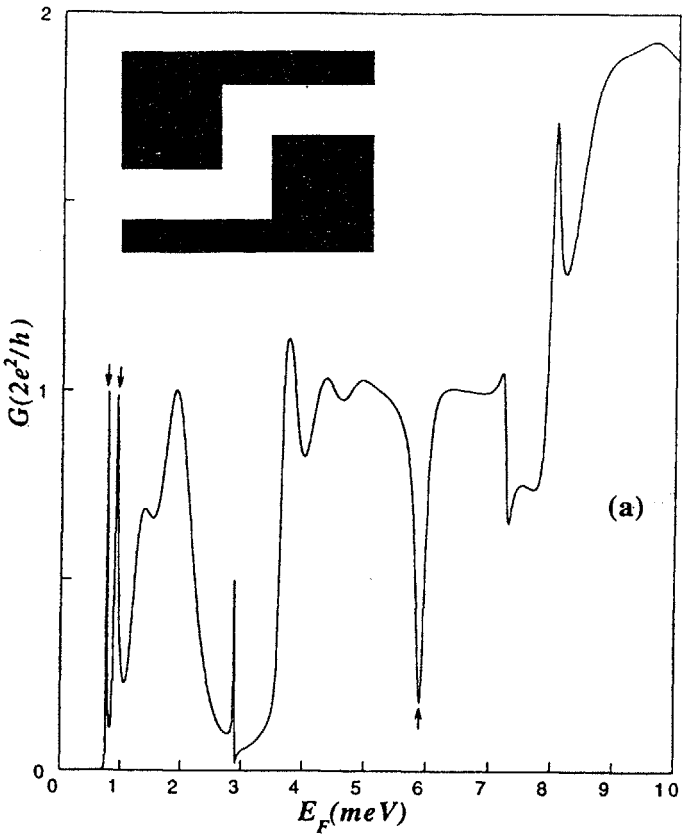

Fig. 5.24. Conductance G in units $G_0 = 2e^2/h$ vs. electron energy E_F for a double bend quantum wire with width $W = 80\,\text{nm}$, external leads of length $L = 70\,\text{nm}$, and aspect ratio $R = 2.5$ (inset). Assuming an effective mass appropriate to a GaAs/AlGaAs heterostructure, the continuum threshold is at $E_{th} = 0.88$ meV. Two sharp peaks near the conductance threshold are noted by downward arrows. These peaks occur at $E_F = 0.77$ meV and 0.93 meV. An upward arrow marks the location of a deep dip in the conductivity, at $E_F = 5.90$ meV. From [104]

temperature electrons in a wire with two right angle bends, coupled to 2DEG reservoirs at each end of the wire. The wire dimensions are: external lead length $L = 70$ nm, width $W = 80$ nm, and aspect ratio $R = 2.5$. Normalized to a wire of unit width, the dimensionless external lead length is 0.875 and the straight section between bends has length $l = 0.5$. For this geometry, assuming an effective mass appropriate for a GaAs system [14], the continuum

[14] For all quantum wire systems considered in this and the following chapter, the electron effective mass is assumed to be $m^* = 0.067m_e$, appropriate for electrons in GaAs/AlGaAs systems.

threshold energy is $E_{th} = 0.88$ meV. The $n = 2$ and $n = 3$ transverse mode thresholds occur at energies $E_2 = 3.51$ meV and $E_3 = 7.89$ meV, respectively.

The following qualitative features are observed in the conductance. First, two very sharp peaks are observed at or below conductance threshold (noted by the arrows pointing downward in Fig. 5.24). Above threshold, the conductance rises rapidly. The maximum of the first conductance plateau is one (in units of G_0), but two or three sharp peaks are observed below the second transverse mode. Just before the opening of each new transverse mode, there is a deep dip in the conductance. This dip gives nearly zero conductance for energies shortly below E_2, and another deep minimum occurs just below the third transverse mode. In the second conductance plateau, there is also some sharp structure but for the most part the conductance is approximately one. After the third transverse mode opens the conductance increases to roughly $1.9 - 2G_0$.

All these features follow from our understanding of the transmission amplitudes. The two peaks below or just at the continuum threshold are due to electron tunneling through the bound and quasi-bound states in the double bend wire [15]. The sharp conductance peaks in the first "plateau," below the opening of the second transverse mode, occur at wave numbers where standing waves can be set up in the wire. Both the number and approximate location can be obtained from the SMA condition $\cos(\phi(k)) = 0$, where ϕ is the Bloch phase given in (5.37). The deep minima in the conductance, seen just before the opening of the second and third transverse modes, are manifestations of the destructive quasi-bound resonances which were discussed in Sect. 3.1.1. This minimum just below the second transverse mode has been observed using microwave studies in a double bend waveguide. Figure 4.3 shows the transmission probability in a waveguide with two bends and an aspect ratio $R = 6$, as a function of the microwave frequency, as measured by Harle [136]. The deep minimum at a frequency near 15 GHz is caused by the quasi-bound state.

For an ideal straight wire, it was shown in Sect. 3.4 that the conductance increased in integer steps of the "quantum" of conductance $G_0 = 2e^2/h$. Although a second conductance plateau appears when the second transverse mode opens, the theoretical conductance G in Fig. 5.24 does not get much larger than one except for the occasional sharp maximum. Similarly, in the third conductance plateau the conductance does not exceed about 1.9 in units of G_0. This occurs because of the substantial channel coupling for the double bend system. A large amount of reflection is caused by the two sharp bends in the wire, and this reflection prevents the conductance from showing the unit jumps typical of more transparent geometries.

[15] From Fig. 5.19, for a double-bend system two bound states will exist when the aspect ratio $R \geq 2.6$. For this structure, with $R = 2.5$, there should be a sub-threshold conductance peak from the bound state, and a conductance peak just above continuum threshold from the quasi-bound state; this is what is observed in Fig. 5.24.

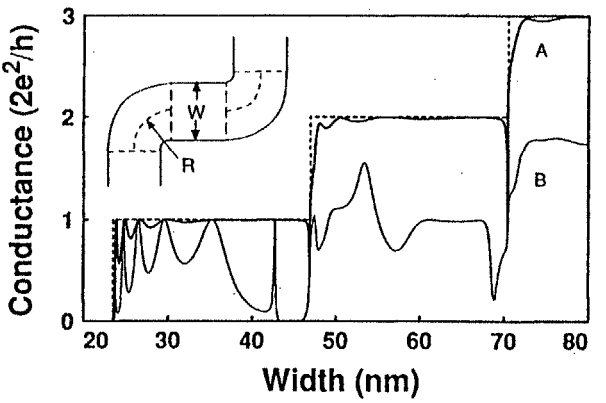

Fig. 5.25. Conductance vs. width for a quantum wire with two 90° bends. Curve A is calculated for a channel with circular bends, as shown in the inset. Curve B is the conductance for the corresponding wire with right-angle corners. From [66]

Wu *et al.* [159] compared electron conductance through quantum wires with two circular bends with 90° bend angle, and wires with two L-shaped bends. Some features of the transmission, such as subthreshold conductance peaks from tunneling through bound states, and quasi-bound states at energies just below transverse mode thresholds, should be qualitatively similar for both geometries. However, one expects the reflection to be much smaller for circular bends than for right angle bends, based on the increased reflection in the L-shaped system. These expectations are borne out in the work of Wu *et al.*. Figure 5.25 shows their calculation of conductance vs. width for zero temperature electrons of fixed energy. Varying the width of the wire for fixed energy electrons has some similarities to varying the wave number k for fixed geometry. There is a minimum value of W, below which no continuum conductance is allowed. New transverse modes become allowed at equal intervals of W. In this calculation the distance L_{cc} between the centers of the two bends was kept constant, and for this graph $L_{cc} = 177$ nm [16].

The lower curve (labeled B) is the conductance for two L-shaped bends, while the upper curve (labeled A) is for two circular bends each with a total bend angle of 90°. For circular bends the conductance exhibits jumps of almost unit magnitude (measured in the fundamental units $2e^2/h$) with the opening of each new transverse mode. The circular bend system is almost reflectionless, so except for small conductance fluctuations just above each transverse mode threshold, the conductance remains almost constant until the opening of the next transverse mode. Extremely sharp and deep dips in

[16] Note that varying the channel width for fixed energy and fixed length between the two bends changes the aspect ratio of the wire.

conductance, due to the destructive quasi-bound resonances introduced in Sect. 3.1, are observed just below each transverse mode opening.

For right-angle bends, the jumps in conductance associated with opening of new transverse modes are much smaller. There is far greater reflection due to the sharp corners. Furthermore, there are pronounced maxima and minima in transmission through the right angle bends, which occur at energies where standing waves can be set up in the wire. These oscillations occur also for the circular bends, but since the single-bend transmission probability is almost one, the relative size of the oscillations is much smaller than for the L-shaped bends. Finally, the quasi-bound state resonances, just below the opening of each transverse mode, produce deep and rather broad minima in the conductance for the L-shaped bends, rather than the very sharp dips seen for circular bends. As was discussed in Sect. 3.1.1, this occurs because for right angle bends the coupling of the quasi-bound states to the open channels is considerably larger than for circular bend systems. As a result the resonance has a significantly greater width for the sharp bend wires, which makes the conductance minimum relatively broad. For the circular bend wire the channel coupling is very weak, which produces a quasi-bound state with an extremely narrow width.

The two sharp conductance peaks below the threshold for continuum transmission (the peaks with downward arrows in Fig. 5.24) arise from electron tunneling through the bound and quasi-bound states in the wire. Wang, Berggren and Ji [127] examined in detail the conductance near threshold, and the influence of quantum wire geometry on these tunneling peaks. Figure 5.26 shows the near-threshold conductance for zero temperature electrons in a quantum wire with two right-angle bends, for five different geometries. In all cases, the structures have external straight leads of length $L = 50$ nm, and wire height $H = 100$ nm. The width W and aspect ratio R of the wire are varied. The system dimensions are listed in Table 5.1, along with the renormalized lead length and aspect ratio. Note that since the width of the quantum wires is varied, the continuum threshold energy E_{th} changes for each different geometry.

Figure 5.26, calculated by Wang, Berggren and Ji [127], shows the near-threshold conductance as a function of the geometry of a quantum wire with two L-shaped bends. This can be understood by reviewing the properties of bound states in such systems, as was discussed in Sect. 5.4.1. For aspect ratio $R \geq 2.6$, a wire with two right angle bends will possess both a symmetric and antisymmetric bound state. However, with increasing aspect ratio, Fig. 5.19 shows that the energies of the two bound states will become more and more identical. At some aspect ratio, the two bound state peaks will coalesce and only a single peak would be observed. For $R = 2.6$, the symmetric state is bound but the antisymmetric state appears right at the continuum threshold. For smaller values of R, only the symmetric state will be bound, and the antisymmetric state will appear as a quasi-bound state in the continuum.

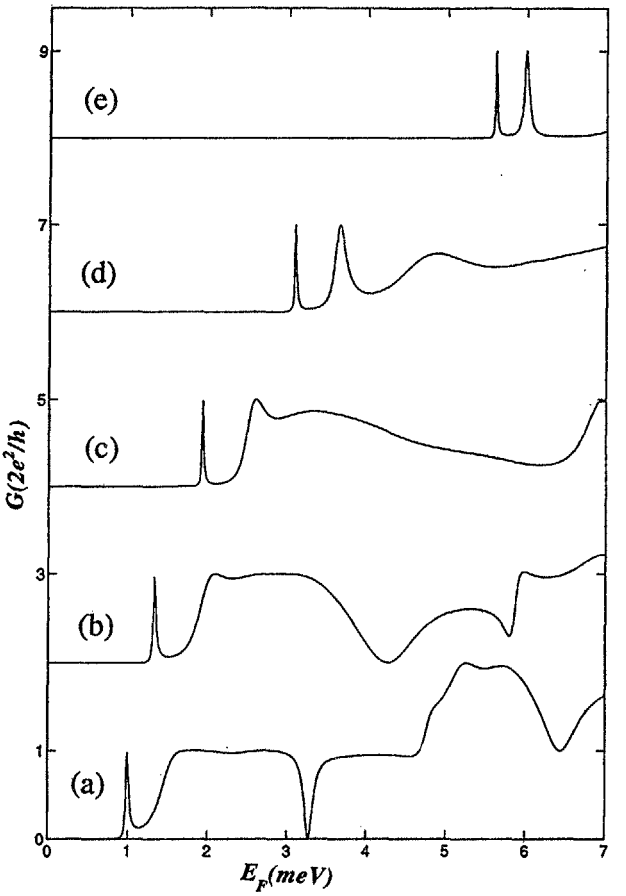

Fig. 5.26. Conductance G (in units $G_0 = 2e^2/h$) as a function of the Fermi energy E_F for a double bend quantum wire (graph (a) of Fig. 5.19). System dimensions and threshold energies are given in Table 5.1. For clarity, each curve is offset vertically by two units in G_0. From [127]

Table 5.1. Dimensions of double bend wires in Fig. 5.28

Wire parameter	a)	b)	c)	d)	e)
height H (nm)	100	100	100	100	100
external lead l (nm)	50	50	50	50	50
width W (nm)	70	60	50	40	30
aspect ratio R	1.43	1.67	2.00	2.50	3.33
renormalized lead	0.714	0.833	1.00	1.25	1.67
threshold E_{th} (meV)	1.45	1.56	2.24	3.51	6.24

These features are observed in the calculated conductance. Curve e in Fig. 5.26e, which corresponds to aspect ratio $R = 3.33$, clearly shows two well separated peaks below the continuum threshold at 6.24 meV. The lower energy peak is the symmetric state and the peak at higher energy is the antisymmetric bound state. For curve d in Fig. 5.26, corresponding to $R = 2.5$, tunneling through the symmetric bound state produces a sharp peak below conductance threshold. The antisymmetric state produces a peak in the conductance at an energy slightly above the continuum, which opens up at 3.51 meV. For smaller aspect ratios, the antisymmetric peak moves up into the continuum, as shown in Fig. 5.26 (c), (b) and (a). For sufficiently small aspect ratio the antisymmetric quasi-bound state merges with the continuum and is no longer visible in the conductance, as can be seen in curve a of Fig. 5.26, which corresponds to aspect ratio $R = 1.43$.

In Sect. 3.5 it was demonstrated that as the electron temperature increases, the zero temperature conductance peaks broaden and eventually disappear. Figure 5.26 is a zero temperature calculation. Wang, Berggren and Ji [127] showed that the width of the subthreshold peaks increased rapidly with increasing electron temperature, and the height of the peaks decreased correspondingly. For example, they showed that for $T = 1.16$ K the height of the lower (upper) peaks in curve e of Fig. 5.26 were reduced by factors of 10 and 5, respectively, from their $T = 0$ values.

Experimental studies have been carried out for quantum heterostructures with a shape which approximates a wire with two right angle bends, by Wu *et al.* [66, 152, 159], and also by Hannan *et al.* [160]. Figure 5.27b shows a scanning electron micrograph of the double bend split-gate structure, and 5.27a gives a schematic picture of the bent system. It looks very similar to the double bend structure shown schematically in Fig. 5.24. As was discussed in Sects. 3.3 and 3.4, one assumes that the quantum heterostructure can be described as a conducting surface with a double bend, connected on both sides by a two-dimensional electron gas (2DEG). In addition, it is assumed that the potential is constant inside the bent wire, that the wire has a sharp boundary with a hard wall potential at the surface, and that the electron transmission is well described in terms of single-particle ballistic motion.

Figure 5.28a shows measurements by Wu *et al.* of conductance vs. gate voltage in the double-bend quantum wire, for three electron temperatures [66]. As was discussed in Sect. 3.3, varying the gate voltage modifies the effective dimensions of the quantum wire. At $T = 100$ mK (curve G1), there are clear "plateaus" in the conductance vs. gate voltage. The plateau structure becomes less pronounced as the electron temperature increases, and at the highest temperature ($T = 4.2$ K, curve G3) the plateau structure has disappeared. As was described in Sect. 3.4, increasing the electron temperature means that the conductance is averaged over progressively larger energy intervals, and this averaging eventually washes out the zero temperature

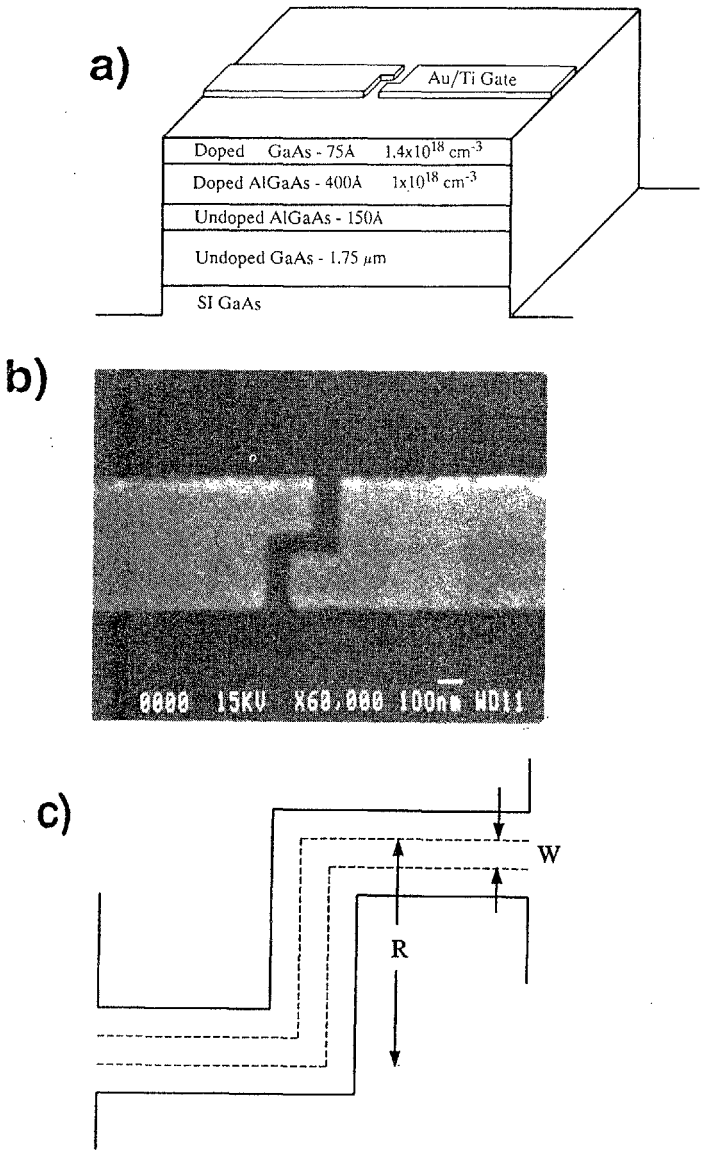

Fig. 5.27. (a) Schematic of epitaxial layer structures and split-gate structure used by Wu *et al.*, [66] to produce double bend constriction. The split gate heterostructure has the same form as shown in Fig. 3.7a. (b) Scanning electron micrograph of double bend split-gate structure. (c) Change in effective width W_e and aspect ratio R_e of double bend constriction with gate voltage. As the gate voltage is made more negative, the effective dimensions of the quantum wire change from the solid to the dashed lines

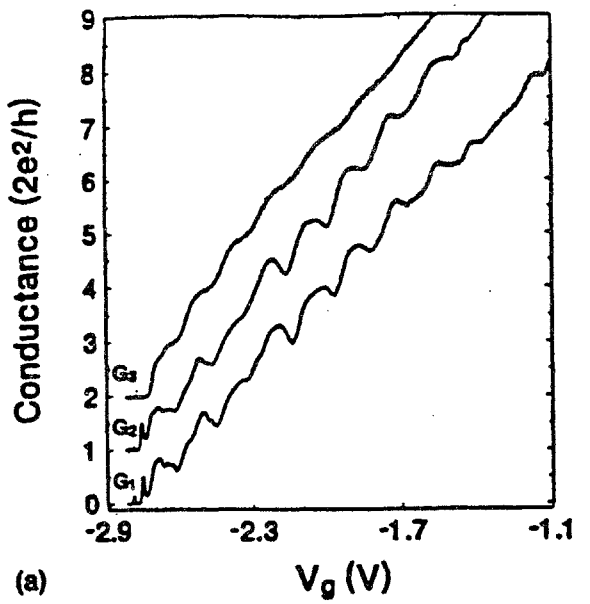

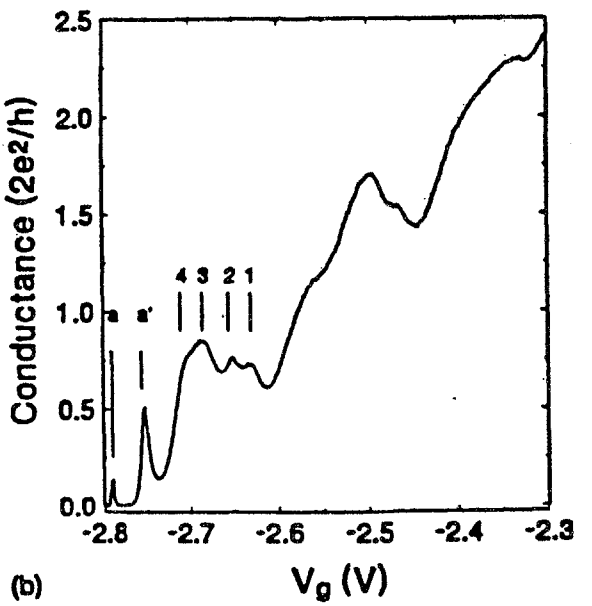

Fig. 5.28. (a) Measurement by Wu *et al.*, [66], of conductance vs. gate voltage V_g for double bend wire shown in Fig. 5.27 at three electron temperatures, 100 mK (G1), 1 K (G2) and 4.2 K (G3). (b) Conductance of sample at temperature 250 mK, in the region of the lowest plateau

structure in the conductance. Figure 5.28b shows an expanded graph of the conductance at temperature 250 mK, in the region of the lowest plateau.

As the gate voltage becomes progressively more negative, the effective width of the quantum wire decreases and the aspect ratio increases, as is shown schematically in Fig. 5.27c (the effective dimensions move from the solid to dashed curves as the gate voltage becomes more negative). For small negative gate voltages, many transverse modes will be open, and one expects that the resulting conductance will be large. As the gate voltage becomes progressively more negative, the effective width decreases, the number of open transverse modes decreases and the conductance should show downward steps. Some gate voltage V_0 will correspond to the threshold for conductance, since at that voltage the effective width $W_e(V_0) = \pi/k_F$ will equal the threshold for continuum transmission through the channel. Except possibly for subthreshold effects arising from tunneling through bound states in the quantum structure, there should be zero conductance for gate voltages more negative than V_0.

The qualitative expectations outlined in the preceding paragraph can be compared to the experimental data shown in Fig. 5.28. Plateaus in the conductance appear at roughly equal intervals of the gate voltage. If the effective channel width is assumed to vary linearly with the gate voltage, this would give qualitative agreement with the experimental data. In fact, from the "width" of the plateaus with respect to the gate voltage, one can estimate the effective width as a function of the gate voltage.

One striking feature of the double-bend electron conductance of Fig. 5.28b is the presence of a peak which appears to be located below the first conductance plateau, and a second peak which is close to, and possibly below, the conductance threshold (these are the experimental peaks seen at $V_g = -2.78$ V and $V_g = -2.74$ V, respectively, and labeled a and a' in Fig. 5.28b). The observed peaks could arise either from electron tunneling through the bound states caused by the bending of the quantum wire, or they could be due to scattering through impurity states. The latter possibility was suggested by Wu *et al.*, based on calculations by McEuen *et al.* [67] and Alphenaar *et al.* [161] of the transmission due to tunneling through an impurity site in a constriction.

The theoretical calculations of Wang [104], shown in Fig. 5.24, show two sharp sub-threshold conductance peaks. However, in Wang's model, the external leads of the wire are very short, and the wire has a small aspect ratio. Both conditions are crucial for observing sub-threshold tunneling through the bound states. The bound state wave function decays exponentially in the leads, so as the leads increase in length the sub-threshold conductance peak becomes so small that it cannot be observed. If the effective aspect ratio R is large, the two sub-threshold bound states will coalesce into a single peak, as is clear from Fig. 5.19. Carini *et al.* [158] estimate that for gate voltages $V_g \sim -2.75$ V, the effective aspect ratio of this wire will be about 8, and at

this value the symmetric and antisymmetric bound state energies are identical. Therefore, the most likely explanation for the conductance peaks, seen at or below the first conductance plateau in Fig. 5.28b, is scattering through impurity states.

In Fig. 5.24, there is a deep minimum in the conductance at $E = 5.90$ meV (indicated by the upward arrow). As was mentioned in Sect. 3.2, minima in the transmission are generally accompanied by formation of large vortices in the quantum probability current. The size and location of the vortices prevents flux from being transmitted through the wire. Wang [104] showed that substantial vortex formation occurs at this energy. Incoming flux is squeezed to pass through the vortices, and this decreases the transmission through the wire. As was observed in Sect. 3.2, the rotation of the probability current about the vortices changes direction very rapidly as the electron energy passes through the conductance minimum. For electron energies sufficiently far above or below this conductance minimum, the probability flow once again becomes laminar.

Substantial vortex formation associated with a conductance minimum is also seen in systems with two circular bends. Berggren and Ji [102] and Ji [103] considered transmission through a tube with this geometry. If one studies the quantum probability flow through such a system, a zero or very deep minimum in the transmission will generally be associated with the formation of large vortices in the probability current. At these energies, the direction of rotation about a given vortex will change sign extremely rapidly as the particle energy crosses the zero in transmission. Berggren and Ji [128] studied the electron probability flow through a tube with two circular bends. The probability current distributions are shown in Fig. 5.29, where the electron energy corresponds to a deep minimum in conductance just below the opening of the second transverse mode.

As was discussed in Sect. 3.2, the decrease in the conductance is accompanied by the sudden appearance of vortices in the velocity flow, which increase in size as the conductance decreases. Figure 5.29a is taken at an energy just below the zero in the conductance. At this energy, several dramatic vortices dominate the velocity flow. The stream lines form very large, roughly triangular areas around the large vortices. Each successive vortex rotates in opposite directions, with fixed points occurring at the tube boundaries. Transmission through the system is dramatically reduced because stream lines traveling through the tube must avoid these large vortices. Figure 5.29b shows an energy just above the deep minimum in the conductance, where the conductance is once again increasing ($G = 0.4(2e^2/h)$). The vortices are still present but have reversed in sign over a very small energy interval, as was predicted in Sect. 3.2. The vortices disappear rather rapidly with further increase in energy, and the flow is laminar once the conductance again reaches a plateau.

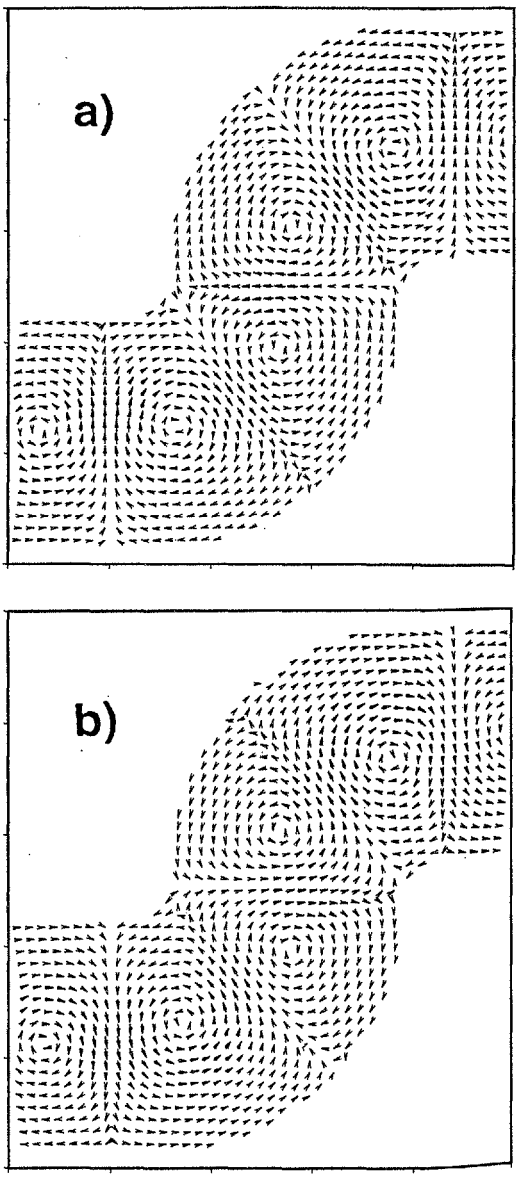

Fig. 5.29. Velocity distribution patterns for a quantum wire with two right angle circular bends. Case (**a**) shows the onset of vortices at the first dip in conduction, just below the second subband threshold. Here, $G \approx 0.2G_0$. Case (**b**) corresponds to a value of E_F just greater than the same conductance minimum; here, $G \approx 0.4G_0$. The flow pattern reverses direction around each vortex over this very small change in energy. From [102]

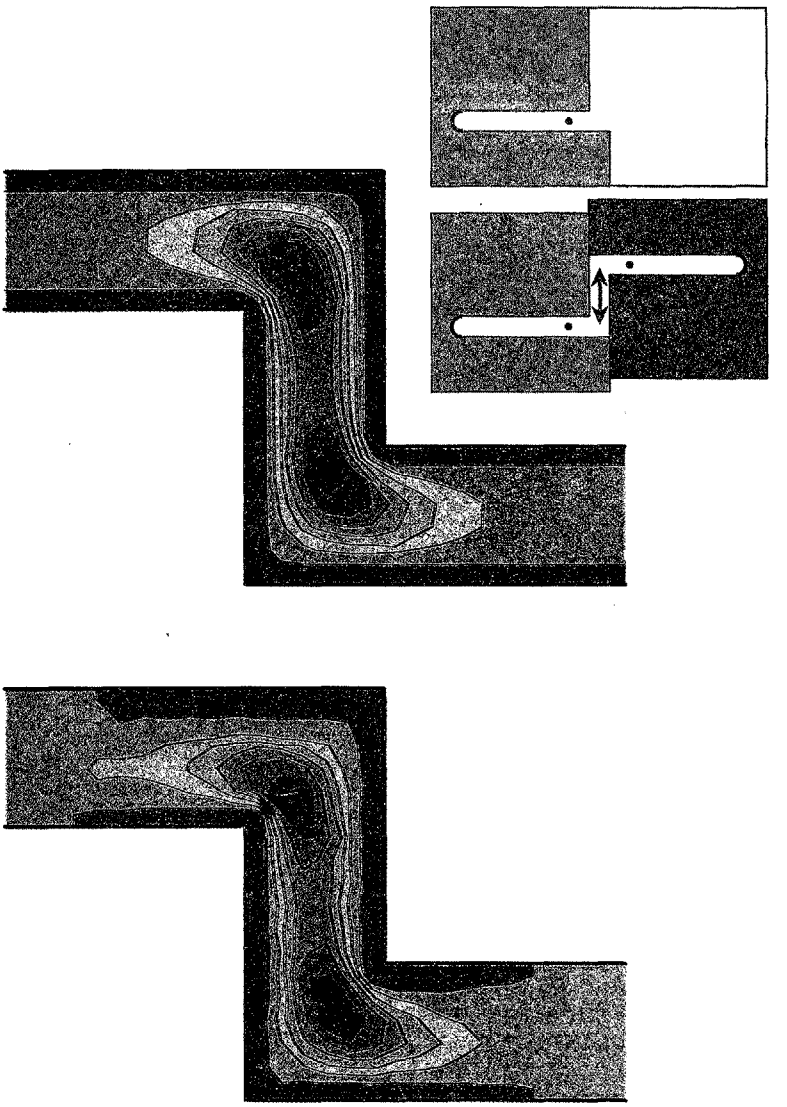

Fig. 5.30. [Inset: design for a tunable double-bend waveguide, from [134]. Light and dark shapes represent identical aluminum plates with the second plate inverted with respect to the first. The empty space between the plates forms a waveguide double bend. Relative motion in the direction of the double arrow varies continuously the aspect ratio R. Small holes (black dots) provide clearance for semirigid coaxial lines.] (a) Theoretical contour plot of resonant frequency shift $\Delta f_0/f_0$ for the lower frequency confined mode in a double bend waveguide with aspect ratio $R = 3.0$, from (4.12). (b) Experimental measurement of resonant frequency shift for electromagnetic field energy. Red denotes negative frequency shift, blue denotes positive frequency shift. The most negative frequency shift was -152 MHz (expt), while theory predicted -127 MHz using enhancement factor $c_0 = 2.46$ in (4.12). The most positive shift was 34 MHz (expt), while theory predicted 23 MHz

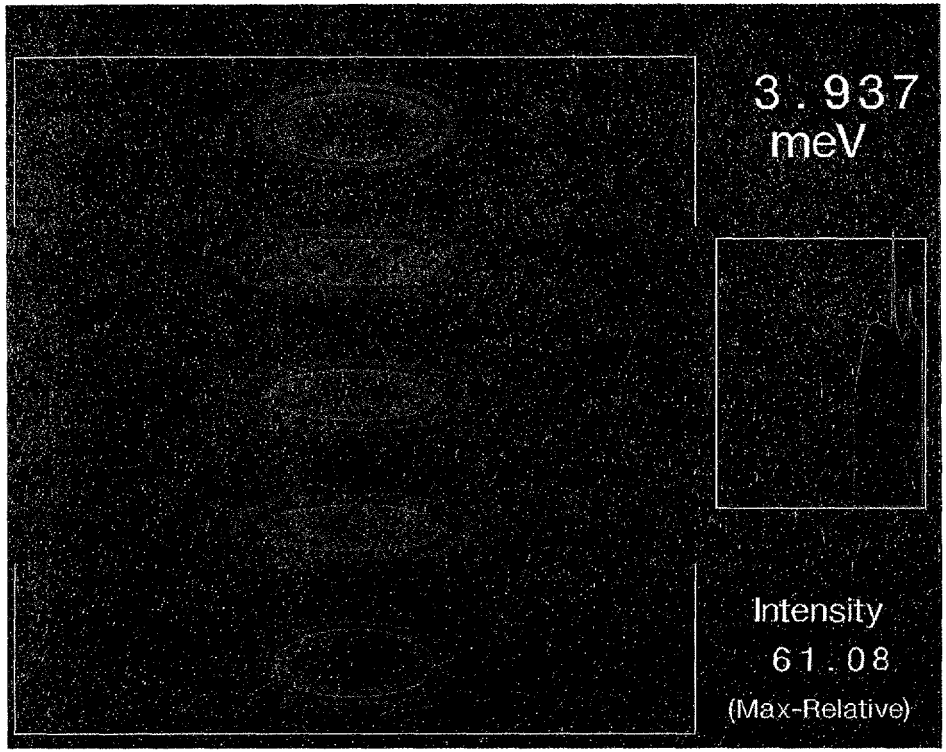

Fig. 5.31. Electron probability distribution for a resonance in a quantum dot structure. Wire dimensions: $w = 2a = 100$ nm, $b = 200$ nm (as defined in Fig. 5.13), $E_e = 3.937$ meV. Inset at right shows conductance vs. electron energy; the energy E_e is denoted by the boundary between red and blue regions. E_e corresponds to a sharp conductance peak, associated with a standing wave resonance in the stubs. The highest probability region is dark red and the lowest probability is magenta. From [100]

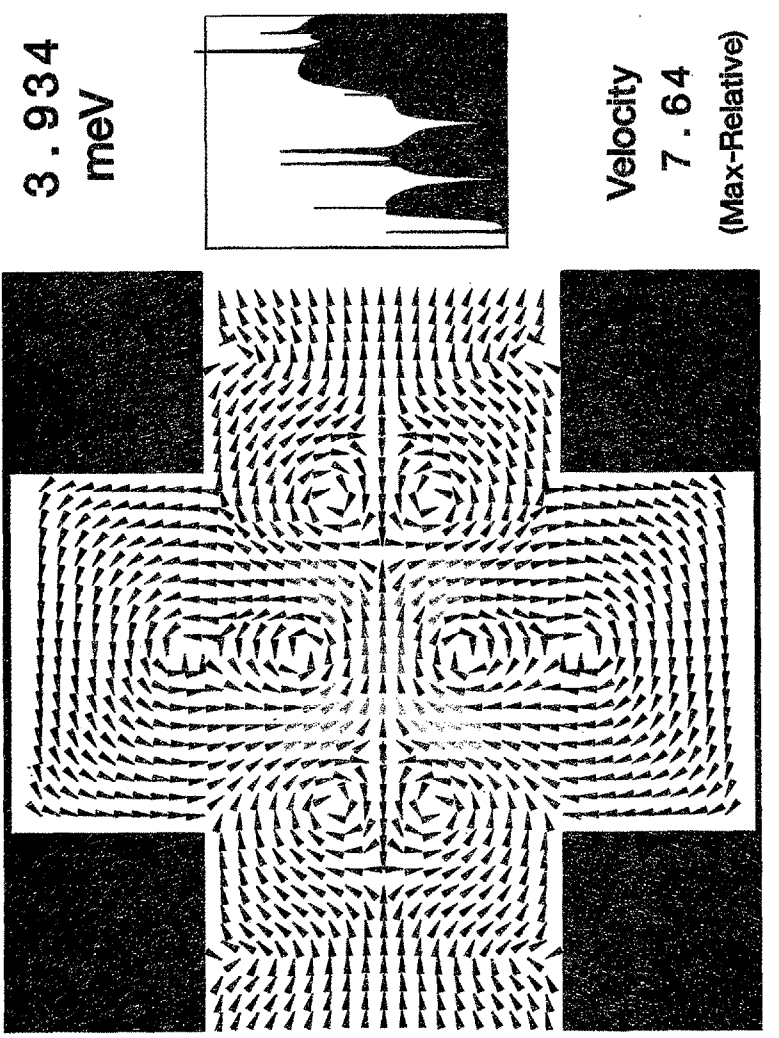

Fig. 5.32. Quantum probability current distribution for the quantum dot structure of Fig. 5.31. The arrows show the direction of $\mathbf{j}$, defined in (3.26). The highest velocity is violet and the lowest is blue. Electron energy $E_e = 3.934$ meV, just below the conductance peak. Eight vortices are visible in the probability current, and are symmetrically placed about the center of the tube

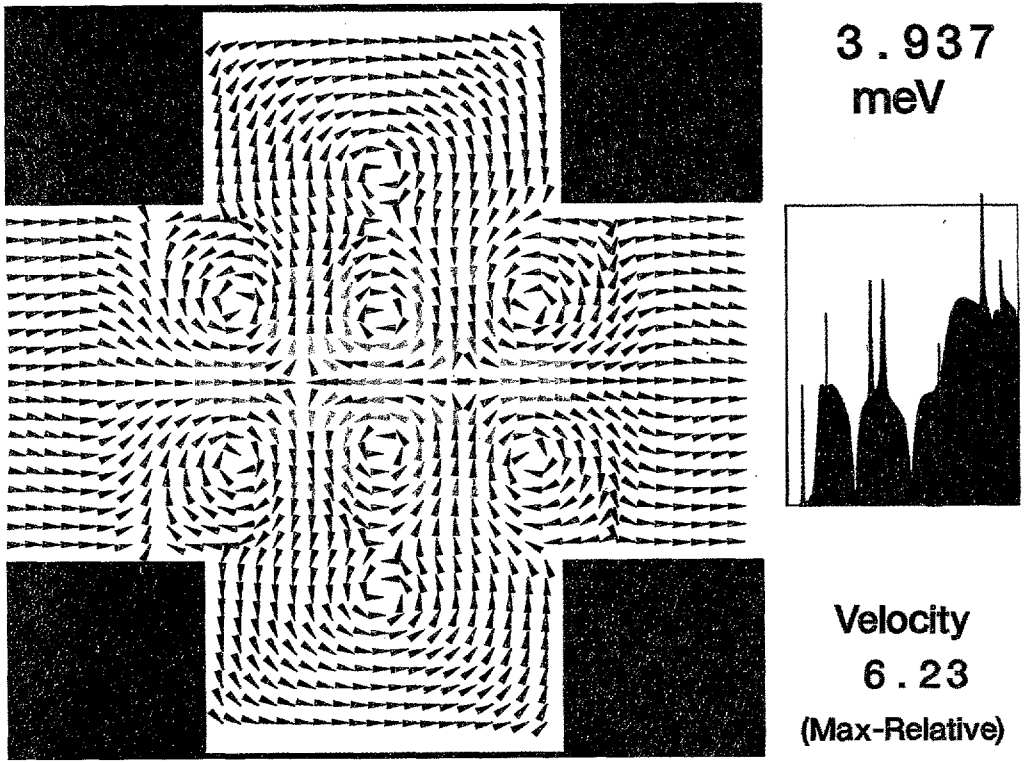

Fig. 5.33. Quantum probability current distribution **j** for the quantum dot structure of Fig. 5.31. The notation is that of Fig. 5.32. Electron energy $E_e = 3.937$ meV, just above the conductance peak. Comparing with Fig. 5.32, note the dramatic change in flow direction around each vortex, over a very small energy region

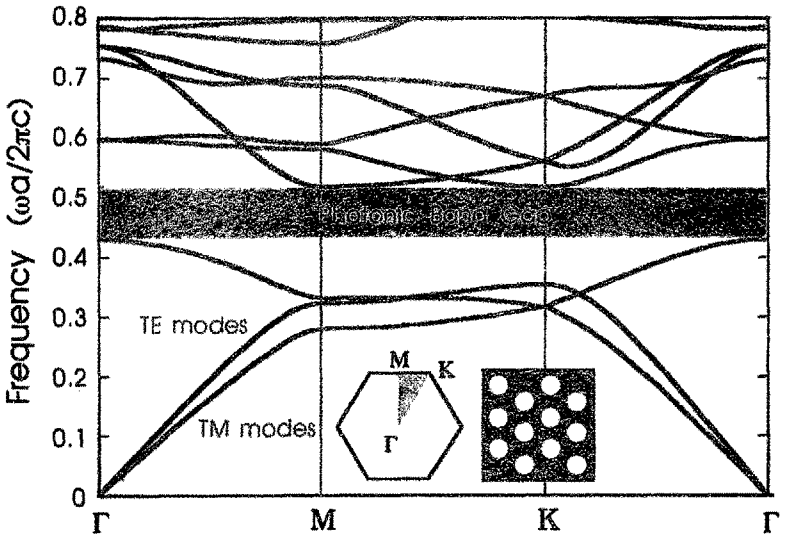

Fig. 5.34. Photonic band structure for the modes of a triangular array of air columns in a dielectric substrate, as shown in Fig. 7.1b. The lattice parameter is $r/a = 0.48$. Blue lines represent TM bands, and red lines show TE bands. A complete photonic band gap exists for both polarizations, and is shown as the horizontal yellow band. The inset shows high-symmetry points at the corners of the irreducible Brillouin zone (shaded light blue region). From [25]

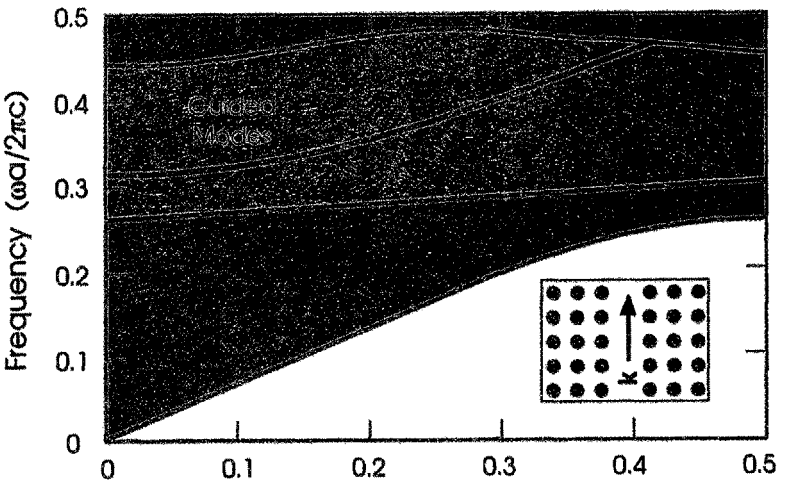

Fig. 5.35. Projected band structure of TM modes for a waveguide in a square lattice of dielectric rods in air. The blue shaded region contains the continuum of extended crystal states. The yellow region is the photonic band gap. The red line is the band of guided modes inside the waveguide, which is formed by removing one row of dielectric rods in the (10) direction in the crystal as shown in the inset. From [25]

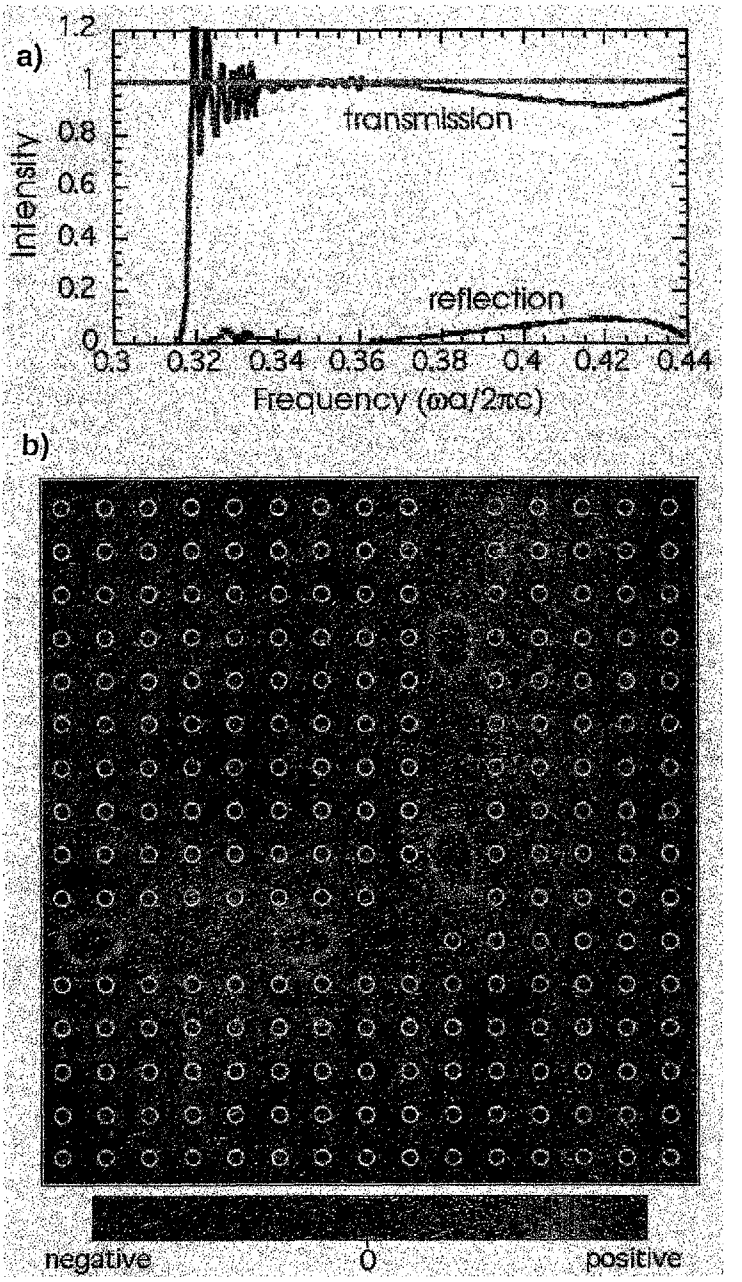

Fig. 5.36. (**a**) Computed transmission and reflection coefficients for EM pulses traveling around a waveguide containing a sharp 90° bend, carved out of a square lattice of dielectric rods. (**b**) Displacement field of a TM mode traveling through the waveguide bend. From Refs. [25] and [162]

6. Two-Dimensional Systems with Finite Periodic Structure

In Sect. 5.4 bound state and scattering properties were analyzed for the case of two-dimensional structures (tubes or wires) with two identical elements, or "cells." In this chapter that analysis will be extended to treat systems which contain a finite periodic series of identical cells. The qualitative features of bound states, transmission and conductance will be derived for such systems. The structure which emerges in systems consisting of identical cells in series will be illustrated with two general examples. The first example discussed will be systems which consist of a series of identical right angle bends separated by straight sections. The second general example will consist of tubes in which a number of identical T-stubs, or quantum dots, are connected in series. Many groups have investigated scattering phenomena in such systems [38, 75, 80, 104, 140, 141, 163].

Although the conductance in these 2-D systems frequently shows much detailed structure, this book will focus primarily on the main qualitative effects which emerge, in the limit as more and more identical elements are connected in series. In Sect. 2.1.4 it was shown that transfer matrix methods were particularly suited to treating transmission through a series connection of N identical components. This occurs because the transfer matrix $\mathbf{M}$ for a single cell gives the transmission amplitude for propagation across an individual component of the system. Consequently transmission through N identical cells is obtained by multiplying the single cell transfer matrix $\mathbf{M}$ N times. In Chap. 2 it was proved that either a bend or a cavity in a tube could be well approximated as the site of a local attractive potential. If a particle moves through a system containing a series of identical components, it traverses a regularly spaced sequence of identical effective potentials. In solid state physics, this is just the physical situation which produces band structure for electrons. Consequently, in the limit of a system with a very large number of identical elements, one expects to see band structure emerging in the particle transmission amplitudes [1].

We will find that for finite periodic systems, regularities in the transmission coefficients – alternating regions of allowed transmission and essentially

[1] Perhaps "*bend structure*" would be a more appropriate term for the bands in the transmission spectrum caused by the periodic effective attraction arising from a series of bends in a tube.

J. T. Londergan, J. P. Carini and D. P. Murdock: LNPm 60, pp. 145 - 179, 1999
© Springer-Verlag Berlin Heidelberg 1999

zero "*forbidden bands*", analogous to the band structure in infinitely periodic systems – do appear in these 2-D systems. It is interesting how rapidly the band-like features arise in finite periodic systems. As will be seen, "*miniband*" structure will appear when even relatively small numbers of components (say, three) are connected in series. The emergence of miniband structure in transmission, arising from the periodic (but finite) structure of serially connected systems, was emphasized by Sols *et al* [38, 140]. The main qualitative features of low-energy transmission in periodic systems, in particular the origin of forbidden and allowed bands, are found in the single-mode approximation to the transfer matrix. This formalism has previously been studied for systems with one and two elements or cells; the miniband structure which emerges here is the natural extension of the results obtained in preceding sections.

This chapter begins with a review of the number of bound states, and their properties, which are found in a 2-D system with N identical cells. Sect. 6.2 reviews the general features of transmission through tubes with finite periodic structure. Using the transfer-matrix formalism, it will be demonstrated that miniband structure arises in such systems, and that this gives rise to the familiar band structure in the limit as the number of cells becomes infinitely large. Sect. 6.3 analyzes transmission properties in two types of periodic systems: tubes containing a series of identical right angle bends, and systems composed of a series of identical T-stubs (in quantum heterostructures, this is the so-called "*quantum dot superlattice*" structure [141]). In Sect. 6.4 we review briefly the qualitative effects produced when one element is modified in an otherwise identical series of cells. This is the analog of a single "*defect*" in a crystal.

6.1 Bound States in Periodic 2-D Systems

For a single cell, the bound state condition for the transfer matrix is

$$\mathrm{M}_{11} = 0 \ , \tag{6.1}$$

for energies below the continuum threshold. At these energies, the longitudinal channel momenta are all imaginary, *i.e.*

$$\alpha_n = i|\alpha_n| = i\sqrt{(n\pi)^2 - k^2} \ . \tag{6.2}$$

In SMA, the bound state condition for a single cell has the form of (2.44),

$$(B + |\alpha|)^2 = A^2 \ . \tag{6.3}$$

In Chap. 2 it was proved that at least one bound state exists for a tube which becomes straight at large distances, and which has at least one isolated bend or cavity. In the case of N identical cells connected in series, the system will have a bound state at wave numbers k below continuum threshold where

$$[\mathbf{M}^{(N)}]_{11}(k) = 0 \ , \tag{6.4}$$

where $\mathbf{M}^{(N)}$ in (6.4) is the transfer matrix for the N-cell system.

The finite periodic 2-D geometries studied in this book consist of coupled elements in which a single isolated cell contains exactly one bound state. If a single cell will support one bound state (*i.e.*, there is one energy below continuum threshold where $\mathbf{M}_{11} = 0$ for a single cell), then in a periodic system with N identical cells in series, the single bound state supported by one cell is converted into a "miniband" of N states. The interaction between states located at different sites in the system will shift the eigenmodes from their value for a single isolated cell. If the resulting modes are located below the continuum threshold, they will be real bound states. If they are shifted above continuum threshold, they will appear as quasi-bound states.

Sect. 5.4 examined the case of two identical cells in series, separated by a straight section of length l. The number of bound states, and the relative separation between the energies of the different bound states, was studied as one varied the length l of the straight channel separating the cavities. For two cells in the limit $l \to \infty$, it was demonstrated (in SMA) that the two bound state energies became degenerate, with energy equal to the bound state energy for a single isolated cell. This will also be true for N cells in series. In the limit of infinitely long connecting straight sections between elements, the wave functions in the individual cells do not interact. The system will have N bound states which are degenerate in energy, and all of the bound state energies are equal to the bound state energy for a single cell.

In Sect. 2.1.4, we introduced the transfer matrix approach for systems containing a single structure or cell. For binding and low-energy scattering, good qualitative estimates were obtained with the "single-mode approximation" [SMA], where all transverse channels were neglected except for the lowest mode. In SMA, it was shown in (2.45) that the transfer matrix $\mathbf{M}^{(N)}$ for N identical cells could be written in terms of the transfer matrix $\mathbf{M}$ for a single cell and the Bloch phase ϕ,

$$\mathbf{M}^{(N)} = \frac{1}{\sin(\phi)}[\sin(N\phi)\mathbf{M} - \sin((N-1)\phi)\mathbf{I}]$$

$$\frac{1}{t_N} = [\mathbf{M}^{(N)}]_{11} \ . \tag{6.5}$$

In (6.5) the quantity t_N is the elastic scattering transmission amplitude.

Below continuum threshold, the matrix $\mathbf{M}$ is real. The subthreshold regions can be characterized in terms of the Bloch phase, just as the continuum region was analyzed. Regions where $|\cos(\phi)| < 1$ are "*allowed*" regions, where ϕ characterizes the phase shift across a single cell, and regions with $|\cos(\phi)| > 1$ are "*forbidden*" regions. In forbidden regions, the wave function decreases exponentially in crossing a single cell. It is straightforward to show [153] that in allowed regions (2.45) can be rewritten as

$$[\mathbf{M}^{(N)}]_{11} = \frac{\sin(N\phi + \delta)}{\sin(\delta)} \quad ,$$
$$\tan(\delta) \quad = \frac{\sin(\phi)}{\mathbf{M}_{11} - \cos(\phi)} \quad . \tag{6.6}$$

In forbidden regions, it can be shown that

$$[\mathbf{M}^{(N)}]_{11} = (-1)^{(Np)} \frac{\sinh(N\theta + \eta)}{\sinh(\eta)} \quad ,$$
$$\tanh(\eta) \quad = \frac{\sinh(\theta)}{(-1)^p \mathbf{M}_{11} - \cosh(\theta)} \quad . \tag{6.7}$$

In forbidden regions, the Bloch phase is defined as $\phi = i\theta + p\pi$, where $p = 0$ if $\cos(\phi) > 1$ and $p = 1$ if $\cos(\phi) < -1$. We also define $\eta = i\delta$ [2].

In allowed regions, the bound state condition is

$$N\phi + \delta = m\pi \quad , \tag{6.8}$$

for some integer m. Any time this condition is satisfied one has a bound state for the N-cell system. For the simple geometries studied in this book (circular bends, sharp-angle bends, quantum dots) the effective potential for each cell can be expressed as a square well. A tube consisting of identical cells thus has an effective potential which looks like a series of identical square wells, spaced by equal intervals. In systems composed of series connections of N identical cells, we have never found bound states in "forbidden" regions. The bound state wave functions which occur in the allowed regions are distributed throughout the N cells.

All the systems studied in this book are symmetric with respect to reflection about the center of the tube. If one arranges the bound states in the "allowed" regions in order of increasing energy, the m^{th} bound state will possess $m - 1$ nodes, and the bound states will form alternating states with even and odd parity, respectively, with respect to reflection. Along the longitudinal direction, the bound states occurring in allowed regions resemble somewhat the N lowest standing waves on a string fixed at both ends.

For sufficiently large values of l, the straight sections connecting adjacent cells, the resulting wave functions are essentially zero in the straight sections, and the wave functions in each cell look almost identical, differing only in the sign of the wave function in each cell. In the limit of very large l, it can be understood why all bound states should become degenerate, at the energy for a single cell. From (2.37) and (2.42), we see that as $l \to \infty$, both the Bloch angle and the transfer matrix element $\mathbf{M}_{11}$ grow exponentially and become very large below continuum threshold, except in the immediate vicinity of the bound state (the point where $\mathbf{M}_{11} = 0$). Thus, the allowed region becomes extremely narrow, and all N bound states are found in this

[2] Note that with this definition for η, it is possible that η is not a real angle.

region. As the straight sections l decrease in length, the bound states interact with one another. The bound state energies, which are initially degenerate for very large l, broaden to become a "miniband" of energies. The requirement that the higher modes possess an increasing number of nodes pushes these modes progressively higher in energy, until for sufficiently small separation between adjacent cells, the higher modes move above continuum threshold and become quasi-bound states.

The bound states which occur in forbidden regions have much different character from those occurring in allowed regions. From (6.7), the condition for bound states in forbidden regions is

$$N\theta + \eta = 0 \quad . \tag{6.9}$$

Whereas bound states in allowed regions occur whenever the sum of the phases goes through an integer times π, as seen from (6.8), bound states in forbidden regions will only occur when $N\theta$ and η are equal and opposite. As these states are below the continuum threshold, the wave function decays exponentially as one goes into the external leads, and as they are "forbidden" inside the cells, they also decay into the interior of the tube. These states are thus localized right at the junction of the cells with the external leads. Such states are fairly common in condensed matter physics, where they are known as "surface states."

A review of surface states (together with the history of this field) is given in the book by Davison and Steslicka [164]. A series of identical effective one-dimensional square wells, which we have discussed up to this point, will not produce surface states. Such states might be produced if one or more cells were modified in an otherwise periodic series. This is the analog of the effect of "*defects*" in a crystal, and will be covered briefly in Sect. 6.4. Surface states produced by modifying the outermost cell in a series are called "*Tamm states*" [165]. Surface states produced through defects in a series of cells, which give rise to a band crossing which produces surface localization, were first described by Shockley [166]. Examples of surface states are found in the review of defects in Sect. 6.4, and will also appear in our discussion of photonic crystals in Chap. 7.

For electrons in quantum wires, the conductance is related to the transmission amplitudes through the Landauer formula of (3.37). Bound states appear as subthreshold peaks in the conductance, and quasi-bound states are seen as low-energy peaks just above continuum threshold. As was discussed previously, the subthreshold conductance peaks characteristic of true bound states are quite sensitive to the wire geometry. If the external straight sections of the wire are sufficiently long, the peaks will become so small and narrow that they cannot be seen experimentally. If quasi-bound peaks are sufficiently far above continuum threshold, they will become so broad that they cannot be separated from the continuum. An example of this can be seen in Fig. 5.26.

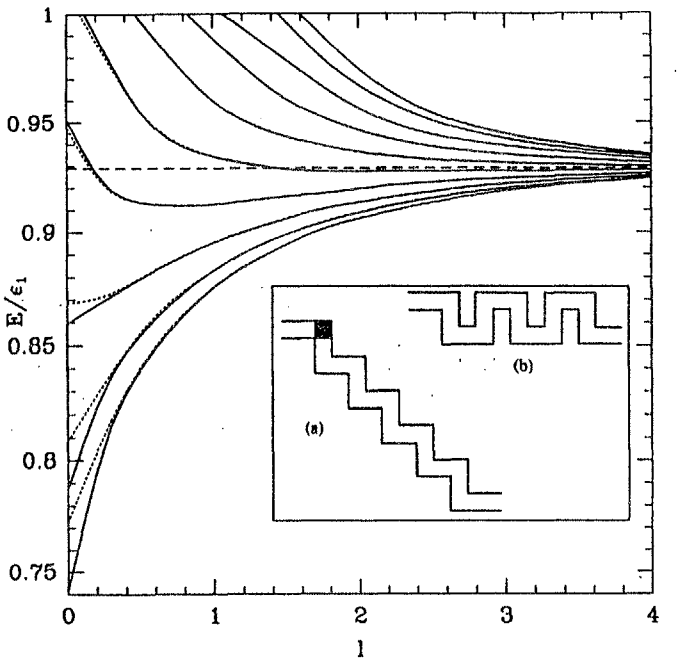

Fig. 6.1. Bound state energies $\epsilon = E_b/\pi^2$ for a ten-bend tube with open ends, vs, the length l of the straight section joining adjacent bends. Solid lines are for the snake shape (b); dotted lines are for the staircase shape (a), both illustrated in the inset for $l = 1$. The horizontal dashed line represents the bound state energy for a tube with a single right angle bend. From Wu and Sprung, [80]

As a simple example of a periodic system, consider a tube composed of a series of identical sharp right angle bends. Two basic geometries will be considered for this structure: the multistep or "*staircase*" shape and the "*snake*" type (these are respectively shapes (a) and (b) shown in the inset to Fig. 6.1). Each cell consists of a unit square, coupled to a straight lead of length l. A system with a single L-bend was studied in Sects. 2.1.5 and 3.1.1. Tubes with two right angle bends were discussed in Sect. 5.4. The transfer matrix for a single cell, for a tube with L-shaped bends, has the form

$$\mathbf{M} = \mathbf{U}^{-1}\mathbf{V}\mathbf{F} \ , \tag{6.10}$$

where $\mathbf{U}$ and $\mathbf{V}$ are defined in (2.30). For the snake tube, the matrix $\mathbf{F}$ is the unit matrix; for the staircase tube, $\mathbf{F}$ is defined in (5.34). The bound state energies for a tube with N cells are obtained from the solutions of (6.4). Note that in the single-mode approximation $\mathbf{F}$ is just the unit matrix, so the SMA predicts that both bound state energies and low-energy transmission properties should be identical for staircase and snake tubes.

Figure 6.1 plots the exact bound-state energies for a tube with ten bends and open ends, as calculated by Wu and Sprung [80]. The quantity plotted is $\epsilon = E_b/\pi^2$, the ratio of the bound state energy to the continuum threshold energy. This is plotted against l, the length of the straight section between bends (in units of the tube width). The solid curves are the exact bound state energies for the snake tube; the dotted curves are the energies for the staircase shape. The bound state energies for the two configurations are remarkably similar, in agreement with the SMA prediction of identical binding energies. In the limit as the length of the straight section $l \to \infty$, the energies of all bound states become identical, and they approach the bound state energy of a tube with a single L-shaped bend, *i.e.* $E_b = 0.929\,\pi^2$ ($\epsilon_b = 0.929$); this is the straight dashed line in Fig. 6.1. The "miniband" of ten energy states is the generalization to $N = 10$ bends of the result for the double bend system, shown in Fig. 5.19.

Consider the case $l = 0$, where a multibend system is formed by joining together a series of N unit squares with no straight connecting leads. For this geometry, in the limit where the number of cells N is large, the energy of the lowest bound state can be predicted using the effective square well potential introduced in Sect. 2.1.4. In single-mode approximation a symmetric tube with straight leads at the ends can be modeled with an effective one-dimensional square well potential. Expanding this to lowest order in the (small) binding energy gives an effective square well for a single L-shaped bend with depth $V \approx 3$ and width $w \approx \pi/(3\sqrt{3})$, as can be seen from (2.47) and (2.51). If a system is formed by connecting a series of N identical cells, then the effective one-dimensional potential consists of N identical square wells, each separated by a distance l. When $l = 0$ the respective square wells just touch one another. For this geometry, the effective potential for a system of N cells is therefore a square well with depth $V = 3$ and width $w_N \approx N\pi/(3\sqrt{3})$.

The lowest energy state for this square well potential will approximate the lowest energy state in the multibend tube. Since the effective width increases linearly with the number of bends, in the limit of very large N the lowest bound state energy will simply move to the bottom of this square well. Thus one predicts that for either a staircase or snake system with many bends and $l = 0$, the lowest bound state energy should approach

$$\begin{aligned} E_b &\to \pi^2 - 3 = 0.696\pi^2 \ , \\ \text{or } \epsilon &= 0.696 \ . \end{aligned} \tag{6.11}$$

For the ten-bend systems shown in Fig. 6.1, the exact lowest bound state in the staircase tube has energy $\epsilon = 0.77$, while the lowest bound state energy for the snake configuration is $\epsilon = 0.75$.

It can be seen from Fig. 6.1 that for the ten-bend structure all ten states are bound whenever $l > 1.6$ (states with $\epsilon < 1$ are bound, while states with $\epsilon > 1$ have been pushed into the continuum). When $l = 1$, seven of the states

are bound, while for $l = 0$, only four states are bound, and the remaining six states are in the continuum. Fig. 6.1 shows clearly that the interaction between the various states for finite l leads to the formation of minibands, and that the spread in energy between the bound states increases as the distance l between the cells decreases. The periodic effective 1-D potential in the multibend tube gives rise to band structure of the Kronig–Penney type [167].

An interesting example of bound state structure occurs in a tube consisting of a series of identical T-stubs, each separated by a distance l. If the stubs are sufficiently far apart, the bound state energies will all approach the energy for a single stub. As the distance between adjacent stubs is decreased the states will interact, and the transmission coefficients will exhibit minibands. It was shown in Sect. 2.1.4 that each stub can be approximated as the site of an effective square well potential. Because the bound state wave functions are highly localized in the vicinity of each stub, Ji and Berggren [101] considered the states as interacting one-dimensional sites, or "quantum dots." Each stub was taken as the site of a quantum dot, and the dots were assumed to interact weakly through a nearest-neighbor potential V.

In this case, for three identical T-stubs connected in series, the bound states should split into three energies E_j. The wave function for the n^{th} energy mode will have $n-1$ nodes, hence the probability density will have $n-1$ zeroes. Labeling the energy levels j in order of increasing energy, the states with odd (even) values of j have even (odd) reflection symmetry. The energies and their eigenvectors $\mathbf{C}_j$ for the three states are predicted from the nearest-neighbor weak-coupling model to be

$$\begin{aligned} E_{1,3} &= E_0 \mp \sqrt{2}V \ , \\ \mathbf{C}_{1,3} &= (1, \pm\sqrt{2}, 1)/2 \ , \\ E_2 &= E_0 \ , \\ \mathbf{C}_2 &= (1, 0, -1)/\sqrt{2} \ . \end{aligned} \tag{6.12}$$

In (6.12), E_0 is the bound state energy for a single stub. Figure 6.2a plots the probability density for a single isolated stub. Figs. 6.2 b-d show the electron densities for the bound states in a system with three T junctions, in order of increasing energy. The system has channel width and stub width 100 nm, stub height 220 nm, and 20 nm distance between adjacent stubs (normalized to unit channel width the corresponding tube parameters are $2a = 1$, $b = 2.2$, and straight section $l = 0.2$ between adjacent cells).

The exact bound state wave functions clearly possess the structure suggested by the weak "nearest-neighbor" coupling model of (6.12). The odd-parity $n = 2$ mode shown in Fig. 6.2c has almost no amplitude in the center dot, and wave functions of opposite sign (and equal probability density) in the two outer dots. The even-parity $n = 1$ and $n = 3$ modes shown in Figs. 6.2b and 6.2d have zero and two nodes, respectively, and relatively large probability density in all three quantum dots.

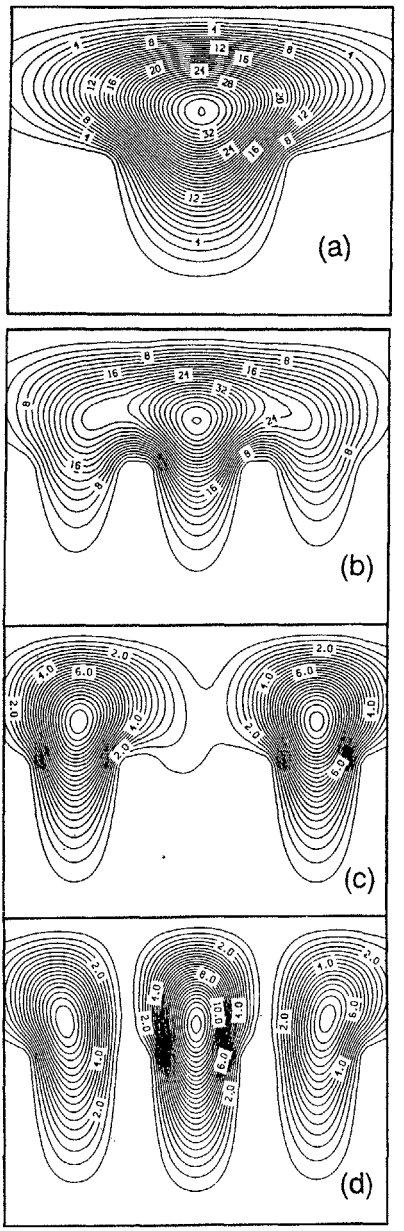

Fig. 6.2. Bound state electron probability densities for system of 3 coupled T-stub cavities. Relative dimensions of system: channel width and stub width $2a = 1$; stub height $b = 2.2$; length of connecting leads $l = 0.2$. (**a**) Bound state density for a single isolated T-stub. (**b**)-(**d**) show probability densities of bound states, in order of increasing energy. The structure of the bound states agrees with a weak-coupling model of quantum dots interacting with nearest neighbors, (6.12). From [101]

6.2 Origin of Band Structure in Periodic Systems

In this section we review the transfer matrix results for a 2-D system composed of a series of identical elements, or "cells." Although some of this material was derived earlier in Sects. 2.1 and 5.4, the qualitative results are summarized here since they are especially relevant for systems with finite periodic structure. Transfer matrix analysis is particularly well suited to such systems. As was discussed in Sect. 2.1.4, the transfer matrix for a tube with a number of cells connected in series is obtained by multiplying together the transfer matrix for each individual cell. We will briefly review the qualitative results for transmission and reflection in finite periodic systems.

Consider a tube containing N identical cells in series. Each cell consists of a single bend or cavity, connected to the next structure by a straight section of unit width and length l. The transfer matrix $\mathbf{M}$ for a single cell connects the wave function on either side of a cell, and has the form

$$\mathbf{M} = \mathbf{U}^{-1}\mathbf{V} \quad , \tag{6.13}$$

where the matrices $\mathbf{U}$ and $\mathbf{V}$ are given in (2.36). For N identical cells the transfer matrix across the entire system is given by $\mathbf{M}^{(N)}$. The transfer matrices can be expanded in terms of a set of transverse channel basis functions ϕ_n in the straight section of the tube, as defined in (2.3). In general the transfer matrix includes a sum over an infinite number of transverse channel basis states. To calculate the transfer matrix this infinite dimensional expansion is truncated after m basis functions, in which case the auxiliary matrices $\mathbf{A}$ and $\mathbf{B}$, defined in (2.31), are $m \times m$ matrices, and the transfer matrix $\mathbf{M}$ is a $2m \times 2m$ matrix [3].

A useful approximation involves truncating the basis expansion to include only those transverse modes which are open for a particular value of the energy. Modes which are "closed" at a given energy have an imaginary longitudinal wave number, so the particle wave function in such a mode decays longitudinally along the channel. For reasonable values of the length l of the straight section, the contributions from closed transverse modes are frequently small except at energies close to the opening of a new transverse mode. As was shown in preceding chapters, the "open-mode" approximation of neglecting all closed transverse channels is particularly illuminating for bound states or transmission below the opening of the second transverse mode, where only the lowest transverse mode needs to be considered. In the "single-mode approximation" [SMA], the matrix $\mathbf{M}$ (and hence $\mathbf{M}^{(N)}$) is a 2×2 matrix, and the auxiliary matrices $\mathbf{A}$ and $\mathbf{B}$ are simply numbers.

[3] In general the transfer matrix is defined in terms of four auxiliary matrices, $\mathbf{A}$, $\mathbf{A}'$, $\mathbf{B}$, and $\mathbf{B}'$, given in (2.31). All examples studied in this monograph involve symmetric cavities for which $\mathbf{A}' = \mathbf{A}^T$ and $\mathbf{B}' = \mathbf{B}$, so this assumption is made in all equations presented in this chapter.

It was shown by Vezzetti and Cahay [77], and also by Wu, Sprung and Martorell [105], that in single-mode approximation the transmission amplitude $t^{(N)}$ and transmission coefficient $T^{(N)}$ through N identical cells are related to the corresponding transmission amplitude and transmission coefficient $t^{(1)}$ and $T^{(1)}$ through a single cell, respectively, by

$$\begin{aligned}
\frac{1}{t^{(N)}} &= [\mathbf{M}^{(N)}]_{11} = \frac{1}{\sin(\phi)}\left[\sin(N\phi)\mathbf{M}_{11} - \sin((N-1)\phi)\right] \\
&= \frac{1}{\sin(\phi)}\left[\frac{\sin(N\phi)}{t^{(1)}} - \sin((N-1)\phi)\right] \quad , \\
\frac{1}{T^{(N)}} - 1 &= \frac{|\sin(N\phi)|^2}{|\sin(\phi)|^2}\left(\frac{1}{T^{(1)}} - 1\right) \\
\cos(\phi) \equiv \mathrm{Tr}(\mathbf{M})/2 &= \frac{B}{A}\cos(\alpha l) - \frac{A^2 - B^2 + \alpha^2}{2\alpha A}\sin(\alpha l) \qquad (6.14)
\end{aligned}$$

In (6.14), A and B are respectively the (11) matrix elements of the matrices $\mathbf{A}$ and $\mathbf{B}$ defined in (2.31), α is the longitudinal momentum α_1 in the first transverse mode as defined in (2.3), and ϕ is the Bloch phase for transmission through a single cell.

The relation (6.14), which follows since the matrix $\mathbf{M}$ is a unimodular 2×2 matrix, gives an analytic relation between transmission probabilities for one cell, and N cells in series. The general characteristics of minibands in a finite periodic system can be easily derived from this relation, and were summarized by Wu, Sprung and Martorell [30].

- **Forbidden Bands:**.
  - When $|\cos(\phi)| > 1$, then for large N one has $|\sin(N\phi)|^2/|\sin(\phi)|^2 >> 1$. In this case there is no allowed path for a particle through one of the cells. The transmission through a single cell will be exponentially damped; through N cells the transmission probability becomes progressively smaller, so that for large N, $T^{(N)} \to 0$. This will produce a "forbidden band" in regions where the absolute value of the cosine of the Bloch phase is greater than one.
  - In addition, the transmission probability through N cells will vanish at any wave number which has zero transmission probability through a single cell.
- **Transparency:**.
  - There is complete transparency, *i.e.* $T^{(N)} = 1$, for any wave number where $T^{(1)} = 1$. If a single cell has 100% transmission (or reflection) at a certain wave number, it makes sense that there should be complete transmission (reflection) through N identical cells connected in series.
  - In addition, in "allowed" regions where the Bloch angle $\cos(\phi)$ varies between -1 and $+1$, the quantity $\sin(N\phi)/\sin(\phi)$ vanishes at $N-1$ points. From (6.14), the SMA requires that $T^{(N)} = 1$ at each of these points also. The vanishing of $\sin(N\phi)$ signifies that an integral number of half

wavelengths can be accommodated in the tube; this is the condition that standing waves can be set up in the system at this wave number, and this resonant condition produces a peak in the transmission.

- **Allowed Bands:**.
  - In allowed regions $\cos(\phi)$ varies between -1 and $+1$. For large N, the factor $|\sin(N\phi)|^2/|\sin(\phi)|^2$ is a rapidly oscillating function. It has $(N-1)$ zeroes which correspond to maxima in the transmission, $T^{(N)} = 1$, as discussed above, at energies where standing waves can be set up in the system.
  - There are also $(N-2)$ local minima in $T^{(N)}$, which correspond roughly to the points $|\sin(N\phi)| = 1$. Thus the local minima can be approximated by an "envelope function" of the form

$$\frac{1}{T^{(N)}_{min}} \approx 1 + \frac{1}{|\sin(\phi)|^2}\left(\frac{1}{T^{(1)}} - 1\right) \tag{6.15}$$

- **Relation of $T^{(N)}$ to $T^{(1)}$:**
  - The transmission probability $T^{(1)}$ for a single cell provides the overall qualitative shape of the transmission through N cells. This follows since, at the center of an allowed band, one has the relation $\sin^2(\phi) = 1$, at which point (6.15) predicts that $T^{(N)}_{min} = T^{(1)}$, *i.e.* the envelope function for the transmission minima has the same value as the transmission through a single cell, at the center of every allowed band.
  - Thus, the "single-mode approximation" predicts that the transmission probability through N identical cells should exhibit the following behavior. The transmission probability for a single cell determines the "overall shape" of the transmission through N cells. Superimposed on the overall shape given by the transmission probability $T^{(1)}$ is a very sharply varying series of maxima (where $T^{(N)} = 1$) and minima, in the allowed region where the Bloch phase $|\cos(\phi)| < 1$. In the allowed region a rather good approximation for the local average of the transmission probability is [4]

$$\frac{1}{T^{(N)}_{av}} \approx 1 + \frac{1}{2|\sin(\phi)|^2}\left(\frac{1}{T^{(1)}} - 1\right) \tag{6.16}$$

  It is sometimes incorrectly stated that in the limit of very large N the average transmission approaches 1 throughout an allowed region.
  - The "allowed" regions of transmission will be separated by "forbidden" regions characterized by $|\cos(\phi)| > 1$. In the forbidden regions the transmission probability $T^{(N)} \approx 0$. In the limit of an infinite number of cells, $N \to \infty$, the number of sharp oscillations in the allowed bands grows without limit.

[4] The relation (6.16) is obtained by averaging the rapidly oscillating function $|\sin(N\phi)|^2$ over one half cycle. The correct approach would be to average the scattering amplitude first, and then square it. However, Fig. 6.3 shows that (6.16) gives good agreement with the exact minima for this geometry.

- From (6.14), the transmission probability $T^{(N)}$ through N cells will be smaller than the probability $T^{(1)}$ through a single cell whenever $|\sin(N\phi)| > |\sin(\phi)|$. This is always true for the forbidden regions where $|\sin(\phi)| > 1$. However, it is also true for portions of the allowed regions.
- As the number of cells becomes very large, the transmission probability *vs.* wave number will possess a regular series of forbidden bands, with zero transmission, separated by allowed bands, with a series of sharp maxima oscillating about an envelope of minima for the transmission. In this way one recovers the alternating series of "bands" [allowed bands] and "gaps" [forbidden bands] which characterize the classic work of Kronig and Penney [167] on the origin of band structure in solid state systems.
- For a small number of cells, the rapid oscillations in the allowed region are visible. As the number of cells becomes very large, the number of oscillations increases and the spacing between them decreases, so individual oscillations cannot be isolated. The transmission in allowed regions then approaches the more featureless, apparently continuous distribution characteristic of solid state systems.

The results summarized above are strictly true only in the single-mode approximation. However, it will be seen that very good agreement is obtained between the SMA estimates and exact calculations, for particle energies below the opening of the second transverse mode. As the energy approaches the second transverse mode, the SMA predictions for the transmission probabilities will become progressively less accurate, but one still observes all the major qualitative features predicted in SMA.

6.3 Transmission and Conductance in Periodic 2-D Systems

In this section we will review the basic properties of transmission and conductance in periodic systems containing N identical cells in series. This will be illustrated for two different geometries. The first example is the "staircase" tube, where each cell consists of a right-angle bend coupled to a straight section of length l. The second example is the "quantum-dot superlattice," where each cell consists of a cross coupled to a straight section. Extensive use will be made of the SMA approximation employed in the preceding section to obtain 1-D estimates of the transmission.

6.3.1 Transmission in a "Staircase" System

Figure 6.3 shows the results of calculation of transmission through a ten-bend staircase with open ends and a straight section with length $l = 1$. The transmission probability exhibits all of the features which were predicted in the preceding section. The upper curve of Fig. 6.3 shows the cosine of

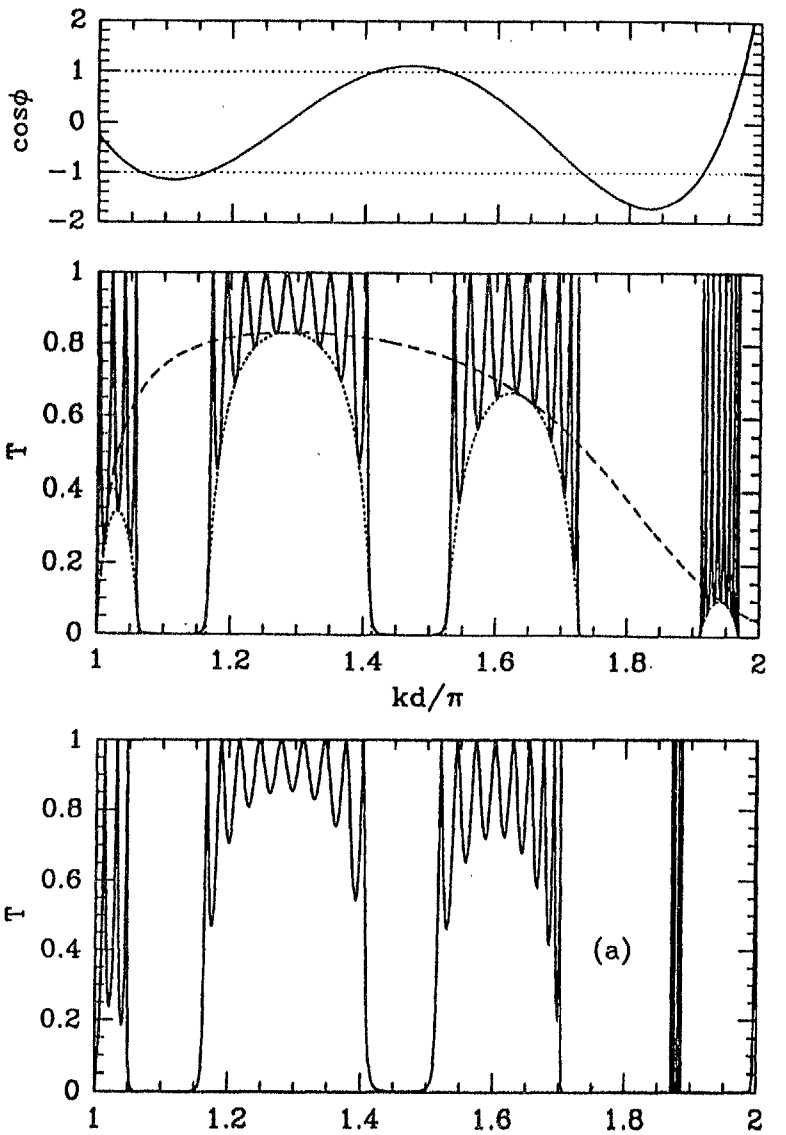

Fig. 6.3. Transmission coefficient through a ten-bend staircase tube (shown in inset (a) of Fig. 6.1). Upper curve: cosine of Bloch phase ϕ defined in (6.14). Middle curve: Single-mode approximation to transmission. Solid line: transmission coefficient $T^{(10)}$ vs. wave number k/π, from (6.14). Dotted line: predicted envelope of minima, from (6.15); dashed line: transmission coefficient $T^{(1)}$ for a single right angle bend. Lower curve: exact result for transmission coefficient $T^{(10)}$ in ten-bend staircase tube. From [80]

the Bloch phase for a single cell. The middle solid curve plots the single-mode approximation to the transmission probability $T^{(10)}$ for such a system, from threshold to the opening of the second transverse mode, $k = 2\pi$. The dotted curve is (6.15), the predicted envelope function for the minima of $T^{(10)}$. The dashed curve in the middle plot in Fig. 6.3 is the SMA estimate of the transmission probability $T^{(1)}$ for a single L-shaped bend. It goes through the envelope function of the minima for transmission through ten bends, at the center of each allowed band. The transmission probability $T^{(10)}$ has forbidden bands in the regions where $|\cos(\phi)| > 1$. In each allowed region, where $\cos(\phi)$ varies between -1 and $+1$, the transmission has nine transparent points where $T^{(10)} = 1$. These occur where $|\sin(N\phi)| = 0$, or when a standing wave can be set up in the tube.

Near the continuum threshold $k/\pi \approx 1$, three sharp peaks are seen in the transmission probability. When the straight section between bends has length $l = 1$, there are seven true bound states and three quasi-bound states, as can be seen from Fig. 6.1. The three peaks in the transmission correspond to propagation through the quasi-bound states. If the external leads were sufficiently short, it would also be possible to see sharp sub-threshold peaks in the conductance below continuum threshold. These sub-threshold peaks would correspond to particles tunneling through the true bound states in the system. As was discussed in Sect. 5.4, the ability to see these subthreshold tunneling peaks depends on the precise geometry of the tube.

The bottom curve in Fig. 6.3 shows the exact transmission probability for a tube with a ten bend staircase and $l = 1$, in the region below the second transverse mode. All of the qualitative features predicted in the SMA – forbidden bands, sharply oscillating transmission in the allowed bands, the number of transmission peaks in the allowed bands, an "envelope" for the minima in the transmission, and an overall shape for the transmission function given by the transmission probability through a single cell – are seen in the exact transmission coefficient. For low energies, corresponding to wave numbers $k < 1.8\,\pi$, the exact transmission probability is in good quantitative agreement with the SMA prediction. Above this energy, although the qualitative features of forbidden and allowed bands are still seen, the detailed structure of the exact transmission probability does not agree with the SMA prediction.

Figure 6.4 plots the exact calculated conductance for the ten-bend staircase tube [30] with separation $l = 1$ between adjacent bends, plotted in units of the "quantum" for conductance $G_0 = 2e^2/h$. The familiar plateaus in the conductance are observed to occur with the opening of each new transverse mode, at $k = n\pi$. Because of the significant reflection present in a system with sharp bends, the conductance does not increase in jumps of magnitude $2e^2/h$ as each new transverse mode opens. Above the second transverse channel threshold, the conductance exhibits the following qualitative features. First, the broad and sharply-defined forbidden zones so prominent in the near-

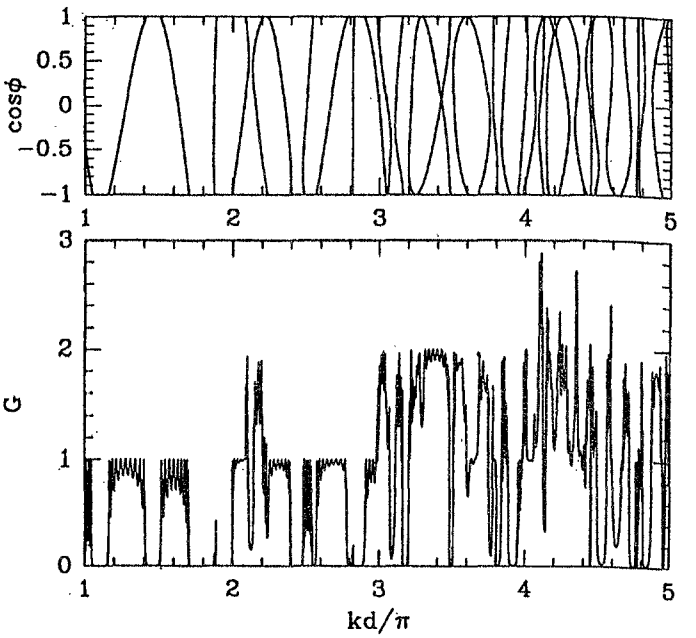

Fig. 6.4. Electron conductance for ten-bend staircase system, shown in inset of Fig. 6.1, with separation $l = 1$ between adjacent bends. Upper curve: cosine of exact Bloch phase ϕ defined in (6.17), shown in those regions where ϕ is real. Lower curve: conductance G, in units $G_0 = 2e^2/h$, vs. wave number k/π. From [80]

threshold conductance become less and less common as the energy increases. The width of the forbidden zones decreases markedly for energies above the second transverse channel threshold. In the energy regions between the thresholds for transverse channels, the conductance exhibits plateaus which describe the average behavior of G. Superimposed on these plateaus are a series of sharp maxima and minima, with occasional sharp increases in conductance, of magnitude approximately G_0, or very deep minima (essentially zeroes) in the conductance.

The qualitative features of the conductance can be understood in terms of the Bloch phase(s) ϕ for the many-channel problem. These are the solutions of the eigenvalue equation

$$\mathbf{U}\psi = \exp(i\phi)\mathbf{V}\mathbf{F}\psi \quad , \tag{6.17}$$

where the matrices appearing in (6.17) are given in (2.30) and (5.34). The eigenphases $\pm\phi$ appear as conjugate pairs, where each real pair denotes an allowed channel through which electrons can propagate. The upper curve in Fig. 6.4 shows the cosines of the Bloch phases for the ten-bend staircase tube, when ϕ is real. We can make the following general statements regarding the conductance in regions above the second transverse channel threshold.

- **Local Peak Conductance:**
  - It is apparent that the local peak conductance, in units of $G_0 = 2e^2/h$, is essentially equal to the number of allowed channels available to the electrons. When no real channel is available, one has forbidden minibands and essentially zero conductance. When one channel is allowed, the conductance is approximately G_0. For those energies where two (or three) pairs of Bloch phases ϕ are allowed, the peak conductance increases to about two (three) times G_0.
  - Superimposed on this averaged behavior are the very sharp oscillations discussed previously for low-energy transmission.
- **Forbidden Regions:**
  - Below the second transverse mode ($k < 2\pi$), there are very well defined forbidden regions for transmission. In the region below the third transverse mode, $2\pi < k < 3\pi$, the miniband structure is still visible in some regions. However, as the energy increases, the forbidden regions tend to disappear. This occurs because a forbidden band will exist only if there is no allowed path in *any* of the open channels. The existence of an allowed path depends on the longitudinal wave number α_n of (2.3), which is different for every transverse channel. When the energy is above the second transverse threshold, the additional number of open transverse modes makes it more and more likely that at least one allowed electron path will exist.
  - Sharp maxima and minima are still seen in the transmission, but the "*forbidden zones*" for the electrons become fewer in number and narrower in energy. Thus, the miniband structure, characterized by broad and well-defined forbidden zones, will be confined mainly to the region between the first and second transverse modes for the system.
  - The detailed structure of the conductance for the "staircase" and "snake" configurations is quite similar below the second transverse mode, as predicted by the single-mode approximation, but differs substantially above the second transverse mode.

The presence of bound states will lead to conductance below threshold, which is not shown in Fig. 6.4. From Fig. 6.1, for this geometry one would expect seven peaks below conductance threshold, and some resonant structure just above conductance threshold, arising from the bound and quasibound states, respectively, in the ten-bend tube with $l = 1$. The subthreshold conductance tunneling peaks will be visible only when the external leads are sufficiently short.

Figure 6.5 shows the conductance for a multibend snake quantum wire, as calculated by Wang [104]. Here the distance between bends is different in the horizontal and vertical directions, so the basic "cell" is a double-bend structure, shown schematically in Fig. 5.26. It consists of squares of side $W = 80$ nm, with a vertical straight section of length 40 nm, and horizontal straight legs of length 35 nm. This basic structure is connected to form two-cell (four-bend) and three-cell (six-bend) structures. At each end of the wire,

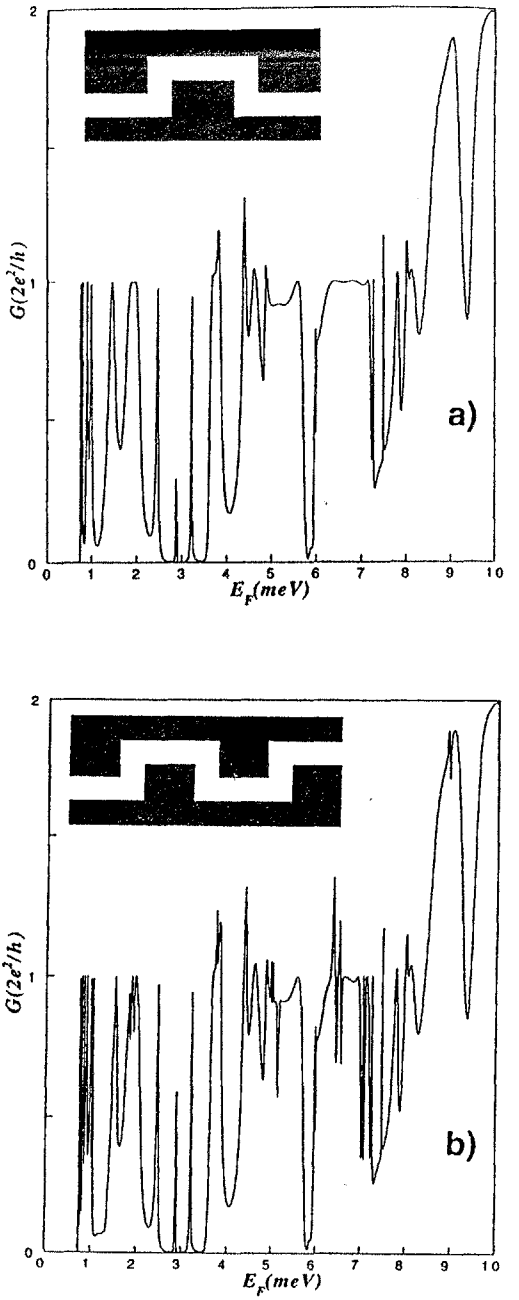

Fig. 6.5. Electron conductance G vs. electron energy E_F in meV, for a "snake" system with several right angle bends. The unit cell is a double bend quantum wire with dimensions given in Fig. 5.24. (a) Conductance for two cells joined in snake series, as shown in inset. (b) Conductance for three cells in series. From [104]

an additional straight section of length 35 nm is included. The conductance for the two-bend quantum wire was shown in Fig. 5.24. Figures 6.5a and 6.5b show the corresponding graphs of conductance vs. electron energy. The threshold for conductance is $E_1 = 0.88$ meV, and the second and third transverse modes open up at $E_2 = 3.51$ meV and $E_3 = 7.89$ meV, respectively.

The conductance shows sharp subthreshold peaks due to the bound states in the multibend system. For the two-bend wire with this geometry, there is one true bound state and a second quasi-bound state right at the threshold for conductance. For systems with four or more bends, some very sharp structure is seen in the conductance just above threshold; this structure arises from quasi-bound states in the wire. This can be seen for example in Fig. 6.5b. Comparing Figs. 5.24 and 6.5, a forbidden band is beginning to form in the region below the second transverse mode. For example, the two-bend quantum wire has conductance minima just above $E_F = 1$ meV, and in the region $E_F \sim 2.7$ meV. In Fig. 6.5b, these minima have become deeper and broader for the six-bend wire. If the number of cells was increased, these minima would broaden to form forbidden bands. The miniband structure, which arises in systems composed of many identical cells in series, is already evident in quantum wires with as few as three cells.

Another interesting feature is the deep, sharp minimum in the second conductance plateau, at energy $E_F = 5.90$ meV (arrow in Fig. 5.24). Pronounced vortex structure is observed in the velocity distribution at energies very close to this minimum. This sharp minimum in conductance also persists in the four-bend and six-bend structures shown in Fig. 6.5 [104]. Both the location and depth of this conductance minimum persists, no matter how many cells are joined together. This behavior is just what was predicted from our SMA approximation of transmission in periodic systems. If at a given energy a single cell has 100% reflection, then total reflection will be observed at this energy when it is joined in series with any number of additional cells, since after the first cell there is no transmitted flux.

6.3.2 Transmission in the "Quantum Dot Superlattice"

The preceding section has analyzed the qualitative features of transmission in systems with a series of identical right angle bends. For tubes which have a series of identical T-stubs or quantum dots, one would predict the same qualitative features as were found for right angle bends. In quantum heterostructures, such a system is called a "*quantum dot superlattice.*" The term *superlattice* is used since the system has an underlying lattice structure (*i.e.*, the lattice of atoms formed by the semiconductor) with an additional periodic structure (the series of quantum dots) superimposed on the atomic lattice.

If the external straight leads are sufficiently short, one expects to see subthreshold conductance peaks arising from resonant tunneling through the bound states of the system. Above the continuum threshold, plateaus should be seen in the average value of the conductance. As more identical cells are

added in series, forbidden bands should develop where the conductance is essentially zero. In between the forbidden bands, one should see allowed bands characterized by very sharp maxima in the conductance, at energies where integer half waves in the longitudinal momentum can be supported in the wire. These forbidden and allowed minibands should be particularly strong in the region between conductance threshold and the opening of the second transverse mode. Haug, Lee and Hong [144, 145] observed significant fluctuations in experimental measurements of a system of identical T junctions. They suggested that the observed peaks could arise from resonant tunneling through bound states in this system.

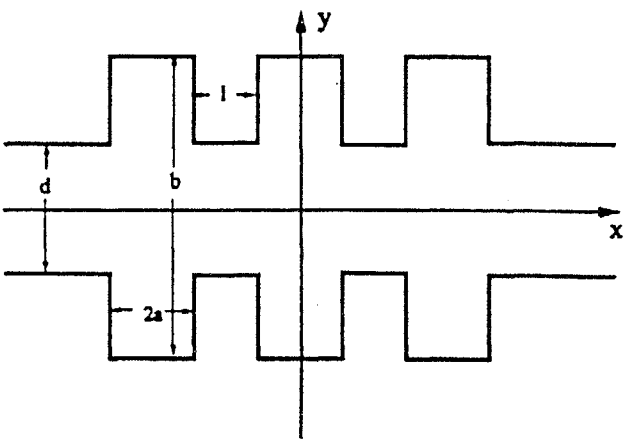

Fig. 6.6. Schematic picture of the "quantum dot superlattice" structure, a series of identical quantum dots of width $2a$ and height b connected by straight sections of length l and width $d = 1$

In this section we will analyze transmission and conductance in a periodic 2-D system composed of a series of identical quantum dots, connected by straight sections. The basic geometry is shown in Fig. 6.6. Straight sections normalized to width $d = 1$ and length l couple rectangular cavities of width $2a$ and total height b. The origin of the system is placed at the center of the first cavity. As was discussed in Sect. 5.3, the symmetry of the system, with respect to reflection about the longitudinal or x axis, insures that the even and odd parity transverse modes do not mix. Thus one can independently calculate scattering properties for the even and odd-parity modes. The auxiliary matrices $\mathbf{A}$ and $\mathbf{B}$ for an individual quantum dot were calculated in (5.29) and (5.31).

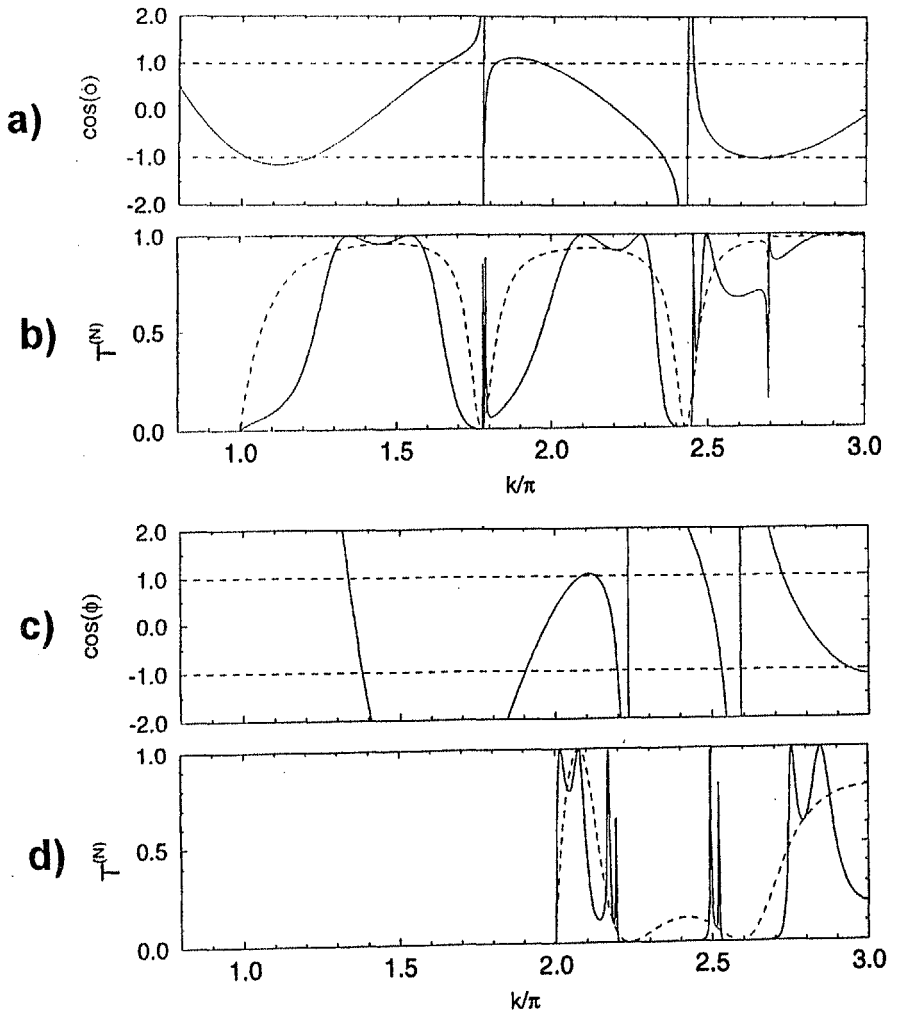

Fig. 6.7. (a) SMA prediction for the Bloch phase $\cos(\phi)$ for even parity modes in a quantum dot, vs. wave number k/π. The relative dimensions of the quantum dot are $2a = 1$, $b = 2$, $l = 0.2$. (b) Transmission coefficient for even parity modes through a series of quantum dots with dimensions as in part (a). Dashed curve: transmission coefficient $T^{(1)}$ through a single quantum dot; solid curve: transmission $T^{(3)}$ through three quantum dots in series. (c) Bloch phase for odd parity modes in this quantum dot. (d) Transmission through odd parity modes, with same notation as in part (b)

Ji and Berggren [101] made theoretical calculations of the conductance for zero temperature electrons through a series of identical quantum dots. Each cell of the quantum dot system of Ji and Berggren had a cavity of width 100 nm and height 200 nm, connected by straight sections with width 100 nm and length 20 nm. Normalized to unit channel width, this system corresponds to cell parameters $2a = 1$, $b = 2$ and $l = 0.2$. The geometry for these quantum dots is similar (although not identical) to that discussed for quantum dot bound states in Figs. 5.13 and 6.2. Figure 6.7 shows the cosine of the Bloch phase ϕ and the transmission coefficients predicted in SMA, as a function of the wave number k/π. Figure 6.7a shows $\cos(\phi)$ for the even parity modes. The solid curve in Fig. 6.7b gives the transmission coefficient $T^{(3)}$ for transmission through three cells, and the dashed curve shows the transmission through a single cell. Figs. 6.7c and 6.7d show the corresponding cosine of the Bloch phase and transmission coefficients for the odd parity modes.

The SMA predictions for transmission through three quantum dots are qualitatively similar to the results for transmission through a series of right angle bends. The transmission probability is very small where $|\cos(\phi)| > 1$, and oscillates in regions where $\cos(\phi)$ varies between -1 and $+1$. The transmission through three cells is beginning to develop the forbidden bands characteristic of propagation through a large series of cells. For the even parity modes, Fig. 6.7a shows that $\cos(\phi)$ has poles at $k/\pi \approx 1.78$ and $k/\pi \approx 2.43$. From the single-mode approximation expression for the cosine of the Bloch phase

$$\cos(\phi) = \frac{B}{A}\cos(\alpha l) - \frac{A^2 - B^2 + \alpha^2}{2\alpha A}\sin(\alpha l) \quad , \tag{6.18}$$

poles of $\cos(\phi)$ occur at zeroes of A. As will be seen shortly, the zeroes of A occur because of interference between contributions from various cavity modes in the quantum dot, as seen in (5.31).

Figure 6.8 shows the calculations of the conductance from Ji and Berggren [101], for zero temperature electrons through one, two or three quantum dots in series, as a function of the Fermi energy E. The arrows denote the transverse channel thresholds. The arrow at $E = 0.56$ meV denotes the opening of the continuum threshold, corresponding to $k/\pi = 1$, and the arrow at $E = 2.25$ meV shows the opening of the second transverse mode, corresponding to $k/\pi = 2$ [5]. Figure 6.8a shows the conductance for a single quantum dot. There is a single subthreshold peak, labeled E_1, corresponding to the single bound state in this system. The conductance reaches the value $G_0 = 2e^2/h$ at this energy [6]. The conductance then rises to a rather broad plateau, with conductance $G \approx G_0$.

[5] To compare results in Figs. 6.7 and 6.8, use the correspondence $k/\pi = \sqrt{E/E_{th}}$, where $E_{th} = 0.56$ meV.

[6] Note that the external leads in this system are very short, which allows one to see the subthreshold conductance peaks.

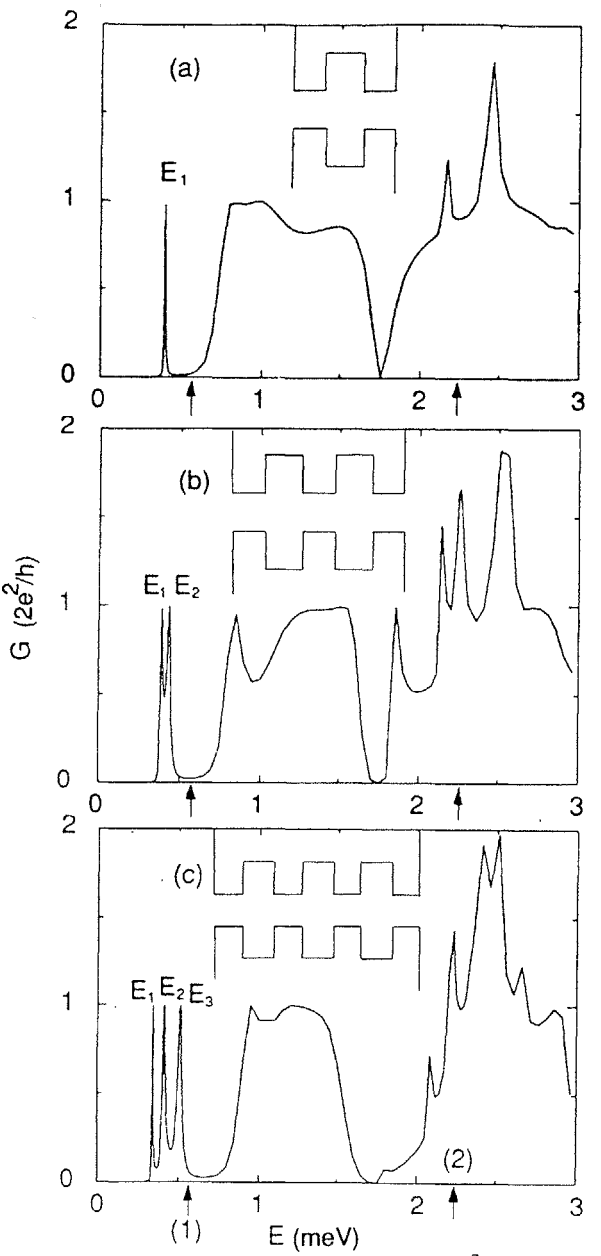

Fig. 6.8. Conductance G in units $G_0 = 2e^2/h$ for zero temperature electrons as a function of the Fermi energy E, from [101], for the system of quantum dots shown schematically in Fig. 6.6. Channel width and stub width are 100 nm, stub height 200 nm, distance between stubs 20 nm (relative dimensions are identical to those in Fig. 6.7). (**a**) Conductance for a single quantum dot. (**b**) Conductance for two quantum dots in series. (**c**) Conductance for three quantum dots. Arrows denote location of conductance threshold (1), and threshold for second transverse mode (2). E_j $(j = 1, 2, 3)$ denote energies where subthreshold resonant tunneling through bound states occurs

Above the continuum threshold, the exact conductance is obtained by adding the even parity and odd parity transmission coefficients from the single-mode approximation, shown in Fig. 6.7 (for a single quantum dot, these are the dashed curves in Fig. 6.7b and 6.7d). The zero in the exact calculation of the conductance occurs at nearly the same energy as predicted in the SMA calculation. Furthermore, from Fig. 6.7a and 6.7c, the local peak values of the conductance agree with our prediction that they should equal $\overline{G} \approx n(G_0) = n(2e^2/h)$, where n is the number of allowed paths through the system, as given by the number of pairs of real Bloch phases ϕ at that energy. In Fig. 6.8a the conductance through a single quantum dot goes to zero at $E \sim 1.8$ meV. From Fig. 6.7a, it is clear that the zero in conductance arises because the Bloch phase $\cos(\phi)$ has a pole at this energy (corresponding to $k/\pi \sim 1.78$). Since the transmission is very small when $|\cos(\phi)| > 1$, the pole in the Bloch phase produces the zero seen in the conductance at this energy.

The theoretical conductance for a tube with two quantum dots is shown in Fig. 6.8b. Two sharp subthreshold peaks labeled E_1 and E_2 correspond to the two bound states in this system. The zero in transmission below the second transverse mode, seen in the case of a single quantum dot, is beginning to broaden. The resonant structure above the second transverse mode is more pronounced for two quantum dots, compared with one quantum dot; this is seen by comparing Figs. 6.8a and 6.8b. This pattern continues with the addition of a third quantum dot as shown in Fig. 6.8c. There are now three bound states which appear as sharp spikes below conductance threshold, and the region of energy below 2 meV is turning into a forbidden miniband. The structure of the bound states was discussed in Sect. 5.3, and the probability densities for the three bound states in a series of quantum dots with similar geometry was shown in Fig. 6.2.

As was discussed earlier in this chapter, the formation of minibands in these systems can be understood by analyzing the Bloch phase for a single quantum dot. Regions which have small transmission probability for a single cell, because there is no allowed path for the particle at this wave number, develop into regions where the transmission probability $T^{(N)} \approx 0$ for a system of N cells in series. As was observed for the case of tubes with right angle bends, miniband structure emerges even for systems containing a small number of quantum dots in series. From Fig. 6.8, for example, recognizable miniband structure is already present for a system with only three quantum dots.

Figure 6.9 shows the theoretical transmission coefficients through a system with ten quantum dots. In this figure the geometry is chosen to agree with that originally calculated by Brum [141], and also studied by Wu, Sprung and Martorell [105]. When the width of the external leads is normalized to one, the relative system dimensions are $2a = l = 1$ and $b = 1.6$. Figure 6.9a shows the cosine of the Bloch phase for the even parity modes, and Fig. 6.9b gives the transmission coefficient, for even parity modes, in single-mode

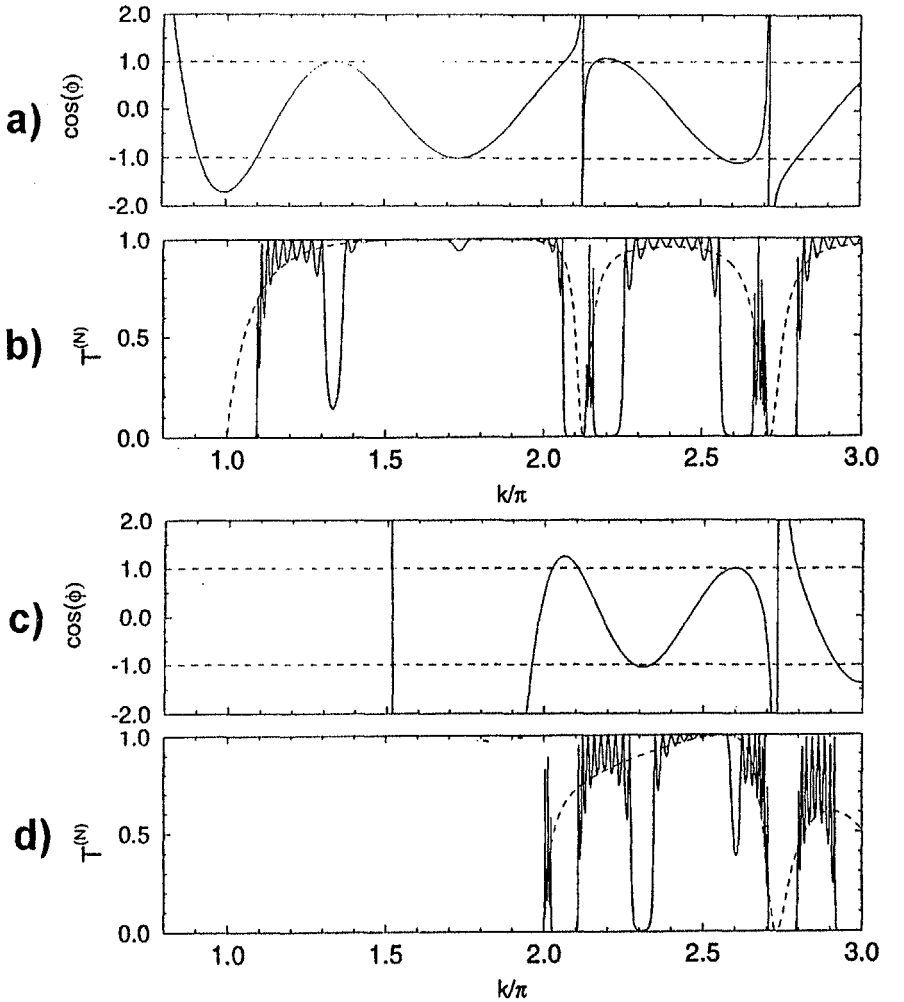

Fig. 6.9. (a) SMA estimate of Bloch phase $\cos(\phi)$ for even parity modes in a quantum dot superlattice, vs. wave number k/π. Relative dimensions of quantum dot are $2a = l = 1$, $b = 1.6$. (b) Transmission coefficient for even parity modes. Dashed curve: transmission $T^{(1)}$ through a single quantum dot; solid curve: transmission $T^{(10)}$ through ten quantum dots in series. (c) Bloch phase for odd parity modes in this quantum dot. (d) Transmission through odd parity modes, with same notation as in part (b)

approximation. The dashed curve gives the transmission $T^{(1)}$ through a single dot, and the solid curve is the transmission $T^{(10)}$ through ten quantum dots in series. Figs. 6.9c and 6.9d show $\cos(\phi)$ and $T^{(N)}$ for the odd parity modes, respectively.

For the even parity modes, the transmission coefficient for a single quantum dot is nearly one over a fairly broad region. $T^{(1)}$ has zeroes at $k/\pi = 2.14$ and $k/\pi = 2.72$. These occur at values where $A = 0$. As was discussed previously, in single-mode approximation poles arise in $\cos(\phi)$ whenever $A = 0$. The transmission coefficient $T^{(10)}$ develops two forbidden bands in the region around the zero in the transmission through a single dot. Between the two forbidden bands is a narrow region with very sharp structure in the transmission coefficient. This was explained by Wu *et al.* [105]. From (5.31) it is clear that an element of the matrix **A** will have a family of poles at values

$$K_r = \frac{j\pi}{2a}, \quad j = 1, 2, \ldots \quad , \tag{6.19}$$

for a given mode r. From (5.29), this corresponds to wave numbers

$$\frac{k^2}{\pi^2} = \left(\frac{j}{2a}\right)^2 + \left(\frac{r}{b}\right)^2 \quad . \tag{6.20}$$

Equation (6.20) is just the condition for confined modes in a rectangular cell of dimensions $(2a, b)$. In (6.20) r takes on odd (even) integer values for the even (odd) parity modes.

If only a single mode contributed to the matrix **A** in (5.31), a given matrix element would have a series of poles but no zeroes. The zeroes of the elements of the matrix **A** arise because of interference between modes with higher values of r and those with lower r. For example, for the geometry being studied in Fig. 6.9 ($2a = l = 1$, $b = 1.6$), the poles in **A** corresponding to the lowest even parity $r = 3$ modes occur at $k/\pi = 2.125$ ($r = 3, j = 1$) and 2.74 ($r = 3, j = 2$), or $(k/\pi)^2 = 4.52$ and 7.52, respectively. The poles of $\mathbf{A}_{11}$ are very close to the poles of $\cos(\phi)$ (*i.e.*, the zeroes of $\mathbf{A}_{11}$) seen in Fig. 6.9a. The zeroes in $\mathbf{A}_{11}$ arise because of interference between the $r = 1$ and $r = 3$ modes. The location of the zeroes of **A** is very close to the position of the poles in the higher modes. For the even (odd) parity modes one would have $r \geq 3$ ($r \geq 4$). The poles in $\cos(\phi)$ can thus be predicted rather accurately from the location of poles in **A** given by (6.20).

This is shown in Fig. 6.10, which plots the lowest even parity and odd parity matrix elements, $\mathbf{A}_{11}$ and $\mathbf{A}_{22}$, respectively, vs. the quantity k^2/π^2, for the quantum dot with dimensions identical to those in Fig. 6.9. The matrix element has a series of poles given by (6.20). For example, the zero of $\mathbf{A}_{11}$ (the solid curve in Fig. 6.10) at $k/\pi \approx 2.71$ ($(k/\pi)^2 \approx 7.36$) arises because of interference between the $r = 3$ mode which has a pole slightly above this value, and the lower $r = 1$ mode. Similarly, the odd-parity matrix element $\mathbf{A}_{22}$ (the dashed curve in Fig. 6.10) has a zero at $k/\pi \approx 2.73$ ($(k/\pi)^2 \approx 7.46$)

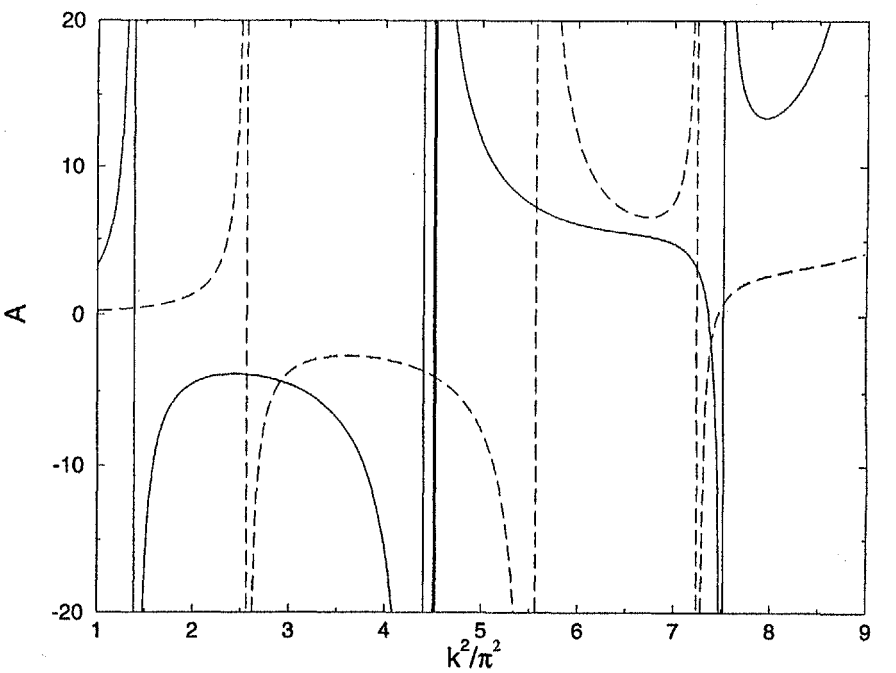

Fig. 6.10. Elements of the matrix **A** defined in (2.31) for the quantum dot whose relative dimensions are given in Fig. 6.9. Solid curve: even parity matrix element A_{11}; dashed curve: odd parity matrix element A_{22}

which results from interference between the $r = 4$ mode with a pole slightly below this value, and the $r = 2$ mode. As pointed out by Wu *et al.* [105], a one-dimensional approximation to this problem would predict a single broad forbidden band in this region. However, the interference, which arises from the propagation of the particle inside the cavity in various modes, splits the forbidden region into two forbidden bands, separated by a narrow region where the transmission probability varies extremely rapidly. This narrow, rapidly-varying region of transmission is a true two-dimensional effect arising from this interference, and cannot be explained in a quasi 1-D picture, where we would neglect interference between different modes inside the quantum dot.

Figure 6.11 shows the exact calculations of the theoretical conductance through a system with ten quantum dots, vs. the electron energy E in meV, as calculated by Brum [141]. Figure 6.11a and Fig. 6.11b are the conductance in the even and odd-parity modes, respectively. Below the third transverse channel threshold at $k = 3\pi$, the exact conductance resembles closely the

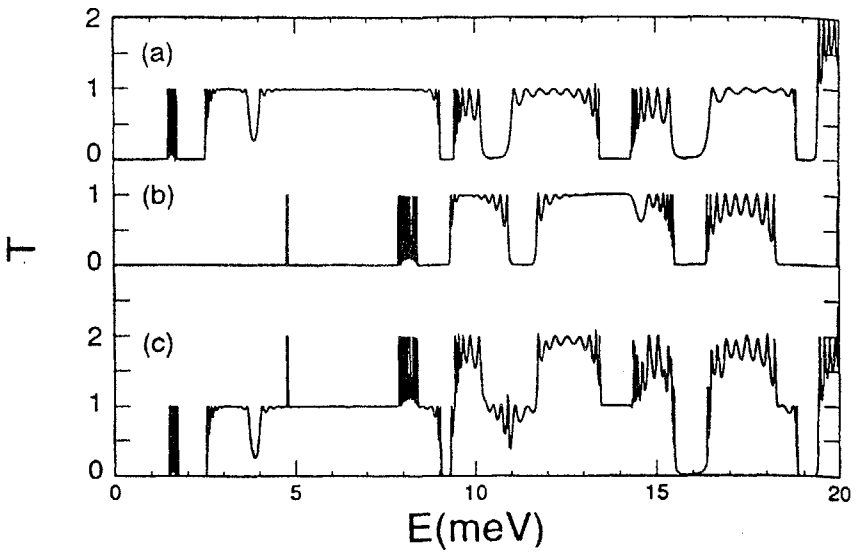

Fig. 6.11. Exact calculation of the theoretical conductance through a quantum-dot superlattice with ten dots, vs. the electron energy E, in meV. Dimensions of the structure: channel width = stub width = 50 nm; total height of dot = 80 nm (same relative dimensions as Fig. 6.9). From [141]

SMA predictions shown in Figs. 6.9b and 6.9d [7]. To compare with the SMA results shown in Fig. 6.9, use the correspondence $k/\pi = \sqrt{E/E_{th}}$, where $E_{th} \sim 2.15$ meV. In the exact calculation, the allowed band of states between two forbidden regions, which occurs at roughly $9.5 - 10.2$ meV and $14 - 15$ meV, correspond to the sharp bands of states seen in Fig. 6.9b between two forbidden regions. In Fig. 6.11a a series of sharp sub-threshold conductance peaks are seen due to quantum tunneling through the bound states in this system. When the higher transverse channels open up, the averaged conductance in a given region can be interpreted as showing the number of real Bloch phases which exist at that energy.

Figure 6.9c and Fig. 6.11 show an odd-parity bound state at $k/\pi \approx 1.52$ ($E \sim 5$ meV). This is a "*bound state in the continuum.*" It occurs above continuum threshold for the even parity modes, but is a real bound state because the even and odd parity modes are not coupled. If one could induce a transition between even and odd parity modes at this energy, it would be possible to produce a long-lived "*trapped*" state. For example, imagine a cavity with these dimensions, coupled to long external leads. At this energy

[7] Since the even and odd parity states do not mix, the SMA conditions are valid here until the opening of the third transverse channel.

an even parity state can travel freely through the tube. But if a perturbation were applied which excited the particle to the odd parity bound state, such a state would be trapped inside the cavity. In a realistic cavity this state could escape only by coupling between the odd and even parity modes, resulting either from small asymmetries in the geometry or small admixtures of the "wrong" parity state. Such a state can exist only if the symmetry of the system is broken. These highly localized resonances are similar to effects produced by "defects" in an otherwise symmetric system. Defect states will be discussed in the next section, and in our discussion of photonic crystal modes in Chap. 7.

The formation of allowed and forbidden energy bands makes it possible to fabricate quantum heterostructure systems which will mimic the action of many common circuit devices, on a much smaller length scale. For example, Datta [147] and also Datta and McLennan [168] discuss several nanostructures which are the quantum analogs of conventional optical or microwave devices. The proceedings of the Symposium on Nanostructure Physics and Fabrication [4] contains a number of talks from a session on quantum devices and transistors.

6.4 Defects in Quantum Wire "Crystals"

Earlier in this chapter it was shown that a 2-D system composed of a finite series of identical cells produces quasi-crystalline behavior. Since each cell serves as the site of an attractive potential, the net effect of this series of potentials produces a series of forbidden bands in the transmission, separated by allowed "minibands" of rapidly oscillating transmission peaks. In this section, we consider the qualitative effects which occur when one or more cells in this series are modified. Such a modification breaks the symmetry of the system, and has the equivalent effect as the introduction of a "*defect*" into a crystal. Our discussion of these effects will be extremely brief. We will discuss only two effects, and will restrict our discussion to 1-D effects in a very simple geometry.

To demonstrate the qualitative effects of a defect in a quantum wire system with finite periodic structure, we consider transmission through a sequence of N 1-D T-stubs. Each cell is a T-stub of height L coupled to a straight section of length l, in the limit where the channel width is negligible with respect to L. This picture was previously introduced in Sect. 5.3.1 for a single T-stub. In this periodic system, the 2×2 transfer matrix $\mathbf{M}$ for an individual cell was shown by Xia [83] and Deo and Jayannavar [85, 86] to be the product of two 2×2 matrices, one for the stub and the second for the straight section,

$$\mathbf{M}(L) = \begin{pmatrix} 1 + \frac{i}{2}\cot(kL) & \frac{i}{2}\cot(kL) \\ -\frac{i}{2}\cot(kL) & 1 - \frac{i}{2}\cot(kL) \end{pmatrix} \cdot \begin{pmatrix} e^{-ikl} & 0 \\ 0 & e^{+ikl} \end{pmatrix} , \qquad (6.21)$$

where in (6.21) k is the longitudinal wave number. The cells are numbered sequentially from left to right. The length of the j^{th} stub in this series (the "*defect cell*") is changed, $L_j = L_d \neq L$. The resulting transfer matrix for the quantum crystal containing a total of N cells, with a defect cell at location j, is

$$\mathrm{M}^{(N)} = \mathrm{M}(L)^{(j-1)}\,\mathrm{M}(L_d)\,\mathrm{M}(L)^{(N-j)} \quad . \tag{6.22}$$

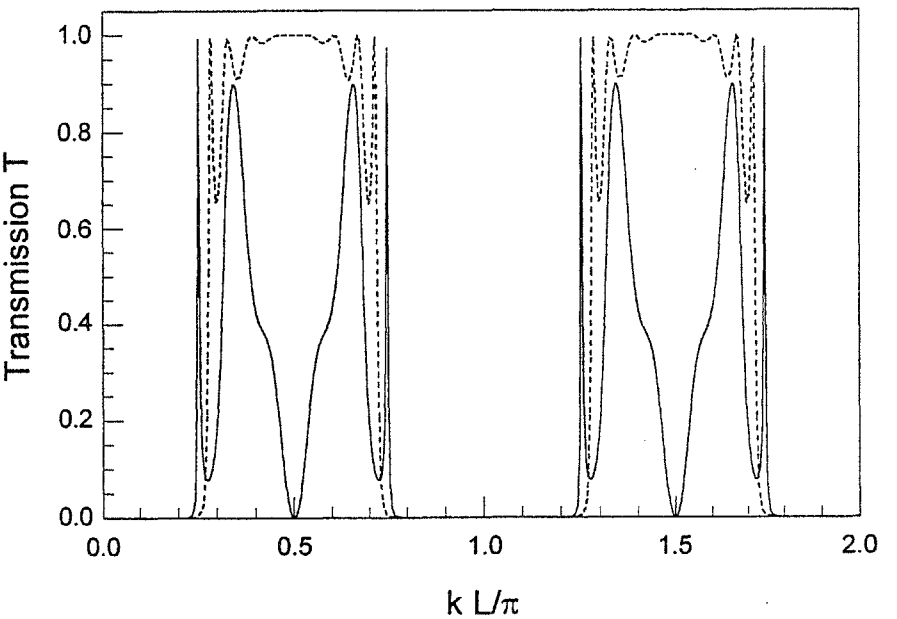

Fig. 6.12. Transmission coefficient through a lattice with nine 1-D T-stubs of length $L = 1$ coupled by straight sections $l = 1$, vs. the wave number kL/π. Dashed curve: all T-stubs identical. Solid curve: center "defect" T-stub has $L_d = 2$

The resulting transmission matrix differs from that for the "perfect crystal," the completely symmetric periodic structure where all the cells are identical. Figure 6.12 plots the transmission coefficients vs. kL/π, for a quantum wire with a total of nine cells with the defect T-stub in the center. This was originally calculated by Deo and Jayannavar [86]. The cells have $L = l = 1$ and the defect stub has $L_d = 2$. The dashed curve is the result when all nine cells are identical; the solid curve is the result with one defect stub in the center.

The defect has a dramatic effect on the transmission coefficient. The general periodic structure seen in perfect lattices – allowed regions separated by forbidden gaps – is still preserved in this geometry. However, the pres-

ence of the defect stub produces two significant qualitative changes in the transmission.

- **Complete Reflection at Specific Wave Numbers:** The presence of the defect produces additional zeroes in the transmission. For this particular geometry, the zero appears in the center of the "allowed" region. From (6.22) we can see that the overall transmission will have a zero at any energy where either the single cell transfer matrix for the basic cell **M**, or the defect cell $\mathbf{M}_d$, has a transmission zero. At such an energy, there will be complete reflection from the cell in question and hence zero transmission through the entire crystal. Transmission zeroes from the defect cell which occur in "forbidden" regions will make very little qualitative difference in the transmission. However, it is possible that adding a defect will produce additional zeroes in the allowed regions of the transmission. Furthermore, for a 1-D system the location of these new transmission zeroes will be independent of the location of the defect in the crystal. Since by judicious choice of the defect stub length, one can produce a transmission zero at any desired energy inside an allowed band (see the discussion in Sect. 5.3.1), by introducing a defect one could insure that certain predetermined wave numbers inside an allowed band would experience total reflection.
- **Resonances in Forbidden Zones:** In addition, the defect produces additional sharp peaks, or transparent points, in the forbidden region of the perfect crystal. For this geometry, these transparent points lie just outside the allowed region for the perfect crystal (they are the solid peaks just outside the allowed region defined by the dashed lines). Thus, by breaking the symmetry of the periodic structure it is possible to produce wave numbers with complete reflection in "allowed" regions, and isolated points with relatively large transmission in "forbidden" regions.

The detailed transmission properties are highly dependent on the precise geometries of the system, and both the length and location of the defect stub. For the case shown in Fig. 6.12, since the stub lengths and separations are all rational fractions, the transmission in this model is periodic. For the dimensions shown here, the period of the argument kL/π is one. Furthermore, the defect length $L_d/L = 2$ was chosen so that the zero in transmission from the defect stub was located right in the middle of the allowed region. Deo and Jayannavar [86] examined transmission for several different stub geometries, and Gu [87] examined the effect of varying the lengths of several of the stubs in a lattice of 1-D cells.

6.4.1 Trapped Modes in Band Gaps

In the preceding section, it was shown that the presence of a single "defect," produced by modifying the properties of a single cell in a lattice of otherwise identical cells in series, could produce states which lie in the "forbidden" or "band gap" region of the perfect crystal. In this case, the defect cell contains

a resonance which lies in the forbidden region of the crystal. This produces a sharp peak inside the cell in question at the resonant energy. However, since at this energy there is no allowed mode for propagation through the crystal, the magnitude of the resonant wave function will decrease exponentially as it passes through the other cells of the system.

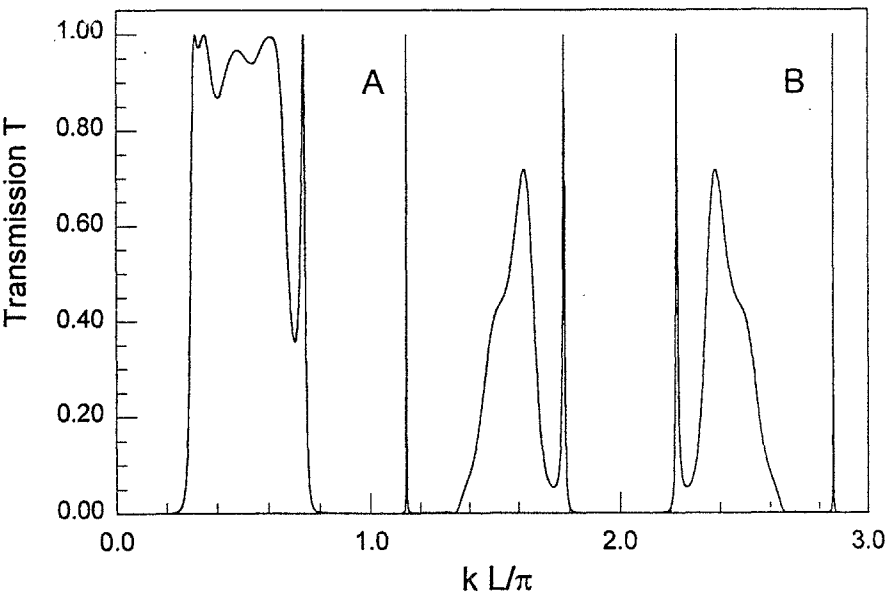

Fig. 6.13. Transmission coefficient vs. wave number kL/π through a lattice of seven 1-D T-stubs coupled by straight sections with length $l = 1$. All stubs have length $L = 1$, except for the center "defect" T-stub which has $L_d = 0.75$

Figure 6.13 plots the transmission coefficient vs. kL/π, for a system with $N = 7$ one-dimensional T-stubs connected by straight sections of length l, as was discussed in the preceding section. The cells have $L = l = 1$, except for the center defect stub which has $L_d = 0.75$. The sharp peaks labeled A and B in Fig. 6.13 (originally calculated in [86]) show the transmission peaks which denote resonant states trapped in the defect stub. Such states represent a type of "bound state in the continuum." As the number of T-stubs in the lattice increases, the transmission peaks become extremely sharp

because of the exponential decrease of the wave function in the "normal" cells. When there are a large number of T-stubs, the transmission peaks for these states become exceptionally narrow. They would never be seen in experiments with detectors of moderate resolution. Furthermore, these sharp peaks occur only for electron temperature $T = 0$. For finite temperatures, the smearing of these peaks would essentially make them disapper. Nevertheless, these trapped resonant modes inside the defect stubs, which occur at energies within "forbidden bands" in the crystal, produce sharp spikes in the density of states of the system at energies corresponding to the resonant modes. This is true even in systems with a large number of cells, where the transmission peaks corresponding to these states can no longer be seen [86].

In Fig. 6.13, since all dimensional ratios are rational fractions, the transmission coefficient in this 1-D model is periodic in the variable kL/π with period four. The perfect crystal has transmission zeroes at $kL/\pi = n$ for integer n, while the defect stub produces zeroes at $kL/\pi = 4n/3$. The transmission peak at A occurs at a value of k approximately midway between the $n = 1$ zero for the perfect crystal and the $n = 1$ zero from the defect stub.

Modes localized in the vicinity of a defect in a semiconductor superlattice have been observed in an ingenious experiment by Capasso *et al.* [169]. The authors produced a series of alternating planar layers of AlInAs and GaInAs, by molecular beam epitaxy. A transmission electron micrograph of a cleaved cross-section of the structure is shown schematically in Fig. 6.14a. The superlattice was composed of alternating narrow layers of GaInAs and AlInAs. The basic structure consisted of a 16 Å thick layer of GaInAs followed by a 39 Å layer of AlInAs (the gray and black layers, respectively, in Fig. 6.14a). In the center of this structure was a single "wide" 32 Å layer of GaInAs, with six pairs of GaInAs-AlInAs layers on either side.

The alternating bands of AlInAs and GaInAs layers would produce a one-dimensional lattice, quite similar to the Fabry–Perot interferometer which is produced from a series of regularly spaced layers of materials with two different dielectric constants [170]. The additional wide GaInAs layer in the center of the device plays the role of a "defect" state, since it breaks the symmetry of the system. The perfect lattice would produce a series of allowed and forbidden energy bands. As we have outlined, introduction of a defect will produce forbidden lines for certain energies in the allowed energy bands, and can also produce trapped resonant modes localized in the defect cells. The energies corresponding to these trapped modes lie within the forbidden bands of the perfect quasi-crystal.

The resulting energy levels are shown in Fig. 6.14. The structure possessed an electron ground state at $E_1 = 204$ meV. There was then an energy gap before the first conduction miniband of allowed states, at conduction band edge E_{c_1}. This was followed by a gap of width 266 meV, and then a second conduction miniband. Inside this energy gap is a state at $E_2 = 560$ meV. This is an allowed state in the 32 Å GaInAs "defect" layer. However, since it lies

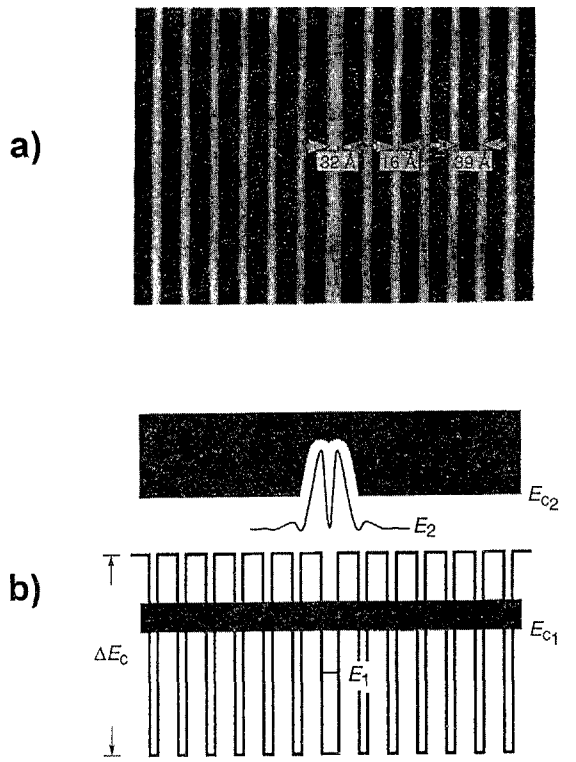

Fig. 6.14. (a) Transmission electron micrograph of GaInAs-AlInAs heterostructure. A superlattice is formed from alternating planes of 16 Å thick layers of GaInAs (gray) separated by 39 Å thick layers of AlInAs (black). In the center of the structure is a single 32 Å wide layer of GaInAs. (b) Schematic picture of energy levels of GaInAs-AlInAs structure. The system has a ground state at energy $E_1 = 204$ meV, and conduction bands with bandheads E_{c_1} and E_{c_2}. The state at energy $E_2 = 560$ meV is localized in the central "defect" GaInAs layer. Its wave function decays exponentially in the rest of the superlattice "crystal." From [169]

in a forbidden region in the GaInAs-AlInAs superlattice, the wave function for this state is large in the vicinity of the central GaInAs layer, but decays exponentially in the surrounding AlInAs-GaInAs layers.

The state at energy E_2 represents a trapped mode localized in the vicinity of the defect in the otherwise perfectly periodic "*quasicrystal*." Capasso *et al.* observed the state by optically exciting electrons from the bound state at energy E_1. The resulting absorption spectrum had a sharp peak centered at energy 360 meV, in excellent agreement with the calculated value $E_2 - E_1 = 356$ meV. The energy and width of the observed resonance could be adjusted by changing the layer widths and the number of layers in the superlattice

[171, 172]. The shape of the absorption peak was also in qualitative agreement with theoretical expectations.

The quantum heterostructure produced by Capasso and collaborators [169] closely resembles optical systems. In fact, the dimensions of the narrow semiconductor layers were tailored so that they would act like "mirrors" on the electron wave function. The resulting reflections produce a constructive interference which will support a localized state at the appropriate energy. A very similar optical device was produced by Yablonovitch *et al.* [173, 174]. They constructed a "lattice" from machined plastic, and introduced defect states in the lattice. The resulting defect states were studied by microwave diffraction.

The states produced by defects in periodic systems have many potential applications in quantum heterostructures. Our brief discussion in this section is simply meant to illustrate the type of effects which can occur for defects in otherwise periodic two-dimensional systems. The phenomena discussed here are analogous to effects arising in optical systems, and particularly in photonic crystals, which are discussed in the following chapter.

7. Localized Modes in Photonic Crystals

In previous chapters we have focused our attention on the properties of bound states and transmission in open two-dimensional geometries, and have discussed these properties in the context of electron propagation in quantum wires, and the transmission of microwaves in waveguides. Localized modes can also arise in optical systems. For example, in Sect. 6.4.1 we showed that trapped modes localized at a "defect" in a layered quantum heterostructure were analogous to states observed in Fabry–Perot interferometers. It has been demonstrated [162, 175] that electromagnetic radiation at optical frequencies can be trapped inside open structures in dielectric materials known as *photonic crystals*. In this chapter we will review the properties of such states, with particular attention to the conditions under which trapped modes can be produced in photonic crystals. We will contrast these properties with comparable features which are found in quantum wires and conventional waveguides. In some cases the states found in photonic crystals will have analogs in wires and waveguides, whereas in other situations one can produce states which are apparently unique to optical systems.

A *photonic crystal* is a lattice of macroscopic dielectric materials which is designed to control the propagation of light. A crucial feature of photonic crystals is the ability to produce gaps in the dispersion relation between the frequency $\omega(\mathbf{k})$ and wave number $\mathbf{k}$, for in-medium light propagation. These gaps in frequency, called *photonic band gaps*, arise from the structure and dielectric properties of the macroscopic crystal. Frequencies inside a band gap will be completely reflected, while frequencies in allowed regions can be transmitted through the material.

The basic effect has long been used in dielectric mirrors and optical filters, which are made from alternating layers of low-loss dielectric materials that will not permit the propagation of normally-incident light at specific frequencies. In photonic crystals, one extends this idea to two or three dimensions so as to forbid light propagation in *any* direction for a certain range of frequencies. Such a *complete* band gap occurs for electron propagation in semiconductors, between the valence and conduction bands. These materials have many potential applications in optical devices because of the control they offer over light propagation. A review of earlier theory and experiment in this field can be found in the proceedings of a NATO Advanced Research

J. T. Londergan, J. P. Carini and D. P. Murdock: LNPm 60, pp. 181 - 195, 1999
© Springer-Verlag Berlin Heidelberg 1999

Workshop, edited by Soukoulis [176]. Ho, Chan and Soukoulis [177] showed the existence of a band gap for a periodic lattice of dielectric spheres. A very clear introduction to the subject of photonic crystals and their properties is provided in the recent book by Joannopoulos, Meade and Winn [25].

A two-dimensional photonic crystal can be constructed from a lattice of parallel dielectric rods. A material commonly used is GaAs, with a dielectric constant $\varepsilon = 13$; the rods are separated by air, which has $\varepsilon = 1$. Alternatively, one could use alumina rods, which have $\varepsilon = 8.9$. A schematic picture of a 2-D photonic crystal, composed of a square lattice of long cylindrical dielectric rods, is shown in Fig. 7.1a. Here one defines the direction of the (very long) rods as the z-direction; the resulting material is periodic in the $x - y$ plane. A 2-D photonic crystal could also be produced by cutting an array of air columns into a sample of dielectric material. Figure 7.1b shows a scanning electron microscope image of a triangular array of air columns cut into a block of GaAs, from Wendt *et al.* [178]. In all systems discussed in this chapter, the high-dielectric material is chosen to have the same dielectric constant as GaAs.

7.1 Maxwell's Equations in a Dielectric Medium

We will briefly summarize Maxwell's equations for electromagnetic waves in mixed dielectric media. A more complete treatment can be found in the book by Joannopoulos *et al.* [25]. In our theoretical treatment of photonic crystals we will restrict our attention to isotropic macroscopic systems with fields small enough that the displacement field $\mathbf{D}$ can be written as a linear function of the electric field. Then to a very good approximation the displacement field can be written

$$\mathbf{D}(\mathbf{r}) = \varepsilon(\mathbf{r})\,\mathbf{E}(\mathbf{r}) \quad . \tag{7.1}$$

In (7.1), the displacement field can be related to the electric field $\mathbf{E}(\mathbf{r})$ by a scalar dielectric constant. In general, the dielectric constant $\varepsilon(\mathbf{r})$ is a function of the frequency. However, we will use the value of the dielectric constant which is appropriate to the desired frequency range for a given physical system. Furthermore, we will restrict our attention to low-loss dielectrics, so that the dielectric constant is assumed to be real.

For materials of interest for photonic crystals, the magnetic permeability is nearly unity, so that one can set $\mathbf{B} = \mathbf{H}$. When these assumptions are made, the macroscopic Maxwell equations for fields with harmonic time dependence of angular frequency ω give the following relations for the divergences of electric and magnetic fields,

$$\begin{aligned} \nabla \cdot \mathbf{H}(\mathbf{r}) &= 0 \\ \nabla \cdot \mathbf{D}(\mathbf{r}) &= 0 \quad . \end{aligned} \tag{7.2}$$

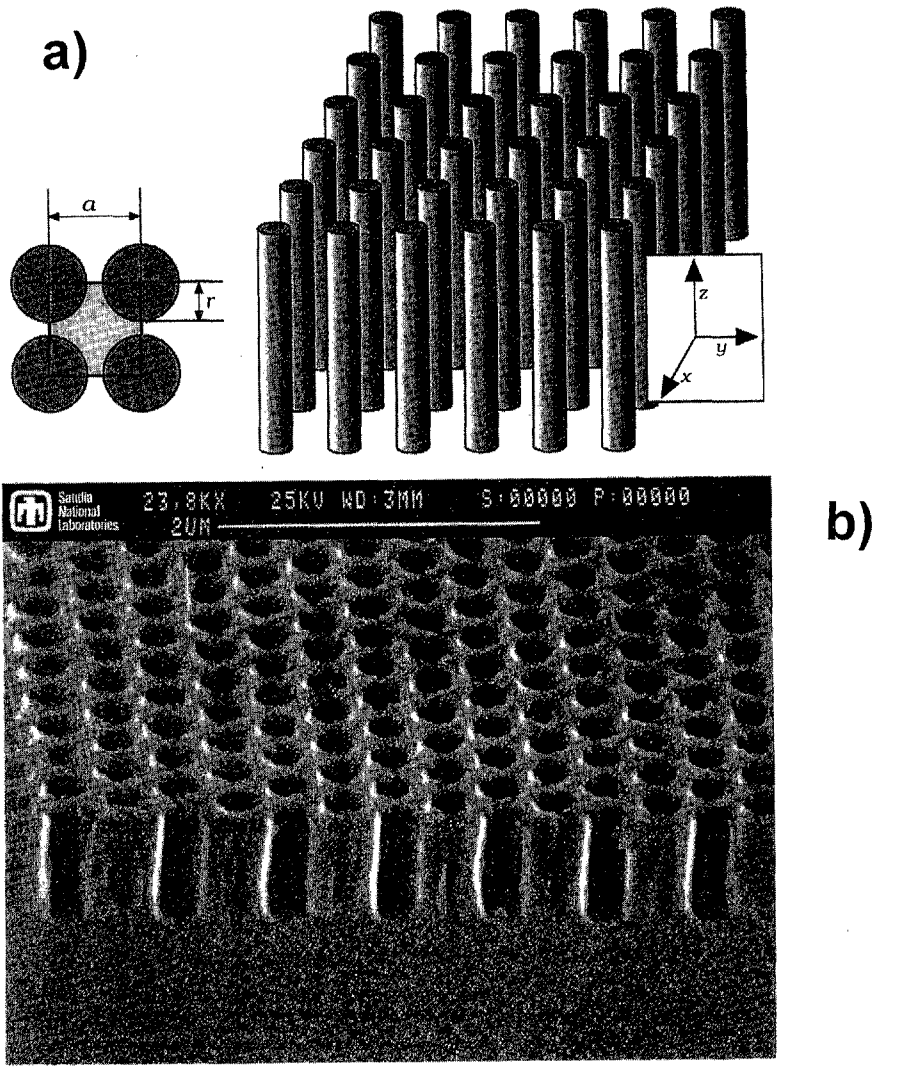

Fig. 7.1. Examples of two-dimensional photonic crystals. (**a**) A square lattice of long cylinders, with radius r, lattice constant a and dielectric constant ε, in air. The z direction is defined by the orientation of the cylinders; the system is periodic in the $x-y$ plane. The inset shows the square lattice viewed from above. From [25]. (**b**) Scanning electron microscope image of a triangular array of air columns in a GaAs ($\varepsilon = 13$) substrate. The columns have radius $r = 122.5$ nm, lattice constant $a = 295$ nm, column height 600 nm. From [178]

The relation (7.2) expresses the fact that the charge and current densities in the medium are zero. The resulting electric and magnetic fields which satisfy (7.2) are thus required to be transverse to the direction $\mathbf{k}$ of wave propagation.

The remaining Maxwell equations can be used to eliminate the electric field and obtain a "*master equation*" for the $\mathbf{H}$ field:

$$\begin{aligned} \nabla \times \left(\frac{1}{\varepsilon(\mathbf{r})} \nabla \times \mathbf{H}(\mathbf{r}) \right) &= \left(\frac{\omega}{c} \right)^2 \mathbf{H}(\mathbf{r}) \\ \text{or} \qquad \Theta \mathbf{H}(\mathbf{r}) &= \left(\frac{\omega}{c} \right)^2 \mathbf{H}(\mathbf{r}) \\ \text{where} \qquad \Theta &\equiv \nabla \times \frac{1}{\varepsilon(\mathbf{r})} \nabla \times \quad . \end{aligned} \tag{7.3}$$

In (7.3) the quantity Θ is a differential operator which acts on the magnetic field $\mathbf{H}(\mathbf{r})$. The relation (7.3), together with the transversality condition (7.2), can be used to determine completely the magnetic field.

Once $\mathbf{H}(\mathbf{r})$ is found, the $\mathbf{E}$ field can be found from Maxwell's equations

$$\mathbf{E}(\mathbf{r}) = \left(\frac{-ic}{\omega \varepsilon(\mathbf{r})} \right) \nabla \times \mathbf{H}(\mathbf{r}) \quad . \tag{7.4}$$

It is advantageous to work with the $\mathbf{H}$ field since the differential operator Θ in (7.3) can be shown to be Hermitian. The role of this operator in photonic crystal studies is similar to that of the Hamiltonian in quantum mechanics, and (7.3) is the analog of the time-independent Schrödinger equation.

The *electromagnetic variational theorem* plays an important role in understanding the physical origin of the photonic band gap. One can show that the lowest-frequency mode is the field $\mathbf{H}(\mathbf{r})$ which minimizes the electromagnetic energy functional:

$$\begin{aligned} E_f[\mathbf{H}] &= \frac{(\mathbf{H}, \Theta \mathbf{H})}{(2\mathbf{H}, \mathbf{H})} \\ &= \frac{\int d\mathbf{r} \frac{1}{\varepsilon(\mathbf{r})} |\frac{\omega}{c} \mathbf{D}(\mathbf{r})|^2}{2 \int d\mathbf{r} \, |\mathbf{H}(\mathbf{r})|^2} \quad . \end{aligned} \tag{7.5}$$

Once one has found the eigenmode $\mathbf{H}_0$ corresponding to the lowest frequency, the next lowest eigenmode will minimize the energy functional E_f in the subspace orthogonal to $\mathbf{H}_0$. In this way one can define a systematic procedure to locate the eigenmodes of the Hamiltonian for a photonic crystal. From (7.5) it is clear that the energy functional will be minimized when the displacement field $\mathbf{D}$ is concentrated in regions of high dielectric constant, subject to the restriction that a given mode be orthogonal to modes with lower frequencies.

7.1.1 Band Structure in a Photonic Crystal

Systems can be constructed where the different dielectric materials possess 1-D, 2-D or even 3-D symmetry. Because of the discrete translational sym-

metries of the system, the magnetic field modes can be written in Bloch form,

$$\mathbf{H}_{\mathbf{k}}(\mathbf{r}) = e^{i\mathbf{k}\cdot\mathbf{r}}\mathbf{u}_{\mathbf{k}}(\mathbf{r}) \quad , \tag{7.6}$$

where $u_{\mathbf{k}}(\mathbf{r}) = u_{\mathbf{k}}(\mathbf{r}+\mathbf{R})$ for all the lattice vectors $\mathbf{R}$ of the system. Then for all $\mathbf{k}$ in the Brillouin zone one can solve for the frequency ω of the mode $\mathbf{H}_{\mathbf{k}}$. In this way, the photonic band structure of the dielectric crystal can be determined.

The spatial periodicity of the system implies that Bloch states with different wave numbers and frequencies are identical. For example, for a system which is periodic in the x direction with lattice constant a, Bloch states with wave vector $k_x + 2\pi m/a$ are identical to those with wave vector k_x, for any integer m. The mode frequencies are also identical under this translation of wave vector, *i.e.*

$$\omega(k_x + 2\pi m/a) = \omega(k_x) \quad . \tag{7.7}$$

As a consequence, one needs only to consider those values of the wave number which are not redundant. For our example, we need consider only wave numbers in the range

$$-\pi/a < k_x \leq \pi/a \quad . \tag{7.8}$$

The region which includes the non-redundant values of the wave number is called the *Brillouin zone*. The smallest region within the Brillouin zone for which the frequencies are not related by the symmetries of the system is called the *irreducible Brillouin zone*.

For numerical work, it is useful to convert (7.3) to a system of linear equations using plane-wave expansions for $\mathbf{H}_{\mathbf{k}}(\mathbf{r})$ and $[\varepsilon(\mathbf{r})]^{-1}$. Both of these functions have the same spatial periodicity as the lattice. We can write an expansion for the magnetic field,

$$\mathbf{H}_{\mathbf{k}}(\mathbf{r}) = \sum_{\mathbf{G}\,\lambda} h_{\mathbf{G}\lambda}\hat{\mathbf{e}}_{\lambda}\mathrm{e}^{i(\mathbf{k}+\mathbf{G})\cdot\mathbf{r}} \quad , \tag{7.9}$$

where $\mathbf{G}$ are the reciprocal lattice vectors [25, 58] for the crystal structure and λ indexes the polarization vectors $\hat{\mathbf{e}}_{\lambda}$. The vanishing divergence of $\mathbf{H}$ (7.2) requires that

$$\hat{\mathbf{e}}_{\lambda}\cdot(\mathbf{k}+\mathbf{G}) = 0 \quad . \tag{7.10}$$

For any $\mathbf{G}$ we can also expand the reciprocal of the dielectric constant,

$$\frac{1}{\varepsilon(\mathbf{r})} = \sum_{\mathbf{G}'} \varepsilon^{-1}(\mathbf{G},\mathbf{G}')e^{i(\mathbf{G}'-\mathbf{G})\cdot\mathbf{r}} \quad . \tag{7.11}$$

Inserting (7.9) and (7.11) into (7.3), one obtains the *matrix* eigenvalue equation

$$\sum_{(\mathbf{G}\,\lambda)'} \Theta^{\mathbf{k}}_{(\mathbf{G}\,\lambda),(\mathbf{G}\,\lambda)'} h_{(\mathbf{G}\,\lambda)} = \left(\frac{\omega}{c}\right)^2 h_{(\mathbf{G}\,\lambda)} \quad , \tag{7.12}$$

where the matrix Θ depends on the wave vector $\mathbf{k}$ and is given by

$$\Theta^{\mathbf{k}}_{(\mathbf{G}\,\lambda),(\mathbf{G}\,\lambda)'} = [(\mathbf{k}+\mathbf{G}) \times \hat{\mathbf{e}}_\lambda] \cdot [(\mathbf{k}+\mathbf{G}') \times \hat{\mathbf{e}}_{\lambda'}] \varepsilon^{-1}(\mathbf{G}, \mathbf{G}') \quad . \tag{7.13}$$

See [179] for a thorough discussion of numerical methods for solving (7.12).

The 1-D photonic crystal is just a multilayer film composed of alternating layers of materials with two different dielectric constants. A detailed discussion of mode patterns for such systems is given in Joannopoulos, Meade and Winn [25]. We will concentrate exclusively on band structure in 2-D photonic crystals. For systems with a symmetry plane, we can define the direction normal to the symmetry plane as the z-axis. *Transverse-electric* (TE) modes are defined as those which have $\mathbf{H}$ normal to the $x-y$ plane, *i.e.*

$$\begin{aligned} \mathbf{H} &= H(x,y)\hat{\mathbf{z}} \\ \text{and} \quad \mathbf{E} \cdot \hat{\mathbf{z}} &= 0 \quad . \end{aligned} \tag{7.14}$$

Transverse-magnetic (TM) modes are analogously defined by

$$\begin{aligned} \mathbf{E} &= E(x,y)\hat{\mathbf{z}} \\ \text{and} \quad \mathbf{H} \cdot \hat{\mathbf{z}} &= 0 \quad . \end{aligned} \tag{7.15}$$

An important feature of a photonic crystal is the *band structure* for the modes in the crystal. Consider propagation of EM waves in the symmetry plane of the crystal. We plot the mode frequencies for wave numbers in the irreducible Brillouin zone. For a given polarization state (TE or TM), a *complete band gap* exists if there is a region of mode frequencies which cannot be obtained for any wave vector in the irreducible Brillouin zone. It is possible to construct photonic crystals which have complete photonic band gaps for either TM or TE mode propagation within the symmetry plane. In fact, it is even possible to design a system which has a complete photonic band gap for *both* polarization states.

Fig. 5.34 shows the band structure for a 2-D photonic crystal which possesses a complete band gap for both polarization states (this is the fifth color plate). The crystal is a triangular array of air columns drilled in a dielectric material with $\varepsilon = 13$, and the ratio of the column radius to the lattice constant is $r/a = 0.48$ (this is similar to the array shown in Fig. 7.1b) [1]. The spatial lattice and irreducible Brillouin zone are shown in the inset. TE and TM modes are denoted by red and blue lines, respectively.

From Fig. 5.34 it is clear that for this crystal, there is a range of frequencies for which *no* mode of any wave number $\mathbf{k}$ will propagate in the symmetry plane for either polarization. This is shown as the yellow band in Fig. 5.34.

[1] Photonic crystals are systems which possess perfect scaling behavior. Therefore, all system dimensions can be expressed in terms of a single system parameter. By varying that quantity, any parameter in the system can be "tuned" to a desirable or feasible value. In this chapter all dimensions are defined in terms of the lattice constant a.

If EM waves with frequencies within the band gap are introduced into the crystal, such a mode would decay exponentially as it passed through the system. A photonic crystal with such a band gap could be used as a frequency filter, since this crystal would transmit frequencies outside the band gap, but would not transmit EM waves with frequencies within the band gap.

One can understand how band gaps arise by recalling a heuristic argument for the occurrence of band gaps for electron motion in a periodic attractive one-dimensional potential. At the edges of the irreducible Brillouin zone, there are wave numbers for which the associated electron density has the same spatial frequency as the effective potential of the crystal. There are two permitted electron states at such a value of k, one for which the density is in step with the potential and whose energy is lowered, and one for which the density is out of step and for which the energy is raised. This discontinuity in energy constitutes the electron band gap.

In the same way, at wave numbers where the field energy has the same spatial periodicity as the regions of high dielectric constant, the degeneracy of modes where the field intensity is localized on or between the high-ε regions is lifted. This gives rise to a difference in frequencies ω for these modes. From the second equation in (7.5) it is clear that the energy will be minimized for a state whose displacement field $\mathbf{D}$ is concentrated in regions of high dielectric constant.

7.2 "Waveguides" in Photonic Crystals

If one removes a single rod from an otherwise perfect 2-D lattice, or changes its properties relative to the rest of the lattice, the symmetry of the system is broken. Alternatively, one could break the symmetry of a 2-D photonic crystal by removing several rods. In this section we will concentrate on symmetry breaking which involves removing either one or a few rods in a 2-D photonic crystal, or by removing one or more rows of rods. The effects of breaking the symmetry in a 2-D photonic crystal are analogous to the effects which arose from the introduction of defects in periodic tubes, which was discussed in Sect. 6.4. As a general rule, the breaking of the crystal symmetry will have two effects.

- **Forbidden Frequencies in "Allowed" Regions**: Certain frequencies which were allowed in the perfect crystal may be forbidden in the broken-symmetry case.
- **Resonant States in "Forbidden" Regions**: The defect may introduce additional resonant states into the system. When these states occur at frequencies within a photonic band gap, it will be possible to support modes which are localized in the vicinity of the "defect." In the symmetry plane of a two-dimensional photonic crystal, such states must necessarily decay exponentially in the bulk of the crystal. They are analogous to modes in a cavity surrounded by reflecting walls.

We are interested in examining the properties of two-dimensional channels, or "*waveguides*", which can be produced in a 2-D photonic crystal. We will compare and contrast the properties of bound states and guided modes which can be produced in photonic crystals, with those we have studied previously in conventional waveguides and quantum wires. By changing the parameters of a photonic crystal system, we can produce a great variety of different effects. In this brief review we will concentrate on some of the more interesting and unusual effects which can be produced in optical systems with mixed dielectric media.

For example, a straight "waveguide" in a 2-D photonic crystal can be formed by removing adjacent rows of dielectric rods (or filling in rows of air columns) in a crystal which otherwise has perfect 2-D symmetry. Before the rods are removed and the symmetry of the crystal is broken, it is not possible for light with frequencies within the photonic band gap to propagate in the symmetry plane. Within the waveguide, however, light of frequencies which were previously blocked (*i.e.*, within the photonic band gap) may now be able to propagate. At these frequencies, light could travel freely down the waveguide channel, but would be confined within the channel, decreasing exponentially as it moved into the crystal.

Figure 5.35 shows the bands of states which can propagate through a crystal composed of long cylindrical dielectric rods with radius $r/a = 0.18$, arranged in a square lattice, surrounded by air (this is the sixth color plate). A single row of rods has been removed from the crystal in the (10) direction; this is shown in the inset to Fig. 5.35. The blue shaded regions represent modes of light which can propagate through the bulk of the crystal. At intermediate frequencies there is a band gap, and within this gap a single curve represents the modes for which light can propagate along the axis of the waveguide. If more adjacent rows had been removed, there would be more bands inside the band gap where transmission could occur along the waveguide.

The existence of these guided modes, which travel freely along the waveguide axis but decay exponentially as light moves into the crystal, can have very interesting properties and potential commercial applications. An example of this is shown in Fig. 5.36b (this is the seventh color plate), which shows the displacement field for a TM mode traveling around a 90 degree bend in a photonic crystal waveguide [2], from Mekis *et al.* [162]. In this case the frequency chosen is $\omega a/2\pi c = 0.353$, which is seen from Fig. 5.35 to be roughly in the center of the photonic band gap. At this frequency, the light cannot escape into the crystal, and hence has no choice but to follow the waveguide.

A fascinating feature of photonic crystals is the very high transmission probability in the right angle waveguide. Because of the sharp bend, EM waves in a conventional waveguide would be very strongly reflected. Similarly,

[2] Note that for a conventional waveguide, where the modes are labeled relative to the direction of propagation of the wave, this would be labeled a "TE mode," in the notation of Jackson [129].

conventional dielectric waveguides with such a sharp bend would experience large radiation losses at the corners. Figure 5.36a shows the computed transmission coefficients for the photonic crystal waveguide. The transmission is found to be between 95-100% over a wide range of frequencies within the photonic band gap, even though the radius of curvature of the bend is of the order of the wavelength of the transmitted light.

Such properties of photonic crystals suggests that they may have important applications as guides for monochromatic light. Mekis *et al.* [162] were able to explain the high transmission rate by modeling the sharp bend as a series of coupled waveguide sections oriented in different directions, and they calculated the transmission probability by matching modes at the interfaces of the waveguide sections.

Our discussion in this book will focus on localized modes which are created when rods are removed from the interior of a crystal lattice. However, another possibility is that a row of rods could be altered at the *surface* of a large crystal – *e.g.*, the last row of rods could be removed, or a surface could be terminated by cutting in half the last row of cylindrical columns. For some geometries it may be possible to support localized modes in photonic band gaps; and under certain special conditions *surface states* may be produced [25]. Such modes decay exponentially both into the bulk of the crystal, and in the air surrounding the crystal, and are large only right at the crystal surface. These surface states were discussed briefly in Sects. 6.1 and 6.4.

7.3 "Bound States" in Photonic Crystal Waveguides

In Chap. 4 we showed how "*bound states*" could be produced in conventional waveguides. These were stable confined EM modes where the fields were localized in a finite section of the system. The fields could not propagate into the rest of the system, as they decay exponentially as they travel through the waveguide. In waveguides, it was shown that a local deformation (*e.g.*, a bulge or bend) produced an effective attractive interaction, and thus lowered the energy of the system in the vicinity of the deformation. Stable states could then be supported with frequencies below the cutoff frequency for the waveguide. The fields were large in the vicinity of the deformation, and decayed exponentially as one traveled along the waveguide axis. While a bulge lowered the local energy, a constriction raised the energy, so that stable confined modes could not be supported in the vicinity of a constriction in an otherwise straight rectangular waveguide.

Similar bound states or confined EM modes will be found for "photonic crystal waveguides," formed by removing rows of rods in 2-D photonic crystals. A unique feature of photonic band gap [PBG] waveguides is that, unlike conventional waveguides, they can possess *mode gaps*. Because of the existence of mode gaps, it will be possible to produce localized modes in PBG systems which have no analog in conventional waveguides. In particular, it

will be possible to produce *bound states* in PBG systems which are localized in parts of the waveguide, but which appear *in the continuum*, i.e. the confined mode frequencies lie above the frequencies for guided modes in the semi-infinite waveguide channels.

For example, one type of waveguide which can be created in a photonic crystal arises from coupling a channel of finite length between two semi-infinite channels, where the width of the finite channel differs from the width of the long channels. In this case one can produce a photonic crystal waveguide containing either a localized bulge, or a constriction. Because of the presence of mode gaps in PBG systems, it is theoretically possible to create a PBG waveguide in which the guided modes for the finite section lie between modes for the long sections, and where both of these modes lie within the band gap for the extended crystal. In this way one could produce confined modes which lie above the cutoff frequency for guided modes in the semi-infinite channels. Resonant states could be produced where the fields were large in the finite sections of the PBG waveguide, but which decay exponentially both along the semi-infinite section of the waveguide, and also into the bulk of the crystal.

The corresponding situation in quantum wires was discussed in Sect. 6.4. There we showed that the introduction of defects into otherwise perfect periodic 1-D superlattices could produce confined modes above continuum threshold. This occurred at energies where resonances were associated with the defect cells, but where the resonant energies fell within forbidden bands in the quantum wire "crystal."

7.3.1 Bound States in Local Constrictions

Mekis *et al.* [175] demonstrate how this can occur in a two-dimensional photonic crystal made of a square array of dielectric rods in air (the geometry is similar to that shown in Fig. 7.1a). In their simplest example, they consider channels made by removing a single infinite row of dielectric rods. They compare the dispersion relation for this "thin" guide with that of a "wide" guide produced by removing several parallel rows. In a conventional waveguide, confined modes can be produced by sandwiching a wide guide of finite length between two semi-infinite narrow guides, thus producing a local "bulge" in the waveguide. Confined states arising from bulges in 2-D tubes were discussed in Chap. 2. These states can also be produced in PBG materials, provided that the states produced lie inside a band gap.

However, in PBG materials it is also possible that the short waveguide section can have a guided mode which lies inside a band gap between the guided modes in the semi-infinite sections. Mekis *et al.* found a geometry which would produce such a state. They formed a waveguide by coupling two semi-infinite channels, so-called "wide" channels, formed by removing four rows of rods in the (1 1) direction, with a finite length "thin" channel in which only a single row of rods was removed in the same direction. This is

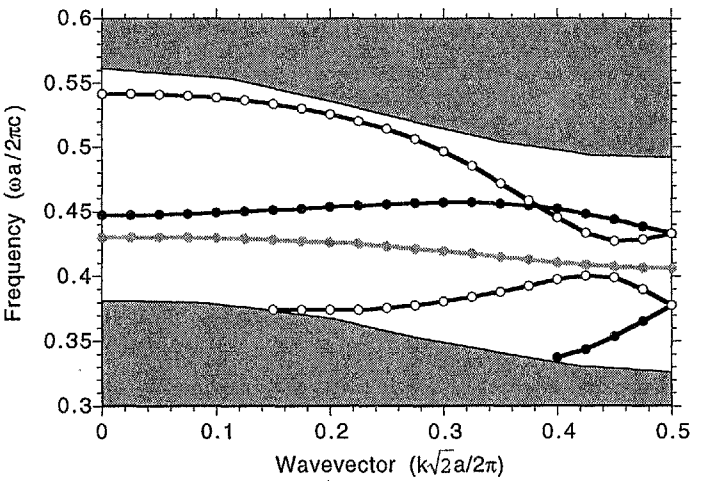

Fig. 7.2. Dispersion relations for TM modes in photonic crystal waveguide shown in Fig. 7.3. The radius of the rods is $r/a = 0.12$. Black line: guided modes for the wider guide, formed by removing four rows of rods in the (1 1) direction, from a square array of GaAs dielectric rods in air. Gray line: guided modes for the narrow guide, formed by removing one row of rods in the (1 1) direction. Filled circles: modes with even reflection symmetry; open circles correspond to odd modes. The gray shaded areas show the projected band structure of the extended crystal. From [175]

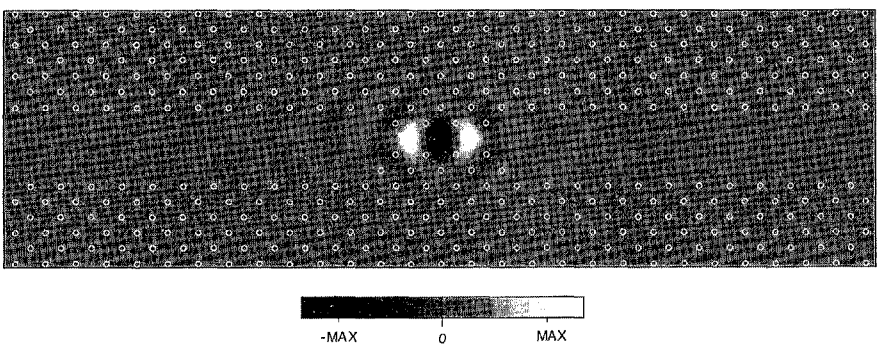

Fig. 7.3. The electric field for the bound state in a photonic crystal waveguide. Four rows of rods were removed in the (1 1) direction, from a square array of GaAs dielectric rods in air, with dimensions given in Fig. 7.2. A narrow constriction of length $3\sqrt{2}a$ was formed inside the wider guide, by removing one row of rods in the (1 1) direction. The bound state for this configuration appears at $(\omega a)/(2\pi c) = 0.411$. The small white circles denote the dielectric rods. From [175]

shown schematically in Fig. 7.3, where the white circles denote the location of the dielectric rods. In this system, the rods were chosen to have radius $r = 0.12a$.

Figure 7.2 shows the dispersion relations for TM modes in the two coupled guides. The gray shaded areas are the projected band structure for the perfect crystal. The black lines show the guided modes for the wider guide, which has four bands of guided modes. The filled circles correspond to modes with even reflection symmetry, and the open circles denote modes of odd reflection symmetry. The wider guide possesses a mode gap for frequencies $0.390 < (\omega a)/(2\pi c) < 0.417$. The thin guide possesses a single guided mode band. For this geometry, the thin channel guided mode band (the gray line in Fig. 7.2) fits entirely within the mode gap of the bands for the wide guide. This indicates that if a finite thin guide section has long "wide" guides as leads (with this geometry), one can produce a mode which is localized in the thin section and which cannot propagate either in the wide guides, or in the extended crystal. In this way it is possible to trap light in a section of an *open* photonic waveguide.

For example, if one chooses a configuration of rods such that a thin section (removing one row of rods in the (1 1) direction) of length $3\sqrt{2}a$ is set between two semi-infinite wide sections (formed by removing four rows of rods), one finds a bound state at frequency $(\omega a)/(2\pi c) = 0.411$. The geometry of this device and the electric field for the standing wave are shown in Fig. 7.3. The electric field is clearly concentrated in the "thin" guide.

Mekis *et al.* [175] also examined a different geometry, where a waveguide was formed with a U-shaped structure. In this case the semi-infinite wide channel joins the finite thin section at right angles. When the wide and narrow channels were chosen to have the same dimensions (width and length) as is shown in Fig. 7.3, a bound state was found for the "U-bend" tube at the same frequency as for the straight case.

It would be impossible to produce these states in conventional hard-wall waveguides. In such systems, as was discussed in Chap. 2, a constriction tends to raise the energy while a bulge lowers the energy. Thus in a conventional waveguide, modes in the constriction would necessarily lie higher in energy than the continuum of modes in the bulge, and localized modes could not occur in a waveguide formed by coupling a finite-length narrow channel between two semi-infinite wide channels [3]. The crucial difference in PBG waveguides is the presence of mode gaps, which allows for the possibility that modes in the short section might lie in the mode gaps for the semi-infinite channels.

[3] It would be possible to produce localized modes in the narrow channel, provided that it had sufficiently large curvature, as shown in (2.25) in Sect. 2.1.3. However, for a straight narrow channel localized modes could not be produced in a conventional waveguide.

7.3.2 Bound States in Curved Photonic Band Gap Waveguides

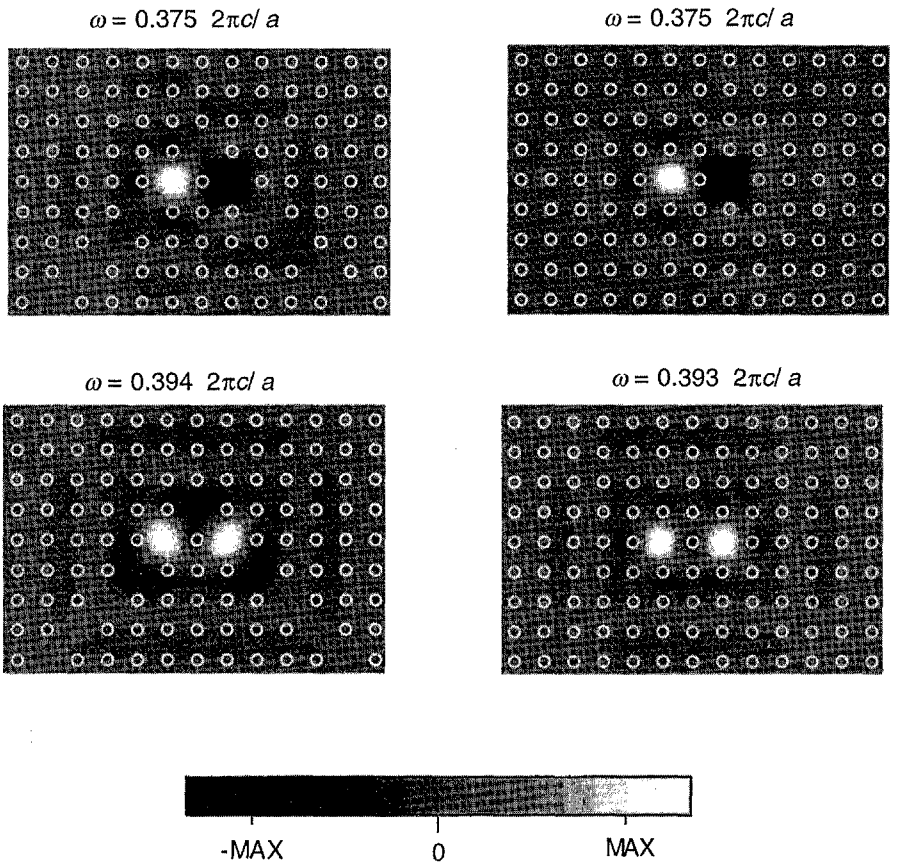

Fig. 7.4. Left panels: electric fields and frequencies for the two bound states inside a "90° bend" PBG waveguide, formed by removing a single row of rods in the (1 1) and (1 −1) directions from a square array of GaAs rods in air. Right panels: electric fields and frequencies for the corresponding cavity modes in the same photonic crystal. From [175]

In the examples given in the preceding section, the bound states arise from trapping which occurs when the width of a waveguide channel is changed. Bound states in photonic crystal structures can also occur if two semi-infinite channels of the *same* width meet at an angle. In fact, such systems can have multiple bound states. Mekis *et al.* [175] also studied the properties of these confined states. In one example, an analog to the 90° bend waveguide

discussed in Sect. 2.1.5 is constructed by joining two semi-infinite channels formed by removing a single row of rods along the (1 1) and (1 −1) directions. The original crystal is formed from a square array of GaAs rods in air, with $r = 0.18a$. The geometry for this bent waveguide is shown in the left panels of Fig. 7.4 [175], along with the electric field strengths for the two bound states.

The confined modes in the PBG waveguide are quite different from the conventional or quantum wire 90° waveguides. The PBG waveguide has *two* bound states, and for neither one is the electromagnetic energy density localized in the corner. This can be contrasted with the 90° quantum wire bound state shown in Fig. 2.3b. It has a single confined mode, and the wave function for this mode has a maximum in the center of the bend, and no nodes. Instead, the modes in the PBG waveguide have their energy localized at the vacancy sites a distance $\sqrt{2}a$ away from the corner. There is a state with odd reflection symmetry (with respect to the center of the waveguide) with frequency $(\omega a)/(2\pi c) = 0.375$, and an even symmetry state with frequency $(\omega a)/(2\pi c) = 0.394$. The bound states and the corresponding frequencies are also extremely similar to the cavity modes produced when the semi-infinite channels are closed off. The right panels of Fig. 7.4 show the corresponding cavity modes and their frequencies.

The authors give the following explanations for these phenomena. First, the state localized in the corner of the 90° bend (the analog of a cavity formed by removing a single rod from the crystal) has frequency $(\omega a)/(2\pi c) = 0.385$. For this geometry, the frequency of this state falls within the guided range of the semi-infinite channel. Consequently the state at this frequency appears as a resonance and not a bound state. The bound states correspond to two cavity modes, where each cavity is formed by removing a single rod, and the cavities are separated by two lattice constants. This is evident from the right panels in Fig. 7.4. The finite coupling between the two cavities splits the initially degenerate modes into two levels, one with odd reflection symmetry and one with even symmetry. The frequencies of these two states lie below and above the frequency for a single cavity. The resulting frequencies fall just below and just above the guided mode range for the semi-infinite channel, hence these appear as "bound states" in the bent waveguide.

In conventional waveguides, both the EM fields and the frequencies corresponding to cavity modes will in general differ greatly from the confined modes which are localized in waveguide bends. When the semi-infinite channels are closed off, the resulting cavity fields must terminate abruptly on the cavity surface. Thus the boundary conditions on EM fields for open waveguides and cavities differ greatly. In PBG waveguides, however, the modes in the waveguides decay exponentially into the semi-infinite waveguide channels; this boundary condition is essentially the same as for the cavity (where the modes decay exponentially into the extended crystal). The similarity of the two boundary conditions explains why the two states bear such a close resem-

blance in PBG waveguides. Mekis *et al.* also studied properties of confined modes in different geometries.

We hope that this brief discussion is sufficient to illustrate the novel features which can be produced in "waveguide" channels created in photonic crystals. One can vary the system geometry to create a range of phenomena which could have important contributions to the control of light propagation in optical systems. Since (within a certain range of frequencies) the systems obey perfect scaling, the system dimensions could be varied to produce devices which preferentially transmit or reflect certain desired frequencies. In addition, one can produce highly localized states of known frequencies at specific sites inside a photonic crystal. We refer the reader to the literature [25, 162, 175] for more complete discussions of the properties of confined modes in PBG structures.

8. Epilogue

In this book we have presented a survey of binding and transmission in constrained two-dimensional systems. Our intent was to convey the range of different phenomena which appear in very simple geometries. In many cases we were able to construct accurate analytic approximations of simple 2-D systems. These constrained 2-D systems exhibit a fascinating array of structure, including localized states both below and above continuum threshold, trapped modes, and quasi-bound states. The transfer-matrix approach provides a framework which allows one to extract the dominant physical processes, particularly for tubes with periodic structure. Plots of the probability current can provide an intuitive understanding of the mechanisms for transmission. In these simple models one can differentiate between quasi 1-D phenomena, and true 2-D effects.

For reasons of space and economy, we have placed very strong restrictions on the physical conditions in the 2-D structures studied here. One can readily imagine a host of more complicated and perhaps more realistic models, *e.g.* tubes with multiple leads, effects of strong external magnetic fields, inclusion of inter-particle interactions in quantum heterostructures, effects of spin, approaches to chaos in 2-D systems, etc. One could also examine more complicated geometries (multiply-connected tubes, rings, side bands). A large number of such systems are currently being explored in both theory and experiment.

We hope that we have succeeded in conveying both the simplicity and power of these simple models, and that we have shown how these 2-D systems are relevant to understanding and comparing the physics of conventional waveguides, quantum wires, and photonic crystals.

J. T. Londergan, J. P. Carini and D. P. Murdock: LNPm 60, pp. 197 - 197, 1999
© Springer-Verlag Berlin Heidelberg 1999

A. Comparison of Various Approximate Quantum Wells

In this book we have analyzed the properties of particles or fields in constrained two-dimensional geometries. The objects in question (*e.g.*, electrons in quantum heterostructures or EM fields in rectangular waveguides) are assumed to move essentially in two dimensions. Their motion is further constrained by an effective interaction which confines them to a finite area. For the effective confining force, we have taken a square well of infinite depth, *i.e.* infinite hard wall boundary conditions.

For EM fields in a rectangular waveguide, the infinite hard wall potential is a reasonably realistic interaction – the electric fields vanish sufficiently rapidly on the metal waveguide surfaces that this approximation gives good agreement with measured fields in waveguides. For electrons in quantum heterostructures, the infinite hard wall approximation is less well founded. Fig. 3.8 shows the calculated effective potential for a split-gate GaAs/AlGaAs structure, as calculated by Laux, Frank and Stern [112]. As was mentioned in Sect. 3.3, a series of approximations are necessary to derive the effective one-body potential. In their book on quantum heterostructures, Mitin, Kochelap and Stroscio [3] give a detailed review of electron properties in doped quantum heterostructures. We recommend this book to readers interested in a more rigorous discussion of these systems.

Insofar as it makes sense to treat the problem of electrons in quantum wires as constrained 2-D motion with a one-body effective interaction, the effective potential should realistically have a finite depth and a diffuse surface. What are the qualitative differences one would expect between the infinite hard-wall effective potentials we have used, and other effective quantum wells for transverse confinement of electrons? We will consider the effects on three different quantities: the transverse energy spectrum, the confined wave functions in the transverse direction, and the effects of different potentials on transmission through a quantum waveguide. The book by Davies [11] on the physics of low-dimensional systems contains a useful comparison of various quantum wells and the properties of their eigenfunctions and energies. We will summarize here the discussion in Davies' book.

J. T. Londergan, J. P. Carini and D. P. Murdock: LNPm 60, pp. 199 - 202, 1999
© Springer-Verlag Berlin Heidelberg 1999

A.1 Effects of a Diffuse Surface

A realistic description of the transverse confining interaction for electrons in quantum heterostructures would be a finite quantum well with a diffuse surface. In this section, we will consider the effect of replacing the hard wall interaction with an alternative potential which has infinite depth, but a diffuse surface. Such a diffuse interaction could be simulated by either of two soluble one-dimensional confining potentials – a parabolic potential, or a triangular (linearly rising) interaction. In Table A.1 we compare these interactions with the infinite square well. We consider the eigenenergy spectra for these systems, the functional form of the bound state wave functions of the Schrödinger equation, and the asymptotic behavior of the eigenfunctions at large distances.

Table A.1. Comparison of Soluble Infinite Quantum Wells

Type of Potential	Eigenenergies	Eigenfunctions; Large-x Behavior
Infinite Hard Wall	$E_n \sim n^2 E_1$	Sine functions: $\psi = 0$
Parabolic	$E_n \sim n E_1$	Hermite Polynomials: $\psi \to x^{n-1} \exp(-x^2/x_0^2)$
Triangular	$E_n \to (n - 1/4)^{2/3} E_1$	Airy Functions: $\psi \to x^{-1/4} \exp(-\frac{2}{3}(x/x_0)^{3/2})$

The nature of confinement (hard wall *vs.* parabolic or triangular) changes the energy spectrum of the transverse modes. The energies for the infinite hard wall potential go like n^2, so the energy difference between successive states increases with increasing n. The parabolic potential produces equally-spaced eigenstates, while for the triangular well the states become more closely spaced at large n (in Table A.1 the energy behavior for the triangular case is correct in the limit of very large n). The calculated binding energies for systems with sharp corners will generally be greater than in quantum wires, both because the hard wall potential is deeper than a corresponding parabolic or triangular potential, and because the assumption of sharp corners puts more space in the idealized wires. It is possible to compensate for this effect. For example, Wu *et al.* [180] found an energy scaling which correlates levels with hard wall and parabolic confining potentials for wires with circular bends.

There are also qualitative differences between the transverse mode wave functions with these three confining interactions. For the infinite hard wall

potential, the wave function is forced to vanish on and outside the boundary. The eigenfunctions for the parabolic potential go to zero like a Gaussian times a power law, while the wave functions with the triangular potential are Airy functions. For the Airy functions, all of the bound state wave functions go to zero asymptotically like $\exp(-2(x/x_0)^{3/2}/3)/x^{1/4}$.

A.2 Potentials of Finite Depth

A realistic effective interaction for electrons in quantum heterostructures would not only have a diffuse surface, but it would also have a finite depth. We can estimate the effects of finite well depth on bound state energies and wave functions by comparing the infinite square well interaction with a finite square well, since we can also obtain analytic solutions for bound state energies and wave functions with the finite square well.

Consider a one-dimensional square well of depth V_0 and width a, centered at $x = 0$. Because the interaction is symmetric with respect to reflection about the center of the well, the lowest bound state wave function will have even reflection symmetry in x. Higher energy bound states will have alternating odd and even reflection symmetry. Matching the logarithmic derivative of the bound state wave functions at the edge of the square well gives the condition for bound states,

$$\left\{ \begin{array}{c} \tan(\theta) \\ -\cot(\theta) \end{array} \right\} = \sqrt{\frac{\theta_0^2}{\theta^2} - 1} \ . \tag{A.1}$$

In Eq. (A.1), the upper (lower) equation is satisfied by the states with even (odd) reflection symmetry, and the quantities θ and θ_0 are given by

$$\begin{aligned} \theta &= \frac{ka}{2} \\ \theta_0^2 &= \frac{m^* V_0 a^2}{2\hbar^2} \end{aligned} \ . \tag{A.2}$$

The bound state energies are given by the wave numbers k for which A.1 is satisfied. These can be determined straightforwardly by graphical methods. The number of bound states N_{bd} is given by

$$N_{bd} = \mathrm{Int}\left[\frac{2\theta_0}{\pi} + 1\right] \ , \tag{A.3}$$

where the number of bound states in (A.3) is given by the largest integer contained in the term on the right hand side. From (A.3), it is clear that there will always be at least one bound state for any attractive square well, a statement proved in Sect. 2.1.

Outside the well, the bound state wave function for the finite well has the form

$$|\psi(x)| \quad \propto \exp(-\kappa|x|)$$
$$\text{where } \kappa^2 = \frac{2m^*V_0}{\hbar^2} - k^2 \ . \tag{A.4}$$

The bound state wave function thus decreases exponentially outside the well, and as the bound state energy gets larger (*i.e.*, the value of k increases), the wave function decreases more and more slowly outside the confining well.

A.3 Effect of Sharp Boundaries on Transmission

Another qualitative difference between 2-D surfaces with sharp potentials and those with diffuse surfaces is that tubes with hard walls and sharp corners will generally produce greater reflection than tubes with diffuse transverse potentials and/or rounded corners. The hard wall condition requires that the wave function go abruptly to zero at the tube boundary, so that the first derivative of the wave function is discontinuous. For the case of a diffuse potential (or one with a finite depth), the wave function decreases exponentially but continuously in the classically forbidden region.

One qualitative effect of the sharp potentials is on the transmission coefficients for electrons in quantum wires. Wu *et al.* [180] have calculated transmission coefficients for a circular bend wire where the transverse confining potential is parabolic. In order to make meaningful comparisons between wires with differing transverse potentials, instead of using the energy E, they used the WKB approximation to define an effective transverse quantum number $\nu(E)$:

$$\nu(E) = \sqrt{\frac{2m^*}{\hbar^2}} \int_{-y_t}^{+y_t} \sqrt{E - V(y)} \frac{dy}{\pi} \ + \ \frac{1}{2} \ , \tag{A.5}$$

where $\pm y_t$ are the classical turning points of the potential $V(y)$ for energy E [78]. (Note, the $\frac{1}{2}$ term does not appear for hard wall confinement.) In fact, for both harmonic and hard wall potentials, (A.5) gives the exact answers for the successive thresholds.

Wu *et al.* found that the basic features of transmission for the circular bend for hard wall and harmonic confining potentials were similar when plotted against the parameter $\nu(E)$. We also note that Lent [137] included the case of a square well channel with finite potentials walls in his calculation of transmission through a circular bend; he chose a height of $48E_1$, where E_1 is the energy of the lowest transverse mode, and the channel width was chosen to match the thresholds. The effect of finite walls is to reduce reflection and mode mixing. In Fig. 5.25 we compared conductance through a tube with two bends. One tube had sharp right-angle bends, while the second tube had two circular bends each with a total bend angle of 90°. The tube with sharp bends had much lower transmission than the circular-bend tube. Again, the reflection was significantly reduced for a tube with gentle bends.

B. Conducting Sphere on a Grounded Surface

In Sect. 4.2 an expression (4.12) was derived for the resonant frequency shift in a waveguide, when a small metal sphere of radius r was placed onto the lower conducting surface of a waveguide with electric field E_0. In deriving that expression the induced electric dipole moment was assumed to be given by

$$p = E_0 r^3 \quad . \tag{B.1}$$

The fact that the conducting sphere is in contact with the lower conducting surface makes (B.1) a poor approximation for the induced dipole moment. In this Appendix, the method of images is used to derive a better model for the induced dipole. Using this model, the dipole moment acquires an extra multiplicative factor $c_0 = 2\zeta(3) \approx 2.404$, so that using the induced dipole given by $p = c_0 E_0 r^3$, a more accurate expression for the cavity frequency shift measurements is given by the relation

$$\frac{\Delta f_0(x,y)}{f_0} = \frac{-r^3}{2U_{\rm Tot}} \left[c_0 |E(x,y)|^2 - \frac{c^2}{2\omega^2} |\nabla E(x,y)|^2 \right] \quad , \tag{B.2}$$

where we use the notation of Chap. 4, in which E is the root-mean-square magnitude of the electric field inside the cavity; $\zeta(n)$ is the Riemann Zeta Function of argument n (see Chap. 23 of [132]).

The electrostatics problem solved here is to find the induced dipole moment of a conducting sphere resting on an infinite conducting plane. The potential is constrained to be zero on both the conducting plane (defined to be the $z = 0$ plane) and on the surface of the sphere. The electric field around the sphere approaches $\mathbf{E} = E_0 \hat{\mathbf{z}}$ at distances large compared with r, the radius of the sphere. This is an interesting example of an image charge problem which is soluble in closed form, even though it requires an infinite number of image charges. We have not been able to find the solution to this problem in the extensive literature devoted to electrostatic boundary value problems.

This problem can be solved using the method of images, by constructing image charges both inside the conducting sphere *and* on the underside of the conducting plane. To form a uniform $\mathbf{E}$ field in a way amenable to the image charge method, define the origin of the coordinate system to be the point where the conducting sphere touches the plane. Place a charge $-Q$ at $z = R$

J. T. Londergan, J. P. Carini and D. P. Murdock: LNPm 60, pp. 203 - 207, 1999
© Springer-Verlag Berlin Heidelberg 1999

and a charge $+Q$ at $z = -R$. This gives a field

$$\mathbf{E} = \frac{2Q}{R^2}\hat{\mathbf{z}} \tag{B.3}$$

at the origin, and ensures that the plane $z = 0$ remains at potential $\Phi = 0$. The field will approach a uniform value all around the sphere by taking the limits

$$Q \to \infty, \qquad R \to \infty, \qquad \text{with} \quad \frac{2Q}{R^2} = E_0 \ . \tag{B.4}$$

This configuration is shown schematically in Fig. B.1.

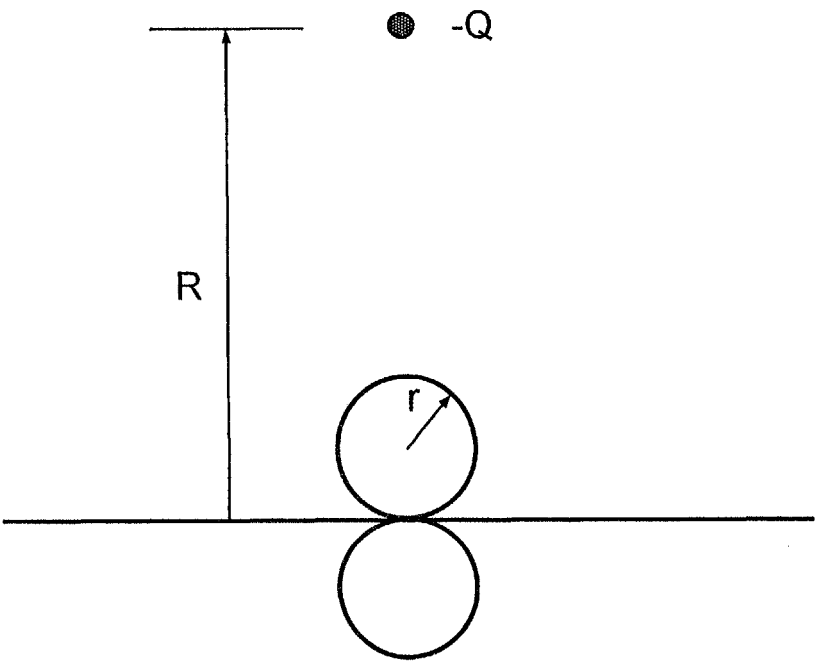

Fig. B.1. Charges $\mp Q$ are placed at the points $z = \pm R$, directly above and below a conducting sphere in contact with a conducting plane at $z = 0$ held at zero potential. In the limits defined by (B.4), these charges produce a uniform E field

In the method of images (see Sect. (2.2) of [129]), to form an image charge for a zero-potential conducting plane, an opposite charge is placed at the same distance on the opposite side of the plane. Here, one has a charge q which is located at a distance s from the center of a conducting sphere of radius r. The spherical conducting surface can be held at zero potential by placing a charge of magnitude q' at a distance s' from the center of the sphere, where

$$q' = -\frac{rq}{s} \qquad \text{and} \quad s' = \frac{r^2}{s} \ . \tag{B.5}$$

The charges $+Q$ and $-Q$ thus produce two image charges inside the conducting sphere. The values of the image charges and their z coordinates are straightforwardly found from (B.5) to be

$$\begin{aligned} q_1^{(1)} &= \frac{r}{R-r}Q \qquad z_1^{(1)} = \frac{rR}{R-r} \\ q_2^{(1)} &= -\frac{r}{R+r}Q \qquad z_2^{(1)} = \frac{rR}{R+r} \ , \end{aligned} \tag{B.6}$$

where the superscript (1) in (B.6) indicates a first iteration for placing image charges inside the sphere. To maintain the condition of zero potential on the plane $z = 0$, additional image charges must be placed below the plane, with charges and coordinates given by

$$\begin{aligned} \widetilde{q}_1^{(1)} &= -q_1^{(1)} \ , \quad \widetilde{z}_1^{(1)} = -z_1^{(1)} \\ \text{and} \ \ \widetilde{q}_2^{(1)} &= -q_2^{(1)} \ , \quad \widetilde{z}_2^{(1)} = -z_2^{(1)} \ . \end{aligned} \tag{B.7}$$

These charges can be interpreted as part of the dipole induced on an image of the conducting sphere located just below the plane, as shown in Fig. B.2. However, the new charges below (above) the plane destroy the condition that the surface of the upper (lower) sphere be held at zero potential. To remedy this we must construct new image charges inside the upper (lower) sphere. The new charges will have magnitudes $q_1^{(2)}$ and $q_2^{(2)}$, and positions $z_1^{(2)}$ and $z_2^{(2)}$, respectively. The necessary charges and locations are found in the same way as for the first set of image charges. This new pair of image charges will then require the placement of a corresponding set of charges $\widetilde{q}_1^{(2)} = -q_1^{(2)}$ and $\widetilde{q}_2^{(2)} = -q_2^{(2)}$ placed symmetrically below the plane, to again satisfy the boundary condition on the plane.

Proceeding in this way, it is eventually necessary to place an infinite set of image charges inside the upper and lower spheres. It is straightforward to show that the n^{th} set of image charges have magnitudes and z coordinates given by

$$\begin{aligned} q_1^{(n)} &= \frac{r}{nR-r}Q \quad z_1^{(n)} = \frac{rR}{nR-r} \ ; \\ q_2^{(n)} &= \frac{-r}{nR+r}Q \quad z_2^{(n)} = \frac{rR}{nR+r} \ ; \end{aligned}$$

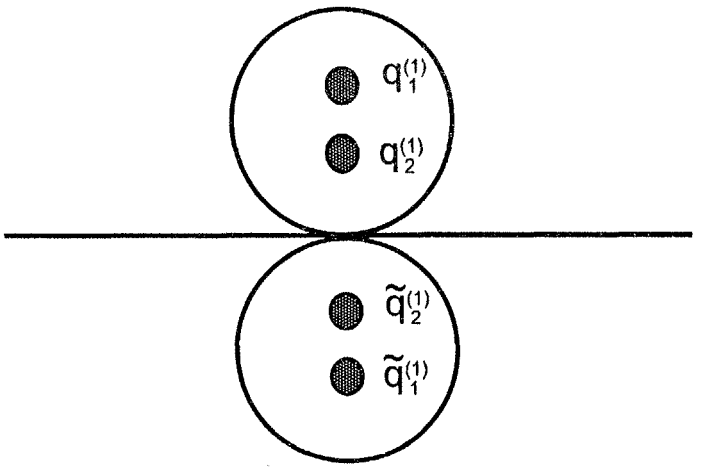

Fig. B.2. Image charges $q_1^{(1)}$, $q_2^{(1)}$, $\tilde{q}_1^{(1)}$ and $\tilde{q}_2^{(1)}$ of (B.6) and (B.7). The two charges inside each sphere are the image charges needed to produce zero potential on the sphere, with the external charges $\pm Q$ of Fig. B.1. This is the first iteration of an infinite series of image charges, for a conducting sphere in contact with an infinite plane, with both the sphere and plane held at zero potential

$$\begin{aligned} \tilde{q}_1^{(n)} &= -q_1^{(n)} \qquad & \tilde{z}_1^{(n)} &= -z_1^{(n)} \ ; \\ \tilde{q}_2^{(n)} &= -q_2^{(n)} \qquad & \tilde{z}_2^{(n)} &= -z_2^{(n)} \ . \end{aligned} \tag{B.8}$$

Though only the region with $z > 0$ is meaningful here, we have found the solution to the problem of two conducting spheres (one just above and one just below the plane $z = 0$) placed in an initially uniform $\mathbf{E}$ field having the value $\mathbf{E} = E_0\hat{\mathbf{k}}$ everywhere. In this problem the two spheres together have a net charge of zero so it is meaningful to calculate their dipole moment:

$$\begin{aligned} p_z &= \sum_{n=1}^{\infty} \left\{ q_1^{(n)} z_1^{(n)} + q_2^{(n)} z_2^{(n)} + \tilde{q}_1^{(n)} \tilde{z}_1^{(n)} + \tilde{q}_2^{(n)} \tilde{z}_2^{(n)} \right\} \\ &= \frac{8Qr^3}{R^2} \sum_{n=1}^{\infty} \frac{n}{(n^2 - r^2/R^2)^2} \ . \end{aligned} \tag{B.9}$$

The dipole moment is obtained by taking the limits (B.4) which produce the uniform E field. Upon taking these limits in (B.9), one obtains the induced dipole moment

$$p_z \to 4E_0 r^3 \sum_{n=1}^{\infty} \frac{1}{n^3} = 4E_0 r^3 \zeta(3) \ , \tag{B.10}$$

where $\zeta(3)$ in (B.10) is the Riemann Zeta Function of argument 3. The change in the field energy for the single-sphere-and-plane problem is therefore

$$\Delta U_{\mathrm{el}} = -E_0^2 r^3 \zeta(3) \quad . \tag{B.11}$$

Comparing this result with the lowest-order estimate for the change in electric field energy

$$\Delta U_{\mathrm{el}}^{(0)} = -\frac{1}{2} E_0^2 r^3 \quad , \tag{B.12}$$

shows that a correction factor of

$$c_0 = 2\zeta(3) \approx 2.40411 \tag{B.13}$$

should be applied to the induced electric dipole of the metal sphere and subsequently to the first term of (4.12), giving (B.2) for the fractional shift in the resonant frequency $\Delta f_0 / f_0$.

References

1. Datta S. (1995): Electronic Transport in Mesoscopic Systems. Cambridge Univ. Press, Cambridge
2. Ferry K., Goodnick T. (1997): Transport in Nanostructures. Cambridge Univ. Press, Cambridge
3. Mitin V.V., Kochelap V.A., Stroscio M.A. (1999): Quantum Heterostructures: Microelectronics and Optoelectronics. Cambridge Univ. Press, Cambridge
4. Reed M.A., Kirk W.P., eds. (1989): Nanostructure Physics and Fabrication. Academic Press, Boston
5. Beenaker C.W.J., van Houten H. (1991): Quantum Transport in Semiconductor Nanostructures. In: Ehrenreich H., Turnbull D. (eds.) Solid State Physics **44**. Academic Press, Boston. pp. 1–228
6. Bastard G., Brum J.A., Ferreira R. (1991): Electronic States in Semiconductor Heterostructures. In: Ehrenreich H., Turnbull D. (eds.) Solid State Physics **44**. Academic Press, Boston. pp. 229–415
7. Kramer B. (ed.) (1991): Quantum Coherence in Mesoscopic Systems, Vol. 254 of NATO Advanced Study Institute, Series B: Physics. Plenum, New York
8. Altschuler B.L., Lee P.A., Webb R.A. (eds.) (1991): Mesoscopic Phenomena in Solids. North-Holland, Amsterdam
9. Tejedor C. (ed.) (1996): Proc. 7^{th} International Conference on Modulated Semiconductor Structures. Solid St. Electr. **40**. pp. 1–823
10. Cahay M., Leburton J.P., Bandyopadhyay S., Lockwood D.J. (eds.) (1997): Proc. 4^{th} International Symposium on Quantum Confinement: Nanoscale Materials, Devices and Systems. Electrochemical Society, Pennington, NJ
11. Davies J. (1998): The Physics of Low-Dimensional Semiconductors. Cambridge Univ. Press, Cambridge
12. Weisbuch C., Vinter B (1991): Quantum Semiconductor Structures. Academic Press, Boston
13. Kelly M. J. (1995): Low-Dimensional Semiconductors: Materials, Physics, Technology, Devices. Oxford Univ. Press, Oxford
14. Duclos P., Exner P. (1995): Curvature-Induced Bound States in Quantum Waveguides in Two and Three Dimensions. Reviews in Math. Phys. **7**, 73–102
15. Schult R.L., Ravenhall D.G., Wyld H.W. (1989): Quantum Bound States in a Classically Unbound System of Crossed Wires. Phys. Rev. **B39**, 5476–5479
16. Peeters F.M. (1989): The Quantum Hall Resistance in Quantum Wires. Superlattices & Microstructures **6**, 217–225
17. Lenz F., Londergan J.T., Moniz E.J., Rosenfelder R., Stingl M., Yazaki K. (1986): Quark Confinement and Hadronic Interactions. Ann. Phys. (NY) **170**, 65–254
18. Goldstone J., Jaffe R.L. (1992): Bound States in Twisting Tubes. Phys. Rev. **B45**, 14100–14107

19. Exner P., Seba P. (1989a): Bound States in Curved Quantum Waveguides. J. Math. Phys. **30**, 2574–2580
20. Exner P. (1989b): Resonances in Curved Quantum Wires. Phys. Lett. **A141**, 213–216
21. Carini J., Londergan J.T., Mullen K., Murdock D.P. (1992): Bound States and Resonances in Waveguides and Quantum Wires. Phys. Rev. **B46**, 15538–15541
22. Carini J., Londergan J.T., Mullen K., Murdock D.P. (1993): Multiple Bound States in Sharply Bent Waveguides. Phys. Rev. **B48**, 4503–4515
23. Avishai Y., Bessis D., Giraud B.G., Mantica G. (1991): Quantum Bound States in Open Geometries. Phys. Rev. **B44**, 8028–8034
24. Sols F., Macucci M. (1990): Circular Bends in Electron Waveguides. Phys. Rev. **B41**, 11887–11891
25. Joannopoulos J., Meade R.D., Winn J.N. (1997): Photonic Crystals. Princeton Univ. Press, Princeton
26. Bulla W., Gesztesy F., Renger W., Simon B. (1997): Weakly Coupled Bound States in Quantum Waveguides. Proc. Amer. Math. Soc. **125**, 1487–1495
27. Martorell J., Klarsfeld S., Sprung D.W.L., Wu H. (1991): Analytical Treatment of Electron Wave Propagation in Two-Dimensional Structures. Solid State Commun. **78**, 13–18
28. Wu H., Sprung D.W.L., Martorell J. (1992): Effective One-Dimensional Square Well for Two-Dimensional Quantum Wires. Phys. Rev. **B45**, 11960–11967
29. Sprung D.W.L., Wu H., Martorell J. (1993): Scattering by a Finite Periodic Potential. Am. J. Phys. **61**, 1118–1124
30. Wu H., Sprung D.W.L., Martorell J. (1993): Periodic Quantum Wires and their Quasi-One-Dimensional Nature. J. Phys. D: Appl. Phys. **26**, 798–803
31. Wu H., Sprung D.W.L. (1994): Validity of the Transfer-Matrix Method for a Two-Dimensional Electron Waveguide. Appl. Phys. A **58**, 581–587
32. Landauer R. (1957): Spatial Variation of Currents and Fields due to Localized Scatterers in Metallic Conduction. IBM J. Res. Dev. **1**, 223–231
33. Landauer R. (1970): Electrical Resistance of Disordered One-Dimensional Lattices. Philosoph. Mag. **21**, 863–867
34. Lewin L. (1975): Theory of Waveguides. Newnes-Butterworth, London
35. Morse P.M., Ingard K.U. (1968): Theoretical Acoustics. Princeton Univ. Press, Princeton
36. Timp G., Chang A.M., Mankiewich P., Behringer R., Cunningham J.E., Chang T.Y., Howard R.E. (1987): Quantum Transport in an Electron Waveguide. Phys. Rev. Lett. **59**, 732–735
37. Exner P., Seba P. (1990): Trapping Modes in a Curved Electromagnetic Waveguide with Perfectly Conducting Walls. Phys. Lett. **A144**, 347–350
38. Sols F., Macucci M., Ravaioli U., Hess K. (1989): On the Possibility of Transistor Action based on Quantum Interference Phenomena. Appl. Phys. Lett. **54**, 350–352
39. Timp G., Baranger H.U., deVegvar P., Cunningham J.E., Howard R.E., Behringer R., Mankiewich P.M. (1988): Propagation around a Bend in a Multichannel Electron Waveguide. Phys. Rev. Lett. **60**, 2081–2084
40. Bastard G. (1988): Wave Mechanics Applied to Semiconductor Heterostructures. Halsted, Les Ulis: Les Editions de Physique, New York
41. Morse P.M., Feshbach H. (1953): Methods of Theoretical Physics. McGraw-Hill, New York
42. Exner P., Vugalter S.A. (1997): Bound-state asymptotic estimates for window-coupled Dirichlet strips and layers. J. Phys. A: Math. Gen. **30**, 7863–7878
43. Exner P., Vugalter S.A. (1997): Bound States in a Locally Deformed Waveguide: The Critical Case. Lett. in Math. Phys. **39**, 59–68

44. Marcus R.A. (1966): On the Analytical Mechanics of Chemical Reactions. Quantum Mechanics of Linear Collisioins. J. Chem. Phys. **45**, 4493–4499
45. Jensen H., Koppe H. (1991): Quantum Mechanics with Constraints. Ann. Phys. **63**, 586–591
46. da Costa R.C.T. (1981): Quantum Mechanics of a Constrained Particle. Phys. Rev. **A23**, 1982–1987
47. da Costa R.C.T. (1982): Constraints in Quantum Mechanics. Phys. Rev. **A25**, 2893–2899
48. da Costa R.C.T. (1983): Constrained Particles in Quantum Mechanics. Lett. Nuovo Cimento **36**, 393–396
49. Picca D. (1982): Constraints in Quantum Mechanics. Lett. Nuovo Cimento **36**, 449–452
50. Switkes E., Russell E.L., Skinner J.L. (1977): Kinetic Energy and Path Curvature in Bound State Systems. J. Chem. Phys. **67**, 3061–3067
51. Renger W., Bulla W. (1995): Existence of Bound States in Quantum Waveguides under Weak Conditions. Lett. Math. Phys. **35**, 1–12
52. Yoshitomi (1998): Band Gap of the Spectrum in Periodically Curved Quantum Waveguides. J. Diff. Eq. **142**, 123–166
53. Dunne G., Jaffe R.L. (1993): Bound States in Twisted Aharonov-Bohm Tubes. Ann. Phys. (N.Y.) **223**, 180–196
54. Reed M., Simon B. (1978): Methods of Modern Mathematical Physics. IV. Analysis of Operators. Academic Press, New York
55. Exner P., Seba P., Stovicek P. (1990): Semiconductor Edges can Bind Electrons. Phys. Lett. **A150**, 179–182
56. Exner P. (1999): private communication
57. Merzbacher E. (1970): Quantum Mechanics. Second Edition. John Wiley & Sons, New York
58. Ashcroft N.W, Mermin N.D. (1976): Solid State Physics. Holt Rinehart & Winston, New York
59. Tang K.T., Kleinman B., Karplus M.J. (1969): Solvable Quantum-Mechanical Model of Three-Body Rearrangement Scattering. J. Chem. Phys. **50**, 1119–1126
60. Eyring H., Walter J., Kimball G. (1944): Quantum Chemistry. John Wiley & Sons, New York
61. Parker R., Stoneman S.A.T. (1989): The excitation and consequences of acoustic resonances in enclosed fluid flow around solid bodies. Proc. Inst. Mech. Engrs. **203**, 9–19
62. Evans D.V., Levitin M., Vassiliev D. (1994): Existence Theorems for Trapped Modes. J. Fluid Mech. **261**, 21–31
63. Roukes M.L., Scherer A., Allen Jr. S.J., Craighead H.G., Ruthen R.M., Beebe E.D., Harbison J.P. (1987): Quenching of the Hall Effect in a One-Dimensional Wire. Phys. Rev. Lett. **59**, 3011–3014
64. Baranger H.U., Stone A.D., DiVincenzo D.P. (1988): Resistance Fluctuations in Multiprobe Microstructures: Length Dependence and Nonlocality. Phys. Rev. **B37**, 6521–6524
65. Wegscheider W., Pfeiffer L.N., Dignam M.M., Pinczuk A., West K.W., McCall S.L., Hull R. (1993): Lasing from Excitons in Quantum Wires. Phys. Rev. Lett. **71**, 4071–4074
66. Wu J.C., Wybourne M.N., Yindeepol W., Weisshaar A., Goodnick S.M. (1991): Interference Phenomena due to a Double Bend in a Quantum Wire. Appl. Phys. Lett. **59**, 102–104
67. McEuen P.L., Alphenaar B.W., Wheeler R.G., Sacks R.N. (1990): Resonant Transport Effects due to an Impurity in a Narrow Constriction. Surf. Sci. **229**, 312–315

68. Kirczénow G. (1989a): Bend Resistance and Junction Resonances in Narrow Quantum Conductors. Solid State Commun. **71**, 469–472
69. Kirczenow G. (1989b): Mechanism of the Quenching of the Hall Effect. Phys. Rev. Lett. **62**, 2993–2996
70. Fisher D.S., Lee P.L. (1981): Relation between Conductivity and Transmission Matrix. Phys. Rev. **B23**, 6851–6854
71. Stone A.D., Szafer A. (1988): What is Measured when You Measure a Resistance?: The Landauer Formula Revisited. IBM J. Res. Dev. **32**, 384–413
72. Baranger H.U., Stone A.D. (1989): Electrical Linear-Response Theory in an Arbitrary Magnetic Field: A New Fermi-Surface Formation. Phys. Rev. **B40**, 8169–8193
73. Lent C.S., Kirkner D.J. (1990): The Quantum Transmitting Boundary Method. J. Appl. Phys. **67**, 6353–6359
74. Frohne H.R., McLennan M.J., Datta S. (1989): An Efficient Method for the Analysis of Electron Waveguides. J. Appl. Phys. **66**, 2699–2705
75. Xu H., Ji Z.-L., Berggren K.-F. (1992): Electron Transport in Finite One-Dimensional Quantum-Dot Arrays. Superlattices and Microstructures **12**, 237–242
76. Wu H., Sprung D.W.L., Martorell J. (1999): Addendum to Ref. [30]. to be published
77. Vezzetti D.J., Cahay M. (1986): Transmission Resonances in Finite, Repeated Structures. J. Phys. **D19**, L53–L55
78. Schiff L.I. (1968): Quantum Mechanics, 3^{rd} Edition. McGraw-Hill, New York
79. Wu H., Sprung D.W.L., Martorell J., Klarsfeld S. (1991): Quantum Wire with Periodic Serial Structure. Phys. Rev. **B44**, 6351–6360
80. Wu H., Sprung D.W.L. (1993): Theoretical Study of Multiple-Bend Quantum Wires. Phys. Rev. **B47**, 1500–1505
81. Griffith J. S. (1953a): A Free-Electron Theory of Conjugated Molecules, Part I - Polycylic Hydrocarbons. Trans. Faraday Soc. **49**, 345–351
82. Griffith S. (1953b): A Free-Electron Theory of Conjugated Molecules, Part II - A Derived Algebraic Sturcture. Proc. Camb. Phil. Soc. **49**, 650–658
83. Xia J. (1992): Quantum Waveguide Theory for Mesoscopic Structures. Phys. Rev. **B45**, 3593–3599
84. Mao J.M., Huang Y., Zhou J.M. (1993): The Role of Impurity Scattering in the Quantum Waveguide. J. Appl. Phys. **73**, 1853–1857
85. Deo P.S., Jayannavar A.M. (1993): Persistent Currents due to Evanescent Modes. Mod. Phys. Lett. **B7**, 1045–1051
86. Deo P.S., Jayannavar A.M. (1994): Quantum Waveguide Transport in Serial Stub and Loop Structures. Phys. Rev. **B50**, 11629–11639
87. Gu B.-Y. (1995): Characteristics of the Conductance of a Quantum Waveguide Containing an Array of Stubs: Numerical Simulation . Phys. Rev. **B51**, 16840–16847
88. Shi J.-R., Gu B.-Y. (1997): Quantum Waveguide Transport with Side-Branch Structures: A Recursive Algorithm. Phys. Rev. **B55**, 4703–4709
89. Yeh P. (1988): Optical Waves in Layered Media. Wiley, New York
90. Exner P. (1990): Bound States and Resonances in Quantum Wires. In: Exner P., Neidhardt H. (eds.) . Order, Disorder, Chaos in Quantum Systems. Birkhäuser Verlag, Basel. pp. 65–84
91. Kugler M., Shtrikman S. (1988): Berry's Phase, Locally Inertial Frames, and Classical Analogues. Phys. Rev. **D37**, 934–937
92. Takagi S., Tanzawa T. (1992): Quantum Mechanics of a Particle Confined to a Twisted Ring. Prog. Theor. Phys. **87**, 561–568

93. Newton R. (1982): Scattering Theory of Waves and Particles. Second Edition. Springer-Verlag, New York
94. Goldberger M.L., Watson K.M. (1964): Collision Theory. John Wiley & Sons, New York
95. Trinkle D. (1995): Theoretical Studies of Bent Two-Dimensional Quantum Wires. Indiana University Summer Undergraduate Research in Nuclear Physics, unpublished
96. Bayman B.F., Mehoke C.J. (1983): Quasibound-State Resonances for a Particle in a Two-Dimensional Well. Am. J. Phys. **51**, 875–883
97. Barnett R.M., Carone C.D., Groom D.E., Trippe T.G., Wohl C.G., Armstrong B., Gee P.S., Wagman G.S., James F., Mangano M., Mönig K., Montanet L., Feng J.L., Murayama H., Hern'andez J.J., Manohar A., Aguilar-Benitez M., Caso C., Crawford R.L., Roos M., Törnqvist N.A., Hayes K.G., Hagiwara K., Nakamura K., Tanabashi M., Olive K., Honscheid K., Burchat P.R., Shrock R.E., Eidelman S., Schindler R.H., Gurtu A., Hikasa K., Conforto G., Workman R.L., Grab C., Amsler C. (1996): Review of Particle Physics. Phys. Rev. **D54**, 1–708
98. Lin K., Jaffe R.L. (1996): Bound States and Threshold Resonances in Quantum Wires with Circular Bends. Phys. Rev. **B54**, 5750–5762
99. Lent C.S. (1990): Ballistic Current Vortex Excitations in Electron Waveguide Structures. Appl. Phys. Lett. **57**, 1678–1680
100. Berggren K.-F., Besev C., Ji Z.-L. (1992): Transition from Laminar to Vortex Flow in a Model Semiconductor Nanostructure. Phys. Scripta **T42**, 141–148
101. Ji Z.-L., Berggren K.-F. (1992): Quantum Bound States in Narrow Ballistic Channels with Intersections. Phys. Rev. **B45**, 6652–6658
102. Berggren K.-F., Ji Z.-L. (1993): Transition from Laminar to Vortical Current Flow in Electron Waveguides with Circular Bends. Phys. Rev. **B47**, 6390–6394
103. Ji Z.-L. (1993): Ballistic Transport through a Double Bend in an Electron Waveguide. J. Appl. Phys. **73**, 4468–4472
104. Wang C.-K. (1995): Quantum Bound States in a Ballistic Quantum Channel with a Multiple Double-Bend Discontinuity. Semicond. Sci. Technol. **10**, 1131–1138
105. Wu H., Sprung D.W.L. (1993): Quantum Probability Flow Patterns. Phys. Lett. **A183**, 413–417
106. Bohm D. (1952): A Suggested Interpretation of the Quantum Theory in Terms of "Hidden" Variables. I. Phys. Rev. **85**, 166–179
107. Bohm D. (1952): A Suggested Interpretation of the Quantum Theory in Terms of "Hidden" Variables. II. Phys. Rev. **85**, 180–193
108. Dirac P.A.M. (1931): Quantised Singularities in the Electromagnetic Field. Proc. Roy. Soc. **A133**, 60–72
109. Hirschfelder J.O. (1977): The Angular Momentum, Creation and Significance of Quantized Vortices. J. Chem. Phys. **67**, 5477–5483
110. Sharvin Yu V. (1965): A Possible Method for Studying Fermi Surfaces. Sov. Phys. JETP **21**, 655–656
111. Sharvin Yu V., Bogatina N.I. (1969): Investigation of Focusing of Electron Beams in a Metal by a Longitudinal Magnetic Field. Sov. Phys. JETP **29**, 419–423
112. Laux S.E., Frank D.J., Stern F. (1988): Quasi-One-Dimensional Electron States in a Split-Gate GaAs/AlGaAs Heterostructure. Surf. Sci. **196**, 101–106
113. Kojima K., Mitsunaga K., Kyuma K. (1989): Calculation of Two-Dimensional Quantum-Confined Structures using the Finite Element Method. Appl. Phys. Lett. **55**, 882–884

114. Martorell J., Wu H., Sprung D.W.L. (1994): Systematic Trends in Self-Consistent Calculations of Linear Quantum Wires. Phys. Rev. **B50**, 17298–17308
115. Webb R.A., Washburn S., Umbach C.P., Laibowitz R.B. (1985): Observation of h/e Aharonov-Bohm Oscillations in Normal-Metal Rings. Phys. Rev. Lett. **54**, 2696–2699
116. Baranger H.U. (1990): Multiprobe Electron Waveguides: Filtering and Bend Resistances. Phys. Rev. **B42**, 11479–11495
117. Büttiker M., Imry Y., Landauer R. (1983): Josephson Behaviour in Small Normal One-Dimensional Rings. Phys. Lett. **A96**, 365–367
118. Büttiker M., Imry Y., Landauer R. (1983): Josephson Behavior in Small Normal One–Dimensional Rings. Phys. Lett. **A96**, 365–367
119. Landauer R. (1987): Electrical Transport in Open and Closed Systems. Z. Phys. **B68**, 217–228
120. Anderson P.W., Thouless D.J., Abrahams E., Fisher D.S. (1980): New Method for a Scaling Theory of Localization. Phys. Rev. **B22**, 3519–3526
121. Economou E.N., Soukoulis C.M. (1981): Static Conductance and Scaling Theory of Localization in One Dimension. Phys. Rev. Lett. **46**, 618–621
122. van Wees B.J., Kouwenhoven L.P., Willems E.M.M., Harmans C.J.P.M., Mooij J.E., van Houten H., Beenaker C.W.J., Williamson J.G., Foxon C.T. (1991): Quantum Ballistic and Adiabatic Electron Transport Studied with Quantum Point Contacts. Phys. Rev. **B43**, 12431–12453
123. Castaño E. , Kirczenow G. (1990): Theory of Nonlinear Transport in Narrow Ballistic Constrictions. Phys. Rev. **B41**, 3874–3877
124. Wang C.-K., Berggren K.-F. (1996): Nonlinear Transport in a Ballistic Quantum Channel Modulated with a Double-Bend Structure. Semicond. Sci. Technol. **11**, 207–213
125. Kirczenow G. (1989): Resonant Conduction in Ballistic Quantum Channels. Phys. Rev. **B39**, 10452–10455
126. Szafer A., Stone A.D. (1989): Theory of Quantum Conduction through a Constriction. Phys. Rev. Lett. **62**, 300–303
127. Wang C.-K., Berggren K.-F., Ji Z.-L. (1995): Quantum Bound States in a Double-Bend Quantum Channel. J. Appl. Phys. **77**, 2564–2571
128. Berggren K.-F., Ji Z.-L. (1991): Resonant Tunneling via Quantum Bound States in a Classically Unbound System of Crossed, Narrow Channels. Phys. Rev. **B43**, 4760–4764
129. Jackson J.D. (1999): Classical Electrodynamics, Third Edition. John Wiley, New York
130. Maier L.C., Slater J.C. (1952): Field Strength Measurements in Resonant Cavities. J. Appl. Phys. **23**, 68–83
131. Amato J.C., Herrmann H. (1985): Improved Method for Measuring the Electric Fields in Microwave Cavity Resonators. Rev. Sci. Instrum. **56**, 696–699
132. Abramowitz M., Stegun I.A. (1964): Handbook of Mathematical Functions. National Bureau of Standards, Washington, DC
133. Carini J., Londergan J.T., Murdock D.P., Trinkle D., Yung C.S. (1997): Bound States in Waveguides and Bent Quantum Wires. I. Applications to Waveguide Systems. Phys. Rev. **B55**, 9842–9851
134. Yung C.S. (1995): Localized States in Waveguides and 'Quantum Wires' - Experimental Studies of Two-Dimensional Systems, with Applications to Condensed Matter Physics and Transmission in Waveguides. Indiana University Summer Undergraduate Research in Nuclear Physics, unpublished
135. Sridhar S. (1991): Experimental Observation of Scarred Eigenfunctions of Chaotic Microwave Cavities. Phys. Rev. Lett. **67**, 785–788

136. Harle L. (1996): Resonant States in Bent Microwave Waveguides. Indiana University Summer Undergraduate Research in Nuclear Physics, unpublished
137. Lent C.S. (1990): Transmission through a Bend in an Electron Waveguide. Appl. Phys. Lett. **56**, 2554–2556
138. Sprung D.W.L., Wu H. (1992): Understanding Quantum Wires with Circular Bends. J. Appl. Phys. **71**, 515–517
139. Fano U. (1961): Effects of Configuration Interaction on Intensities and Phase Shifts. Phys. Rev. **124**, 1866–1878
140. Sols F., Macucci M., Ravaioli U., Hess K. (1989): Theory for a Quantum Modulated Transistor. J. Appl. Phys. **66**, 3892–3906
141. Brum J.A. (1991): Electronic Properties of Quantum-Dot Superlattices. Phys. Rev. **B43**, 12082–12084
142. Kouwenhoven L.P., Hekking F.W.J., van Wees B.J., Harmans C.J.P.M., Timmering C.E., Foxon C.T. (1990): Transport through a Finite One-Dimensional Crystal. Phys. Rev. Lett. **65**, 361–364
143. de Aguiar F.M., Wharam D.A. (1991): Transport through One-Dimensional Channels. Phys. Rev. **B43**, 9984–9987
144. Haug R.J., Lee K.Y., Hong J.M. (1990): Transport in Lateral Superlattices with Few Periods. In: Berger S.D., Craighead H.G., Kern D., Smith III T.P. (eds.) Nanostructures: Fabrication, Physics, (MRS Symposia Proceedings No. EA-26). Materials Research Society, Pittsburgh. pp. 29–32
145. Haug R.J., Lee K.Y., Smith III T.P. , Hong J.M. (1990): Magnetotransport Studies of One-Dimensional Superlattices with Few Periods. In: Joannopoulos J. (ed.) Proceedings of the 20th International Conference on the Physics of Semiconductors. World Scientific, Singapore. pp. 2443–2446
146. Lent C.S., Sivaprakasam S., Kirkner D.J. (1989): A Two-Dimensional Hot Carrier Injector for Electron Waveguide Structures. Solid-State Electron. **32**, 1137–1141
147. Datta S. (1989): Quantum Devices. Superlattices and Microstructures **6**, 83–93
148. Porod W., Shao Z., Lent C.S. (1992): Transmission Resonances and Zeros in Quantum Waveguides with Resonantly Coupled Cavities. Appl. Phys. Lett. **61**, 1350–1352
149. Porod W., Shao Z., Lent C.S. (1993): Resonance-Antiresonance Line Shape for Transmission in Quantum Waveguides with Resonantly Coupled Cavities. Phys. Rev. **B48**, 8495–8498
150. Weisshaar A., Lary J., Goodnick S.M., Tripathi V.K. (1991): Analysis and Modeling of Quantum Waveguide Structures and Devices. J. Appl. Phys. **70**, 355–366
151. Jacak L., Hawrylak P., Wojs A. (1998): Quantum Dots. Springer-Verlag, New York
152. Yindeepol W., Chin A., Weisshaar A., Goodnick S.M., Wu J.C., Wybourne M.N. (1992): Interference Phenomena due to Bend Discontinuities in Point Contact Structures. In: Kirk W.P., Reed M.A. (eds.) Nanostructures, Mesoscopic Systems. Academic Press, Boston. pp. 139–149
153. Sprung D.W.L. (1998): private communication
154. Weisshaar A., Lary J., Goodnick S.M., Tripathi V.K. (1989): Analysis of Discontinuities in Quantum Waveguide Structures. Appl. Phys. Lett. **55**, 2114–2116
155. Kawamura T., Leburton J.P. (1993): Quantum Conduction through Double-Bend Electron Waveguide Structures. J. Appl. Phys. **73**, 3577–3579
156. Yalabik M.M. (1993): Electronic Transport in a Laterally Patterned Resonant Structure. In: Balkan N. et al (eds.) Negative Differential Resistance, Instabilities in 2-D Semiconductors. Plenum Press, New York. pp. 171–177

157. Yalabik M.M. (1994): Electronic Transport through a Kink in an Electron Waveguide. IEEE Trans. on Elect. Dev. **41**, 1843–1847
158. Carini J., Londergan J.T., Murdock D.P. (1997): Bound States in Waveguides and Bent Quantum Wires. II. Electrons in Quantum Wires. Phys. Rev. **B55**, 9852–9859
159. Wu J.C., Wybourne M.N., Weisshaar A., Goodnick S.M. (1993): Waveguide Effects in Quantum Wires with Double-Bend Discontinuities. J. Appl. Phys. **74**, 4590–4597
160. Hannan M., Giannetta R.W., Grundbacher R., Adesida I., Eom J., Chandrasekhar V. (1996): Conductance Studies in a Double-Bend Quantum Structure. Superlattices and Microstructures **20**, 427–433
161. Alphenaar B.W., McEuen P.L., Wheeler R.G., Sacks R.N. (1991): The Influence of Impurities on Inter-Landau-Level Equilibration. Physica B **175**, 235–238
162. Mekis A., Chen J.C., Kurland I., Fan S., Villeneuve P., Joannopoulos J. (1996): High Transmission through Sharp Bends in Photonic Crystal Waveguides. Phys. Rev. Lett. **77**, 3787–3790
163. Lent C.S., Leng M. (1991): Bloch States of Electrons in a Corrugated Quantum Channel in a Magnetic Field. Appl. Phys. Lett. **58**, 1650–1652
164. Davison S., Steslicka M. (1992): Basic Theory of Surface States. Oxford Univ. Press, New York
165. Tamm I.E. (1932): Über ein Mögliche Art der Elektron Bindung an Kristalloberflächen. Z. Phys. **76**, 849–850
166. Shockley W. (1939): On the Surface States Associated with a Periodic Potential. Phys. Rev. **56**, 317–323
167. Kronig R. de L., Penney W.G. (1930): Quantum Mechanics of Electrons in Crystal Lattices. Proc. Roy. Soc. **A130**, 499–513
168. Datta S., McLennan M.J. (1990): Quantum Transport in Ultrasmall Electronic Devices. Rep. Prog. Phys. **53**, 1003–1047
169. Capasso F., Sirtori C., Faist J., Sivco D.L., Chu S–N G., Cho A.Y. (1992): Observation of an Electronic Bound State Above a Potential Well. Nature **358**, 565–567
170. Fowles G.R. (1989): Introduction to Modern Optics. Dover, New York
171. Sirtori C., Capasso F., Faist J., Sivco D.L., Chu S-N G., Cho A.Y. (1992): Quantum Wells With Localized States at Energies Above the Barrier Height: a Fabry–Perot Electron Filter. Appl. Phys. Lett. **61**, 898–900
172. Sirtori C., Faist J., Capasso F., Sivco D.L., Cho A.Y. (1993): Narrowing of the Intersubband Absorption Spectrum by Localization of Continuum Resonances in a Strong Electric Field. Appl. Phys. Lett. **62**, 1931–1933
173. Yablonovitch E., Gmitter T.J., Meade R.D., Rappe A.M., Brommer K.D., Joannopoulos J.D. (1991): Donor and Acceptor Modes in Photonic Band Structure. Phys. Rev. Lett. **67**, 3380–3383
174. Washburn S. (1992): Trapped in Mid-Air. Nature **358**, 537–538
175. Mekis A., Fan S., Joannopoulos J. (1998): Bound States in Photonic Crystal Waveguides and Waveguide Bends. Phys. Rev. **B58**, 4809–4817
176. Souloulis C.M., *ed.* (1993): Photonic Band Gaps and Localization (NATO ASI Series Vol. 308). Plenum Press, New York
177. Ho K.M., Chan C.T., Souloulis C.M. (1990): Existence of a Photonic Gap in Periodic Dielectric Structures. Phys. Rev. Lett. **65**, 3152–3155
178. Wendt J.R., Vawter G.A., Gourley P.L., Brennan T.M., Hammons B.E. (1993): Nanofabrication of Photonic Lattice Structures in GaAs/AlGaAs. J. Vac. Sci. & Tech. **B11**, 2637–2640

179. Meade R.D., Rappe A.M., Brommer K.D., Joannopoulos J.D., Alerhand O.L. (1993): Accurate Theoretical Analysis of Photonic Band–Gap Materials. Phys. Rev. **B48**, 8434–8437
180. Wu H., Sprung D.W.L., Martorell J. (1993): A Comparison of Confining Potentials in the Quantum Wire Problem. Appl. Phys. **A56**, 127–131

Index

acoustic resonance 67
allowed region 29, 147, 157
– for periodic system 156
auxiliary matrices 25
auxiliary wave function 24, 31, 111

band structure 145, 154–157
– allowed band 156
– forbidden band 155
– in photonic crystals 184–187
bends in tubes
– two coupled bends 113–136
Bessel function 83
binding energy 32, 85, 97
Bloch phase 28, 128, 147, 148, 155, 160, 166, 168
– allowed and forbidden regions 147
Bloch states 185
Bohm formulation 48
bound states 7
– existence proofs 13, 15, 17, 33
– from bulges 11–15
– from curvature 15–18
– in circular bend 86–91
– in continuum 172, 176
– in deformed tubes 18–23
– in double bends 114–123, 128
– in forbidden regions 149
– in L-shaped tube 20, 32, 43
– in periodic systems 146–152
– in photonic crystals 189–195
– in quantum dot 103, 108
– in series of stubs 152
– in sharply-bent tube 98
– in staircase and snake 149–152
– in stubs 103–104
– nodes in 32, 148, 152
– three-dimensional tubes 33–35
boundary condition 38
– continuity 25
– Dirichlet 7
– hard wall 7, 8, 83
– photonic waveguides 188, 194
Brillouin zone 185
bulges in tubes 11–15

cavity perturbation method 73
circular bend
– large bend angle 88–91
– small curvature 84–86
– square well approximation 84, 90
– transmission in 91–95
complete band gap 186
conductance 58–63, 65
– effect of sharp corners 129, 159
– in double-bend wire 126–136
– in L-shaped tube 69
– in multi-bend tube 159
– in quantum dot 112
– in series of quantum dots 166, 171
– in straight channel 64–66
– quantized behavior 62, 63, 67, 128, 132, 159
– subthreshold peaks 23, 110, 128, 130, 135–136, 149, 159, 161, 163, 166, 172
– temperature dependence 62, 63, 66, 68, 132
conducting sphere
– frequency shift 74, 77, 100, 121, 203
– on grounded surface 203–207
continuum threshold 9, 28, 38, 43, 93, 128, 159, 168
cross geometry *see* quantum dot
current conservation method 31
curved tubes
– three-dimensional 33–35
– two-dimensional 15–18

defects 173–179
– and transmission minima 175
– and transparency 175
– and trapped modes 175–179
density of states 177

dielectric constant 182
dimensions
– and scaling laws 11
donor 54
double bends 113–136
– bound states 114–123, 128
– transmission 123–136
– with circular bends 129, 136

effective mass 11
effective potential 13, 16, 21, 33, 82
effective square well 30
– for circular bend 84, 90
– for double bend 119
– for L-shaped tube 32
– for multibend wire 151
electric current 59
electric dipole moment 206
electron conductance *see* conductance
energy functional
– electromagnetic 184
energy gap 8
envelope function 156, 159

Fabry–Perot interferometer 177
Fano resonance 95
Fermi distribution 66
Fermi energy 59
Fermi momentum 64
Fermi wavelength 58
forbidden region 29, 147, 157, 159, 164, 166
– and bound states 149
– for periodic system 155
– resonance within 175–179
Frenet frame 33

GaAs
– in photonic crystals 182
GaAs/AlGaAs systems 54–57
– confining potentials in 56
gate voltage 56, 62, 105, 135

Helmholtz equation 11, 72

impurity site 135
induced dipole 206

Kronig–Penney model 152, 157

L-shaped tube 31–33
– bound state 20, 32, 43
– probability currents in 50
– transmission in 40

laminar flow 51, 136
Landauer formula 59–62, 126, 149
lasing 23
longitudinal resonance 67

mapping EM energy density 73–75, 77, 100, 121–123
master equation 184
– matrix form 185
Maxwell equations 72
– for mixed dielectric media 182–184
mean free path 58
method of images 203–206
miniband 146, 151, 152, 155, 161
multiple-bend tube
– bound states 149–152, 159
– transmission 157–163

nodes 32, 148
– and vortices 48

open mode approximation 27, 30, 154
orthonormal solutions 24

parallel transport frame 34
periodic systems
– band structure 154–157
– bound states 146–152
– transmission 157–173
phase coherence length 58
photonic band gap 181, 187
– and guided modes 188
– complete 186
photonic crystals 181
– band structure 184–187
– bound states 189–195
– waveguides in 187–189
plateau *see* conductance, quantized behavior
probability current density 47–54, 136
– in quantum dot 112
probability density
– in quantum dot 108, 112
– in series of stubs 152

quantum confinement 22
quantum dot 108, 152
– and rectangular cell 170
– bound state 103, 108
– superlattice 163
quantum heterostructure 7, 54–58, 173
– experimental studies 132, 164, 177–179

quantum point contact 56, 67
quantum potential 48
quantum transistor 105
quantum vortex 49
quantum waveguide 8
quantum wire 56
quasi-bound state 42, 44–47, 94, 117, 128, 130, 147, 149, 159, 163
quasicrystal 178

reflection amplitude 28, 38, 123
reflection coefficient 38
– for circular bend 91
reflection probability 39
reflection symmetry 39
resonating cavity 72

S-matrix 40, 44
– poles of 43, 44
– unitarity 40
series of identical cells 29, 145
– defects in 173–179
– right angle bends 149–152, 157–163
– stubs 152
– two cells 113–136
series of stubs
– bound states 152
– transmission 163–173
sharply-bent tube 95–102
single-mode approximation 27, 30, 146–148
– for circular bend 92
– for double bend 115, 123–126
– for L-shaped tube 32, 41
– for periodic systems 154–157
– for quantum dot 111
– series of quantum dots 166
spiral tube 18
square well potential 30, 32, 84, 119, 151
stream lines 49, 136
stubs 102–113
– bound states 103–104
– periodicity in transmission 105
– transmission in 104–113
subthreshold peak *see* conductance, subthreshold peaks
superlattice 163
surface state 149
surface states
– in photonic crystals 189
symmetry
– broken 187
– crystal lattice 185
– under reflection 25, 31, 83, 87, 115, 130, 148, 194

T-stub *see* stubs
Tamm state 149
TE mode 186
TM mode 143, 186
torsion 33, 35
transfer matrix 123
– bound state condition 29, 146
– definition 26
– for double bend 115
– for multiple bends 150
– for quantum dot 110–111
– for series of identical cells 154
– formalism 23–31
– symmetric cell 25
– technical difficulties 27
transmission
– maxima 52, 125, 156
– minima 51, 124, 136, 155, 156, 159, 163, 168
– from defect 175
– perfect 124, 155
transmission amplitude 28, 38, 43, 123
– Argand diagram for 45, 93
– behavior near threshold 43
– pole 94
transmission coefficient 38, 104
– for circular bend 91–95
– periodic system with defect 176
– photonic crystal waveguide 189
– series of quantum dots 166, 168
transmission matrix 62
transmission probability 39, 42, 92, 108, 124, 156, 159
transparency *see* transmission, perfect
transverse eigenfunction 11, 37, 83, 154
tube 2, 7
– width, rescaled 11
tunneling 63, 110, 128, 130, 159, 163
– through impurity site 135
two-dimensional electron gas 55, 58, 132

unitarity of S-matrix 40

variational proof 13, 17, 33
variational theorem
– electromagnetic 184
velocity node 49

vortex 48–54, 136
– in quantum dot 112–113

waveguides
– confined modes in 72, 76–78
– EM energy density 73
– in photonic crystals 187–189
–– bent 193–195
–– U-shaped 192
–– with constrictions 190–192
– microwave measurements in 75–80, 99–102, 121–123
– transmission 78–80
wire 2